The Tritium Recoil-Ion Mass Spectrometer Experiment

Ying-Ting Lin

A dissertation
submitted in partial fulfillment of the
requirements for the degree of

Doctor of Philosophy

University of Washington

2019

Reading Committee:

Diana Parno, Chair

Hamish Robertson

Jason Detwiler

Program Authorized to Offer Degree:
Physics

University of Washington

Abstract

The Tritium Recoil-Ion Mass Spectrometer Experiment

Ying-Ting Lin

Chair of the Supervisory Committee:
Professor Diana Parno
Department of Physics

The Tritium Recoil-Ion Mass Spectrometer (TRIMS) experiment measures the branching ratio between bound ($^3HeT^+$) and unbound (T^+, $^3He^+$) ions that are produced by molecular tritium (T_2) beta-decay. This measurement will help validate the current molecular final-state theory utilized by direct neutrino mass experiments such as KATRIN and Project 8. The TRIMS experiment sets up a uniform guiding magnetic field of 0.24 T and a uniform electric field of 60 kV/25 cm that run parallel to each other and coaxial with a cylindrical acceleration chamber. Inside the chamber, tritium decays and the product ions are accelerated toward a silicon ion detector at the cathode and the betas to a silicon beta detector at the anode. By performing energy and time of flight measurements of the coincident ions and betas, TRIMS can categorize these events and so derives the branching ratio in question. The preliminary results from the TRIMS experiment are in agreement with the modern theory.

TABLE OF CONTENTS

ACKNOWLEDGMENTS

First and foremost, I would like to thank Diana Parno for being such an excellent advisor. Her philosophy of creating simple and descriptive plots has guided my training as an experimentalist; to some extent, my analysis work can be summarized as making "pretty plots" to debug and interpret our data. Diana also kept on reminding me to record my progress, and then she would make countless comments and suggestions on top of what I had written down. This turns out to be one of the most valuable life lesson I received; it is a practice that allows me to not lose my track even at times when I was overwhelmed.

I owe many thanks to Hamish Robertson, who apparently never ran out of brilliant ideas to push the experiment forward. He got this "this is what we can try next" at every stage of the experiment, no matter whether it was hardware construction or data analysis development. What amazes me the most is that, out of all exotic events that we observe in our data, we can explain all of them, thanks in large part to Hamish. His vast knowledge base and his care of the TRIMS group are what motivated me to continue my studies everyday.

I would like to thank all the TRIMS members, especially Laura Bodine who passed down the essentials of TRIMS to me, Matt Kallander who has always been very skilled in putting things together, Eric Machado who has the best sense of humor in town, and Ana Paula Vizcaya Hernández who is picking up the remainder of the TRIMS work. It is because of our combined work that we can keep the TRIMS experiment going and being enjoyable at the same time. I also appreciate the CENPA engineers for always supplying us with all the most delicate instruments and IT supports. In particular Tom Burritt, Gary Holman, David Peterson, Eric Smith, Tim Van Wechel, and Doug Will, I never cease to be impressed by their skills and their pick-up-your-completed-parts reminders the next morning. And I just

want to say thanks to the fascinating community at CENPA. Not only do I enjoy the physics discussions after the seminars, during the journal club, or when we all got too tired from coding, but I also enjoy the discussions about Hollywood or non-Hollywood movies some other time. In particular, I want to thank Micah Buuck and Ian Guinn my long-time office mates; listening to their discussion that alternate between difficult technical concepts and some goofy topics always amused me. CENPA is a lively place to work.

I want to thank Daniel Gochnauer for being my awesome friend through my graduate studies, who shares with me his amusing stories about laser physics and board game strategies. I also want to thank my friend Natalie Klco, who is popular and always travels to conferences, for showing me how the vast nuclear theoretical work can be connected to quantum computing. I am always inspired by my dear friend Pak Kau Lim for his fearless pursuit of physics and mathematics. I have no doubt he will be a fine condensed matter theorist in no time. Lastly, I want to thank my physics-education-expert friend Sheh Lit Chang for reminding me that there are many other interesting topics besides just physics. Thank you friends, graduation school turns out to be fun because of you guys!

Finally, I would like to thank all my family members for supporting my decision to live abroad for almost 10 years. A special thank to my sister, who shares a similar life style with me. She is always there to talk about anything. Our pet dog 566 is a symbol of our family bond while we are far away from each other.

My work has been supported by the Department of Energy Office of Science, Office of Nuclear Physics Program under grant No. DE-FG02-97ER41020.

DEDICATION

To 566

LIST OF FIGURES

LIST OF TABLES

GLOSSARY

2WS Double Woods-Saxon function: the function we used to fit two-particle events (Sec. 5.3.4)

2TF Double-Trapezoidal Filter: the signal processing method that we used to extract pulse amplitude (Sec. 5.2.1)

ADC Analog-to-Digital Converter: the unit used to describe the uncalibrated pulse amplitude that depends specifically on the electronics

BEANS Building ... Analysis ... Sequence: a signal processing software developed for the KATRIN experiment; we used its framework on our signal processing chain (Sec. 5.4)

BR Branching Ratio

COMSOL a multi-physics software developed by COMSOL Inc.; we used it to simulate the electromagnetic fields in our apparatus (Sec. 3.3)

CFD Constant Fraction Discriminator: a general signal processing method for pulse timing extraction

dCFD digital Constant Fraction Discriminator: the digital version of CFD that we used to extract pulse timing (Sec. 5.3.2)

DAQ Data AQuisition

DDF Data Distribution Function: the output of the scan deconvolution in our analysis; $\mathrm{RCF} = \mathrm{PSF} * \mathrm{DDF}$ (Sec. 8.1)

DOF Degree Of Freedom

ELOG a web logging application; we used it as a log books to record our progress

FET Field Effect Transistor: an sensitive electronic part used in detector preamp designs

FSD Final State Distribution of the molecular tritium decay

FWHM Full Width Half Maximum

FV Fiducial Volume

Geant4 GEometry ANd Tracking: a simulation software developed by CERN; we used it to simulate particle trajectories in our apparatus (Sec. 3.1)

GUI Graphical User Interface

HV High Voltage

IC Internal Conversion

JT Joule-Thomson cooler: a detector cooler that we developed based on Joule-Thomson effect

KAFFEE Katrin Automation Framework ...: an automation software developed for KATRIN; we used it to automate our signal processing chain (Sec. 5.4.3)

ORCA Object-oriented Realtime Control and Acquisition: a DAQ software developed for the SNO experiment; it's our DAQ software of choice

PIPS Passivated Implanted Planar Silicon detectors: silicon detectors produced by CANBERRA Industries - Mirion Technologies; they are our detectors of choice

PSF Point Spread Function: the smearing matrix of the scan deconvolution in our analysis; RCF = PSF $*$ DDF (Sec. 8.1)

RCF Raw Count Function: the input of the scan deconvolution in our analysis; RCF = PSF $*$ DDF (Sec. 8.1)

RGA Residual Gas Analyzer: a device that measure the air composition in a vacuum system

ROOT an object-oriented C++ library developed by CERN for data analysis; we used it in the majority of our data analysis softwares

SRIM Stopping and Range of Ions in Matter: a software that simulate particle response in matter; we used it to study the energy lost of the incident ions to the silicon detector (Sec. 3.2)

SRG Spin Rotor Gauge: a device the measures the pressure of a vacuum system

TOF Time Of Flight

UHV Ultra-High Vacuum

WS Woods-Saxon function: sigmoid function we used to fit our waveforms

Chapter 1

GENERAL NEUTRINO PHYSICS

1.1 Neutrinos in the Standard Model

Neutrinos are elementary particles that barely interact with ordinary matters consist of quarks and leptons. However, neutrino physics has sparked great theoretical as well as experimental interest. In fact, one can say studying neutrinos has guided immense development of nuclear and particle physics for the past 90 years. All this started with beta decay, which was understood as a decay process of a nucleus that turns a neutron into a proton with an electron (or vice versa with a positron). Today, we know that neutrinos are also involved in these beta decays.

The first evidence of neutrinos came from measuring the beta spectrum, i.e. the energy distribution of the emitted electron from a particular beta decay channel. At the beginning, the beta decay was thought to involve only the nucleus emitting the electron. Then by the conservation of energy for a two-body process, the emitted electron ought to have a fixed allowed energy called the Q-value and the beta spectrum would include only a single peak at the Q-value. However, Chadwick's experiment [1] showed in 1914 that the beta spectrum is in fact a continuous energy spectrum ranging from 0 to the Q-value. Around 1930, based on Chadwick's discovery, Pauli [2, 3, 4] hypothesized the neutrino as the third particle in addition to the nucleus and the electron. This hypothetical particle was first postulated to be a massless charge-neutral spin-1/2 fermion that only weakly interact with other particles. Fermi [5] further developed the idea of the neutrino in his well-known theory of weak interactions. Fermi theory of beta decay, modified later to include parity violation, remains widely used today as a valid low-energy theory.

Because neutrinos only weakly interacts with other particles, they were very much a theoretical bookkeeping device until two decades later. Neutrinos were first detected in 1956 by Cowan and Reines [6], who tracked inverse beta decays in a large tank of water near a nuclear reactor. Around the same time, Wu's experiment [7] confirmed parity violation in the weak interaction as proposed by Lee and Yang [8]. And soon afterward, Goldhaber, Grodzins, and Sunyar [9] found that all neutrinos are in fact left-handed. These major experimental discoveries led theorists to establish the modern theory of the weak interaction in the standard model. This theory further predicted that neutrinos have three flavors, ν_e, ν_μ, and ν_τ, which correspond to three charged lepton flavors: electron (e), muon (μ), and tau (τ). Danby *et al.* [10] confirmed the difference between the electron and muon neutrinos in 1962. As for the tau neutrino, while ν_τ was confirmed by Perl and his colleagues [11] in the mid-1970s, it was not until 2000 that the tau neutrino could be directly detected by the DONUT collaboration [12].

The three types of neutrinos, along with the three types of charged leptons, make up six out of twelve fundamental matter particles in the standard model. The theory of the weak interaction was seemingly complete. Nevertheless, the discovery of a new neutrino physics process challenged the assumption of neutrinos being massless in the standard model. This process is known as neutrino oscillation.

1.2 Neutrino Oscillation

The story of neutrino oscillation began with the so-called solar neutrino problem. After Eddington [13] proposed that nuclear fusion is the process that powers the stars, Bethe [14] applied the Fermi theory of weak interaction and worked out the most dominant fusion channel of the sun. This channel is referred to as the proton-proton chain reaction (pp-chain), and it set up the stage for today's standard solar model. According to the standard solar

model, neutrinos are released from the sun*. Moreover, these neutrinos are primarily electron neutrinos, whose number flux density was estimated by Bahcall and his group [16]. Realizing the sun is a bright source of neutrinos, Davis *et al.* started the Homestake experiment in 1968 and did the first measurement of the solar neutrinos. To their surprise, they found that the total number of accumulated events was only 1/3 of what Bahcall predicted [17]; 2/3 of the solar neutrinos were missing. This deficit in solar neutrino flux was referred to as the solar neutrino problem.

In the following year, Pontecorvo [18] proposed the idea of neutrino oscillation to explain the solar neutrino problem. In this model, 2/3 of the solar neutrinos "oscillate" from the original electron flavor into other flavors by the time they reach Earth. And because Homestake's experiment was only sensitive to electron neutrino (Sec. 1.2.1), the other 2/3 of the neutrinos that became the muon and the tau neutrinos would escape detection.

For neutrino oscillation to work, a mixing is required between the neutrino's flavor eigenstates ν_e, ν_μ, and ν_τ and the neutrino's mass eigenstates ν_1, ν_2, and ν_3 that correspond to masses m_1, m_2, and m_3. In other words, each of the neutrino's flavor eigenstates would be a quantum superposition of the neutrino's mass eigenstates. This mixing is encoded in what is referred to as the Pontecorvo-Maki-Nakagawa-Sakata (PMNS) matrix [19] of the weak interaction,

$$\begin{pmatrix} \nu_e \\ \nu_\mu \\ \nu_\tau \end{pmatrix} = \begin{pmatrix} U_{e1} & U_{e2} & U_{e3} \\ U_{\mu 1} & U_{\mu 2} & U_{\mu 3} \\ U_{\tau 1} & U_{\tau 2} & U_{\tau 3} \end{pmatrix} \begin{pmatrix} \nu_1 \\ \nu_2 \\ \nu_2 \end{pmatrix}, \tag{1.1}$$

The PMNS matrix U can be completely described by mixing angles θ_{12}, θ_{23}, θ_{13}, and a

*One caveat is that the neutrinos produced by the pp-chain are generally too low in energy to be detectable. However, there are other fusion channels that provide high energy neutrinos up to tens of MeV [15].

CP-violation term δ_{CP} in the following way,

$$U = \begin{pmatrix} U_{e1} & U_{e2} & U_{e3} \\ U_{\mu 1} & U_{\mu 2} & U_{\mu 3} \\ U_{\tau 1} & U_{\tau 2} & U_{\tau 3} \end{pmatrix} = \begin{pmatrix} 1 & 0 & 0 \\ 0 & c_{23} & s_{23} \\ 0 & -s_{23} & c_{23} \end{pmatrix} \begin{pmatrix} c_{13} & 0 & s_{13}e^{-i\delta_{CP}} \\ 0 & 1 & 0 \\ -s_{13}e^{i\delta_{CP}} & 0 & c_{13} \end{pmatrix} \begin{pmatrix} c_{12} & s_{12} & 0 \\ -s_{12} & c_{12} & 0 \\ 0 & 0 & 1 \end{pmatrix} \tag{1.2}$$

where $s_{ij} \equiv \sin\theta_{ij}$ and $c_{ij} \equiv \cos\theta_{ij}$. This mixing matrix is analogous to the better-known Cabibbo-Kobayashi-Maskawa (CKM) matrix [20] of the strong interaction that describes quark mixing. Furthermore, to oscillate the neutrinos, the three neutrino masses must be different. Consider a simpler two-neutrino case between (ν_e, ν_μ) and (ν_1, ν_2) with a mixing angle θ. Suppose the neutrino has an energy of E, then the probability as a function of distance z of a neutrino starting out in ν_e state and ending up in ν_μ state is given by,

$$P_{\nu_e \to \nu_\mu} = \left(\sin 2\theta \sin \left[\frac{(m_2^2 - m_1^2)c^3}{4\hbar E} z \right] \right)^2 . \tag{1.3}$$

The formula[†] shows that the oscillation amplitude depends on the mixing angle, while the oscillation rate depends on the difference of the squared masses,

$$\Delta m_{12}^2 \equiv m_2^2 - m_1^2. \tag{1.4}$$

In other words, not only the mixing angle must be non-zero, but at least one out of the two neutrino masses must be non-zero for the oscillation to happen. The non-zero neutrino masses imply physics beyond the standard model.

In 1998-2001, the Super-Kamiokande (Super-K) [23] and the Sudbury Neutrino Observatory (SNO) [24] together resolved the solar neutrino problem by confirming neutrino oscillation. Since then, many experimental efforts have been dedicated to find out the PMNS mixing angles. These experiments are generally divided in terms of the source of the neutrinos. There are four categories: solar, atmospheric, reactor, and accelerator.

[†]As a remark about the formula, its formal derivation is actually a lot more intricate than the common practical derivations shown in textbooks [21]. Care must be taken to treat momentum conservation correctly [22].

1.2.1 Solar Neutrinos

The three experiments we have mentioned in this section so far, Homestake, Super-K, and SNO are all sensitive to solar neutrinos. They are the pioneer experiments in the business of neutrino oscillation. This subsection briefly introduces what neutrino scattering processes each of these experiments applied to detect neutrinos.

The Homestake [25] experiment at the Homestake gold mine detected neutrinos using 610 metric tons of tetrachloroethylene. The relevant process is given as the following,

$$\nu_e + {}^{37}\mathrm{Cl} \rightarrow e^- + {}^{37}\mathrm{Ar}, \tag{1.5}$$

which produces radioactive isotope ^{37}Ar that can be counted radiochemically. This process only involves the electron neutrino, and thus raised the solar neutrino problem.

As for Super-K [23], neutrinos were detected by observing neutrino-electron scattering in 50 000 metric tons of ultra-pure water,

$$\nu + e^- \rightarrow \nu + e^-. \tag{1.6}$$

The scattered electrons gained a speed faster than the speed of light in water and produced Cherenkov radiation. These light signals were then detected by arrays of photo-multiplier tubes (PMTs) mounted on the surface of the water container. And because the electrons scattered in the direction of the incoming neutrinos, by reconstructing the direction of the electron using the distribution of the Cherenkov signals on the arrays of PMTs, Super-K was able to identify the neutrinos coming from the sun. Note that in neutrino-electron scattering, while neutrinos of all three flavors contribute, electron neutrinos are about 6 times more likely to scatter [26]*. This scattering efficiency can be accurately provided by the theory however. Then by comparing to the total solar neutrino flux predicted by the standard solar model,

*A qualitative explanation is that all three flavors of neutrinos can interact with an electron via neutral current interactions (weak interactions involving Z bosons), while only the electron neutrino can interact with an electron via charged current interactions (involving W bosons).

the result from Super-K pointed to the correct deficit in the flux predicted by neutrino oscillation.

Finally, the SNO experiment [24] was able to single out electron neutrino events by using 1000 metric tons of ultra-pure heavy water (D_2O) instead of water. In heavy water, neutrino-electron scattering occurs just like in water, but only the electron neutrino can dissociate the deuterons,

$$d + \nu_e \rightarrow p + p + e^-. \tag{1.7}$$

Without relying on the standard solar model, the SNO experiment was able to observe that the electron neutrino does indeed comprise 1/3 of the total solar neutrino flux.

The results from Super-K and the SNO experiment were consistent with neutrino oscillation together with the standard solar model, and thus resolved the solar neutrino problem.

1.2.2 Atmospheric Neutrinos

Atmospheric neutrinos are muon and electron neutrinos produced about 15 km above Earth's surface in the upper atmosphere. As a result of cosmic rays bombarding the Earth's atmosphere, pions are produced, which subsequently decay into muons, and then decay into electrons. Muon neutrinos are produced in a few of these decay processes,

$$\pi^- \rightarrow \mu^- + \bar{\nu_\mu}, \text{ and } \pi^+ \rightarrow \mu^+ + \nu_\mu, \tag{1.8}$$

and

$$\mu^- \rightarrow e^- + \bar{\nu_e} + \nu_\mu, \text{ and } \mu^+ \rightarrow e^+ + \nu_e + \bar{\nu_\mu}. \tag{1.9}$$

These muon neutrinos typically have energies above GeV. The baseline to detect these neutrinos, which refers to the path length a neutrino travels from its production to its detection location, ranges from 10 to 13 000 km. The atmospheric neutrinos have a wide baseline range because they can travel through the bulk of the Earth's materials and be detected on the other side of the Earth. The baseline length is important for neutrino oscillation because it corresponds to the variable z in Eq. 1.3. This means that to measure neutrino oscillation from these cosmogenic atmospheric neutrinos, the detector not only has to be able to

identify muon neutrinos, but also detect their incoming directions to extract their baseline information.

The Super-K experiment was not only able to detect solar neutrinos, but it was also able to detect atmospheric muon neutrinos via inverse beta decay in the muon channel,

$$p + \nu_\mu \rightarrow n + \mu^-, \text{ and } p + \bar{\nu_\mu} \rightarrow n + \mu^+. \tag{1.10}$$

The muons were also detected by the Cherenkov radiation they produced in water. Notice that non-atmospheric electron neutrinos could also induce inverse beta decay. However, at this energy level, Super-K was able to reconstruct the Cherenkov signal such that they could tell muon events from the electron ones. Moreover, as mentioned in the previous subsection, the signal reconstruction also provided the direction of an incoming muon neutrino to derive its baseline. Thence, Super-K was able to estimate the detection rate of muon neutrinos as a function of their baseline. By fitting the plot to Eq. 1.3, Super-K was able to obtain the muon neutrino oscillation frequency in 1998 [27], which was in fact the first evidence of neutrino oscillation[†]. Their result was confirmed by later atmospheric experiments such as MACRO [28] and Soudan-2 [29].

1.2.3 Reactor and Accelerator Neutrinos

Reactor neutrinos refer to those neutrinos produced by nuclear reactors through fission. The energy of these neutrinos are generally at the MeV level, which provides too small a signal to support directional measurement. The advantage of reactor-based neutrino experiments however, is that their baselines are fixed. As it turns out, at MeV level, neutrino oscillation periods can be as short as 1 km to 100 km. This is fortunate because this distance is manageable for terrestrial experiments and there is sufficient neutrino flux for detection after the reduction from the inverse-square law.

[†]Notice that the process is a lot more complicated considering the Mikheyev-Smirnov-Wolfenstein effect, which can modify the neutrino oscillation in matter, e.g. the bulk of Earth.

There are many reactor neutrino experiments, such as Double CHOOZ [30], RENO [31], and Daya Bay [32] were short baseline experiments that measured the θ_{13} mixing angle, and KamLAND [33] was a 185 km long baseline experiment that measured the θ_{12} mixing angle. These experiments generally looked at pressurized water reactors. Reactors only produce electron antineutrinos, and the reactors' thermal output determines the neutrino flux they produce. The typical detection method used is inverse beta decay,

$$\bar{\nu}_e + p \rightarrow e^+ + n. \tag{1.11}$$

By measuring electron-antineutrino "disappearance" rate, the reactor neutrino experiments were able to achieve precision measurements of the period and the mixing angles for the particular neutrino oscillation channel that suited their baseline.

The accelerator neutrino experiments can be thought of as reactor neutrino experiments with very long baseline. But unlike reactor neutrinos that are produced isotropically, accelerator neutrinos are focused onto their designated detectors. This way, the accelerator neutrino experiments can maintain detectable neutrino flux while having much longer fixed baselines. Additionally, accelerator neutrinos have well-controlled high energy as well as desirable neutrino flavors that can improve the quality of their measurements. The first experiment of this type was K2K [34], which already had a baseline as long as 250 km. The MINOS [35] experiment that followed had a baseline of about 730 km. And the planned DUNE experiment [36] would have a baseline of over 1300 km. The accelerator neutrino experiments will achieve the ultimate precision by combining the results with the reactor neutrino experiments, but they are foreseen on a longer timescale.

Combining the current reactor and accelerator neutrino oscillation results, a global analysis gives $\theta_{12} = 33.56\ (^{+0.77}_{-0.75})^\circ$, $\theta_{23} = 41.6\ (^{+1.5}_{-1.2})^\circ$, $\theta_{13} = 8.46\ (^{+0.15}_{-0.15})^\circ$, and $\delta_{CP} = 261\ (^{+51}_{-59})^\circ$, as well as $\Delta m^2_{12} = 7.5\ (^{+0.19}_{-0.17}) \times 10^{-5}$ eV^2 and $|\Delta m^2_{23}| \approx \Delta m^2_{13} = 2.524\ (^{+0.039}_{-0.040}) \times 10^{-3}$ eV^2 [37]. Notice the above results were derived assuming the normal hierarchy that will be discussed in the following section.

1.3 Neutrino Mass

As discussed previously, based on Eq. 1.3, the experimental confirmation of neutrino oscillation told us that at least two neutrino mass eigenvalues are non-zero. The current standard model, on the other hand, assumes all flavors of neutrinos have no mass. The assumption is made to support the parity-violating nature of the weak interaction and to avoid the hierarchy problem of why neutrinos otherwise have considerably lighter masses than other matter particles. Now as the assumption is no longer valid, the standard model needs to be modified to incorporate neutrino masses while keeping all the other physics it correctly describes. The simplest way out is to apply the so-called see-saw mechanism. To understand the simplest version of this mechanism, consider the neutrino-mass terms in the Lagrangian,

$$\mathcal{L}_{\nu,\text{mass}} = -\frac{1}{2}\begin{pmatrix}\bar{\nu}_L & \bar{\nu}_R^c\end{pmatrix}\mathcal{M}\begin{pmatrix}\bar{\nu}_L^c \\ \bar{\nu}_R\end{pmatrix} - \frac{1}{2}\begin{pmatrix}\bar{\nu}_L^c & \bar{\nu}_R\end{pmatrix}\mathcal{M}\begin{pmatrix}\bar{\nu}_L \\ \bar{\nu}_R^c\end{pmatrix}, \tag{1.12}$$

where L stands for the left chirality and R for the right, and the superscript c stands for charge-conjugation. The mass matrix $\mathcal{M}$ can be expressed generally as,

$$\mathcal{M} = \begin{pmatrix} m_M^L & m_D \\ m_D & m_M^R \end{pmatrix}, \tag{1.13}$$

where the subscript M stands for Majorana mass and D for Dirac mass. Because having a zero mass, i.e. having zero Higgs coupling to a particular neutrino eigenstate, is more natural than having the Hierarchy problem, we assume the diagonalized mass matrix has the following form,

$$\tilde{\mathcal{M}} = \begin{pmatrix} m & 0 \\ 0 & M \end{pmatrix}, \tag{1.14}$$

where $m \approx 0$ and M are the eigenvalues of the matrix $\mathcal{M}$. Solving the usual eigenvalue problems give us a formula,

$$m_M^R m_M^L = m_D^2. \tag{1.15}$$

Hence, for a fixed m_D, a large m_M^R would indicate a small m_M^L, which is the reason for the name "see-saw mechanism". If we further assume the transformation between $\mathcal{M}$ and $\tilde{\mathcal{M}}$ is

small, then $m_M^R >> m_D > m_M^L$, i.e. the mass of a right-handed neutrino is much greater than that of a left-handed neutrino. Working out the eigenvectors shows that the eigenvector of the eigenvalue M is composed almost entirely of ν_R. Then, as a result of parity violation in the weak interaction, the heavy right-handed neutrinos are essentially sterile, i.e. not interacting with normal matter. This result is consistent with the current observation that no right-handed neutrinos have been detected [38].

On another note, if we plug Eq. 1.13 into Eq. 1.12 and expand every term, we will find a neutrino mass term of the form $m_M^L \bar{\nu}_L \nu_L^c$ in the Lagrangian that creates two neutrinos out of vacuum. This term violates lepton number conservation provided that m_M^L is not zero. To avoid the violation, we can assume that neutrinos are Majorana particles, i.e. particles that are their own anti-particles. And this assumption leads to the possibility of neutrinoless double-beta decay, which would be an extremely sensitive experimental probe to neutrino mass.

Neutrinos having mass does not only imply physics beyond the standard physics model, it has implications for the standard cosmology model too. For instance, determining the neutrino mass helps constrain the parameter space in the ΛCDM model, where Λ stands for the cosmological constant and CDM for cold dark matter. It would help break the parameter degeneracies in ΛCDM in terms of fitting the cosmic microwave background (CMB) anisotropy spectrum [39]. On the other hand, if lepton number violation is in fact true as a result of neutrinos having mass, it can help explain the leptonic asymmetry, i.e. the mismatch of lepton matter and anti-matter abundance we observe today. The leptonic asymmetry may have an impact on nucleosynthesis that describes the overall matter and anti-matter asymmetry [40].

There are many proposed beyond the standard model theories that can explain neutrinos having mass, and many of which do apply the idea of see-saw mechanism similar to the one described above. To determine which theories are more accurate, we need experimental data.

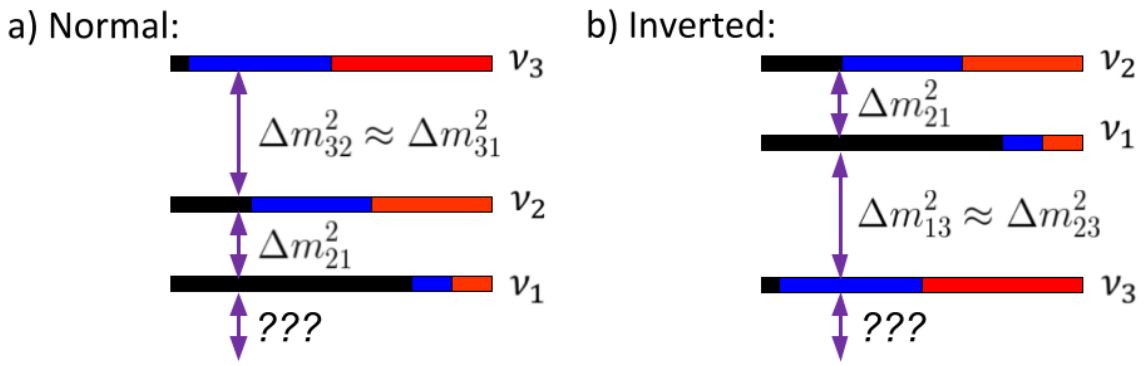

Figure 1.1: Neutrino mass hierarchy [41]. The y-axis qualitatively represents the square of mass in logarithmic scale. The mass expressions are defined by Eq. 1.4. Figure a) shows the normal hierarchy, while figure b) shows the inverted hierarchy. Refer to Eq. 1.3 for the squared mass differences. Within each colored bar, the color scheme shows the mixing of neutrino flavors: black for ν_e, blue for ν_μ, and red for ν_τ. The ratios were roughly based on the results shown at the end of Sec. 1.3. The question marks indicate that the absolute masses are currently unknown.

Since neutrinos have mass, the obvious goal is to find out what exactly their masses are. As the oscillation experiments described in Sec. 1.2 measure the differences of the squared neutrino mass eigenvalues, they provide lower bounds to the heaviest two neutrino masses. Based on the oscillation periods measured so far, there are two degenerate hierarchy scenarios: normal hierarchy and inverted hierarchy as shown in Fig. 1.1[41]. Future experiments such as DUNE [36] or Hyper-K [42] would be able to break the degeneracy. However, oscillation experiments cannot tell us the absolute mass scale as indicated by the question marks in Fig. 1.1. Other techniques are required.

In fact, much experimental effort has been put forth into determining the absolute neutrino mass. So far, there are mainly three types of method in the field: astrophysical and cosmological observation, neutrinoless double-beta decay, and the direct measurement. The first two methods are very sensitive to neutrino mass, but may have to be derived from rare

events and/or can be model-dependent. The direct measurements, on the other hand, observe the weak decay from a purely kinematic point of view and are thus model-independent. Further details about these experiments are given in the following subsections.

1.3.1 Astrophysical and Cosmological Observations

If we look outside our solar system, we can find neutrino sources far more intense than our sun. A prime example is type-II supernovae, which are explosions that occur after sufficiently large stars burn out their fusion source. These extreme processes create vast numbers of neutrinos. However, nearby supernovae are rare. So far the only supernova neutrino detection was from supernova SN1987A that occurred in the nearby Large Magellanic Cloud (LMC). The neutrinos had since travelled $\sim 1.7\times10^5$ light years to reach Earth. This rare opportunity was captured by Kamiokande-II [43], IMB [44], and Baksan Neutrino Observatory (BNO) [45], which measured a total of 25 events. These neutrinos were detected in a $\sim$10 seconds time interval and had energy ranging from $\sim$10 to $\sim 40\,\mathrm{MeV}$ with the higher-energy neutrinos arriving early. Base on the correlation between arrival time and energy, an upper bound of $m_\nu \leq 12\,\mathrm{eV}$ was achieved [46].

The general argument goes as follows: assume a neutrino has a fixed mass m_ν, kinetic energy K, and velocity v, then,

$$K + m_\nu c^2 = E = \gamma m_\nu c^2 = \sqrt{\frac{1}{1-\frac{v^2}{c^2}}} m_\nu c^2. \tag{1.16}$$

Suppose the neutrino is highly relativistic and has small mass, i.e. $K >> m_\nu c^2$, then

$$v = c\sqrt{1-\left(\frac{m_\nu c^2}{K+m_\nu c^2}\right)^2} \approx c\sqrt{1-\left(\frac{m_\nu c^2}{K}\right)^2} \approx c\left(1-\frac{1}{2}\left(\frac{m_\nu c^2}{K}\right)^2\right). \tag{1.17}$$

Suppose further the total distance that the neutrino traveled is $D \approx 1.7\times10^5$ light years, then the overall time required for the neutrino to reach Earth is,

$$t = \frac{D}{v} \approx \frac{D}{c}\left(1+\frac{1}{2}\left(\frac{m_\nu c^2}{K}\right)^2\right). \tag{1.18}$$

Now, if we assume that the earliest neutrino arrived at t_1 with $K_1 \approx 10\,\mathrm{MeV}$ and the latest neutrino arrived at t_2 with $K_2 \approx 20\,\mathrm{MeV}$. Then by plugging Eq. 1.18 to the time difference $\Delta t \equiv t_2 - t_1 \approx 10\,\mathrm{s}$, we arrive at,

$$m_\nu c^2 \approx \sqrt{\frac{2c\Delta t}{D\left(\frac{1}{K_2^2} - \frac{1}{K_1^2}\right)}} \approx 17\ \mathrm{eV}, \tag{1.19}$$

as a simple neutrino mass estimation. Notice that this calculation does not even imply it is an upper bound; much more detailed data analysis was required to validate the $m_\nu \leq 12\,\mathrm{eV}$ upper bound. However, this limit was obtained with only 20 events; imagine how many high-quality events could be captured using the current detectors.

On the cosmological side, the CMB anisotropy spectrum and the evolution of Large Scale Structure (LSS) can also provide constraints on neutrino mass. In the early universe, because neutrinos were able to free-stream through dense matter due to their weakly interacting nature, they enhanced energy dissipation. Dissipation in general hinders the structure-formation process and more so if the neutrinos were highly relativistic, which corresponds to neutrinos having very small mass. By incorporating the dissipation mechanism into the cosmological models, precise CMB measurement by the Planck satellite [47] and the LSS galaxy surveys such as the Sloan Digital Sky Survey (SDSS) [48] were able to indirectly limit the neutrino mass. So far, the combined CMB and galaxy surveys results have set a neutrino mass limit of $\sum m_\nu < 0.18\,\mathrm{eV}$ at 95% confidence level (95% CL) [39]. Nonetheless, it is worth stressing that the limit was model-dependent, particularly on the ΛCDM and the gravitational lensing model. The neutrino mass limit was derived based on a parameter fit to the models, where the neutrino mass is one of the parameters.

Therefore, if there are laboratory-based experiments that can measure the neutrino mass independently, the measurements can limit the neutrino mass fit parameter and so improve our current understanding of the cosmological models.

1.3.2 Neutrinoless Double-Beta Decay

A double-beta decay process refers to a decay process when two beta decays happen simultaneously in the same nucleus. This process is different from when one beta decay is immediately followed by another in that the otherwise intermediate state of a double-beta decay is forbidden; the two beta decays must happen simultaneously to skip the intermediate state. Double-beta decay was first observed directly using ^{82}Se by Elliott, Hahn, and Moe [49] in 1987. And a typical double-beta decay produces two electrons and two anti-neutrinos as shown in Fig. 1.2.a)*.

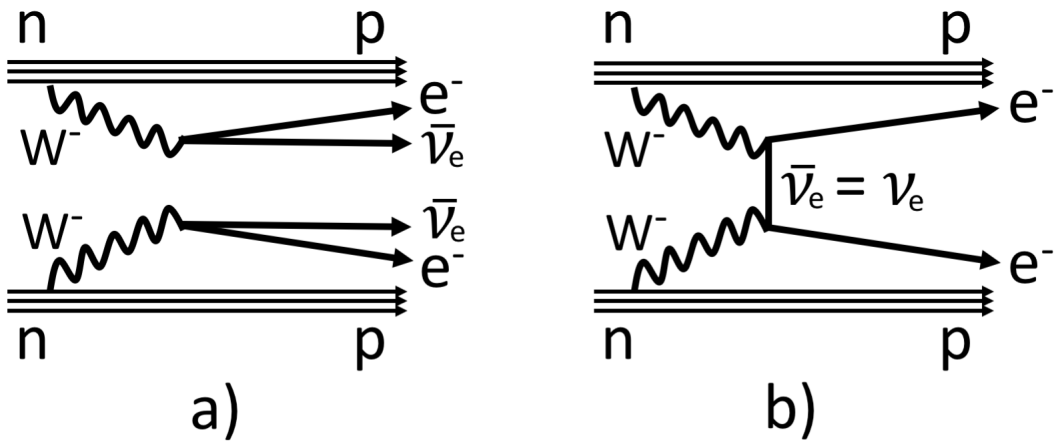

Figure 1.2: Double-beta decay Feynman diagram. Figure a) shows the ordinary double-beta decay ($2\nu\beta\beta$ decay), while figure b) shows the neutrinoless double-beta decay ($0\nu\beta\beta$).

However, if we assume neutrinos are Majorana particles, i.e. they are their own anti-particles, then neutrinos having mass would imply the so-called neutrinoless double-beta decay ($0\nu\beta\beta$ decay) [50]. As its name suggests, the $0\nu\beta\beta$ decay does not produce any neutrinos as shown in Fig. 1.2.b). The signature of a $0\nu\beta\beta$ decay is such that the combined energy of the two betas is mono-energetic at the Q-value up to the recoil energy of the

*There is also double-electron capture that captures two electrons simultaneously and produces two neutrinos.

nucleus. The result would be an excess peak at the Q-value of the $2\nu\beta\beta$ combined beta spectrum. Measuring the amount of the excess can set limits on the $0\nu\beta\beta$ decay lifetime.

While many isotopes do energetically permit $0\nu\beta\beta$, only 35 isotopes are stable against or have highly suppressed single beta decay modes [51]. However, if the assumption that neutrinos are Majorana particles is true, determining the $0\nu\beta\beta$ decay lifetime is so far the most powerful method to measure neutrino mass [52]. Many experiments have been constructed revolving around this idea. Examples are MAJORANA [53] and GERDA [54] that use ^{76}Ge, EXO-200 [55] and KamLAND-Zen [56] that use ^{136}Xe, CUORE [57] that uses ^{130}Te, and SuperNEMO [58] that uses several other elements. The use of different isotopes in their experiments served as a cross check, which would be especially critical if $0\nu\beta\beta$ is finally observed. The current lower limits to the $0\nu\beta\beta$ decay half-life in 90% CL are 2.7×10^{25} yr from the MAJORANA demonstrator [59], 0.9×10^{26} yr from GERDA [54], 3.5×10^{25} yr from EXO-200 [60], 1.07×10^{26} yr from KamLAND-Zen [56], and 1.5×10^{25} yr from CUORE [61] all in one-sigma error. This field has been extremely active in that the several next-generation large-scale $0\nu\beta\beta$ experiments are already in preparation.

On the other hand, if there are experiments that can directly measure the neutrino mass without assuming Majorana neutrinos, they would be valuable independent cross-checks for the $0\nu\beta\beta$ experiments. Furthermore, if the direct experiments actually measure the neutrino mass and the $0\nu\beta\beta$ experiments do not, then we know for sure the neutrinos are Dirac particles, i.e. particle that are not their own anti-particles.

1.3.3 Direct Measurement

The direct measurement in this case refers to a method that probes neutrino mass relying only on the kinematic information of beta decay. In other words, the method applies energy-momentum conservation to derive the theoretical beta spectrum (refined version of Eq. 1.22) and fits it to the physical beta spectrum using neutrino mass as a free parameter. This way, the neutrino mass obtained would be independent of cosmological models and whether or not neutrinos are Majorana particles. The popular beta source used in direct measurements

is tritium (T or ^{3}H) that undergoes,

$$\mathrm{T} \rightarrow {}^3\mathrm{He} + e^- + \bar{\nu}_e, \tag{1.20}$$

where the emitted electron e^- (also referred to as a beta or a beta-particle) has a relatively low Q-value of 18.6 keV and a reasonable half-life of 12.3 yr as shown in Fig. 1.3 [62]. An advantage of the tritium source is that the product ^{3}He has simple atomic structure, such that the effect from electron excitation levels can be readily corrected. Another advantage is that according to Fermi theory, having a low Q-value means the effect of neutrino mass on the beta spectrum shape is most statistically significant near the Q-value. Therefore, experiments can be designed to have high-pass filters that can set limits on the neutrino mass by looking at a only small portion of the decay events.

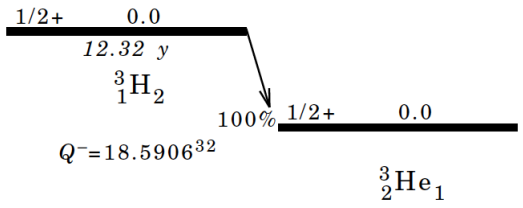

Figure 1.3: Hydrogen-3 (tritium) beta decay [62].

Tritium neutrino mass experiments started out by Curran *et. al.* [63] in 1948. They measured the beta spectrum using a proportional counter that contained an argon-methane mixture. The measurement relies on argon's Auger effect: when an inner-shell electron is knocked out by the beta, the reconfiguration of argon's electron cloud emits yet another electron from the outer shell. The ejected electron was referred to as an Auger electron. The large Auger effect of argon ensures that almost all the beta decay energy was converted to kinetic energy of Auger electrons. The count of these Auger electrons was proportional to the beta decay energy, and thus counting them determines the energy of the beta decay. This design reached an upper neutrino mass limit of $m_\nu < 1000\,\mathrm{eV}$.

To obtain a lower limit, inspecting the effect of neutrino mass near the endpoint of the beta spectrum became relevant, and the idea of an energy filter started to be applied in the 1950s. For instance, Hamilton *et. al.* [64] built what they referred to as a spectrograph. The idea was to place a beta source at center of a hemispherical grid held at an electrostatic voltage. The voltage was tuned such that only the betas near the Q-value had enough energy to pass through. Outside the grid, an hemispherical proportional counter, which covered the same solid angle as that of the grid, was placed to capture the betas that can pass through the grid. Thence, the grid essentially filtered out all the low-energy betas, and focused on the endpoint of the beta spectrum. The spectrograph allowed them to reach a limit of $m_\nu < 500\,\mathrm{eV}$ [65].

One downside of Hamilton's spectrograph however, was that despite having a large solid angle, its energy resolution was limited by the finite size of the beta source; imagine how a beta at the Q-value would be affected by the electrostatic grid when the decay happened off-center. The breakthrough was finally made in the 1970s, when Bergkvist [66, 67] applied an advanced spectrometer. This spectrometer collimated the betas from their full azimuth using a long, toroidal magnetic field, such that the final detections were independent of the initial decay positions and directions. Compared to the past experiments, this approach was superior in both energy resolution and luminosity. This was also the first time the resolution became fine enough that the beta spectrum needed to correct for ^{3}He+ electron excitation levels to match the sensitivity. Later, the ITEP group from Moscow developed a powerful spectrometer known as the Tretyakov spectrometer. The ITEP group did not only set an upper bound but also concluded a finite neutrino mass within $17 < m_\nu < 40\,\mathrm{eV}$ [68].

Unconvinced by the lower limit, other groups decided to check the result based on Tretyakov spectrometers. The groups differed in how their sources were prepared however. The ITEP group used a thin film of tritiated valine, whose solid-state effects such as phonon excitation were difficult to correct. On the other hand, a group at University of Zürich used a very homogeneous Langmuir-Blodget film of carbon-tritium chains (CT_2) fixed to a silicon substrate by single bonds. The final-state beta energy was then corrected using quantum

chemistry methods [69], and a neutrino mass upper bound of $m_\nu < 11.7\,\text{eV}$ [70] was found with 95% CL. Moreover, a group at Los Alamos National Laboratory (LANL) used a windowless gaseous tritium source (WGTS) (Sec. 1.4.1) of molecular tritium (T_2), and arrived at $m_\nu < 9.3\,\text{eV}$ 95% CL [71]. Finally, a group at Lawrence Livermore National Laboratory (LLNL) conducted an upgraded version of LANL and arrived at $m_\nu < 8\,\text{eV}$ 95% CL [72]. All three results ruled out the result of ITEP, whose lower limit was likely caused by an inaccurate knowledge of the final state distribution (FSD) for their valine source compound. The inaccurate Q-value by chance [73] made them think the FSD was right when it was not. Improvements have been made on measuring the Q-value [74].

Nevertheless, there was another serious issue. Note that the neutrino mass parameter in the beta spectrum was actually the square of mass m_ν^2. However, the experiments that followed ITEP, including the later experiments at Tokyo [75] and Beijing [76], despite agreeing within error bars, yielded an unphysical negative m_ν^2 value. The problem was finally resolved by the Mainz and the Troitsk experiments. These experiments upgraded the Tretyakov spectrometer to a so-called magnetic-adiabatic-collimation-with-electrostatic filter (MAC-E filter) (Sec. 1.4.1). As for the tritium source, Mainz used T_2 film condensed onto a graphite substrate similar to Zürich, while Troitsk used a WGTS like LANL. Even these advanced experiments suffered from unphysical m_ν^2 values initially. But upon theoretical/systematics corrections, these experiments yielded the most stringent results for direct neutrino experiment many years, with Mainz at $m_\nu < 2.3\,\text{eV}$ 95% CL [77] and Troitsk at $m_\nu < 2.05\,\text{eV}$ 95% CL [78]. Notice the molecular T_2 component in the sources; one important part of the corrections to unphysical m_ν^2 was to incorporate the molecular FSD correction to the theoretical beta spectrum [79, 80].

1.4 Current and Forthcoming Direct Neutrino Mass Experiments

This section focuses on the upcoming direct experiments: after decades of development, the technology has finally reached a stage that allows direct neutrino-mass measurement down to the sub-eV level. Detailed discussions are addressed in Otten and Weinheimer [80] and

Drexlin *et al.* [81].

1.4.1 KATRIN

The Karlsruhe Tritium Neutrino (KATRIN) [82] experiment is the next-generation direct neutrino-mass experiment that gathers worldwide expertise from previous tritium β-decay experiments, such as Mainz and Troitsk. Following its predecessors, KATRIN continues the designs of using a WGTS and a MAC-E filter.

The WGTS is designed to be "windowless" because a window would attenuate the energy of betas, which adds a substantial systematic to a beta spectrum measurement. However, containing tritium gases without a window is no easy task. To build a WGTS, the KATRIN experiment developed a sophisticated gas-handling system. The basic idea is to continuously inject tritium gas at a steady pressure in the middle of an open-ended cylindrical chamber [83]. The tritium number density drops approximately linearly until the gas is steadily pumped out near both ends. The steadiness ensures there is no turbulence, so that no tritium particles are ejected out of the cylinder due to density fluctuation; the gas is contained. The source gas used is molecular tritium (T_2), which is chemically stable at the design pressure in the WGTS. The source is operated at the cryogenic temperature of 30 K both to increase the gaseous source density and to make sure the source particles do not start out in highly excited molecular states. Once a tritium nucleus decays in the cylinder, the product beta is magnetically guided to exit at either end of the cylinder. The beta that exits at the correct end then enters the next section called the transport system. The transport system further reduces the gas pressure by using multiple stages of differential turbo pumping and cryogenic pumping, while at the same time allowing the beta to pass by without significantly altering its energy. Only after passing through the transport system, can the betas finally arrive at the spectrometers.

The KATRIN main spectrometer is a MAC-E filter. The betas that enter are magnetically guided to the other end of the spectrometer, where they will be detected by a silicon detector. And like the spectrograph, an electrostatic potential near the Q-value is placed across the

spectrometer. The potential is the highest at the center of the spectrometer, so that only the betas that have high enough kinetic energy can pass through the potential well and be reaccelerated to the silicon detector. The high-pass energy filter based on electrostatics explains the "E filter" in MAC-E filter. One problem however, is that the electrostatic potential filters out betas based on their kinetic energy from their longitudinal motion instead of the total kinetic energy. And so to construct a high-pass filter on the total kinetic energy, the betas need to be pointing longitudinally as they arrive at where the potential is the highest. To do so, KATRIN varies the magnitude of the magnetic field along the betas' paths in a specific way, such that the variation generates a force that transforms cyclotron motion of the betas into longitudinal motion, and so collimates the betas at the center of the spectrometer. Moreover, the variation needs to be small so that the whole process is adiabatic, so that the betas have constant orbital magnetic moment as they travel across the filter. The adiabaticity precisely collimates the betas, which is essential to the energy resolution of the filter. This sophisticated technique explains the "MAC" in MAC-E filter.

By analyzing the last 40 eV below the Q-value, the KATRIN experiment was able to set a new limit at $m_{\bar{\nu_e}} < 1.1\,\text{eV}$ 90% CL [84] *. The design goal of the experiment aims to achieve a limit of $m_{\bar{\nu_e}} < 0.2\,\text{eV}$ 90% CL.

1.4.2 Project 8

As MAC-E filter type experiments are approaching their volume scale limit, a novel approach that can potentially further improve the limit is to use cyclotron radiation emission spectroscopy (CRES) [85]. The idea is to measure the beta spectrum by trapping betas from gaseous tritium source inside a magnetic trap and determine their cyclotron radiation using microwave antennae. The bandwidth of the antennae is tuned to be most sensitive to the cyclotron frequency corresponding to the betas near the endpoint energy. Because

*The $m_{\bar{\nu_e}}$ is an effective mass formed from the contribution of the mass eigenstates to the ν_e flavor eigenstate. It is the relevant observable here because only ν_e is involved in Eq. 1.20.

the measurement is frequency-based, with sufficient tracking time, CRES should be able to achieve an energy resolution as fine as 0.04 eV in the final stage of the experiment [86], as compared to 0.93 keV for KATRIN [82]. The tracking time refers to the amount of time that the antennae can track a beta by continuously measuring the beta's cyclotron radiation. On one hand, the tritium gas pressure must be sufficiently low to allow sufficiently long tracking time before electron-tritium scatterings occur and knock the betas out of the magnetic trap. On the other hand, because the betas are tracked within the gaseous source, there are no transport losses and so no intrinsic limitation on the volume scale for CRES type experiments. Moreover, CRES-type experiments can potentially use an atomic tritium source, which would avoid all systematics coming from the molecular effects on the beta spectrum.Achieving an atomic tritium source is no easy task however, given how chemically active it is. Much effort has been placed on pursuing the charming idea.

The upcoming experiment that pursues the CRES technique is called the Project 8 experiment [87], and its current progress shows that CRES is a promising alternative [85].

1.4.3 Microcalorimeters

Another direct measurement method is to use sensitive calorimeters that measure energy through heat flow. The microcalorimeters can measure heat flow at the μW level. The idea is to measure the decay spectrum by containing the whole source inside microcalorimeters, such that all decay energy, except for the neutrino, can be deposited to the microcalorimeters in form of thermal energy. The disadvantage of the calorimeter-type experiment is that the entire decay spectrum has to be measured, not just near the endpoint. And so there is a tradeoff between pileup and collecting enough relevant statistics.

Experiments such as HOLMES [88], NuMECS [89], and ECHo [90] use holmium that undergoes the electron capture,

$$^{163}\mathrm{Ho} + e^- \rightarrow ^{163}\mathrm{Dy}^* + \nu_e, \tag{1.21}$$

where the e^- on the left-hand side comes from the inner shell of ^{163}Ho. The star in ^{163}Dy*

indicates that it is in an electronic excited state. Note that the spectrum obtained from nuclear recoil and de-excitation of $^{163}Dy^*$ does in fact depend on which ^{163}Ho shell the captured electron originally comes from. The decay has a Q-value greater than 2.8 keV and a half-life of 4,570 years [91] that allows enough statistics. Because these experiments are using sources different from tritium, they provide an important cross-check, especially when the neutrino mass is finally measured.

1.5 Theory of Beta Decay in T_2

This section briefly displays the theory of the tritium beta decay that is relevant to neutrino mass, and the emphasis is on the molecular final state effects. Refer to [92] for complete details.

1.5.1 Neutrino Mass in the Beta Decay Spectrum

An illustration of the decay energy spectrum is shown in Fig. 1.4. Figure 1.4.a) shows the full spectrum, while Fig. 1.4.b) shows the spectrum near the endpoint. We can see that even given a neutrino mass m_ν (Sec. 1.3.3) of 1 eV, it changes the spectral shape. The task of the direct neutrino experiments is to accurately determine this shape to derive the neutrino mass.

Notice the scale of the y-axis in Fig. 1.4.a) as compared to that of Fig. 1.4.b), the change in the spectral shape by the neutrino mass is small. A distortion of similar size can be induced by instrumental uncertainties as well as unaccounted theoretical corrections. This poses many challenges. For instance, the current experimental uncertainty on the Q-value is not accurate enough to fix the endpoint of the spectrum. And so, the Q-value needs to be included as a "nuisance parameter".

As for a molecular source that is used in direct experiments such as KATRIN, the sensitivity has reached a stage such that a significant modification to the beta spectrum comes from the excitations of the daughter molecule after the decay. These molecular corrections need to be accounted for in the theoretical framework to reach the design sensitivity. To

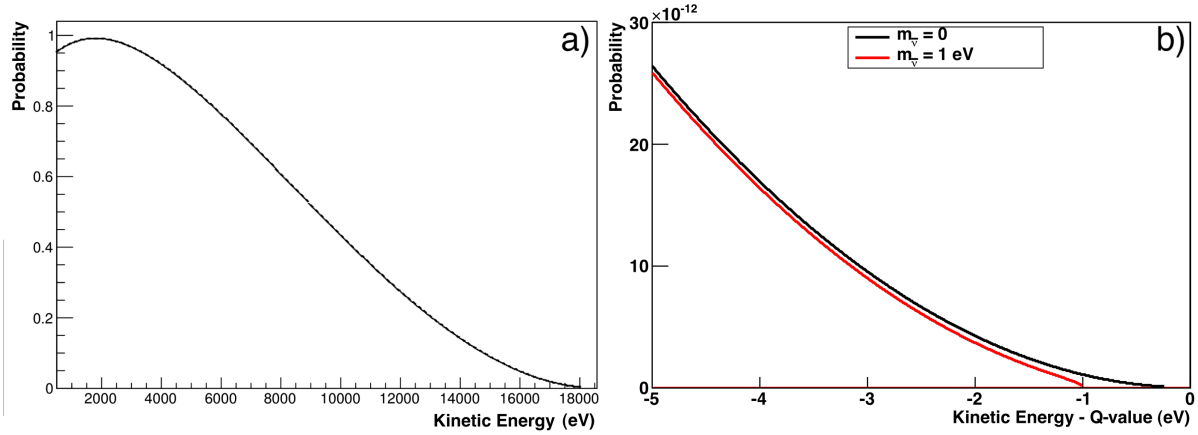

Figure 1.4: Illustration of the neutrino mass effect on the tritium beta spectrum [92]. The distribution is normalized such that the probability density is 1 at the maximum point. Plot a) shows the full distribution and plot b) shows the distribution near the Q-value. In plot b), the black distribution assumes the neutrinos have no mass, while the red distribution assumes $m_\nu = 1\,\mathrm{eV}$.

incorporate the molecular effects correctly, we need to consider the final-state distribution (FSD) of these daughter molecules as will be discussed in the following subsection.

1.5.2 Theory of Beta Decay and the Molecular Final-State Distribution

As mentioned at the beginning of this chapter, tritium beta decay is well described by the Fermi theory of beta decay [5]. The theory gives the following beta spectrum formula, where the units are chosen to have $c = 1$,

$$\begin{aligned}\frac{dN}{dE_e} = \; & \frac{G_F^2 m_e^5 \cos^2\theta_C}{2\pi^3\hbar^7}|M_{\mathrm{nuc}}|^2 F(Z,E_e) p_e E_e \\ & \times \sum_{i,k}|U_{ei}|^2 P_k(E_{\max}-E_e-V_k)\sqrt{(E_{\max}-E_e-V_k)^2-m_{\nu i}^2} \\ & \times \Theta(E_{\max}-E_e-V_k-m_{\nu i}),\end{aligned} \tag{1.22}$$

where N is the probability amplitude and E_e the total energy of the emitted beta electron that includes both the beta's kinetic energy and rest mass. The constants at the front

are $M_{\rm nuc}$ the nuclear matrix element, G_F the Fermi weak-coupling constant, and θ_C the Cabibbo angle. The shape of the spectrum is determined by kinematic relations between E_e, the neutrino mass $m_{\nu i}$, the electron mass m_e, the maximum energy of the electron $E_{\rm max} = Q - E_{\rm rec} + m_e$, and the energies V_k and the probabilities P_k associated with the excited state k of the daughter ion. In the expression of $E_{\rm max}$, Q is the Q-value of the decay and $E_{\rm rec}^{\rm kin}$ the recoil kinetic energy of the daughter molecule. The $F(Z, E_e)$ is the Fermi function that accounts for the effect of the nuclear Coulomb field on the beta, where $Z = 1$ is the atomic number of tritium. The U_{ei} is an entry of the PMNS matrix (Sec. 1.2), where e stands for the electron neutrino flavor eigenstate and i for the neutrino mass eigenstates. The $\Theta(E_{\rm max} - E_e - V_k - m_{\nu i})$ is a Heaviside step function to ensure the conservation of energy [93].

This basic formulation is subjected to multiple corrections due to increase in experimental sensitivities [94, 95, 96]. But formally, if we wish to use the molecular source T_2, Eq. 1.22 contains inaccuracies in accounting for the rotational and the vibrational excitations from the recoil energy; the mass of the nucleus is assumed to be infinite and the recoil energy is added in later as a correction. To resolve the inaccuracies, a three-body kinematic involving the beta, the neutrino, and the daughter molecule is required to accurately account for the recoil effect. The correction also needs to take into account the binding energy of the molecules shown in Fig. 1.5. This full relativistic three-body treatment is discussed in detail in [92].

Once we have an accurate $\frac{dN}{dE_e}$ formulation for molecular tritium, the remaining challenge would be to evaluate the probability P_k in the refined Eq. 1.22. It is the transition probability defined by,

$$P_{if} = \left| \langle \Psi_f^{^3{\rm HeT}^+} | e^{i\vec{k}\cdot\vec{R}} | \Psi_i^{\rm T_2} \rangle \right|^2, \tag{1.23}$$

where $\Psi_i^{\rm T_2}$ is the initial wave function of the parent molecule and $\Psi_f^{^3{\rm HeT}^+}$ the final wave function of the daughter molecule. Vector $\vec{R}$ is the internuclear position vector, i.e. the separation vector of the two atoms in the molecule, and $\vec{k}$ is the recoil momentum of the molecule. So P_{if} is basically the transition probability from $\Psi_i^{\rm T_2}$ to $\Psi_f^{^3{\rm HeT}^+}$ after the recoil induced by the beta decay. As the instrumental techniques have advanced, the experiments

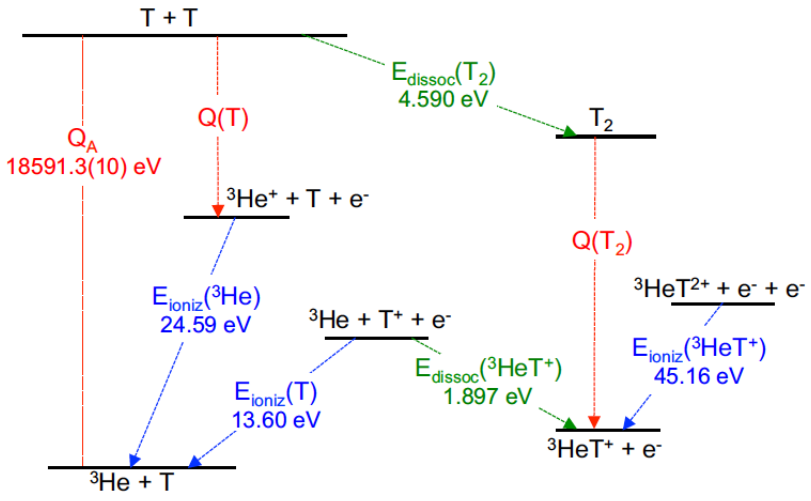

Figure 1.5: Ionization and dissociation energy levels for the T_2 molecule [92, 97].

are getting better at producing the $\Psi_i^{T_2}$ in its ground state. This the reason why P_k only depends on the final state k in Eq. 1.22; $P_k \equiv P_{0k}$ from Eq. 1.23*.

The requirement of P_k is where the FSD comes in, which is given by $\sum_k P_k \Psi_k^{^3\mathrm{HeT}^+}$. Note that the $\Psi_k^{^3\mathrm{HeT}^+}$ consist of bound molecular states as well as the dissociated ones. If we do know all the $\Psi_k^{^3\mathrm{HeT}^+}$ analytically, we can readily perform the integral Eq. 1.23 to obtain P_k; we do not. Fortunately, high-precision FSD calculations are available for the T_2 beta decay [98, 99] under the Born-Oppenheimer approximation that assumes the motion of the nuclei to be slow compared to that of the electrons. The assumption allows the waveform basis to be constructed separately for the waveforms for the nuclei and electrons. Then variational methods can be used to precisely compute $\Psi_k^{^3\mathrm{HeT}^+}$ at each excitation level [100]. This method also tells us about the energy corresponding to each wave function, which is V_k in Eq. 1.22. And the predicted FSD in energy is provided in Fig. 1.6.

*The KATRIN experiment cannot quite achieve the ground initial state due to the ortho- and para-state complication. However, the initial state is still much better known than the final state that covers a wide energy range, and it is folded into the calculation of P_k.

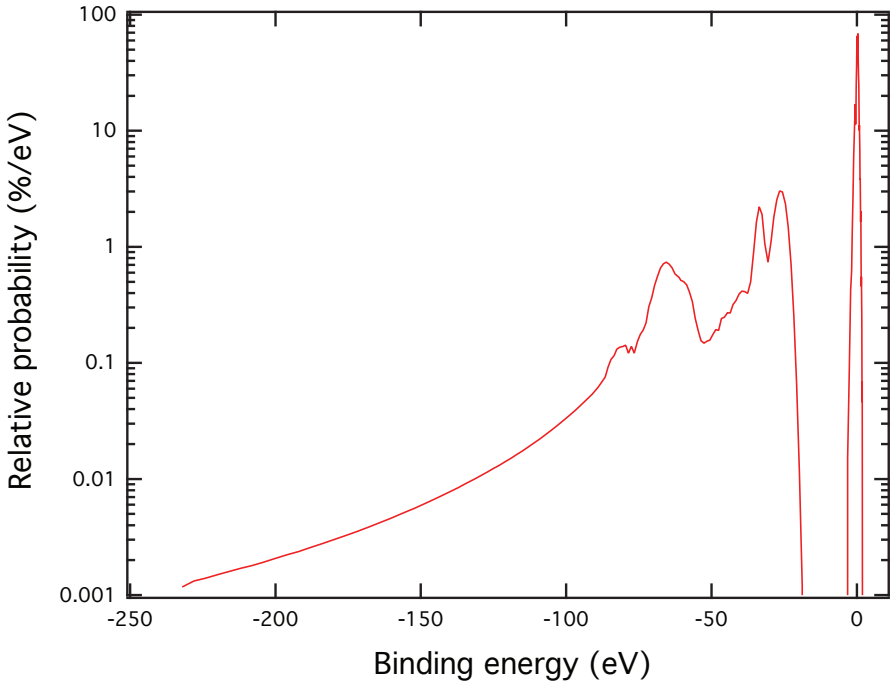

Figure 1.6: Calculated FSD in energy after T_2 beta decay from the ground state [92, 41, 98].

The framework of the modern FSD calculation is based around the so-called geminal basis, which explicitly correlates the two-electron wave function of a diatomic molecule [101]. In fact, the result shown in Fig. 1.6 was calculated using the geminal basis and the recent results can be found in [102]. At the highest precision though, the convergence of this method becomes sensitive to the choice of the basis involved in the calculation [103]. An alternative method uses the so-called configuration-interaction (CI) basis, whose two-electron wave functions are made out of the superpositions of two single-electron wave functions. The CI method was initially used on the HeH^+ molecule [104, 105, 106], but had been updated to HeT^+ for the neutrino mass measurement [107, 108]. The problem with the CI method is that it is more computationally expensive than the geminal method. However, using modern computation power, the CI method shows promising results [109]. The theoretical work is still under active development.

To evaluate the $\frac{dN}{dE_e}$ for the other tritium molecules such as HT and DT, the formulation

is the same, but the FSDs will be different.

Once we have the FSD accurately evaluated, we can measure the neutrino mass by fitting the theoretical beta spectrum covered in this section to the data using the neutrino mass as a fit parameter.

1.5.3 Experimental Validations of the Theory and One Tremendous Disagreement

There are many experiments out there that partially validate the theory described in the previous subsection. For instance, the rotational and vibrational energy levels in the various molecules and ions match nicely between the theory [110, 111] and the experiments using high-precision spectroscopic techniques [112, 113, 114, 115, 116, 117, 118, 119, 120, 121, 122, 123, 124, 125, 126, 127]. An example of such agreement is shown in Fig. 1.7. Another example is the photodissociation cross section of $^4HeH^+$, the theoretical prediction [128] agrees well with the results from the Free-electron LASer in Hamburg (FLASH) experiment [129].

Unfortunately, direct experimental measurement of the FSD is infeasible due to unknown time for further evolution and translational Doppler broadening of the FSD. What is available however, is the branching ratio P_{bound} of the final state being a bound state as compared to a dissociated state*. In fact, experiments from late 1950s had already made such measurements and the results were that P_{bound} is close to 90% for both the T_2 and HT molecules [130, 131]. The modern theory on the other hand, predicts a P_{bound} close to 50% [111]. Their results are shown in Table 1.1, which yields a tremendous disagreement.

---

*Using the terminology from Sec. 1.5.2, $P_{\text{bound}} = \sum_{\text{bound}} P_k$ summing over only the final states that remain a molecule.

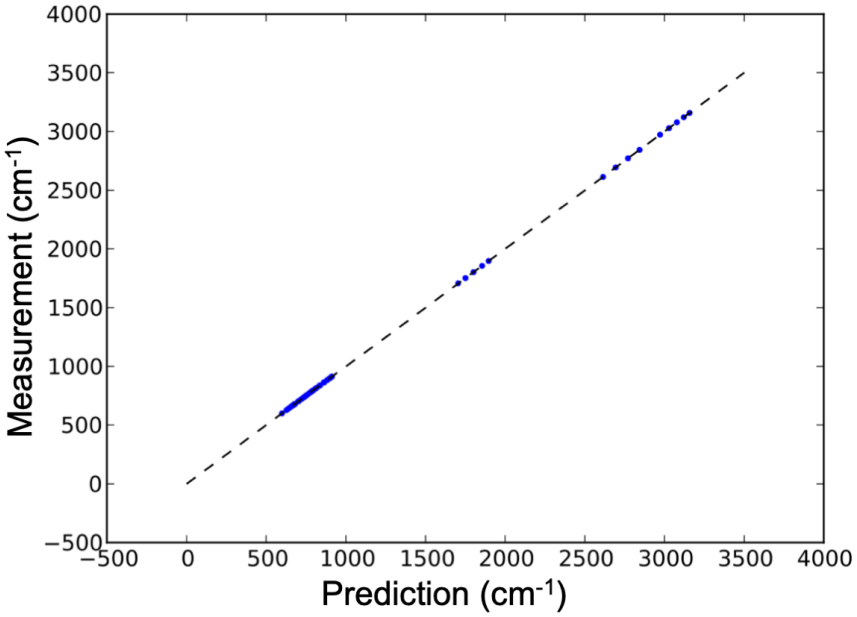

Figure 1.7: Theoretical versus experimental results of the $^4HeH^+$ excitation energies [97]. The energies are given in inverse of the wavelength; $1000\,\mathrm{cm}^{-1} = 0.12\,\mathrm{eV}$. The x-axis shows the theoretical prediction and the y-axis shows the experimental measurement. The uncertainties on the data points are too small to be seen visually. The dashed line is the diagonal line to show the agreement between the x- and y-axis values.

	Theory [111]	Snell [130]	Wexler [131]
$P_{\mathrm{bound}}(\mathrm{T}_2)$	39-57%	$94.5 \pm 0.6\%$	
$P_{\mathrm{bound}}(\mathrm{HT})$	55-57%	$89.5 \pm 1.1\%$	$93.2 \pm 1.9\%$

Table 1.1: Theoretical and experimental results of the branching ratio to the bound molecular ion P_{bound} after the beta decay for T_2 and HT

The upper and lower bounds from the theoretical prediction come from whether or not the quasi-bound molecular final states, i.e. bound states with energy above the binding energy,

dissociate or not. However, even with the uncertainty from quasi-bound states, the P_{bound} from the theory and the experiments still did not match.

It is possible that the disagreement comes from the sudden approximation used by the theory. The approximation assumes that the beta leaves the molecule sufficiently quickly, such that the wave function of the molecular electron cloud is not perturbed. This approximation should be valid for beta energy above 2 keV [132]. On the other hand, the Snell and Wexler experiments cover the whole beta range. Perhaps the breakdown of the sudden approximation at low beta energy can describe the disagreement.

On the past experiments side, there are a few possible systematics that can potentially explain this disagreement. For instance, because the experiments used mass spectrometers to identify the final state ions by their mass, perhaps the difference in transverse momentum of each mass species result in them having different acceptance. Perhaps, the electron multiplier detectors used in these experiments have different detection efficiency for different ion types. Maybe the pressure in the source chamber was not low enough such that charge-exchange scattering occurred. These systematics are difficult to confirm since the experiments were done so long ago.

For this reason, a modern experiment that measures P_{bound} should be in place to validate the theory.

Moreover, the current theoretical calculation still does not have a robust way to estimate its uncertainty, and much ongoing work is required to match the KATRIN requirement. Therefore, a modern measurement of P_{bound} can also help reevaluate the theoretical uncertainty, especially regarding the quasi-bound states. This uncertainty estimation of course does not change the theoretical FSD estimation and so does not enter directly into KATRIN's mass measurement. However, an agreement between the theory and the experiment on P_{bound} will improve confidence in the accuracy of the theory.

1.6 The TRIMS Experiment and the Objective of This Work

The Tritium Recoil-Ion Mass Spectrometer (TRIMS) experiment at University of Washington is a modern experiment that reexamines the P_{bound} branching ratio and addresses the disagreement. The TRIMS experiment addresses some of the issues that the previous experiments had: the guiding magnetic field would mitigate the concern of the transverse ion momentum*, the electric field across the decay chamber as high as $60\,\text{kV}/25\,\text{cm}$ would ensure no recombination occurs, and the operating pressure as low as 10^{-5} Torr would eliminate charge-exchange scattering. Furthermore, the TRIMS experiment sets up a coincidence to detect both the final state ion and the beta of a single tritium decay. Silicon detectors are also used such that the incident ion energy can be accurately measured. These more detailed measurements allow much more flexibility in developing the data analysis schemes.

The objective of this work is to give a full description of the setup of the TRIMS experiment and present the analysis work that leads to TRIMS's result.

As a short orientation to the chapters of this work, Ch. 2 covers the hardware assembly of the TRIMS experiment, Ch. 3 the simulation studies, Ch. 4 the data-taking procedures, and Ch. 5 the waveform signal-processing. Chapter 6 to 8 each covers a particular part of the TRIMS data analysis. Finally, Ch. 9 summarizes the results of the TRIMS experiment and provides the systematic table to the said results.

---

*The gyroradii of the ions are still a problem, but they can be addressed using a data-analysis method called scan-deconvolution (Sec. 8.1).

Chapter 2

TRIMS HARDWARE

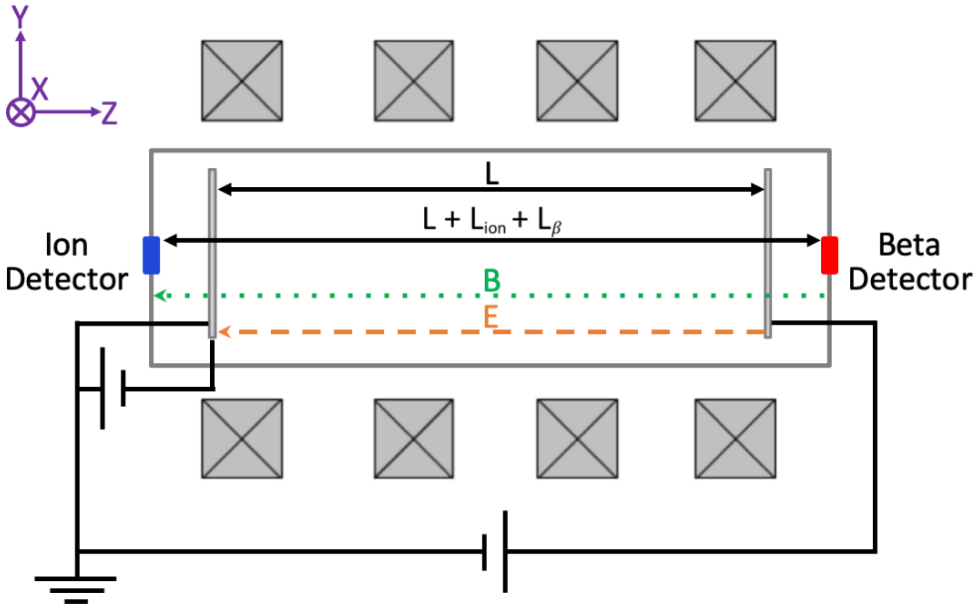

Figure 2.1: Schematic layout of the TRIMS decay chamber [133]. In this idealized sketch, the chamber is a cylinder that has the ion-detector (blue block) located on one end and the beta-detector (red block) on the other. The magnetic field B (green arrow) and the electric field E (orange arrow) run parallel along the axis. The magnetic field is provided by four coils (grey boxes with crosses). The electric field is provided by the electrodes (grey plates) at each end, where a high positive voltage is applied on the beta-electrode and a low negative voltage on the ion-electrode. The physical length L is defined as the distance between the two electrodes. The lengths L_{ion} and L_{β} are defined as the distances between the detector and the electrode on the ion-side and the beta-side. The values of the parameters are provided in Table 2.1.

The Tritium Recoil-Ion Mass Spectrometer (TRIMS) experiment uses modern instruments to measure the branching ratios of the final states from tritium molecule (T_2) beta decays. The primary interest is to find the ratio of molecular bound states (^{3}HeT+) to dissociated states (^{3}He+ or T+). The experimental concept is a simple one as illustrated in Fig. 2.1). Let tritium decays take place in a vacuum chamber, then accelerate and guide the final-state ions and beta electrons with an electric field and a magnetic field that run parallel to each other. Because of their different charges, the ions and the betas travel in opposite directions. So if we place a silicon detector at the end of each direction, we can capture the ions and betas. The energy of the ions yields the positions of the decays. The timing difference between the ions and the betas provides the information of how heavy the ions are; we can use this information to identify the ions and so derive the branching ratio to each ion state. Details on the derivations are given in later chapters; this chapter focuses on apparatus.

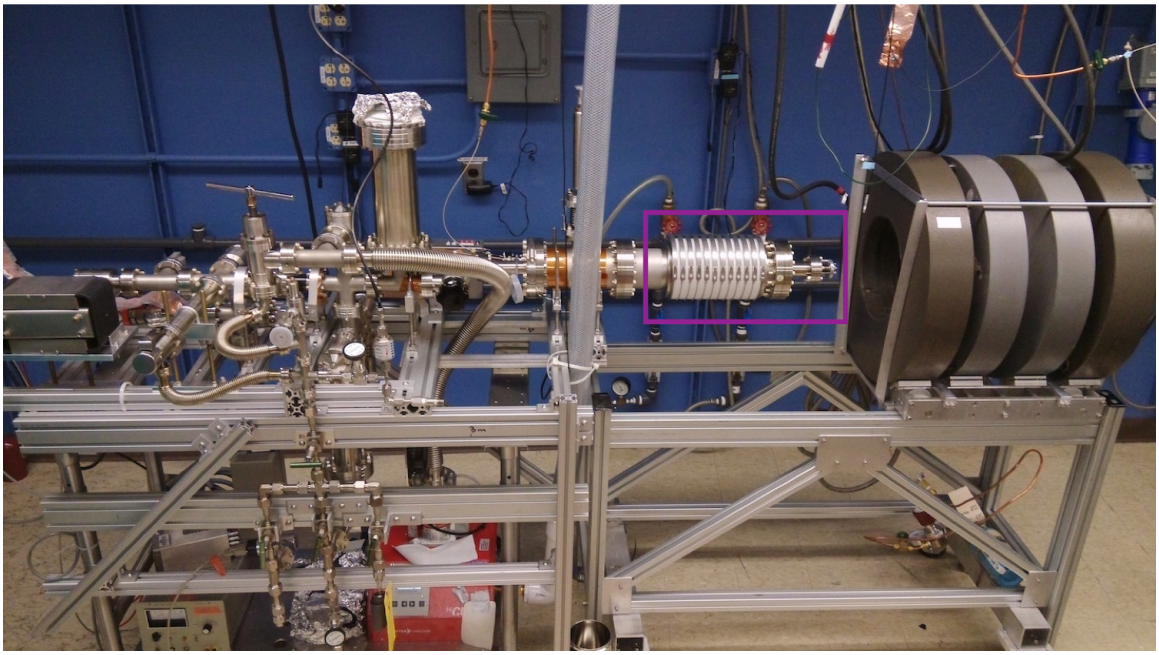

Figure 2.2: Photo of TRIMS main hardware. The decay chamber is boxed in purple. The rest are mainly the vacuum system, except the magnets to the right.

The main TRIMS hardware is shown in Fig. 2.2, where the most important component is boxed in purple. That component is the decay chamber and will be the focus of Sec. 2.1. The other visible components are mainly the vacuum system that will be discussed in Sec. 2.2. Section 2.3 describes the radioactive sources that we used for calibration and taking physics data. Apparatuses related to the electric and the magnetic fields are covered in Sec. 2.4. Details on the silicon detectors, including their data acquisition and coincidence setup, cooling system, and motion mechanism, are discussed in Sec. 2.5. Lastly, a slow-control system that ensures everything functioned properly is covered in Sec. 2.6.

2.1 Decay Chamber

2.1.1 Chamber Geometry

The chamber where we watch the tritium decays is referred to as the decay chamber. To keep the description simple, imagine that the chamber is a perfect cylinder of length $L = 0.235\,\mathrm{m}$ and diameter $D = 0.102\,\mathrm{m}$. The chamber's geometry is shown in Fig. 2.1 and dimensions are given in Table 2.1. Two identical silicon detectors, which are readied to capture incoming decay product particles and read out their energies and incident times, are placed separately at the two ends of the chamber. The detector positioned to detect ions is referred to as the ion-detector, and electrons as the beta-detector. Similarly, the ion-detector side of the decay chamber is referred as the ion-side, and the beta-detector as the beta-side. This cylinder is surrounded by four coaxial magnetic coils that give a total magnetic field of $B = 0.237\,\mathrm{T}$ that is uniform up to 1% (Sec. 4.4.2). An electrode is placed at each side of the chamber and the potential difference between the two electrodes provides an electric field across the chamber. The high-voltage cathode at $V = 60\,\mathrm{kV}$ is on the beta-side and is referred to as the beta-electrode. The anode on the ion-side has a voltage of $V_{\mathrm{ion}} = -100\,\mathrm{V}$ and is referred to as the ion-electrode. Notice that while the beta-detector floats at the same 60 kV as the beta-electrode, the ion-detector is grounded and insulated from the ion-electrode that floats at $-100\,\mathrm{V}$. The $-100\,\mathrm{V}$ mesh ion-electrode serves to suppress secondary-electron emission

from the ion-detector.

Description	Value		
Distance between electrodes	L	=	235 mm (9.24 in)
Distance between ion-electrode and detector	L_{ion}	=	29 mm (1.14 in)
Ion-electrode thickness	l_{ion}	=	0.1 mm (0.004 in)
Distance between beta-electrode and detector	L_β	=	29 mm (1.14 in)
Beta-electrode thickness	l_β	=	2.5 mm (0.1 in)
Chamber inner diameter	D	=	10.2 mm (4 in)
Voltage on the beta-electrode	V	=	60 kV
Voltage on the ion-electrode	V_{ion}	=	−100 V
Magnetic field	B	=	0.237 T

Table 2.1: Physical parameters of the TRIMS experiment. Note that while the beta-detector was floating at the same 60 kV as the beta-electrode, the ion-detector was at ground and insulated from the ion-electrode that floated at −100 V.

One complication is that the detectors are behind the electrodes and electric field is not present outside region L in Fig. 2.1. We define L_{ion} as the distance between the ion-detector's detection surface and the ion-electrode surface that faces toward the inside of the chamber, and define L_β in a similar manner. These non-accelerating regions affect our time-of-flight estimation, which will be discussed in Sec. 6.2.2.

2.1.2 Coordinate Reference

As a general reference to the geometry of the decay chamber, we refer to X-direction, Y-direction, and Z-direction using the coordinates shown in purple on the top right corner of Fig. 2.1. We define the X-direction to be pointing horizontally toward the background wall

in the photo Fig. 2.2 and Y-direction pointing vertically upward. Because the decay chamber is azimuthally symmetric, we define R-direction as the radial direction in the XY-plane.

We also refer to X-position, Y-position, and Z-position as the general position along each direction. The origin for each position will be defined in the context. The XY-position at the axis of the cylinder however, is referred to as the center-position.

2.1.3 HV Discharge Prevention

It turned out that building a high voltage (HV) system for the electric field required major design work to prevent it from discharging.

The original physical decay chamber is shown in Fig. 2.3. This chamber manufactured by Larson Glass Co. was different from the one shown in Fig. 2.2; the final design uses a new chamber for reasons we will discuss in this section. This old decay chamber is a Pyrex glass cylinder sealed to a 6 in ConFlat stainless-steel nipple on each side, and we refer to it as the Pyrex chamber.

During a data-taking session, we applied HV on the beta-side to the right of Fig. 2.3. The inside of the chamber was under vacuum. On the outside, the glass part of the chamber was wrapped by metal rings that were joined by a series of 1 GΩ resistors (divider-chain) to ensure the uniformity of the electric field across the chamber. As for the magnetic field, the magnets were rolled into position so that they contained the whole decay chamber inside their bores. In order to avoid HV breakdown from the divider-chain to the magnets, a quartz tube was inserted in between the chamber and the magnets to create an insulation layer. This quartz tube was coated with Licron Crystal Staticide 6500 ESD spray on the outside so that it would not charge up. The 23.5 cm region in the middle is not coated. Copper coating was applied close to each end of the quartz tube, such that the coating was in contact with the metal ends of the decay chamber. The copper coating was laid out uniformly on the interior of the quartz tube to ensure a well-defined potential. Additionally, an aluminum can (Al-can) was inserted in between the quartz tube and the magnets. The Al-can was held by custom-made holders that gripped the magnet cart. The main purpose of the Al-can was

to hold the fragile quartz tube in place. The Al-can also held in place the beta-detector electronics that floated at HV using additional Delrin parts for insulation; the Al-can was grounded. With insulation from the quartz tube and the Delrin parts, the HV could be maintained at 60 kV for hours without shorting or damaging any electronics.

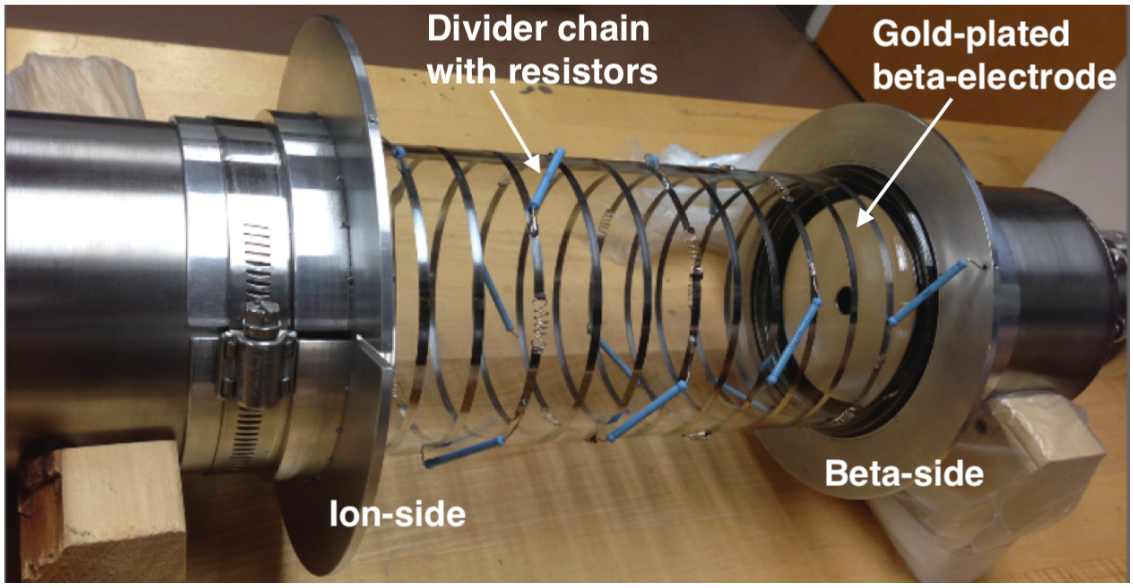

Figure 2.3: Photo of the Pyrex chamber. This chamber was used in the original TRIMS design. The external metal rings and the resistors formed a divider-chain that ensured uniform electric field across the chamber.

However, micro-discharge events were spotted when we turned on the silicon detectors, which regularly generated intermittent event spikes that saturated our data-acquisition capability of 1 kHz (see Sec. 4.1). These sudden event spikes also corresponded to pressure spikes reported by our pressure gauge. This led us to hypothesize the mechanism as: when an electron hit the beta-electrode at high speed, it knocked out ions or even micron-sized charged clusters, which would then be accelerated back to the ion-electrode to knock out even more negative charged particles [134]. This back-and-forth exchange of charged particles between the electrodes could eventually led to a breakdown of the residual gas.

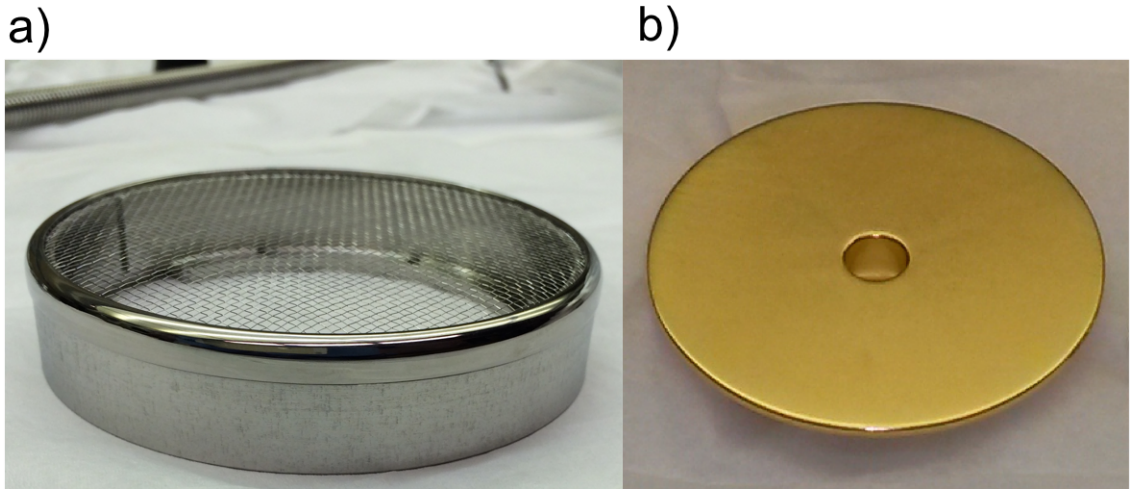

Figure 2.4: Photos of the electrodes. Figure a) shows the ion-electrode consisting of two stainless-steel rings clamped together to hold a piece of stainless-steel mesh. Figure b) shows the gold plated beta-electrode. In each case, the side facing up is the side facing the center of the decay chamber once the electrode is installed.

As an effort to prevent this type of micro-discharge event, we redesigned our electrodes, which were originally simple thin stainless-steel plates with apertures in the middle. The beta-electrode redesign was to coat it in gold as shown in Fig. 2.4.b). The idea is that because the gold atoms are heavy, even the high speed electrons can hardly knock out any gold ions. Moreover, gold is chemically noble, such that hydrogen, tritium, and other atoms do not accumulate on the beta-electrode surface while it is being bombarded by the electrons. As for the ion-electrode, we replaced it with a thin 85%-transmitting Alfa Aesar Type 316 stainless-steel mesh that was clamped in place by two stainless-steel rings as shown in Fig. 2.4.a). While particles can pass through the mesh electrode, a voltage of $V_{mesh} = -100\,\mathrm{V}$ applied on the mesh prevents low-energy negatively charged particles, especially the secondary electrons liberated when the ion is incident on the ion-detector, from wandering into the decay chamber and being accelerated. To charge the mesh electrode inside a fully metallic system, a bare copper wire insulated by a glass "straw" and a few glass "beads" was used to connect the

mesh to an electrical feedthrough. Ceramic stands were also used to make sure the mesh was not shorted to the stainless-steel walls. One small downside of the mesh was that not all the ions that we wish to detect could pass through the mesh, but the effect can be accounted for (Sec. 8.2.4). The electrode designs significantly reduced the rate of micro-discharge events. Unfortunately, we still saw noise events at a rate on par with our design data-taking rate at hundreds of Hz.

Months of testing using the smooth Pyrex glass chamber revealed that our experience with micro-discharge events was consistent with the surface discharge physics described in [135]. The basic mechanism was that a free electron was initially produced at the triple junction of metal-insulator-vacuum on the HV side. Because of the electric and the magnetic fields, the electron was accelerated toward the insulator surface, knocked out more electrons, and eventually created an avalanche of electrons. These electrons induced outgassing on the surface, which created a conducting path across the surface from the beta to the ion-electrode that result in a flashover. These flashovers occurred once every few seconds after the initial buildup. Even though the surface electrons could not be directly detected by the detectors, x-rays produced during the breakdown could. In fact, every time there was a flashover, the x-rays produced would nearly saturate our readout electronics. Thence, we concluded that a decay chamber redesign was necessary to resolve the problem.

The new decay chamber shown in Fig. 2.5 was our solution. The chamber is produced by National Electrostatics Cooperation (NEC) and is specifically designed to prevent discharge across chamber surfaces. The schematic for the decay chamber is given in Fig. 2.6. The cutaway shown in the upper half of the plot reveals the "S-shaped" electrodes. The electrodes are the key design element that can effectively capture the surface electrons and so prevent avalanches from being created. These S-shaped electrodes, which are actually rings by azimuthal symmetry, are connected to thin Kovar rings. These conductive Kovar rings act like electronic feedthroughs: their inner radii are inside the vacuum, while the outer radii are outside. The Kovar rings are insulated from one another by insulating ceramic rings. The alternation between the Kovar and the ceramic rings builds up the decay chamber wall.

Similar to the metal rings on the Pyrex chamber, the Kovar rings are also connected together by a series of resistors on the outside of the chamber to form a divider-chain (Sec. 2.4.1). Compared to external metal rings, the Kovar rings have an extra advantage of having precise separations and fixed positions from the manufacturing process, which provide a more uniformly distributed electric field without the need for careful manual adjustments. Because the Kovar rings are thin, they are covered by corona rings on the outer radii to prevent coronas from forming. One caveat however is that Kovar is magnetic. Fortunately, we did a COMSOL simulation (Sec. 3.3) and it does not significantly perturb the magnetic field to create Penning traps that would cause excess in background events. By using the the NEC decay chamber, our experimental requirement of simultaneously running in high voltage, high magnetic field, and ultra-high vacuum can be satisfied.

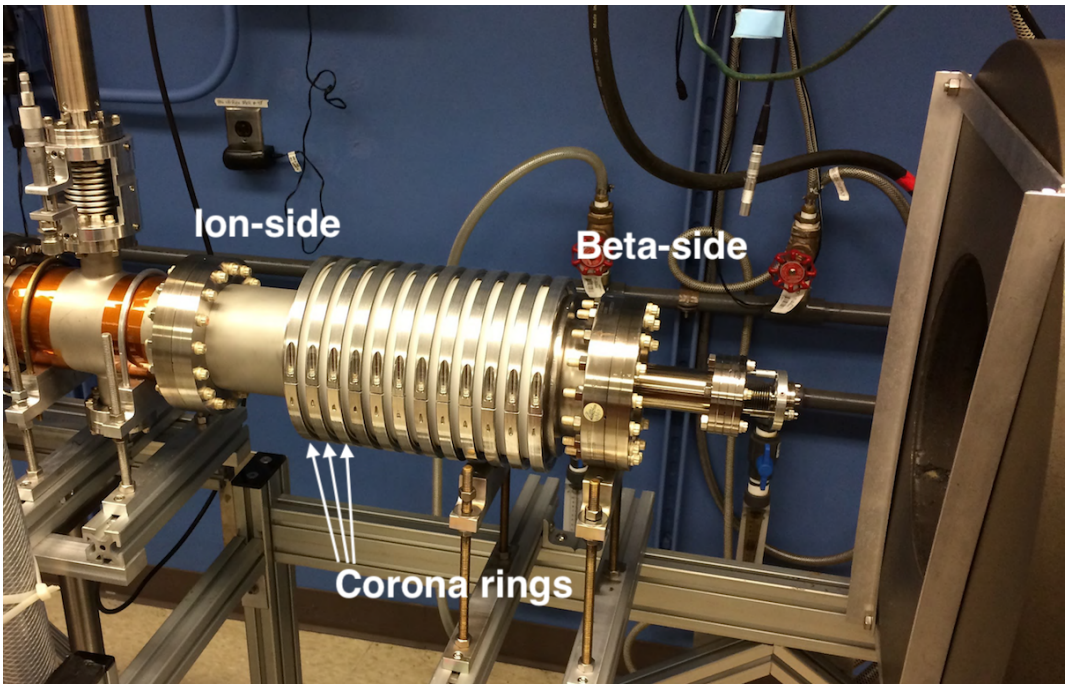

Figure 2.5: Photo of the NEC acceleration chamber. This is also the one boxed in purple from Fig. 2.2. The beta-electrode HV side is to the right, close to the magnet coils. One caveat is that the water valve was attached to the wall, not the chamber.

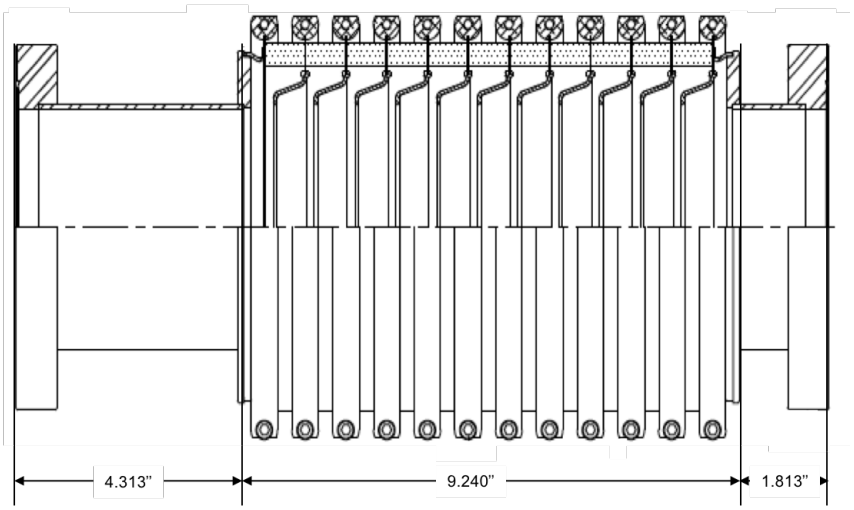

Figure 2.6: Schematic of the NEC acceleration chamber provided by NEC. The chamber is connected to a 6 in ConFlat flange on each side. The upper half shows the cutaway, which reveals the "S-shaped" electrodes connecting to thin Kovar rings. The alternation between conducting Kovar rings and insulating ceramic rings builds up the outer layer of the cylinder.

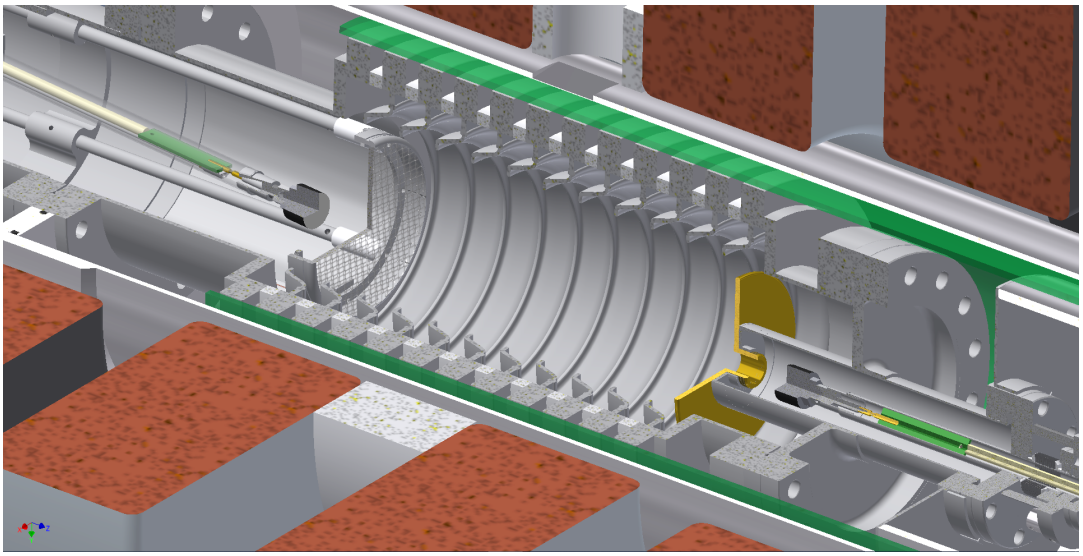

Figure 2.7: TRIMS decay chamber cutaway model [136, 97, 137]. The plot is generated using Autodesk Inventor [138].

After we put together the NEC chamber, as well as the beta and ion-electrode, the system looks like the cutaway model shown in Fig. 2.7. We can see the ion-electrode (Fig. 2.4.a)) on the left and the beta-electrode (Fig. 2.4.b)) on the right of Fig. 2.7.

Finally, discharges can also occur when electrons under voltage concentrate at sharp microscopic edges of conductors. To prevent this type of discharge, we performed HV-conditioning that induced these exact discharges ahead of time to smoothen those metal edges. Both of the detectors were moved off-axis and parked behind shields to prevent them from being damaged during the conditioning. One side note is that while running with the Pyrex chamber, we tried conditioning using a technique called glow-discharge cleaning [139]: the chamber glowed in purple when we ran 3 kV with the chamber filled with argon at 10^{-2} Torr. The discharge condition could be predicted using Paschen's law. Unfortunately, this method sputtered the gold from the beta-electrode and deposited the gold to the chamber's glass surface, which could significantly distort the electric field. We did not repeat the method for the NEC chamber. With the NEC acceleration chamber, we performed conditioning simply by pumping down the chamber to below 10^{-6} Torr and ramping up the beta-electrode to 60 kV. Initially we could see discharge events at tens of Hz, but they went away after a few hours.

Ultimately, the decay chamber was able to run HV discharge-free. The noise event rate in the background when we tune up HV has been consistent with the expected rate of cosmic muons at around 0.1 Hz.

2.2 Vacuum System

2.2.1 Vacuum Setup

The schematic of the TRIMS vacuum system is shown in Fig. 2.8. The main-vacuum system is boxed in blue and it is supported by an extruded aluminum framework. The framework has wheels that allow motion and feet with rubber ends that can be screwed down to settle the framework's position. The main-vacuum system is designed to keep the decay chamber

base-pressure, i.e. pressure in cases when no gaseous sources are introduced, under ultra-high vacuum (UHV). To do that, the main-vacuum system is constructed primarily using stainless-steel ConFlat components and all-metal valves, e.g. all the VAT 54032-GE02 angle valves labeled "AV" in Fig. 2.8. There are also glass insulators that protect the gauges' electronics during a HV breakdown and a UV window that creates a line-of-sight for beta-detector energy calibration (Sec. 5.2.2). Both types of these glass parts are also designed for UHV. Notice that all these materials are non-magnetic, which is necessary to ensure uniform magnetic field in our system. To limit dust contamination, most of the assembly was done in a cleanroom environment with additional work carried out on a laminar-flow cabinet. Moreover, all the parts that went inside the vacuum system were ultra-sonicated first in Alconox solution and then in deionized water.

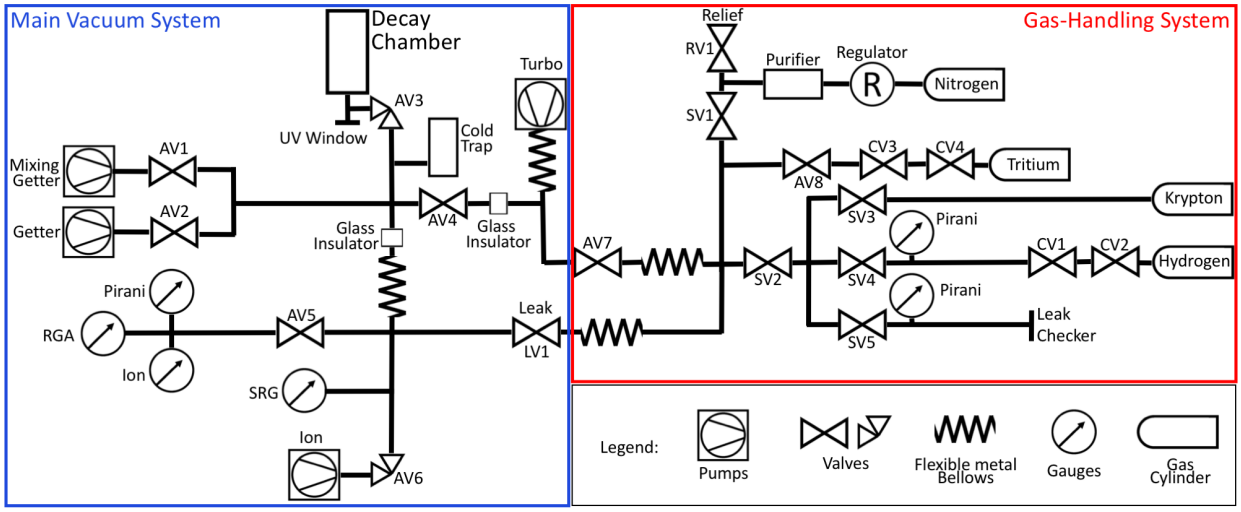

Figure 2.8: Schematic of the TRIMS vacuum system. The main-vacuum system is boxed in blue to the left. The gas-handling system is boxed in red to the right. For the gauges, RGA stands for the residual gas analyzer and SRG for the spinning rotor gauge. For the valves, the AVs are ConFlat, the SVs are VCR, the LV is a leak valve, and the CVs are VCR valves on the source cylinders as in Fig.2.11.

Three types of vacuum pump are used. The first is a Pfeiffer HiCube Eco 80 turbomolecular pump (turbo pump) backed up by a Pfeiffer MVP 015-2 diaphragm pump. As shown in Fig. 2.8, to prevent microphonic noise from the vibration of the pump, the pump is placed on the ground and connected to the main-vacuum system via a long flexible bellows. The turbo pump can bring the pressure from atmospheric pressure all the way down to 10^{-8} Torr level. The second pump is a 20 l/s Varian VacIon ion pump, which can bring the pressure further down to 10^{-9} Torr level and induce no mechanical vibration. It also allows for a completely hermetic operation when we inject radioactive source in main-vacuum system. The system also contains two SAES GP 50, St-101 getter pumps for pumping, storing, and mixing the tritium source; details are provided in Sec. 2.3. To achieve even lower pressure, the system is designed to be bakable. The most significant contribution to pressure at this point is the residual H_2O molecules that can loosely adhere to the steel walls, making them difficult to pump away. Baking the system frees the H_2O gas from the walls so that it can be pumped out by the turbo pump. More details about the bake-out are described in Sec. 2.2.2. The residual H_2O can be further reduced by filling a cold trap cooled with liquid N_2; the H_2O molecules would then adhere to the cooled walls of the cold trap instead of entering the decay chamber. However, each fill only lasts a few hours, and so the cold trap is to be filled before every data-taking session. Finally, the base-pressure achieved has been stable at 2×10^{-9} Torr.

The gas-handling system is boxed in red in Fig. 2.8 and it is supported by the same extruded aluminum framework that supports the main-vacuum system. The gas-handling system is designed to introduce gaseous sources such as T_2 to the main-vacuum system. This system is constructed primarily using stainless-steel VCR parts, e.g. all the Nupro/Swagelok valves labeled "SV" in Fig. 2.8. While the gas-handling system cannot achieve UHV like the main-vacuum system, it is much more lightweight and more flexible in changing configurations such as adding another source. The gas-handling system along with the main-vacuum system was leak-checked using helium. The system is also bakable to reduce H_2O on its surface. The gas-handling system is connected to the main-vacuum system via a VAT angle

valve (AV7) and a NorCal LL-275-133 leak valve (LV1 in Fig. 2.8). The valve AV7 along with valve AV4 allow both systems to share the same turbo pump without contaminating each other. Another use of the AV7-AV4 passage is when we introduced nitrogen during the decay chamber construction to prevent dust from entering the main-vacuum system. The nitrogen purified by a SAES purifier was introduced to the decay chamber site at a pressure slightly greater than atmospheric pressure. A relief valve was installed to prevent over-pressuring the system. Finally, the leak valve LV1 allows us to fine-tune the amount of source gas introduced to the main-vacuum system. This valve is the main control valve for taking tritium data.

As for monitoring the pressure of the vacuum system, three types of gauges are used, where each applies to a different situation. The MKS-317 convection-enhanced Pirani gauges have a range from atmospheric pressure to 10^{-3} Torr. They are typically used during the initial pump down or while leak-checking the system. We have three Pirani gauges in our vacuum system (Fig. 2.8). Since we do not need to access all three pressures at a time, we have only one controller to connect to one of the three gauges at a time when that reading is relevant. The Leybold-Heraeus Ionivac IE-211 nude ion gauge has a range from 10^{-4} Torr to 10^{-9} Torr. It is used when the system is under UHV. These two types of gauge cover the full pressure range. However, we need the MKS-SRG-3 spinning rotor gauge (SRG) when we are introducing gaseous sources to the main-vacuum system. This is because the pumps have to be valved off in this case. The outgassing from an operating ion gauge, which is much faster than the outgassing from the stainless-steel walls, would quickly "flood" the ultra-high-vacuum. It turns out that the ion gauge would convert our source T_2 into HT through ionizing and catalytic effect of the filament (Sec. 2.3.2). Hence, the SRG that operates purely mechanically is used during data-taking instead; we can see from Fig. 2.8 that the SRG is the only gauge in the main-vacuum system that is not valved-off from valve AV5. The SRG has a range of 10^{-4} Torr to 10^{-6} Torr, which is exactly the desirable pressure range when source gas is introduced (Sec. 4.2.1). To better monitor the pressure, readings from all these gauges are displayed live (Sec. 4.1.1) and recorded by our slow control (Sec. 2.6). Other than

pressure gauges, a SRS-RGA100 residual gas analyzer (RGA) is used to periodically check the mass composition of the gases present in the system.

2.2.2 Bake-out

We bake the system to remove the residual H_2O molecules that adhere to the walls so that we can pump them out.

To build a bakable system, all the ConFlat connections need to be sealed with silver-plated copper gaskets and silver-plated bolts and the VCR connections with nickel gaskets. As for heating the system, we enclosed the decay chamber with a BriskHeat SRL flexible silicone rubber heating blanket. The rest of the main-vacuum system and the gas-handling system were wrapped with Omega SRT heating tapes. The Pirani gauges, the SRG, the RGA, and the getter pumps had to be turned off and had their controllers removed for them to be bakable by the heating tapes. Some parts of the system were not covered by the heating devices however. These included the purifier on the nitrogen line that could not be baked, the source cylinders that were separately baked before they were filled with gases, and the ion gauge that needed to be turned on so that we could monitor the pressure during the bake-out. Because the ion gauge has its own degassing functionality, we did not worry about it accumulating H_2O. The turbo pump was turned on during the bake-out to collect the residual H_2O; only the bellows connected to the pump's inlet needed to be baked. After covering the system with the heating blanket and tapes, we wrapped a few layers of aluminum foil on top of these heating devices to increase heating efficiency and uniformity. The next task would be to monitor these heating devices.

The maximal baking temperature was bounded by the UV window at 200 °C, while the maximal rate of heating was bounded by the VAT valves at 60 °C/hr. It is desirable for the decay chamber to be at a higher temperature and be baked longer than the rest of the system; we prioritized vacuum quality of the decay chamber. To achieve such temperature control, the system was separated into 7 sections, where each section was monitored by a type-K SA1XL-K-SRTC thermocouple. These heating devices and thermocouples were then

connected to an Omega CN1507 temperature controller that had 7 control channels. A feedback loop operated at each channel, such that the heating was turned on and off based on the thermocouple reading. The controller's temperature reading was also connected to a slow-control system (Sec. 2.6) to trace temperature over time. An illustration is shown in Fig. 2.9. The red trace shows the decay-chamber temperature, which has a maximum temperature of 200 °C. As planned, this temperature is greater than that shown by the blue trace, whose reading was taken from one of the 7 sections that was right next to the decay chamber. The maximum temperature was also maintained longer for the decay chamber. The black trace in the same plot is the pressure reading from the ion gauge. We can see the baseline pressure improved from 10^{-8} Torr to 10^{-9} Torr because of the bake-out.

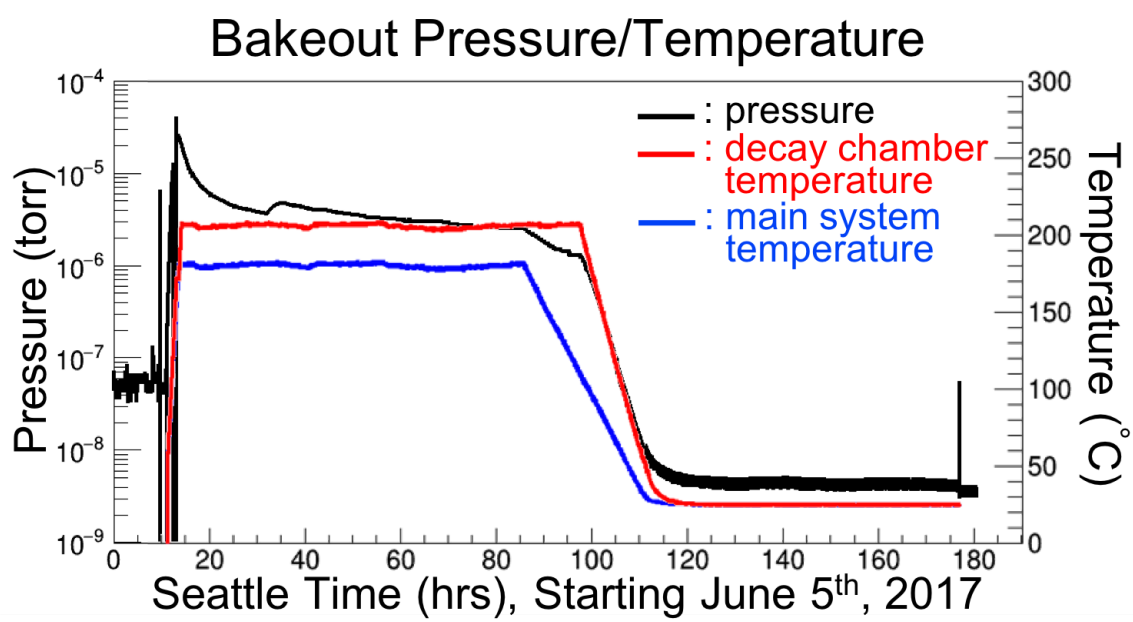

Figure 2.9: Pressure/temperature over time during one of our bake-out sessions. The y-axis has pressure on the left and temperature on the right, while the x-axis is over time.

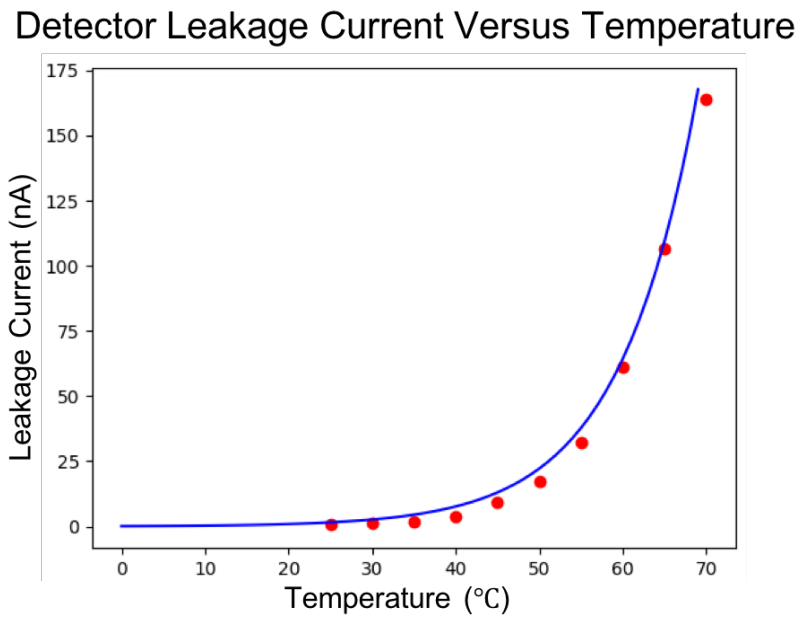

Figure 2.10: Detector leakage current versus temperature [136]. The red dots are from the data, while the blue curve is a fit to the data using an exponential function.

There was a complication with regard to the silicon detectors. They can only be baked up to 80 °C, which is much lower than the 200 °C bound. We had to actively cool the detectors during bakeout. To do that, we connected compressed air lines to the readout feedthroughs of the detectors to cool them down. However, the question was, how would we know whether the cooling was sufficient or not, especially considering the main detector bodies were in the vacuum system. The resolution [140] was to read out detector temperature via leakage current. We biased each detector with a 9 V battery without connecting the detector to its pre-amplifier and read out the leakage current through thin coated wire connecting the detector output to a pico-ammeter. The wire was coated to prevent shorting to the detector's stainless-steel reentrant-tube (Sec. 2.5.4). The readout circuitry is shown as a part of Fig. 2.13. To calibrate the readings, we tested the leakage current to temperature correspondence using a spare detector, thermocouple, and a Cascade Tek oven. We connected

the circuitry to the detector, Kapton-taped the thermocouple to the detector mount, and heated up the detector using the oven. The result is shown in Fig. 2.10*. The red dots are the data points. To account for the delay between the temperature measured at the surface of the detector and the temperature in the bulk of the detector, we always waited until the leakage current reading stabilized before we recorded the reading. The data was fit by an exponential function shown by the blue curve, and it was a good fit as expected [141].

With the ability to read the detectors' temperature, we started baking our system along with our detectors. However, the initial attempts put the detectors at risky temperatures; more efficient cooling was required. The resolution [140] was to install straw-sized Teflon tubes around the sections of the compressed air lines inside the reentrant-tubes. The heat-insulating Teflon tube reduced the heat exchange between in-flow and out-flow, which increased the cooling efficiency. After the installation, the bake-out reached the desirable temperatures, with the detectors surviving the heat. One final small concern was that the residual H_2O would tend to adhere to the detectors because they were at lower temperatures than the surroundings. Fortunately, the detector resolutions were just as good after baking.

2.3 Sources

2.3.1 Radiation Safety

The tritium, krypton, and hydrogen gaseous sources are attached to three separated legs of the gas-handling system as labelled in Fig. 2.8. Since both tritium and krypton are radioactive materials, appropriate safety measures are required before introducing them to the decay chamber. First of all, the TRIMS experiment was conducted in North Physics Lab (NPL) 162† of the Center for Experimental Nuclear Physics and Astrophysics (CENPA) at University of Washington (UW). This lab is designed for radioactive experiments. It has

*This is a functional plot to allow us to bake the detector. However, it does not go into the analysis, so no error bars are provided.

†The room is also known as the Hot Lab.

two fume hoods that draw air in and exhaust at the roof, which creates negative pressure as compared to that of surrounding lab space. Its doors are always locked and only authorized personnel have access; these personnel must have passed radiation safety trainings and must carry a personal dosimeter while they are in the lab. When the radioactive materials arrived in the lab, periodic swipes were taken to measure the level of radioactive contamination in the lab. We also made a comprehensive documentation that includes procedures such as the cleanup in case of a hot swipe and the disposal of the radioactive material at the end of the experiment. The documentation is held by the Radiation Safety Officers (RSO) and CENPA administration.

Specifically for the gaseous tritium source, instrumentation-wise, the gas-handling system was constructed using all metal parts. Plastic and rubber parts would not be ideal because the tritium would diffuse out due to its small atomic size and radiochemical reactions would break down these materials. The sources should be confined inside the system and pumped out only to the designated vent. Once tritium operations started, all TRIMS vacuum-system equipment is considered contaminated because tritium tends to adhere to their metal surfaces. The only exit ports are the relief and the turbo pump shown in Fig. 2.8. For the relief, SV1 is to stay valved-off until the end of the experiment. The exhaust line of the turbo pump is routed to one of the fume hoods. However, before being pumped out from the turbo pump, the tritium should first be collected by one of the SAES getters. At the end of the experiment, the SAES getters should also be activated, while at the same time introducing N_2 from valve SV1. This process will efficiently reduce the tritium contamination of the equipment. If measurements show low radioactivity, valuable dismantled equipment can be reused. Otherwise, the equipment will be disposed of as low-level radioactive waste (LLRW).

As for the gaseous krypton source, because of its short half-life and low-energy electrons, it's not considered a radioactive contamination to the system. However, the rubidium generator of the krypton source does produce 500 keV gammas. Fortunately, the rubidium atoms tend to stick to the wall due to their chemical reactivity and so the gamma hazard is localized to the source cylinder. The cylinder was wrapped by a lead sheet, reducing the dose to

about 4 mR/hr. Even then the lab personnel are required to perform tasks at an increased distance from the source cylinder.

Finally, TRIMS also uses americium sources. The solid sources produce alphas and low-energy gammas at low dose. The alphas are not harmful unless the sources are ingested. As for the gammas, again, the lab personnel are required to perform tasks at an increased distance and to reduce time carrying them whenever possible.

This sums up the safety measures. The following subsections discuss the usage.

2.3.2 T_2 and HT Source

Recall that the primary scientific goal of TRIMS is to study properties of tritium decay (Sec. 1.6). This subsection focuses on the specific usage of a molecular T_2 source in the TRIMS experiment.

In the TRIMS experiment, T_2 gas is introduced at room temperature, which means that we do not need a cryogenic gas-handling system like the one from KATRIN. Instead, the T_2 source is contained in a stainless-steel cylinder that has two VCR valves welded to it as shown in Fig. 2.11[97]. The two-valve design, e.g. valve $CV4$ and $CV3$ in Fig. 2.8, allows us to control the quantity of T_2 that the cylinder releases. The method is to first close $CV3$ and open $CV4$ to let T_2 in the small volume in between the two valves, and then close $CV4$ to trap the source. Now, when we open $CV3$ to release T_2 to the system, we only let out a small amount of T_2 at a time, while minimizing the amount of contamination from the residual gas to the cylinder's main body.

There is an identical cylinder made for H_2. Both cylinders were built in the CENPA instrument shop. Both of the cylinders were helium-leak-tested and baked to 250 °C. The T_2 cylinder was sent under vacuum to American Radiolabeled Chemicals, Inc. and was loaded with about 1 Ci of T_2 gas, while the H_2 cylinder was loaded at CENPA with an equivalent amount of high-purity H_2 gas purchased from Praxair. The sources have since been attached to the gas-handling system via VCR seals.

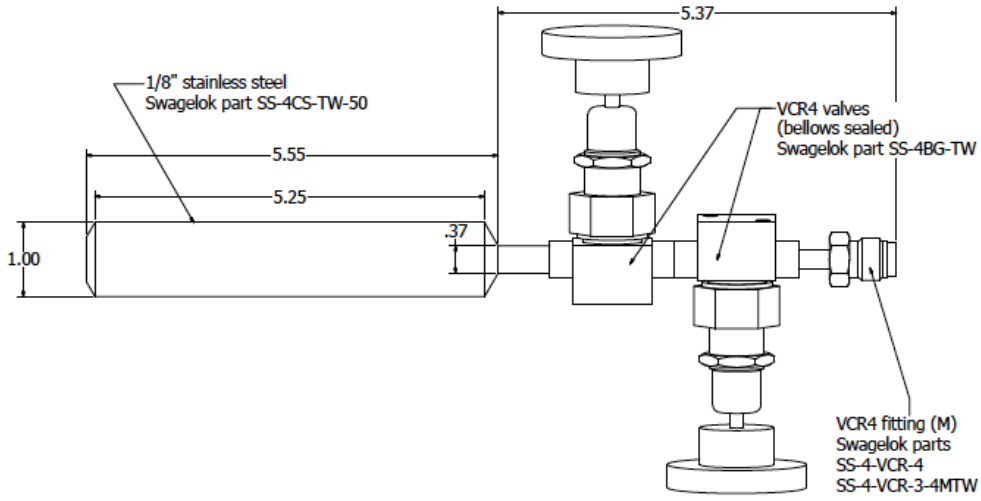

Figure 2.11: Schematic of the T_2/H_2 cylinder [97]. The container is to the left. And from left to right in this figure, the valves are designated CV4 and CV3 for the T_2 cylinder and CV2 and CV1 for the H $_2$ cylinder in Fig. 2.8.

Once the gas-handling system is filled with T_2, we control the amount of T_2 released to the main-vacuum system using a leak valve (Sec. 2.2.1). While an accurate knowledge of the tritium event rate is not necessary for the TRIMS experiment, the event rate should not saturate our data-acquisition (DAQ) system that has a limit of 500 Hz with the two detectors (Sec. 4.1.2). For this reason, we introduce T_2 slowly to reach an event rate of roughly 200 Hz. Afterward, we close the leak valve and are ready for a data-taking session (Sec. 4.2.1).

One problem however is that even if all the AV valves except AV3 are valved off, the walls still outgas. In other words, the pressure is always rising while we are taking tritium data. We can only allow the pressure to reach a certain limit before we pump out the main-vacuum system and refill it with T_2. The pressure limit is determined by the rate of the so-called charge-exchange interaction, which is the interaction between the molecules that makes them ionize each other in a gas. This process also produces ions, and so it can produces background events that look like tritium beta decay events. Suppose we want the charge-

exchange interaction to contribute about 1% of the overall events, then the charge-exchange mean path should be $\lambda \approx 10\,\mathrm{m}$ that is 100 times the average ion travel distance $\approx 0.1\,\mathrm{m}$. The charge-exchange cross section per atom is given by $\sigma \approx 10^{-19}\,\mathrm{m}^2/\mathrm{atom}$ [142]. By using the ideal gas law $P = nRT$, where the number density of the gas is given by $n = 1/(\lambda\sigma)$, we arrive at a pressure limit of,

$$P = \frac{RT}{\lambda\sigma} \approx 3 \times 10^{-5}\mathrm{Torr}. \tag{2.1}$$

To be conservative, we set our pressure limit to be $10^{-5}\,\mathrm{Torr}$, which is conveniently also the pressure that is just in the range of the SRG. At a pressure below this limit, we can neglect charge-exchange interaction. It turned out that it generally takes about 80 min before outgassing hits the pressure limit, which gives us sufficient time to take data before each refill (Sec. 4.2.1).

A vital source of systematic error that we cannot avoid is HT contamination in the T_2 source. Since stainless steel outgases hydrogen, T_2 can easily interact with H_2 to form HT. Yet, unlike H_2 that only contributes a rise in pressure, HT also beta decays. Moreover, the longer T_2 is kept in the cylinder, the larger the proportion of the source gas that becomes HT. Any physical method that removes HT and maintains T_2 purity would require a significant complication to our gas-handling system. Thence, we decided to take HT data alongside the T_2 data and study them both.

The original plan to obtain HT data was to use one of the getter pumps shown in Fig. 2.8. By introducing both T_2 and H_2 gas into the getter and heating the getter up, we expected the source would be "mixed" into HT, and thus the name "mixing getter". Incidentally, we found that the ion gauge filament* contains iridium [143]that acted as a catalyst and turned T_2 and H_2 into HT via isotope-exchange reactions [144]. Since then, we rely on using the ion gauge to convert T_2 to HT (Sec. 4.2.1). The quantitative study of the purity as well as the conversion will be provided in Sec. 7.1.2.

*The Pirani gauge is also believed to contain platinum-group metals.

2.3.3 Krypton Source

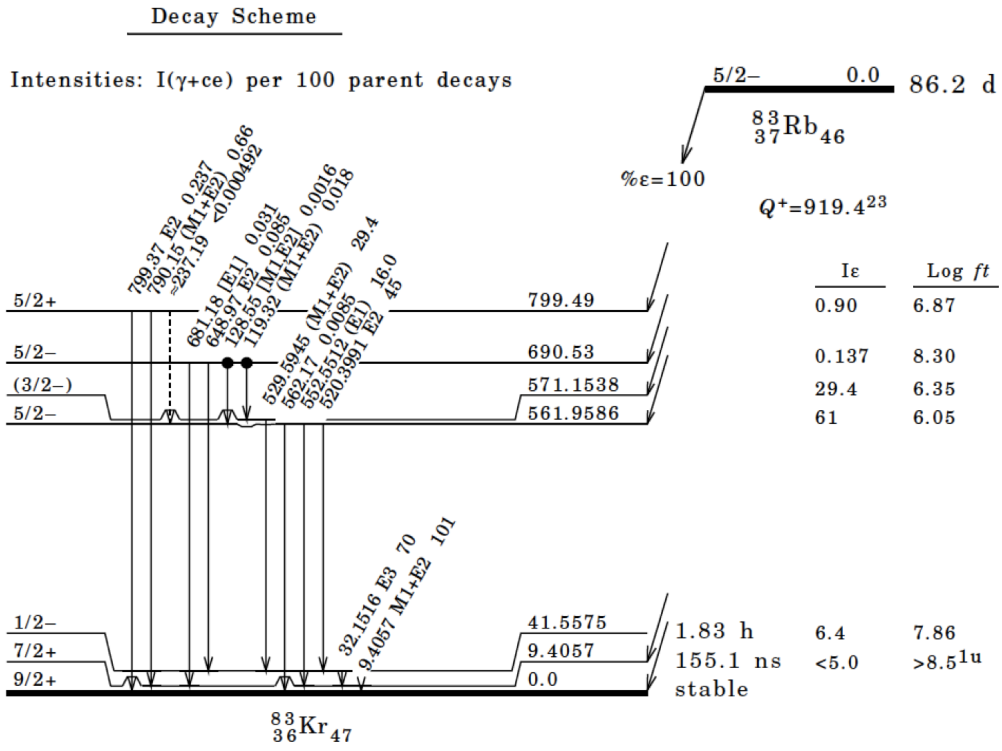

Figure 2.12: Rubidium-83 electron capture [145]. The decay product of interest is the metastable 1/2− isomeric state ^{83m}Kr that decays through internal conversion and has a half-life of 1.83 hr. The decay modes of ^{83m}Kr are provided by Table 2.2.

The krypton source used in TRIMS is krypton-83m (^{83m}Kr). The ^{83m}Kr is the decay product of rubidium-83 (^{83}Rb) through electron capture (a process that was explained in Sec. 1.4.3). The decay has a half-life of 86 days as shown in Fig. 2.12. The "m" in ^{83m}Kr indicates that it is a metastable nuclear isomer. The excited state of interest is the 1/2− isomeric state, which decays into a lower energy state through internal conversion,

$$^{83m}\mathrm{Kr} \rightarrow ^{83}\mathrm{Kr}^{+} + e^{-}. \tag{2.2}$$

Internal conversion (IC) refers to the decay process when an orbital electron interacts with the excited nucleon electromagnetically, and the de-excitation of the nucleus causes the electron to be emitted carrying the de-excitation energy. The ^{83m}Kr electron source is monoenergetic* and serves as a sharp electron calibration source (see Sec. 5.2.2). The isomer is metastable with a half-life of 1.83 hr as shown in Fig. 2.12, which is just long enough that ^{83m}Kr can be effectively used as a gaseous electron source.

Nuclear γ Transition Energy (keV)	Atomic Subshell	Mean IC Electron Energy (keV)	Total Intensity (%)
9.41	L	7.517	80.0
	M	9.125	12.9
	N	9.380	1.3
32.15	K	17.824	24.8
	L	30.446	63.7
	M	31.934	10.7
	N	32.137	0.8

Table 2.2: Conversion-electron lines for ^{83m}Kr, adapted from [146].

The ^{83m}Kr internal conversion channels are provided in Table 2.2. Other than the IC electrons, there are also Auger electrons. An Auger electron is an orbital electron emitted from an outer atomic shell when the atom's electron configuration reconfigures to fill a vacancy from an inner atomic shell. The vacancy in this case is caused by the internal conversion

*It is actually not quite monoenergetic because there are multiple lines that are close together in energy. And of course, each line has its natural width. But resolving these lines is not a task for the TRIMS experiment.

emitting an inner-shell electron. Shake-off electrons may also be emitted when the IC or the Auger electron provides enough perturbation to the atom's electron configuration. As a result, compared to Eq. 2.2, a more ionized ^{83}Kr will be produced along with more electrons. Despite the extra complications, the channels in Table 2.2 do provide monoenergetic calibration electrons in our range of interest (Sec. 5.3.5).

Notice that krypton ions are also produced when the decay emits electrons. These ions are heavy and so if they are accelerated by HV toward a detector, they can degrade the detector sensitivity (Sec. 5.1.2). Therefore, ^{83m}Kr calibration was conducted with no electric field. We still needed the magnetic field to guide the electrons toward the detectors.

The ^{83}Rb cylinder is attached to the gas-handling system and is shown as a gas cylinder labelled "Krypton" in Fig. 2.8. This source was provided by Pacific Northwest National Laboratory (PNNL) and was a decommissioned source from Project 8 (Sec. 1.4.2). The source was in the form of rubidium chloride adsorbed onto zeolite beads that were contained in a small $10\,\mathrm{cm}^3$ stainless-steel cylinder. To take krypton-data, we introduced ^{83m}Kr via the leak valve as with the tritium source. However, because no electric field was required, the decay chamber was not under HV, and so we did not need to worry about the charge-exchange interaction of the gas as the pressure rose. As a result, we could take overnight ^{83m}Kr calibrations.

Noteworthily, even with electric field, the ^{83m}Kr source does generate plenty of coincidence events, i.e. events that trigger both the beta- and the ion-detector (Sec. 2.5.2). These coincidence events come from two electrons being produce in the ^{83m}Kr de-excitation. Because the nucleus does not de-excite to the ground state from the first internal conversion, a follow up internal conversation can knock out yet another electron,

$$^{83m}\mathrm{Kr} \rightarrow^{83m} \mathrm{Kr}^{+} + e^{-} \rightarrow^{83} \mathrm{Kr}^{++} + 2e^{-}. \tag{2.3}$$

The first IC electron can result in a coincidence event with either a prompt 17.8-keV Auger electrons or a second IC electron from Eq. 2.3. We rely on these coincidence events from the krypton-data to align (Sec. 2.5.4) as well as to correct for the time-zero shift between

our detectors(Sec. 6.1.2).

2.3.4 Americium Source

The americium source used in TRIMS is americium-241 (^{241}Am) that has a half-life of 432.2 yr [147] under,

$$^{241}_{95}\mathrm{Am} \rightarrow ^{237}_{93}\mathrm{Np} + \alpha^{2+} + \gamma. \tag{2.4}$$

Although ^{241}Am is a common alpha source, we are interested in the 59.5409 keV gammas. Beside the ^{83m}Kr electrons, we also use the gammas to calibrate our detectors (see Sec. 5.2.2).

Our ^{241}Am source is a puck-shaped solid with an activity of 100 µCi. We place it at the UV window to calibrate the beta-detector. We could also use ^{241}Am source to calibrate the ion-detector when we had the Pyrex chamber because it has transparent chamber walls. With the NEC chamber however, we need other methods to calibrate the ion-detector (Sec. 5.2.2).

2.4 Field Setup

In the TRIMS experiment, we impose an electric field and a magnetic field that are parallel to each other along the axis of the decay chamber. This section describes how the fields are configured.

2.4.1 Electric Field

The electric field is provided by tuning a high voltage (HV) LG-80N-1.5 Glassman power supply and ramping up the beta-side of the chamber to a nominal voltage of 60 kV. The power supply conveniently provides analog voltage readout available for our slow control (see Sec. 2.6), so that any variation from tuning can be tracked (Sec. 4.3.4) and adjusted (Sec. 5.2.3). The power supply is connected to the beta-preamp-can by a HV power cable and a resistor mount. The resistor mount consists of a Teflon tube containing a 400 MΩ resistor that is soldered to a banana plug; the resistor is there as a safeguard to HV shorting. The beta-preamp-can is a cylindrical aluminum-can that holds in place the electronics necessary

for the beta detector and provide sockets to external connectors. The beta-preamp-can is electrically in contact with the ConFlat reducing nipple to the beta-side, i.e. to the right of Fig. 2.5; copper finger-stocks are used to ensure the contact. The beta-preamp-can sits inside the Al-can (Sec. 2.1.3). We mount the two cans together using Delrin parts so that the preamp-can can float at HV while the Al-can is grounded. To ensure uniform electric field, we link together the Kovar rings on the NEC chamber via a divider-chain (Sec. 2.1.3). The divider-chain consists of 76 1-GΩ 1% resistors across 12 Kovar rings, which gives 7 resistors in each gap except the gap to the ground that has 6 resistors. Given that there is a 300 V drop in voltage from the 400 MΩ resistor mount and a -100 V bias applied on the ion-electrode, both of which contribute little, this setup establishes a uniform voltage gradient of $59.8\,\mathrm{kV}/235\,\mathrm{mm} = 254\,\mathrm{V/mm}$.

When using the HV power supplies, we need to be cautious of a possible large breakdown that produces high-frequency transient current. This current would pass right through the glass insulators (Sec. 2.2.1) and damage our electronics. To protect our electronic devices, we need proper radiofrequency (RF) grounding. To do that, we connected the vacuum system via copper straps to a common copper busbar on our electronic rack that holds controller electronics. Moreover, the HV power cable is covered by copper braid and is routed on a cable tray mounted on the ceiling, and the HV power cable is covered by copper braid and is routed on a railing mounted on the ceiling. Even then, we make sure that we ramp up the HV power supply slowly to prevent this type of breakdown from happening.

In certain cases (Sec. 5.2.2), we would also like to run a reversed voltage of -48 kV across our chamber with no magnetic field. The power supply we use in these cases is identical to the one mentioned in the standard setup but supplies negative voltage. The reverse-biased setup must be operated with extra caution because the S-shaped electrodes on the NEC chamber have certain directionality (Fig. 2.6), favoring a positive-voltage setup. No gaseous sources are used in a -48 kV setup.

2.4.2 Magnetic Field

The magnets used in TRIMS are two pairs of Varian NMR copper coils. The inner V3400 pair both have 23 cm inner diameter, 56 cm outer diameter and 9 cm depth. The outer V3401 pair both have 25 cm, 58 cm, and 10 cm.

The magnets are positioned with approximately 4 cm gaps between each other. Their relative positions are fixed by a custom-built aluminum cart. Because we need to enclose the whole decay chamber in the magnets' bores to provide uniform magnetic field, the cart is designed so that two people can effortlessly move the magnets back and forth around the position of the decay chamber. The cart sits on an extruded aluminum stand as shown in Fig. 2.2, and the stand acts like a railway such that the cart can only move in the decay chamber's axial direction. The stand is customized to stand firmly on the floor; its position has been fixed since the initial installation of the magnets to optimize the alignment between the electric and the magnetic field. Each pair of the magnets is independently wired and supplied by a Danfysik 823 power supply that provides a current of 140 A. Both the coils and the power supplies require water cooling provided by CENPA's filtered chilled-water system. We used three flowmeters, one for the coils and one for each power supply, to ensure there is enough water for cooling. The magnets provide a nominal magnetic field of $B = 0.237\,\mathrm{T}$, when both of the power supplies were turned up to 52% of their capacity.

We would like the magnetic field to be as strong as possible so that charged particles can be guided to the detectors with as small gyroradii as possible. The relativistic gyroradius is given by,

$$r_g = \frac{\gamma m v_\perp}{|q|B}, \tag{2.5}$$

where m is the mass of a particle with charge q, and $v_\perp$ is the velocity of the particle perpendicular to the direction of the magnetic field B. As an example, consider a beta with an initial kinetic energy of 10 keV traveling in the R-direction (Sec. 2.1.2), i.e. $v_\perp \approx 0.2c$, that is accelerated to have a final Z-direction kinetic energy of 30 keV, i.e. $\beta c \approx 0.37c$ or $\gamma \approx 1.08$. Then with $B = 0.237\,\mathrm{T}$, the beta's gyroradius is $r_g \approx 1.5\,\mathrm{mm}$. As for an ion, because they

are non-relativistic even after being accelerated by a 60 kV electric potential, $\gamma \approx 1$. Due to momentum conservation, the $mv_\perp$ terms for the ions are roughly the same as that for the beta*, and so are their gyroradii. However, the typical gyroradii would be slightly different between different ion types. And because these gyroradii are in the same order of magnitude as the detector radius of 4 mm, they would cause noticeable bias in detection efficiency, which would be a substantial systematics. Fortunately, this issue can be handled using an analysis method we call the scan-deconvolution (Sec. 8.1).

The stability and the uniformity of the fields will be covered in Sec. 4.4.

2.5 Detector System

2.5.1 Detector Electronics

Both the ion and the beta-detector are partially depleted Passivated Implanted Planar Silicon (PIPS) PD-50-11-500AM detectors manufactured by Canberra [148]. A photo of the detector is shown later in Fig. 2.16. The detectors from this series have an active area of 50 mm^2 (or 4 mm radius) and a thickness of 0.5 mm. These silicon detectors are designed to have low capacitance, low leakage currents, as well as thin dead layers. These are the properties that ultimately lead to a desirable detector energy resolution (Sec. 5.2.5).

Although the manufacturers do provide their measurements for these detector properties, we would still like to test using a simple electronic setup shown in Fig. 2.13. We refer to it as the bias-box. The "BIAS" input on the bias-box is connected to a Tennelec TC 952 high voltage power supply that powers the test detector. To test the capacitance, we connect the detector to the "Detector C-Meas" input and an AADE inductance/capacitance (L/C) meter IIB to the "C-METER" output. The capacitance reading on the L/C meter should tell us the detector capacitance. On the other hand, to test the leakage current, we connect the detector to the "Detector Leakage Meas" input and a Keithley 6485 pico-ammeter to

*The momentum of the ion is usually larger if we take into account the antineutrino and that the ions are the heaviest among them.

the "Pico-ammeter" output. The reading on the pico-ammeter should tell us the detector leakage current. During the test, the detector is covered by a black cap and enclosed in an aluminum box to avoid light and ground contamination. Notice that among several detectors we purchased, we used the one with the best performance as our ion-detector, and the second best as our beta-detector. And the test result shows that at the room temperature with the recommended 130 V detector bias: the ion-detector has a capacitance of 27 pF and a leakage current of 1.5 nA, while the beta-detector has 27 pF and 2.1 nA.

As for the dead-layer thickness, a direct measurement is a lot more difficult. Fortunately, we are able to derive the information later in our data analysis based on SRIM simulations (Sec. 3.2.2). The quote from the manufacturer is 50 nm.

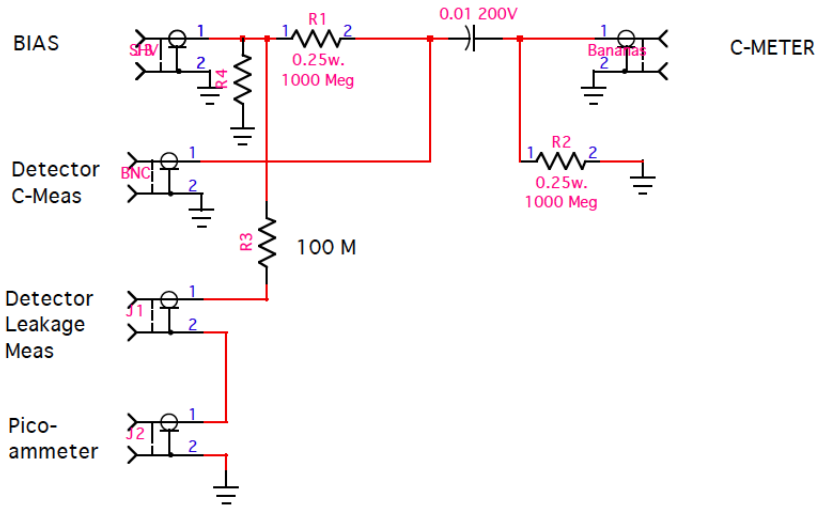

Figure 2.13: Schematic of the detector bias box [149]. The connections on the left correspond to detector bias (BIAS), detector connection for capacitance measurement "Detector C-Meas", detector connection for leakage-current measurement "Detector Leakage Meas", and pico-ammeter connection for the leakage-current measurement "Pico-ammeter". The output on the right corresponds to a capacitance meter for the capacitance measurement "C-METER".

The detectors are connected to SMA vacuum feedthroughs with a pin for the preamp on the air side. Each of these feedthroughs is mounted on one end of a long stainless-steel tube that has the other end welded to a mini-ConFlat flange. We refer to these tubes as reentrant-tubes. The reentrant-tubes have small inner diameters of 1 cm. Notice that the inside of the reentrant-tube is actually on the air side of the feedthrough, which leaves little room for electronics to connect directly. For this reason, the front end of each detector preamplifier (front-end preamp) was assembled on a $1\times\ 3\,\mathrm{cm}^2$ board [149] that is attached to a 3 mm diameter fiberglass pushrod so that the preamps can be inserted into the reentrant-tubes. The size of one of the front-end preamps is shown in Fig. 2.14. The Teflon spacer is there to prevent the front-end preamp electronics from shorting to the reentrant-tube. The Teflon spacer also helps guide the female pin socket through the reentrant-tube to the pin on the feedthrough at the end of the tube. A grounding spring is soldered to the back of the front-end preamp. Mechanically, these reentrant-tubes are designed as detector-arms that allow detector motion (Sec. 2.5.4).

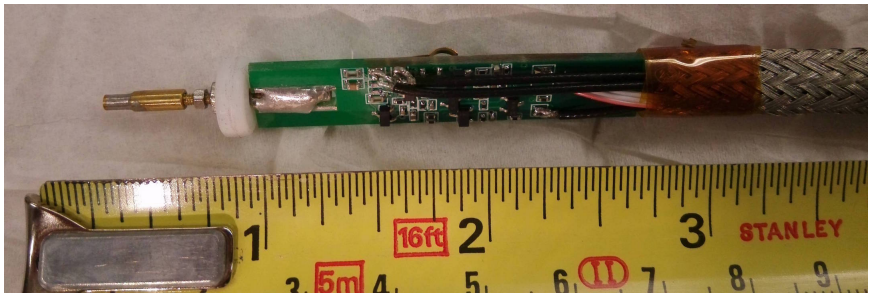

Figure 2.14: Photo of the front-end preamp. This is a section of the preamp that is inserted into the reentrant-tube that has an inner diameter of 1 cm. The placements for each detector can be seen in Fig. 2.7. The front-end preamp connects directly to the detector feedthrough.

The preamps were custom designed at CENPA [149, 150, 140], and a schematic is provided in Fig. 2.15. A preamp powers a detector and amplifies its signal without changing the signal shaping. A more detailed description of silicon detector preamps can be found in Knoll [141]

chapter 16.VIII.A.

The schematic of the front-end preamp is shown on the bottom left of Fig. 2.15 (boxed within coordinates A1, A4, C1, C4). Each of the front-end preamps primarily consists of a resistive-feedback charge-sensitive stage with a BF862 field effect transistor (FET), a double folded cascode stage, and a Darlington output stage from which the feedback is taken back to the gate [151]. The bias resistor and the feedback resistor in this setup are 1 GΩ, while the feedback capacitor is 0.5 pF. The design to insert the front-end preamp inside the reentrant-tube and connect it right behind the detector feedthrough is to reduce distance and hence capacitance between the detector and the BF862 FET; the design helps reduce the series noise that affects the detectors' energy resolution (Sec. 5.2.4).

The braided wires of the front-end preamp shown in Fig. 2.14 lead to what we refer to as a buffer preamp. The schematic of the buffer preamp is shown on the top left of Fig. 2.15 (boxed within coordinates A5, A8, C8, C5)*. The buffer preamp for the beta-detector sits in the beta-preamp-can (Sec. 2.4.1), while the buffer preamp for the ion-detector sits in an aluminum box placed on the extruded aluminum framework of the vacuum system. Both of the buffer preamps are outside the reentrant-tubes. The containers of the buffer preamps also contain rechargeable Li-ion batteries that supply ±7.5 V to power the preamp electronics and 3 V button-cell lithium batteries (CR2032) that are stacked up to supply 130 V to bias the detectors.

The buffer preamps provide "Bias" and ground outputs that allow us to check the battery voltages using a multimeter. Other than powering the detector system, the buffer preamps also drive LED fiber transmitters for signal transmission (schematic shown on the bottom right of Fig. 2.15, boxed within coordinates C1, C3, D1, D3), which is necessary because the beta-preamp-can floats at HV. The ion-preamp uses the same setup as the beta-preamp so that their signals are comparable. The fiber optics also help avoid ground loops. The buffer preamps also have fiber receivers so that we can test the preamps using pulser signals. Other

*The sections on the top right are also part of the buffer preamp.

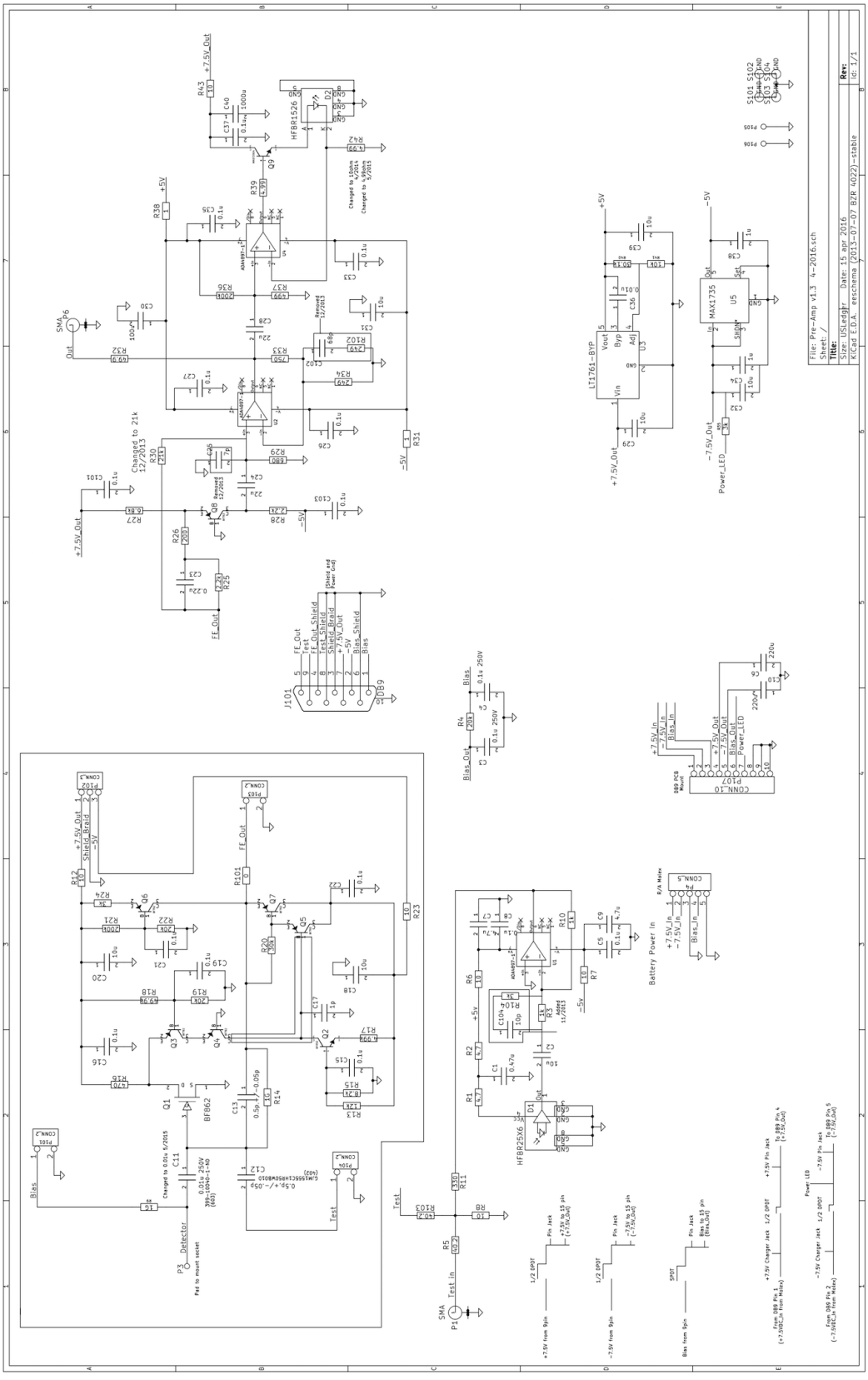

Figure 2.15: Schematic of the preamplifier [149]. It has a front-end preamp section and a buffer preamp section.

than the fiber-optic inputs/outputs, the buffer preamps also have Lemo inputs/outputs.

The tests are usually done using a 20 MHz Agilent 33220A Function/Arbitrary Waveform Generator, or pulser. A photo of the pulser is shown later in Fig. 2.16. The signal of the pulser can be sent to the preamps via either fiber optics or Lemo connections. Testing with fiber optics is reasonable because fiber transmission also prevents noise from ground loops. However, having to power both fiber optics receiver and transmitter, the preamps could only provide signals with limited amplitude range as compared to the Lemo option (Sec. 5.2.3).

2.5.2 Detector Trigger Setup

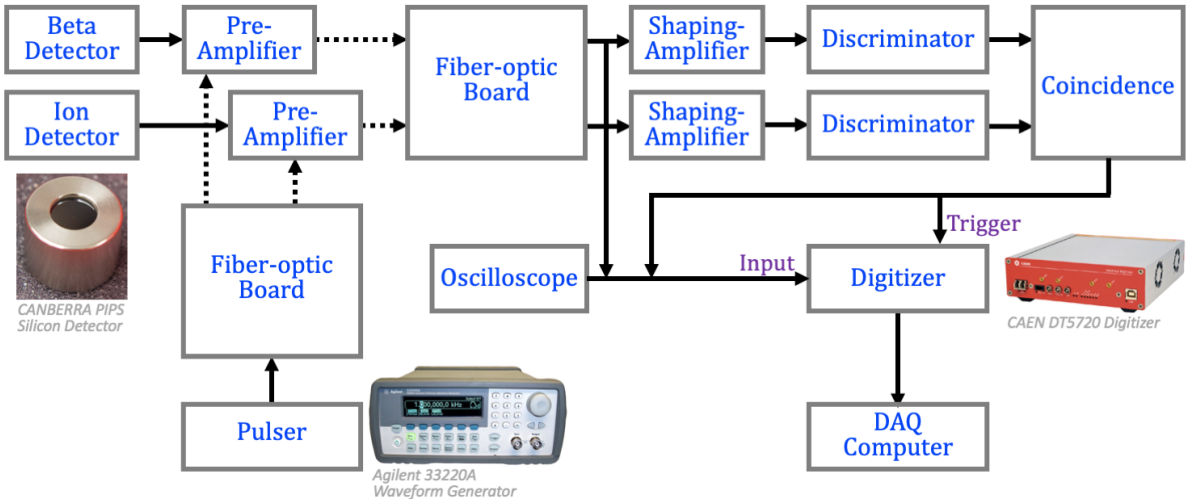

Figure 2.16: Detector coincidence setup. The solid arrows indicate electrical cable connections, while the dashed arrows indicate optical fiber connections. And the fiber-optic board transforms electrical signal to light signal and vice versa. The photos show the detector, the pulser, and the digitizer used in TRIMS. Signals from the beta-detector, the ion-detector, and the pulser are amplified by preamplifiers before being input to the digitizer. The input is teed to an oscilloscope for inspection. The digitized signals are then sent to a DAQ computer for data analysis. The external trigger is obtained by teeing the post-preamp signals to shaping-amplifiers, discriminators, and a coincidence module, and thus completes the coincidence setup.

The TRIMS detector trigger setup is shown in Fig. 2.16. When particles are detected by the beta- and ion-detectors shown on the left of the diagram, the signals are first amplified by preamplifiers (preamps). The signals are transmitted through optical fibers, which are transformed to electrical signals by a fiber optics receiver board. The analog electrical signals are then digitized by a digitizer, and the digitized signals are sent to a DAQ computer for data analysis. The input to the digitizer is teed to an oscilloscope for us to inspect characteristics

such as signal shapes and event rate. Shaping amplifiers, discriminators, and coincidence logic are used to provide a trigger to the digitizer. We also have a pulser that can mimic the detector signals at the preamp input. We used the pulser signals to test the performance of the preamps and to debug the system.

Signals from the preamps are sent through fibers to a fiber optics board that is located in our main electronic rack. Both of the "Fiber-optic Board" boxes in Fig. 2.16 refer to channels of this same board. The board converts light signals from the preamp to electrical signals, which are then sent via coaxial cables to a digitizer and a series of Nuclear Instrumentation Modules (NIMs) for the detector coincidence setup. As for the pulser line, the fiber optics board converts electrical signals to light signals to feed the receivers on the buffer preamps.

The digitizer used in TRIMS is a CAEN DT5720. It has 4 channels, 12-bit resolution, and 250 MHz sampling rate [152]. A photo of the digitizer is shown in Fig. 2.16. The digitizer converts the electronic analog signals to a time series of discrete digital signals, which are then sent to the DAQ computer via a USB cable. The DAQ computer is a Mac Pro (early 2009) desktop updated to OS X Yosemite. In the TRIMS experiment, channel 0 on the digitizer receives signals from the beta-detector and Channel 2 from the ion-detector. Channel 1 in our digitizer was tested to have a rather nonlinear gain, so we switched the beta-detector channel to Channel 0. The digitizer has an option for receiving external triggers; it allows us to set up a coincidence logic between the two detectors.

The detector coincidence setup consists of a few NIM electronics modules: a pair of ORTEC 571 shaping amplifiers, a LeCray 821 quad discriminator, and an LRS 622 quad coincidence. Signals from the beta- and the ion-detector are teed from the digitizer line to the shaping amplifiers. The gain of the amplifiers is set to 140, which is chosen such that the hardware thresholds to trigger the discriminators roughly corresponded to 3 ADC in signal amplitude. The beta and the ion line are each fed to a channel from the quad discriminator, whose output triggers one channel on the quad coincidence. Ideally, the coincidence module could be set to AND-logic so that it is triggered only when the beta- and the ion-detector receive a coincidence within 500 ns. But in the end, we decided to use OR-logic so that we

do not lose information about the singles events, which turn out to be indispensable in our analysis (Sec. 7.1.4). The output of the coincidence module is input to the digitizer's trigger channel and completes the setup.

Additionally, we have an oscilloscope so that we can inspect in real time the analog signals from both the beta- and the ion-detector before they are digitized. The coincidence trigger outputs are also teed to the oscilloscope so that we know the detector coincidence setup is functioning properly during data-taking.

2.5.3 Joule-Thomson Cooler

Each of our front-end preamps dissipates approximately 100 mW of heat during normal operation. Without additional cooling, the heat can only be dissipated by the reentrant-tubes and copper pushrods, which results in an approximately 14 °C rise in temperature. Since the energy resolution improves as temperature decreases (Sec. 5.2.4), we designed specific coolers to cool down the detector and the front-end preamps.

Our coolers apply the so-called Joule-Thomson (JT) effect [153]. It is a cooling effect as a non-ideal gas expands isenthalpically, i.e. at constant enthalpy*. The cooling process is usually achieved by forcing the gas through a porous medium, while preventing heat exchange between the two sides of the medium and the environment. The medium is referred to as a frit (or a throttle).

*The copper pushrods were subsequently replaced by fiberglass ones to reduce heat flow from outside and so maintain the isenthalpic condition.

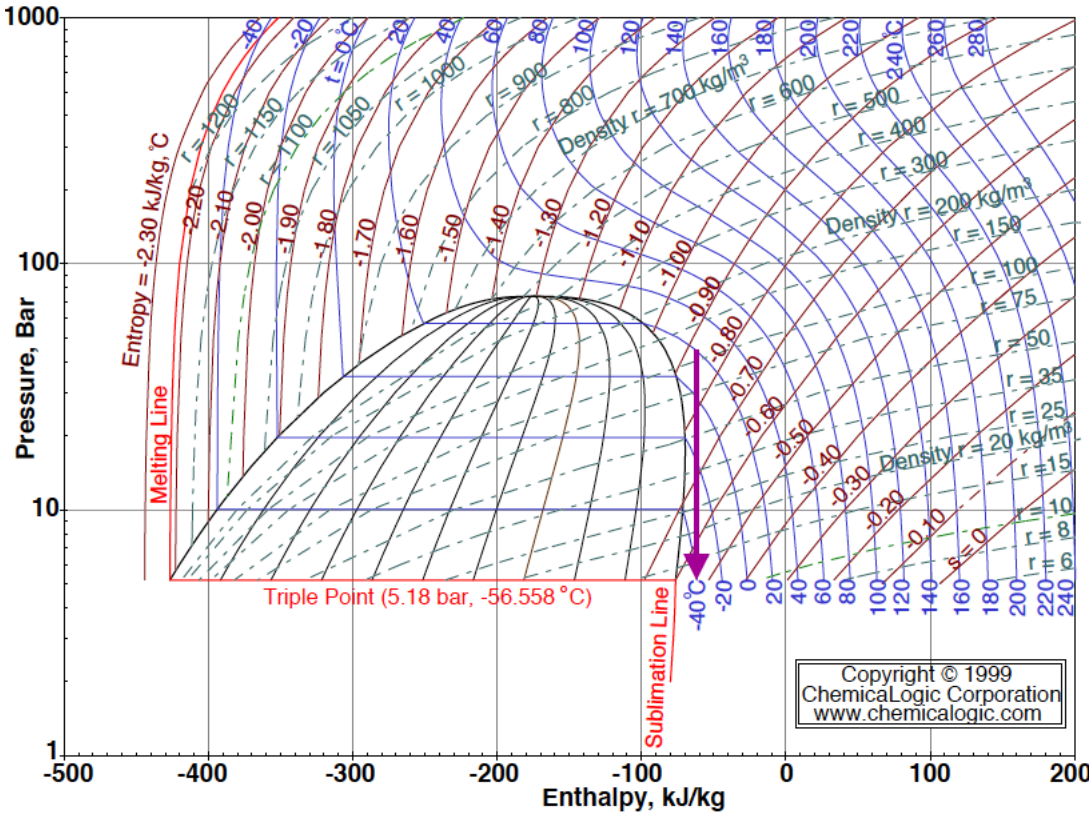

Figure 2.17: Mollier diagram for CO_2 [154]. The plot contains multiple curves with different parametrizations, but what we are interested in are enthalpy on the x-axis, pressure (bar) on the y-axis, and temperature (°C) as the blue gradient curves. The purple arrow that points downward shows our target isenthalpic path for JT-cooling.

While the Joule-Thomson effect can be observed in most gases, our choice is CO_2 due to its high JT-coefficient, i.e. when given the same change in pressure, CO_2 provides a greater temperature change than other common choices such as N_2 or Ar. Our target cooling process is indicated by the purple arrow in Fig. 2.17, which is a Mollier diagram for CO_2. Tracing down the purple arrow, we can see that an isenthalpic expansion from 50 bar to 5 bar ideally produces a temperature drop from 20 °C to −40 °C.

Due to the limited space inside the reentrant-tubes where the front-end preamps are

located, our coolers need to be small in physical size as well to fit into the space. The schematic of our JT cooler is shown in Fig. 2.18, and the photo of the physical instrument is shown in Fig. 2.19. Each cooler consists of a 2 mm diameter aluminum tube with an inlet for dry compressed CO_2. The dryness is required so that water does not freeze in tubing, and the compressed air cylinder is there to allow us to control the pressure gradient for JT-cooling. The tube holds a pack of frits, which are C-409 from IDEX-HS that has a thickness of 0.762 mm and pore size of 0.5 µm. Each frit has a sleeve that has an outer diameter of 1.575 mm and is made out of green PEEK plastic material that provides a gas seal. The frits are packed so that we can manage the air flow at high pressure. To fix the frits in place, we made stainless-steel housings [155] whose inner diameter matches the outer diameter of the frits. The out-flow from the frits goes through the Teflon spacer that hold the front-end preamp in place (Sec. 2.14). We bored more apertures on the Teflon spacer [155] to allow the CO_2 gas to escape.

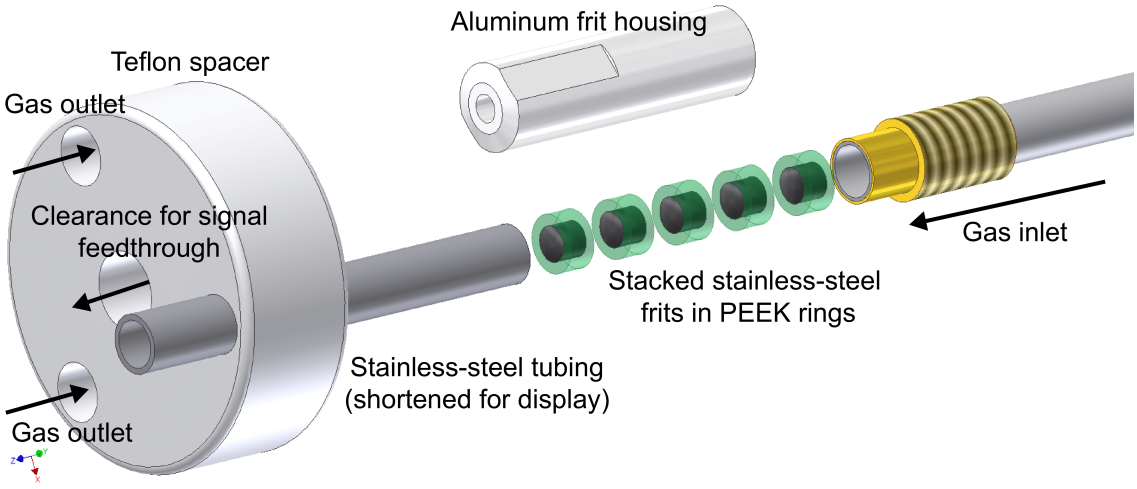

Figure 2.18: Exploded schematic of the JT-cooler [97]. The teflon spacer is the modified version of the one shown in Fig.ŕeffig:frontEndPreamp.

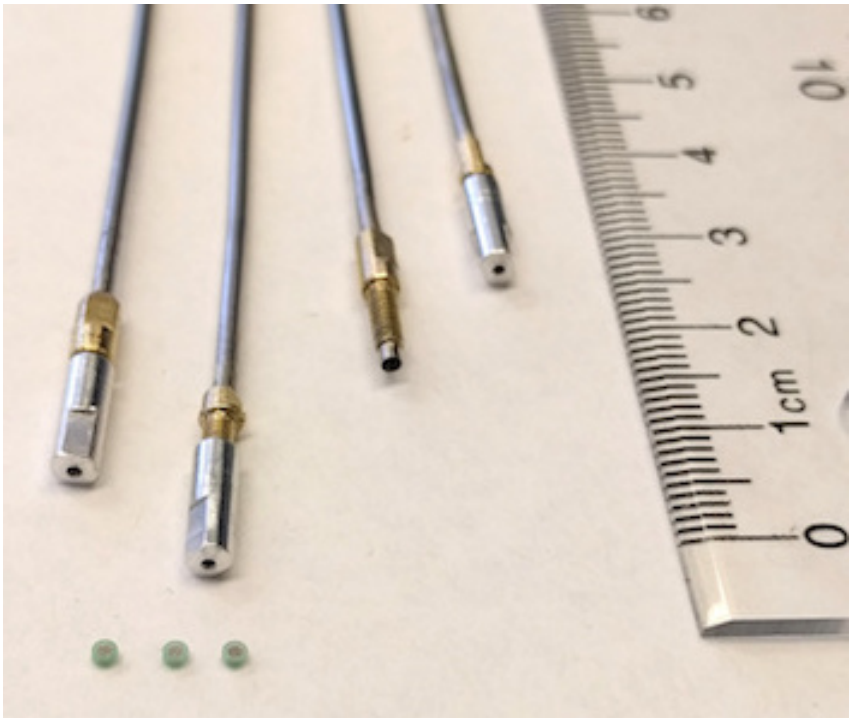

Figure 2.19: Photo of the JT-coolers. The frits are shown on the bottom left of the photo.

We have one cooler built [140, 156] for each detector. The two coolers share the same compressed CO_2 line. The coolers are on during the entirety of our tritium-data taking. How the cooling helps our energy resolution is discussed in Sec. 5.2.5.

As it turns out, by analyzing the improvement in energy resolution, we derived [157] that the final temperature we achieved was 15 °C; we could do a lot better if we had reached our original goal of −40 °C. However, as we increased the CO_2 pressure, we encountered two problems. The first is a high pitched whistling from the escaping gas that produced microphonic noise in our silicon detectors. The second is that we found increasing the CO_2 pressure did not necessarily correspond to lower temperature at the outlet. We speculated that it was caused by CO_2 frost, but more tests are required. Further improvement is still a work in progress (Sec. 9.2.2).

2.5.4 Detector Motion

As shown in Fig. 2.7, each of the detectors is connected to a feedthrough that is mounted on a long stainless-steel reentrant-tube, which we also refer to as a detector-arm. Each of the detector-arms is connected to a bellows on the other side, so that we are able to adjust the XY-position (Sec. 2.1.2) of the detector that the arm is holding. The design is so that we can park the detectors behind their designated hideouts during operations that can potentially damage the detectors, such as conditioning or taking HV krypton-data (Sec.5.1.2). We also hide the detectors during the bakeout to avoid thermal radiation from inside the chamber. These damages could be inflicted regardless of whether the detectors were on or off. And not just the motion to the hideouts, we also need ways to recenter the detectors afterward without disassembling the system. These details of these operations are done differently between the detectors.

For the beta-detector, its detector-arm is a 6.5 in long tube that is mounted on a bellows shown in Fig. 2.5. The bellows is also a ConFlat reducing nipple that connects to the detector-arm on its mini-ConFlat flange and to the decay chamber on its 2.75 in flange. As shown in the figure, there is another 6 in to 2.75 in ConFlat reducing-nipple in between the chamber and the bellows. The hideout for the beta-detector is simply the beta-electrode (Fig. 2.4.b)). The axial symmetry of the beta-electrode means the beta-detector only needs to move in one direction to be hidden. To do that, we first attached a support to the bellows. The support [158] consists of a tabbed aluminum ring with a pin and a bolt. The pin makes sure that the bellows does not bend to gravity. Then by screwing and unscrewing the bolt we can adjust the X-position of the beta-detector. To adjust the beta-detector back to the center, we look through the UV window and visually align the beta-detector to the central aperture of the beta-electrode.

For the ion-detector, the motion is more complicated and requires a dedicated translation stage. A schematic of the detector-arm is shown in Fig. 2.20, which shows that the system is hosted by a ConFlat reducing cross. The reducing cross has two 6 in flanges along the

Z-direction and two 2.75 in flanges along the Y-direction. The decay chamber is attached to the 6 in flange on the left-hand side of Fig. 2.20. The detector-arm is a L_a =14.25 in long tube and is mounted to a mini-ConFlat bellows attached to the 6 in flange on the right-hand side of Fig. 2.20.

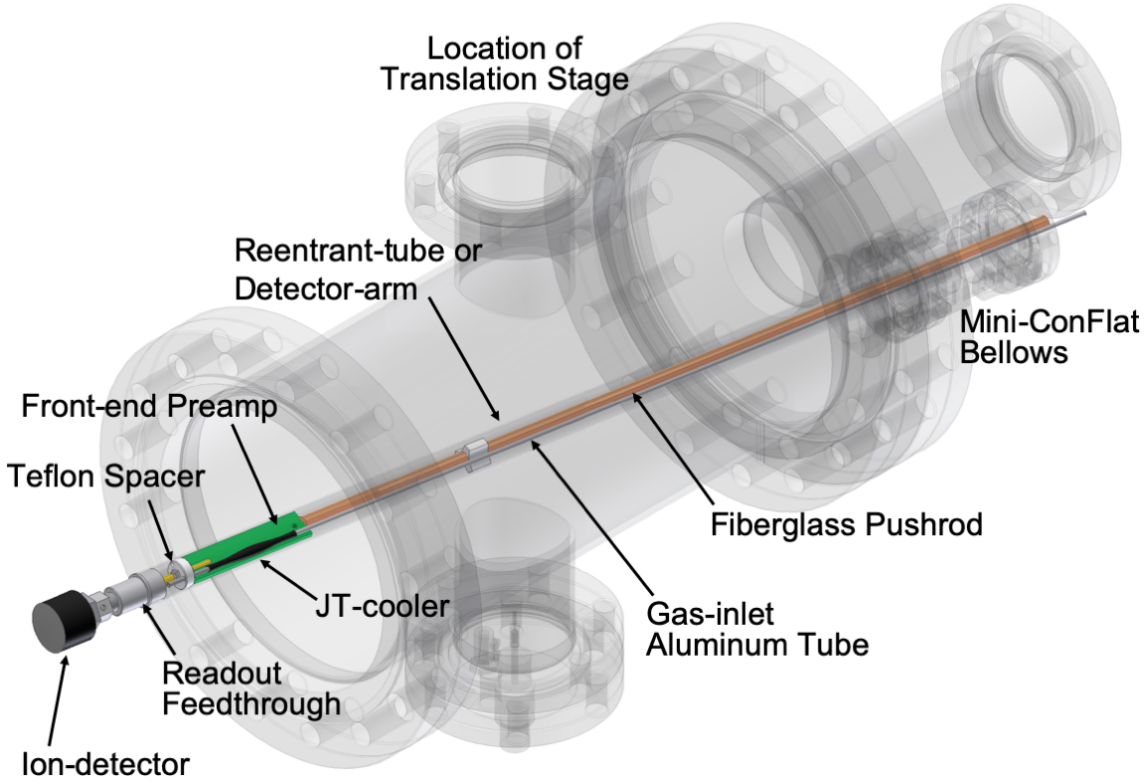

Figure 2.20: Model of the ion-detector arm [97]. The orientation of this plot is when we view the ion-detector from wall on the left side of Fig. 2.2. The system is hosted by a ConFlat reducing cross, whose 6 in flanges on the left-hand side of the plot is connected to the decay chamber. The plot is generated using Autodesk Inventor [138].

The detector-arm is held on the arm body by a holder [155], which is attached to a translation stage. The translation stage comes from Kurt J. Lesker push-pull KLPD series and has a 4 in range. This translation stage is attached vertically to the reducing cross on the top through a 2.75 in bellows as shown in Fig. 2.21. We can control the ion-detector's vertical

position (Y-position) by adjusting the up-and-down motion of the translation stage. There is a micrometer [155] attached to the bellows that allows the entire translation stage to swing left-and-right, which allows us to control the ion-detector's horizontal position (X-position). The ion-detector does not have motion along the decay chamber axis (Z-direction).

Figure 2.21: Photo of the translation stage. The translation stage is also shown on the left of Fig. 2.5. The translation stage allows vertical motion of the ion-detector. All the plastic parts on the translation stage have been replaced by aluminum parts such that the translation stage can be baked up to 200 °C.

The hideout of the ion-detector is a thin piece of aluminum attached to the mesh ion-electrode. The position is chosen such that if we move the translation stage all the way down but right before the holder hits the bottom of the reducing cross, then the ion-detector is parked behind the hideout. To center the ion-detector, we utilize the AND-Logic detector coincidence setup with a tritium source: if the beta-detector has been centered, then

the center position of the ion-detector corresponds to where the detectors receive the most coincidence events.

2.5.5 Detector Alignment and Scanning

The original plan for the ion-detector motion from Sec. 2.5.4 was such that we can align the detectors. Nevertheless, it turns out that we need to scan the ion-detector in both the X-direction and Y-direction (Sec. 8.1). Therefore, we need the following measurement of the ion-detector motion. Prior to sealing the vacuum system, we measured that moving 1 in in the Y-direction changed the reading on the translation stage from 80.5 mm to 92.0 mm and moving 1 in in the X-direction changed the dial on the micrometer from 0.100 in to 0.361 in. Therefore, a step size of 1 mm on the translation stage moves the detector 2.21 mm in the Y-direction; a step size of 0.01 in on the micrometer moves the detector 0.98 mm in the X-direction. With a more detailed geometric calculation though, the step sizes are corrected to 2.27 mm in the Y-direction and 1.1 mm in the X-direction. Moreover, the error on the X-positioning is estimated to be 0.1 mm [132].

To align our detectors, we relied on the ^{83m}Kr coincidence events (Sec. 2.3.3). We first centered the beta-detector to the center of the beta-electrode aperture, which we could see from the UV window. Next, we applied AND-logic in our coincidence module (Sec. 2.5.2), turned on the magnets but not the HV, and released the ^{83m}Kr gas into our decay chamber to produce electron events on the detectors. We then moved the ion-detector until we found the position that corresponds to the largest coincidence count, which only happens when the detectors are aligned. We refer to this as the home-position. The home-position was found to be (0.305 in, 80 mm) in the micrometer and the translation stage scale.

Due to finite precision, the home-position is not the ideal alignment center. We call the true alignment position the center-position to distinguish it from the home-position. Since we cannot figure out where exactly the center-position is, the home-position is our reference position. The offset of the home-position is determined later in the analysis (Sec. 7.2.2).

When we do start scanning the ion-detector while taking data, which we call a run-scan,

we do use the home-position as the origin. Because we mostly scan the ion-detector in the X-direction, we define scan-position X_d as the X-position of the ion-detector and scan-point d is the scan-position index that is an integer in [-10, 10] range. Each increment of the scan-point corresponds to tuning the micrometer by 0.01 in or moving the ion-detector in the X-direction by 1.1 mm. For instance, $X_0 = 0$ mm means the ion-detector parks at the home-position (0.305 in, 80 mm), while $X_{-2} = -2.2$ mm means the ion-detector parks a distance 2.2 mm from the home-position in the negative X-direction. As it turns out, the simple translation is $X_d = d \times 1.1$ mm. Similarly, we call scan-Y-position Y_D with scan-Y-index D to describe the Y-position of the ion-detector.

As a reference to all the naming schemes regarding scanning the ion-detector, we summarize them in Table. 2.3.

Name	Definition
center-position	The ion-detector position when the ion-detector completely aligns with the beta-detector in their line of sight
home-position	The estimated center-position, which we determined to be at (0.305 in, 80 mm) in the micrometer and the translation stage scale. Since we do not initially know where the center-position is exactly, we use home-position as our reference position
scan-position (X_d)	The X-position of the ion-detector from the home-position
scan-point (d)	The index to the scan-position with a range of [-10, 10] in integers. Each increment in d moves X_d by 1.1 mm
left-scan	A scan of the ion-detector from scan-point ($d = -10$) to ($d = 0$) with integer steps
right-scan	A scan of the ion-detector from scan-point ($d = 0$) to ($d = 10$) with integer steps

scan-direction	Reference to either the left- or the right-scan
run-scan	A series of 300 s runs we take using either the T_2 or the HT source for either a left- or right-scan
scan-Y-position (Y_D)	The Y-position of the ion-detector from the home-position
scan-Y-point (D)	The index of the scan-Y-position with a range of [-10, 10] that contains only even integers. Each increment of 2 in D moves Y_d by 2.27 mm

Table 2.3: Naming schemes for scanning the ion-detector. Referring to Sec. 2.1.2 for the coordinate variables X, Y, and Z. The (X_0, Y_0) = (0, 0) coordinate origin corresponds to the home-position. More about the run-scan will be discussed in our standard data-taking procedures (Sec. 4.2.1).

2.6 Slow Control Setup

The slow control in the TRIMS experiment is a setup that automatically records the data that come from devices other than the detectors. These devices include the power supplies and the pressure gauges. The slow control helps us monitor the general condition of our system at any given time.

The DAQ hardware devices of choice for our slow control setup are LabJacks; their USB interfaces provide easy connections to the DAQ computer. LabJacks can read the voltage output provided by the controllers of the HV power supplies, the ion gauge, the Pirani gauges, the SRG, and the ion pump. However, because LabJacks have small internal impedance, the controllers need to connect to a buffer-box [149] for impedance matching. The outputs of the buffer-box can then be connected to differential channels on LabJacks via twisted pairs to provide low-noise readings.

We used two LabJack U12s and a total of 8 differential analog inputs, each with a ± 10 V

input range and a 12-bit resolution. For the slow control, we are only looking for a sampling rate of order 1 Hz, which is easily achievable by the LabJacks that can take up to 8 kHz samples. As shown later in Table 4.1 from Sec. 4.3.1, most of the channels on LabJack U12s are connected to controllers. However, the channels "mag_status", "mag_hall", and "diode_v" record the output from other devices. The "mag_status" channel tells us about the on-and-off status of the magnets. It reads from a simple 3 V battery circuit that normally forms an open circuit with a reed switch. The reed switch is placed near the bore of the magnets, so that the LabJack channel only receives 3 V bias when the magnets are on. The "mag_hall" channel is reserved for a Hall probe that we used for mapping the magnetic field. We do not have a dedicated Hall probe for TRIMS but occasionally use a general CENPA device. We can see from Table 4.1 that "mag_status" and "mag_hall" actually share the same channel. The "diode_v" measures the voltage from back-to-back diodes connected to the ground electrode from the divider-chain (Sec. 2.4.1). The channel was mainly used to diagnose HV breakdowns since micro-discharges could create small voltage spikes at the HV ground; it was even customized to receive a gain of 10 from modifications on the buffer-box. After we resolved the HV problems (Sec. 2.1.3), this channel became a spare channel.

We also used a LabJack U6 in our slow control setup. The LabJack U6 can provide a gain up to 100 compared to 20 from a LabJack U12. The voltage measurement is also finer for the LabJack U6; it also has a ± 10 V input range but with a maximum of 18-bit resolution. The more powerful LabJack was helpful during the bake-outs to record the readings from the thermocouples (Sec. 2.2.2). We teed the thermocouples from the Omega temperature controller directly to the LabJack U6. The thermocouples output voltages of 43 µV per degree Celsius within the LabJack U6 resolution. Moreover, the LabJack U6 has a DB37 connector, which supported all seven thermocouple channels in one unit. This was how we collected the temperature data points in Fig. 2.9 [159]. There are two differential analog inputs available on the LabJack U6 besides the DB37 connector. They are used as channels to read out the SRG and the negative HV power supply (2.4.1).

The readout from these LabJacks will be the topic of Sec. 4.3.

The only readout unavailable to the LabJacks is from the RGA. The RGA data are recorded using a LabVIEW-based software provided by Stanford Research Systems. The software is only available in Windows, and so it is installed and run on a separate computer from the DAQ computer.

Chapter 3

SIMULATION

This chapter covers the simulation setup for the TRIMS experiment. The chapter begins by describing how we use Geant4 (Sec. 3.1) to simulate tritium decay on an event-to-event basis. The Geant4 software applies the Monte Carlo method to generate a decay event and tracks the trajectories of the product charged particles as they travel toward the detectors. Upon the particles' arrival at the detectors, we can extract their energy and time of flight (TOF), which are exactly the information we collect in the actual experiment. The Geant4 simulation helps us understand our data and test the validity of our analysis chain. One major complication for simulating energy detection however, is the dead-layer effect of our silicon detectors. We studied this effect using SRIM (Sec. 3.2), which complements the TRIMS Geant4 simulation as well as providing an energy correction method for our tritium-data. Besides the simulations that track particles, we also use COMSOL (Sec. 3.3) to simulate the electric and the magnetic fields applied to the TRIMS decay chamber. The COMSOL simulation helps us understand the field configurations of our system, especially in cases when direct measurements would be difficult.

3.1 Geant4

The Geant4 (GEometry ANd Tracking) software is a particle physics simulation framework developed by CERN (European Organization for Nuclear Research) [160]. It applies the Monte Carlo method to simulate particle kinematics as the particles travel through different materials and fields. The Geant4 software is a series of toolkits in `C++` that can be used to build apparatus geometry, impose material properties, configure the external fields, and generate detector responses, as well as provide visualization for particle trajectories. The

Geant4 software also incorporates an extensive physics library to account for particle decays and interactions, especially for high-energy particles. As an example, the library provides a readily available way to generate beta-decay energy distributions for any given Q-value. The Monte Carlo aspect of Geant4 accounts for the probabilistic nature of decay or scattering processes. Lastly, the output file of the simulation can readily be saved in the ROOT format for data analysis.

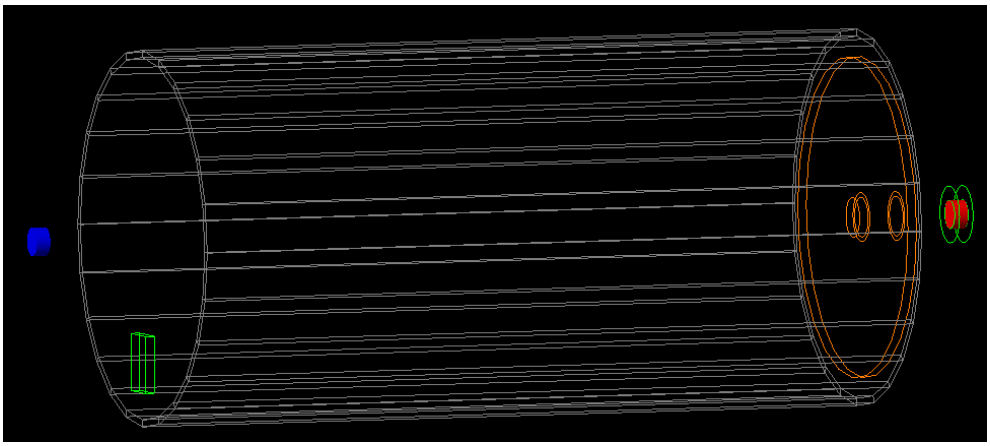

Figure 3.1: Geant4 geometry for TRIMS. The grey cylindrical chamber is modeled on the old Pyrex decay chamber; for the purpose of event simulation, the chamber geometry is approximate. The blue puck represents the ion-detector and the red puck represents the beta-detector. The green plate represents the hideout for the ion-detector and the orange disc represents the beta-electrode. Also in the simulation is the tunnel that extends from the beta-electrode's aperture toward the beta-detector; the cylindrical wall of the tunnel is present but not shown due to the graphic style.

For the TRIMS experiment, our Geant4 (version 10) simulation has a basic geometry shown in Fig. 3.1, which refers to the setup from Fig. 2.1. The chamber in the simulation is a 0.2 cm thick Pyrex (`G4_Pyrex_Glass` material in the Geant4 library) tube that is 21.3 cm long and has an inner radius of 5.08 cm. This grey-edged tube in Fig. 2.1 resembles our old Pyrex chamber but with its length adjusted to match the current NEC chamber. The

simulated chamber is there mostly for visual guidance; the decays we care about happen far away from the chamber walls. In the simulation, the Z-direction points along the axis of the decay chamber cylinder to the right-hand side of Fig. 3.1. The Y-direction points toward the top of Fig. 3.1 and the X-direction points into the figure (equivalent to Sec. 2.1.2). The origin of the coordinate system is at the center of the chamber; i.e. the left of the chamber is at $Z = 10.65\,\text{cm}$ and the right at $Z = -10.65\,\text{cm}$. The red puck represents the active area of the beta-detector, while the blue puck that of the ion-detector. They are 4 mm thick silicon (`G4_Si`) cylinders with radii of 4 mm. For the beta-detector, we also simulate its stainless-steel ring that has an outer radius of 8 mm (see Fig. 2.16). The beta-detector-ring is represented by green traces around the red puck in Fig. 3.1. The beta-electrode (Sec. 2.1.3) is represented by an orange disk close to the beta-detector. The beta-electrode is assumed to be completely made out of gold in the simulation. Also in the simulation is the beta-electrode tunnel of length 13 mm that extends toward the beta-detector from the aperture at the center of the electrode (right plot of Fig. 2.4). On the ion-detector side, the box-shaped stainless-steel hideout (Sec. 2.5.4) is outlined by green traces. The mesh ion-electrode is not simulated due to the difficulty in correctly simulating meshes in Geant4. The locations of the detector and the electrodes all follow L, L_{ion}, and L_{beta} from Table 2.1.

For this simulation, the world is a finite-sized box that is just big enough to contain the entire chamber; all particle tracks end outside the world. All the empty spaces in the world are assumed to be in vacuum (`G4_AIR` with a pressure of 3×10^{-6} torr and a temperature of 300 K). Inside the decay chamber, there is a uniform electric field, whose default strength is calculated by assuming the right-most Z-position of the chamber to be at 60 kV and the left-most at $-100\,\text{V}$. There is also a uniform magnetic field pointing toward the negative Z-direction throughout the world. It has a default strength of 0.237 T. Again, the tracking of particles under the external electromagnetic field can be conveniently evaluated using a package from the Geant4 library. These values can be adjusted using a macro file that will be described in Sec. 3.1.1.

Particle Name	Color Coding	RGB
e^-	yellow	1 1 0
T^+	red	1 0 0
H^+	magenta	1 0 1
$^3He^+$	blue	0 0 1
$^3He^{++}$	cyan	0 1 1
$^3HeH^+$	orange	1 $\frac{1}{2}$ 0
$^3HeT^+$	green	0 1 0

Table 3.1: Color coding for different types of particles in the TRIMS Geant4 simulation.

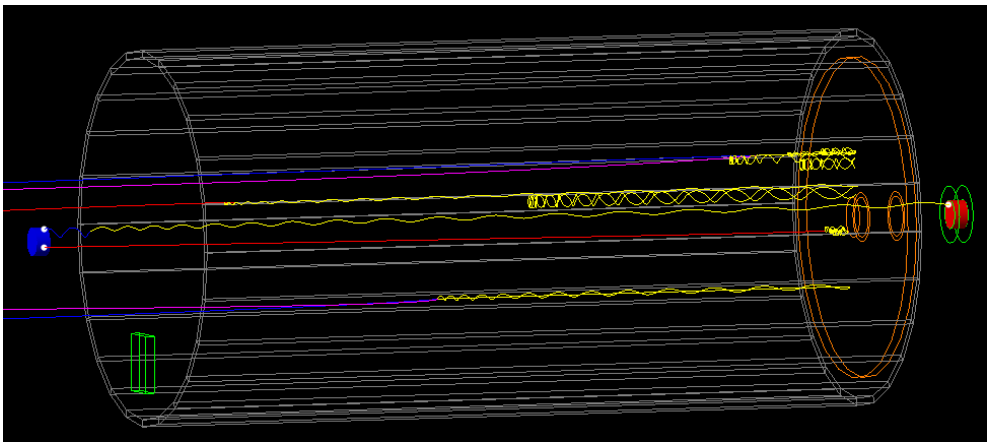

Figure 3.2: Geant4 event simulation for TRIMS. A parallel electric field and magnetic field are added to the Fig. 3.1 geometry along the grey cylinder. Tritium decays happen inside the grey cylinder, each producing either an ion and an electron or a pair of ions and a pair of electrons. Five such events are shown in the figure. The trajectories made by the electrons are colored in yellow. The ions have various colors depending on their types according to Table 3.1. If a particle is detected by either of the detectors, a white dot will be shown at the detection location.

With the setup, if decays happen inside the chamber, the traces of the particles can be visualized as shown in Fig. 3.2. Five decays are shown in the figure, each of which produces either an ion and an electron or a pair of ions and a pair of electrons (later in Sec. 6.1.1). The yellow traces are the electrons, whose helical motion under the magnetic field is conspicuous due to electrons being charged and lightweight. Other traces come from the ions, whose the color scheme is provided in Table 3.1. Once any of these particles hits a detector, a white dot will be shown at the detection location. If both detectors light up due to a single decay, then the detection is registered as a coincidence event and the kinematic information of the detected particles will be recorded in the output ROOT file (Sec. 3.1.2). Out of the five decays in Fig. 3.2, we can see there are three particles detected but only one coincidence event. The rest of the particles either collide with the beta electrode or go out of the chamber. More details on the decay conditions as well as the detection physics are provided in Sec. 3.1.2, 3.1.3, and 3.1.4.

3.1.1 Setup Using a Macro file

The macro files are the input files for Geant4, which allow us to modify simulation settings without having to recompile the `C++` code. The format of a macro file is such that in each line of code, it lists the function name, the input value, and the unit for the value. The Geant4 software also allows user-defined macro file functions. Therefore, for TRIMS, we do define our own functions and they are categorized into three classes: `detector`, `field`, and `generator`, which are provided in Table 3.2, 3.3, and 3.4. As a showcase of a specific line of code in the macro file, take an example from Table 3.2:

```
/TRIMS/detector/SetIonDetX  0.  mm       #-17.mm to 17.mm,
```

where `/TRIMS` indicates the variable is user-defined for the TRIMS experiment, `/detector` shows the class name, and `/SetIonDetX` shows the function name. In this particular case the function set the ion-detector to be at 0 mm in X-position (X-position of the center-position, Sec. 2.1.2). The hash tag is followed by a comment, which shows the available range in this

case. There are also many built-in Geant4 variables allowed in a macro file; an example is the color scheme of the particles shown in Table 3.1.

Function Name	Default Value	Description
`SetIonDetX`	0 (mm)	Ion-detector X-position
`SetIonDetY`	0 (mm)	Ion-detector Y-position
`SetBetaDetRot`	0 (degree)	Beta-detector arm rotation, such that the beta-detector moves along the Y-direction
`SetDeadLayerWidth`	-1 (nm)	Detector dead-layer width
`SetDeadEResFactor`	1	Factor for energy broadening from the dead layer
`SetBetaDetERes`	1 (keV)	Beta-detector energy resolution in standard deviation
`SetBetaDetTResFactor`	1	Factor for beta-detector timing resolution
`SetIonDetERes`	1 (keV)	Ion-detector energy resolution in standard deviation
`SetIonDetTResFactor`	1	Factor for ion-detector timing resolution
`SetIonDetAcceptance`	0.85	Factor to account for the mesh transmission rate (Sec. 2.1.3)

Table 3.2: Class `detector` functions available in a TRIMS Geant4 macro file.

The `detector`-related functions are provided in Table 3.2. The default values for each function are listed in the second column; if a function is not present in the macro file, the simulation code assumes the default value for the function. The descriptions of the parameters set by the functions are given in the third column. The detector position setup corresponds to Sec. 2.5.4. The effect from the dead layer is derived from the SRIM simulation

that will be covered in Sec. 3.2.1; a width of -1 corresponds to using the derivation from Sec. 3.2.2. The `SetDeadEResFactor` factor increases the energy broadening from the dead layer on top of what is predicted by SRIM. The variable is mostly used as a way to turn off the dead-layer broadening by setting the factor to zero. The default values for the detector energy resolutions roughly follow the values derived from the physical detectors that will be covered later in Sec. 5.2.5. Similarly, the timing resolutions are also derived from the physical detectors as will be discussed in Sec. 5.3.3. Since the timing resolution is going to be energy-dependent, we introduce `TResFactor` as a scalar multiplier to adjust the timing resolutions to be better or worse in the simulation. More details on the implementation of these parameters are covered in Sec. 3.1.2.

Function Name	Default Value	Description
`TRIMSFieldVerbose`	1 (0 or 1)	Choose 1 to print out the geometry information where the fields are present
`SetBField`	0.237 (Tesla)	Magnetic field amplitude
`SetBTiltX`	0 (degree)	Magnetic field tilt X-angle. This angle is between the negative Z-axis and the field direction that stays in the XZ-plane. A 0 degrees tilt means, the field points from the beta-side to the ion-side along the Z-axis.
`SetBTiltY`	0 (degree)	Magnetic field tilt Y-angle. This angle is between the negative Z-axis and the field direction that stays in the YZ-plane.
`SetHVVoltage`	60 (kV)	HV across the chamber
`SetMeshVoltage`	-100 (V)	Mesh voltage

Table 3.3: Class `field` functions available in a TRIMS Geant4 macro file.

The `field`-related functions are provided in Table 3.3. The `TRIMSFieldVerbose` function is used to print out information that shows in which regions either of the fields is present. Other functions mostly enable setting field strengths in the macro file. The default values for field strengths come directly from our standard settings for data taking (Sec. 4.2.1). The `SetBTilt` function sets the overall tilt of the magnetic field in Y-direction. The tilt variable is used to study the systematics coming from the misalignment between the magnetic and electric field. More on this will be covered in Sec. 9.1.3.

Function Name	Default Value	Description
`TRIMSEventVerbose`	1 (0 to 2)	Level of details to print out for each event
`TRIMSRootLevel`	2 (0 to 5)	Level of details of the output ROOT file
`SetRandSeed`	5	Random seed for the Monte Carlo simulation
`SetConfig2Ion`	1 (1, 8, or 9)	Ion initial configurations to be discussed in Sec. 3.1.5
`T2_T_BranchRatio`	0.2	Branching ratio for T^+ after T_2 decay
`T2_3He_BranchRatio`	0.2	Branching ratio for $^3He^+$ after T_2 decay
`T2_3HeT_BranchRatio`	0.4	Branching ratio for $^3HeT^+$ after T_2 decay
`T2_3He2p_BranchRatio`	0.1	Branching ratio for $^3He^{++}$ after T_2 decay
`T2_3He_T_BranchRatio`	0.1	Branching ratio for $^3He^+$ and T^+ after T_2 decay
`HT_Level`	0.5	Purity of HT in the T_2 source
`HT_H_BranchRatio`	0.2	Branching ratio for H^+ after HT decay
`HT_3He_BranchRatio`	0.2	Branching ratio for $^3He^+$ after HT decay
`HT_3HeH_BranchRatio`	0.4	Branching ratio for $^3HeH^+$ after HT decay
`HT_3He2p_BranchRatio`	0.1	Branching ratio for $^3He^{++}$ after HT decay
`HT_3He_H_BranchRatio`	0.1	Branching ratio for $^3He^+$ and H^+ after HT decay

Table 3.4: Class `generator` functions available in a TRIMS Geant4 macro file.

Finally, the `generator`-related functions are provided in Table 3.3. The `TRIMSEventVerbose` function sets the details to be printed out for each event during the simulation, while the `TRIMSRootLevel` function sets the details to be saved in the output ROOT file for each event after the simulation. Other functions in this class are mostly related to the Monte Carlo aspect of the simulation. The `SetConfig2Ion` is important, but will be discussed in Sec. 3.1.5.

The branching ratios are exactly the probability of the decay to produce that specific ion or ions (for available channels, see Sec. 6.1.1). The branching ratio functions that start with `T2_` are conditional probabilities assuming the decay originated from T_2, e.g. `T2_3HeT_BranchRatio` sets the probability,

$$P\left({}^3\text{HeT is the decay product}\middle|\ \text{the decay comes from } T_2\right). \tag{3.1}$$

The same applies for the HT branching ratios. The function `HT_Level` sets the purity level of HT in the T_2. Note that this is event purity instead of molecular number purity between T_2 and HT. Because T_2 has two tritium nuclei that can decay, given the same number density of T_2 and HT, T_2 produces two times more decay events. And so, to avoid unnecessary confusion, we set `HT_Level` to be the probability of a given decay to originate from HT.

It is worth mentioning that in Geant4, there is another type of macro file that allows us to loop through any variables listed above. A prime example is that we can loop through `SetIonDetX` from $-10\,\text{mm}$ to $10\,\text{mm}$ in $1\,\text{mm}$ steps with 1 million decays in each step. This is essentially simulating the ion-detector scanning process (Sec. 2.5.5). There are options to save all the simulated results in one output file for each step or in one large combined file. The format of the output file is covered in the next section.

3.1.2 Output ROOT file and the Simulation Process

As mentioned, Geant4 can directly save its output file in the ROOT format. We refer to these output files as the G4-ROOT-files. In a G4-ROOT-file, the values saved can be partitioned into trees. For instance, there is a `parameter`-tree for each G4-ROOT-file that saves all the

setup information from Sec. 3.1.1. An important tree is the `physics`-tree, which has entries identical to the ROOT files for our data (Table 5.4). The idea is to send the G4-ROOT-file through the identical analysis chain as for the data to test the viability of the analysis chain.

However, sometimes we would like to inspect information available in the simulation that is not available physically. We save this extra information in the `hit`-tree in the same G4-ROOT-file; the `hit`-tree will be saved if the `TRIMSRootLevel` from Table 3.4 is set to be greater than or equal to 2. The `hit`-tree only contains coincidence events and the entries saved are provided in Table 3.5. Using the table as a reference, the rest of this subsection will cover the detailed physics implementation in the TRIMS Geant4 simulation.

The decay position in the three spatial coordinates is given by `decayPosX,Y,Z`. The decays are uniformly distributed in the cylindrical space whose radius is determined by the inner radius of the decay chamber and the length by the faces of the two detectors facing into the decay chamber. Events that fall inside the electrode or the hideout are redrawn. To ensure uniform distribution in a cylinder, some care must be taken. Take U as a random variable with uniform distribution in the interval $[0, 1]$. For convenience of notation, whenever U is drawn, we will treat it as independent from its previous draw. Now, suppose the cylinder has radius R and extends from A to B in the Z-direction, then the sampling in cylindrical coordinates is given by [161],

$$r = \sqrt{U}R,\ \theta = U2\pi, \text{ and } z = U(B - A) + A. \tag{3.2}$$

Similarly, the initial momentum direction of the beta `betaInitMomDirX,Y,Z` can be isotropically sampled in spherical coordinatex by [162],

$$\theta = \arccos(2U - 1), \text{ and } \phi = U2\pi. \tag{3.3}$$

In most events, the decay produces only two particles, a beta and an ion. We neglect the neutrino and the neutral atom and take the ion initial momentum direction `ion1InitMomDirX,Y,Z` to be opposite to that of the beta. For decays that produce a pair of electrons and a pair of ions, see Sec. 3.1.4.

For the initial beta kinetic energy `betaInitKE`, Geant4 provides a simple way to generate the distribution according to the Fermi theory (Sec. 1.5). Given the distribution $f(E)$, we first obtained its maximum $\max[f(E)]$, and "normalized" the distribution to,

$$F(E) \equiv \frac{f(E)}{\max[f(E)]/0.9} = 0.9\frac{f(E)}{\max[f(E)]}. \tag{3.4}$$

In other words, the maximum of $F(E)$ has a value of 0.9. Then we apply the Metropolis method to sample the distribution $F(E)$. We first sample energy $E = UQ$, where Q is the Q-value. Then we draw another U, calling the resulting value u. If $u < F(E)$, then we accept it, and the beta will have energy E. If $u \geq F(E)$, then we reject it, and draw a different energy $E' = UQ$ with a new U for the next Metropolis selection until finally an energy is accepted. The factor 0.9 in $F(E)$ is just to ensure the sampling space covers the entire beta distribution. It's less efficient than a factor of 1.0, but then we do not need to worry about the bias created by finite numerical precision.

The most important uncertainty of the TRIMS Geant4 simulation perhaps comes from the initial ion energy `ion1InitKE`. It is the nuclear recoil energy coming from the beta decay. The recoil energy is small but complicated to derive due to the possibility that the beta excites the electronic states of the atom or the molecule. The working initial ion kinetic energies we used as an input are,

T_2:

T^+: $\frac{1}{2}(U(25-5)+5)$eV,

$^3He^+$: $\frac{1}{2}(U(25-5)+5)$eV,

$^3HeT^+$: $U1.7\,$eV,

HT:

H^+: $\frac{3}{4}(U(25-5)+5)$eV,

$^3He^+$: $\frac{1}{4}(U(25-5)+5)$eV,

$^3HeH^+$: $U2\,$eV,

where the energy ranges, e.g. $(U(25-5)+5)$, come from [92]. The derivation of the energy ranges assumes 0 K temperature, i.e. all T_2 and HT start out in the ground electronic state.

Therefore, we have broadened the ranges to account for the uncertainty considering TRIMS operates at room temperature. The fractions of $\frac{1}{2}$ or $\frac{3}{4}$ are there because the reference provides the combined kinetic energy of the ion and neutral atom produced after the decay. These initial energies will impact the ion acceptance as we scan the ion-detector.

After the initial conditions are set, the tracking of the charged particles in the electromagnetic field is provided by Geant4, which uses an advanced Runge-Kutta method. The tracking for the ions stops when the particles go outside the simulated world or when they hit the silicon detectors. For the betas, the stop condition is more complicated due to electron backscattering as will be discussed in Sec. 3.1.3.

Entry Name	(Unit)	Description
`decayPosX,Y,Z`	(cm)	Decay position
`betaInitKE`	(keV)	Initial beta energy
`betaInitMomDirX,Y,Z`		Initial beta momentum direction
`ion1InitKE`	(keV)	Initial ion energy
`ion1InitMomDirX,Y,Z`		Initial ion momentum direction
`beta1Edep_Exact`	(keV)	Exact incident beta energy upon detection
`beta1Edep`	(keV)	Detected beta energy, obtained from applying energy broadening to `betaEdep_Exact`
`beta1TOF_Exact`	(ns)	Exact beta TOF upon detection
`beta1TOF`	(ns)	Detected beta TOF, obtained from applying timing broadening to `betTOF_Exact`
`beta1CapturePosX,Y,Z`	(cm)	Beta incident position upon detection
`beta1CaptureMomDirX,Y,Z`		Beta incident direction upon detection
`ion1Edep_Exact`	(keV)	Exact incident ion energy upon detection
`ion1EdepPostDead`	(keV)	Incident ion energy after the dead layer
`ion1Edep`	(keV)	Detected ion energy, obtained from applying energy broadening to `ionEdepPostDead`

ion1TOF_Exact	(ns)	Exact ion TOF upon detection
ion1TOF	(ns)	Detected ion TOF, obtained from applying timing broadening to ionTOF_Exact
ion1TOFRes	(ns)	Ion-TOF resolution according to ionTOF_Exact
ion1CapturePosX,Y,Z	(cm)	Ion incident position upon detection
ion1CaptureMomDirX,Y,Z		Ion incident direction upon detection
sourceID		Source ID: 1 for T_2, and -1 for HT
decayID		Decay channel ID: see text for details
beta1ID		ID for the particles incident on the beta-detector
ion1ID		ID for the particles incident on the ion-detector
betaHitN		The number of particles detected by the beta-detector from the decay
ionHitN		The number of particles detected by the ion-detector from the decay
eventID		ID for each decay
runID		ID for each run, only used when multiple files are saved for the ion-detector scanning
ion_detposY	(cm)	Ion-detector Y-position
ion_detposX	(cm)	Ion-detector X-position
voltage (mV)		Voltage applied across the decay chamber

Table 3.5: Entries saved in the hit tree of the output G4-ROOT-file. The provided entries are saved for each pair of coincidence events.

For the beta-detector, once it captures a particle, the particle's exact energy betaEdep_Exact, exact TOF betaTOF_Exact, capture position betaCapturePosX,Y,Z, and incident direction betaCaptureMomDirX,Y,Z are recorded. Notice that the captured particle may not neces-

sarily be a beta particle; the naming suggests the particle is captured by the beta-detector. To incorporate energy broadening in the detector response, a simple Gaussian smearing with a mean of `betaEdep_Exact` and a standard deviation from `SetBetaDetERes` from Table 3.2 is applied to obtain the detected beta energy `betaEdep`. If the smeared signal goes below 0 keV, then the detected energy is set to be 0 keV.

To obtain the detected TOF information `beta1TOF`, we first generate an ASCII table based on the blue data points from Fig. 5.12, which shows a timing resolution versus energy (calibrated amplitude) plot based on the pulser-data we collected using the physical detectors. We refer to the ASCII table as the TRes-table. There are two differences between the data points in the TRes-table and Fig. 5.12 however. The first is that Fig. 5.12 shows the timing resolution in FWHM, while the TRes-table shows it in standard deviation. The second is that the results from Fig. 5.12 are obtained using ion-timing to subtract beta-timing, whose broadening has contributions from both of the detectors that received the pulses of the same amplitude. Therefore, the values in TRes-table are obtained by multiplying values in Fig. 5.12 by an extra factor of $1/\sqrt{2}$. The factor of $1/\sqrt{2}$ is to isolate out the contributions from the two detectors assuming they are statistically independent. We tested the assumption by sending pulses whose amplitudes are different between the two detectors and confirmed the statistical independence between beta and ion-detector's timing resolution. Once we have the TRes-table, we use `betaEdep_Exact` as the reference for the energy, linearly interpolate the data points in the TRes-table to get the timing resolution, and use the timing resolution to Gaussian smear `betaTOF_Exact` to get the detected beta TOF `betaTOF`.

For the ion-detector, most of the steps follow in ways identical to that of the beta-detector. One important difference however, is that to obtain the detected ion energy `ion1Edep`, we need to account for the detector dead layer. To simulate the dead-layer effect, we use a software called SRIM, whose output is saved in another ASCII table called the SRIM-table (Sec. 3.2.1). The SRIM-table contains the information both for how much the energy is lost and how much the energy broadens because of the dead layer. Applying both effects to `ionEdep_Exact`, we arrive at `ionEdepPostDead`. Then to obtain the detector ion energy

`ionEdep` we apply the Gaussian smearing again on `ionEdepPostDead` using the standard deviation obtained from `SetIonDetERes` in Table 3.2. We do not apply a dead-layer correction to electron detection because it is small yet complicated to simulate as suggested by [163].

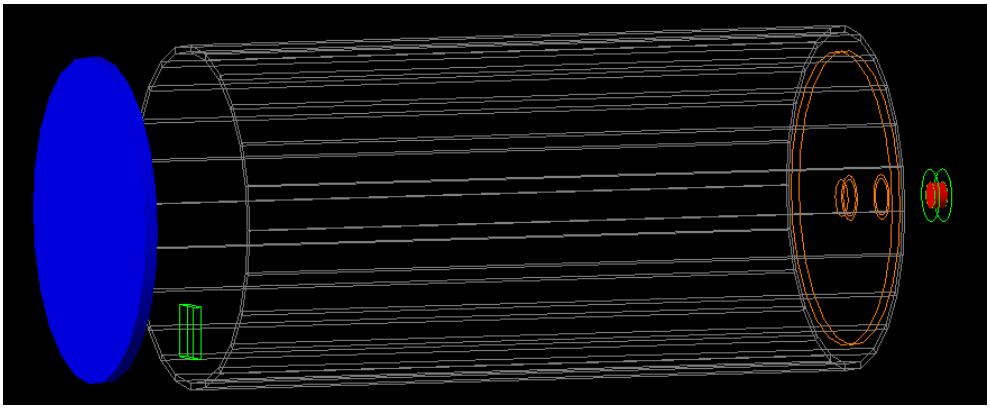

Figure 3.3: Modified Geant4 geometry from Fig. 3.1. In this configuration, the ion-detector has a radius of 50 mm instead of 4 mm. Since the exact ion incident position information is provided by the `hit` tree of the G4-ROOT-file, we can apply cuts later to select events within a detection radius. Then we can essentially obtain the entire ion-detector scanning results in one simulation.

Decay ID	Source	Product Ions	Decay ID	Source	Product Ions
1	T_2	T^+	11	HT	H^+
2	T_2	$^3He^+$	12	HT	$^3He^+$
3	T_2	$^3HeT^+$	13	HT	$^3HeH^+$
5	T_2	$^3He^{++}$	15	HT	$^3He^{++}$
6	T_2	$^3He^+$ and T^+	16	HT	He^+ and H^+

Table 3.6: Number coding for `decayID`.

To obtain the detected ion TOF, a similar procedure is followed, except the input energy to the TRes-table for linear interpolation is `ionEdepPostDead`.

An additional note is that `ion1CapturePosX,Y,Z` can be used to save simulation run-time as we scan the ion-detector. The idea is to set the ion-detector radius to 50 mm instead of 4 mm in the simulation as shown in Fig. 3.3. So instead of using `SetIonDetX` from Table 3.2 to adjust the ion-detector position, we can simply apply `ROOT TCut` to select the events that fall inside the 4 mm radius at any scan-position out of the capture positions on the big ion-detector. Any offset to the scan-positions are also straightforward to implement. This method makes the variables `runID`, `ion_detposY`, and `ion_detposX` obsolete. To further save run time, we can look at the distribution of the decay positions of the coincidence events between the big ion-detector and the actual-size beta-detector. Then we can limit the decay position to within the radial range of the distribution, since decays outside the range would not produce coincidence events.

The `sourceID` is rather intuitive. The `decayID` again follows from Sec. 6.1.1. The number codings are given in Table 3.6.

Similarly, for the particle ID as detected by the beta-detector `beta1ID` and by the ion-detector `ion1ID`, their number codings are given by Table 3.7.

Particle ID	Source	Detected Particle	Particle ID	Source	Detected Particle
0		electron			
1	T_2	$^3T^+$	11	HT	$^3H^+$
2	T_2	$^3He^+$	12	HT	$^3He^+$
3	T_2	$^3HeT^+$	13	HT	$^3HeH^+$
5	T_2	$^3He^{++}$	15	HT	$^3He^{++}$

Table 3.7: Number coding for `decayID`.

Notice that it is not necessarily true that the beta-detector only detects electron and the ion-detector only ions. For instance, if the decay happens right in front of the beta-detector, it is going to detect both the beta and the ion, and so `beta1ID` is not always 0. Our physical detectors also cannot distinguish the type of the detected particles, so a similar situation does happen in the actual experiment too. The `eventID` is given iteratively to each decay whether the product particles are detected or not. And finally the `voltage` will be helpful later to reconstruct the mass of the detected ion event by event.

3.1.3 Electron Backscattering

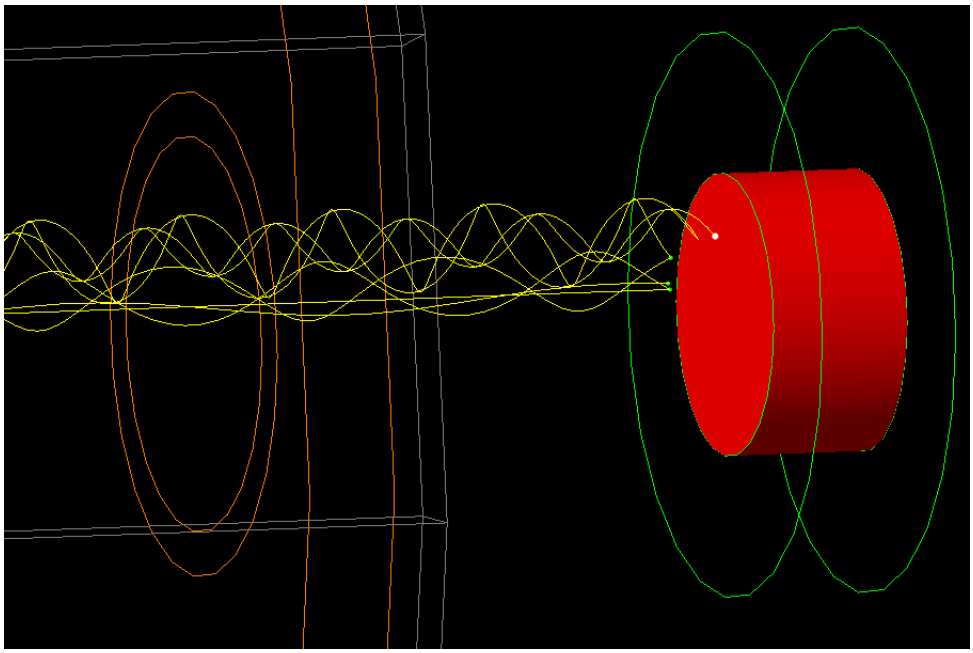

Figure 3.4: Geant4 electron-backscattering simulation for TRIMS. The plot zooms in on the beta-detector and shows the trajectories of two electrons. The first electron backscatters from the sensitive part of the beta-detector before it returns due to the electric field and is detected, where again the detection is indicated by a white dot. The second electron scatters from the beta-detector-ring twice before being captured by it; every incidence on the beta-detector-ring is indicated by a green dot.

Electron backscattering from the beta-detector turns out to be one of our major sources of uncertainty; electron backscattering smears the detected beta energy. This is because a backscattered electron can be reaccelerated back to the beta-detector by the electric field and gets recaptured with some loss in energy. For this reason, we incorporate electron backscattering in our Geant4 simulation as shown in Fig. 3.4. The figure shows the trajectories of two electrons. The first electron backscatters from the beta-detector sensitive area (the red puck) and is guided back by the electric and magnetic field and is detected. The detection is shown by the white dot. The second electron backscatters from the beta-detector-ring twice and gets captured by the ring; every interaction with the beta-detector-ring is represented by a green-dot and there are three green-dots in total. This second electron is lost from detection because it does not enter the sensitive area. However, it is very possible that an electron scatters from the beta-detector-ring but ends up back in the sensitive area and is detected. Similarly, an electron can backscatter from the beta-electrode but still be detected.

To determine the electron-backscattering probability, we use the Geant4 physics package `emstandardSS` that corresponds to the "Single-Scattering" model in Figure 8 of [164]. According to the figure, in our energy range of interest (Sec. 5.3.5), this is the option that matches the physical data the best.

In addition to entries from Table 3.5, entries from Table 3.8 are also saved for each event in the `hit`-tree of the output G4-ROOT-file. These entries record the particle information of the electron when it is incident on the beta-detector for the first time. If no backscattering occurs, then these values are identical to the corresponding values in Table 3.5, which record the information when the electron is detected. For instance, `beta1FirstIncEdep_Exact` would be the same as `beta1_Exact`.

Entry Name (Unit)	Description
`beta1BackScattered`	Beta-backscattering counts: 0 if beta is detected without backscattering; +1 every time the beta backscatters from the beta-detector and +10 from the beta-detector-ring
`beta1FirstIncEdep_Exact`(keV)	Exact incident beta energy upon the first incidence to the beta-detector
`beta1FirstIncTOF_Exact` (ns)	Exact beta TOF upon the first incidence to the beta-detector
`beta1FirstIncPosX,Y,Z` (cm)	Beta incident position upon the first incidence to the beta-detector
`beta1FirstIncMomDirX,Y,Z`	Beta incident direction upon the first incidence to the beta-detector

Table 3.8: Entries saved in the `hit` tree of the output G4-ROOT-file in addition to Table 3.5. These entries are associated with electron backscattering. Notice the beta-detector here refers to the beta-detector sensitive area.

As for ion backscattering, Fig. 3.7 from Sec. 3.2.1 shows that the backscattering probability is smaller by an order of magnitude in our range of interest, and so it is not implemented in the Geant4 simulation.

3.1.4 Charge-Two Events

As hinted by the previous discussions in this section, there are decay channels that produce a doubly charged ion or two ions (Sec. 6.1.1). And in either case, the decay also produces two electrons, one being the beta and another being the shake-off electron. In fact, two such decays are already shown in Fig. 3.1, each of which produces a $^3He^+$ (blue) and a H^+

(violet). If these types of decay produce a coincidence event to the detectors, we call this event a charge-2 event.

To account for these charge-2 events, Table 3.9 is also saved for each event in the `hit`-tree of the output G4-ROOT-file; Table 3.9 is almost a mirror copy of Table 3.5 and Table 3.8 combined to account for the possible second detection. If no second particle is captured, then the recorded entry is set to 0 or -1 depending on convenience.

Entry Name	(Unit)	Description
`eleInitKE`	(keV)	Initial shake-off electron energy
`eleInitMomDirX,Y,Z`		Initial shake-off electron momentum direction
`ion2InitKE`	(keV)	Initial 2^{nd} ion energy
`ion2InitMomDirX,Y,Z`		Initial 2^{nd} ion momentum direction
`beta2Edep_Exact`	(keV)	Exact incident shake-off electron energy
`beta2Edep`	(keV)	Detected shake-off electron energy
`beta2TOF_Exact`	(ns)	Exact shake-off electron TOF
`beta2TOF`	(ns)	Detected shake-off electron TOF
`beta2CapturePosX,Y,Z`	(cm)	Shake-off electron incident position
`beta2CaptureMomDirX,Y,Z`		Shake-off electron incident direction
`beta2BackScattered`		Shake-off electron-backscattering counts
`beta2FirstIncEdep_Exact`	(keV)	Exact incident shake-off electron energy upon the first incidence to the beta-detector
`beta2FirstIncTOF_Exact`	(ns)	Exact shake-off electron TOF upon the first incidence to the beta-detector
`beta2FirstIncPosX,Y,Z`	(cm)	Shake-off electron incident position upon the first incidence to the beta-detector
`beta2FirstIncMomDirX,Y,Z`		Shake-off electron incident direction upon the first incidence to the beta-detector
`ion2Edep_Exact`	(keV)	Exact incident 2^{nd} ion energy upon detection

`ion2EdepPostDead`	(keV)	Incident 2nd ion energy after the dead layer
`ion2Edep`	(keV)	Detected 2nd ion energy, obtained from applying energy broadening to `ionEdepPostDead`
`ion2TOF_Exact`	(ns)	Exact 2nd ion TOF upon detection
`ion2TOF`	(ns)	Detected 2nd ion TOF, obtained from applying timing broadening to `ionTOF_Exact`
`ion2TOFRes`	(ns)	2nd ion-TOF resolution according to `ion2TOF_Exact`
`ion2CapturePosX,Y,Z`	(cm)	2nd ion incident position upon detection
`ion2CaptureMomDirX,Y,Z`		2nd ion incident direction upon detection
`beta2ID`		ID for the 2nd particle incident on the beta-detector
`ion2ID`		ID for the 2nd particle incident on the ion-detector
`betaEdep`	(keV)	Beta energy to match the beta-detector detection
`betaTOF`	(ns)	Beta TOF to match the beta-detector detection
`ionEdep`	(keV)	Ion energy to match the ion-detector detection
`ionTOF`	(ns)	Ion TOF to match the ion-detector detection

Table 3.9: Entries saved in the `hit` tree of the output G4-ROOT-file in addition to Table 3.5 and Table 3.8. These entries are associated with charge-2 events.

The initial shake-off electron energy `eleInitKE` is taken to be $U\times$ 30 eV [92]. The initial direction `eleInitMomDirX,Y,Z` is assumed to be isotropic, independent from the beta's direction.

As an update to the initial ion recoil energy `ion1InitKE` in Sec. 3.1.2, we add `ion2InitKE`

in Table 3.8. And the inputs for the charge-2 events are,

$$\begin{aligned}
T_2\text{:}\quad & {}^3He^{++}\text{:}\quad \tfrac{1}{2}(U(25-5)+5)\text{eV},\\
& {}^3He^{+}\text{:}\quad \tfrac{1}{2}(U(25-5)+5)\text{eV and } T^{+}\text{:}\ \tfrac{1}{2}(U(25-5)+5)\text{eV}\\
HT\text{:}\quad & {}^3He^{++}\text{:}\quad \tfrac{1}{4}(U(25-5)+5)\text{eV},\\
& {}^3He^{+}\text{:}\quad \tfrac{1}{4}(U(25-5)+5)\text{eV and } H^{+}\text{:}\ \tfrac{3}{4}(U(25-5)+5)\text{eV},
\end{aligned}$$

where U is again drawn from a uniform distribution of interval $[0, 1]$ and the formulas follow from basic kinematics in addition to the total recoil energy from [92]. For $^3He^{++}$, its initial ion direction follows the same scheme as that for the "charge-1" case (Sec. 3.1.2). As for the two-ion case, their initial directions are set to be back-to back from each other, but otherwise isotropic; they are now independent from the beta's direction. On top of this configuration, the $^3He^{+}$ receive an additional isotropic momentum "kick" that has an energy of $U\times$ 3.4 eV [92, 140]. The energy of this kick comes from the beta and the antineutrino, but we do not track the antineutrino. The kick is implemented by adding the momentum of the extra kick to the original $^3He^{+}$ momentum.

The last four entries in Table 3.9 are to match the response of the physical detectors. If only one electron or one ion is detected then `betaEdep` is set to `beta1Edep` and similarly for the other three entries. However, because the physical detectors have finite timing resolution, if two particles arrive within an interval much smaller than the resolution, the detectors can only see a single signal. For this reason, the detected beta energy is given by,

$$\texttt{betaEdep} \equiv \texttt{beta1Edep} + \texttt{beta2Edep}. \tag{3.5}$$

The beta TOF is given by

$$\texttt{betaTOF} \equiv (\texttt{beta1TOF\_Exact} + \texttt{beta2TOF\_Exact})/2, \tag{3.6}$$

but is smeared by the sum of the timing resolution found using a beta energy of `betaEdep` and half of the timing difference between `beta1TOF_Exact` and `beta2TOF_Exact`. The sum is to account for the timing broadening caused by detecting two electrons. As for detecting

two ions, the ion energy is similarly given by,

$$\texttt{ionEdep} \equiv \texttt{ion1Edep} + \texttt{ion2Edep}. \tag{3.7}$$

As for the ion TOF, there are two cases. In case of T^+ and $^3He^+$, because the ions are close in mass and are captured roughly at the same time, the ion TOF is set similarly by,

$$\texttt{ionTOF} \equiv (\texttt{ion1TOF\_Exact} + \texttt{ion2TOF\_Exact})/2, \tag{3.8}$$

which is smeared by the sum of the timing resolution found using `ionEdep` and half of the timing difference between `ion1TOF_Exact` and `ion2TOF_Exact`. In case of detecting H^+ and $^3He^+$, because H^+ is much lighter in mass than $^3He^+$, it arrives at the ion-detector much earlier. And by using the method to be introduced in Sec. 5.3.4, we can separate out the two signals in the data. So in this case, `ionTOF` is set to `ion2Edep` to match the setting in Sec. 5.3.4.

3.1.5 Uncertainty in Ion Initial Direction and Energy

Aside from electron backscattering, the most important uncertainty of the simulation comes from the initial ion configuration. The reason is that we do not have an accurate prediction of the ion recoil energy after beta decay at room temperature [92]. We also do not know the exact initial directions for decays that produce two ions. The importance of these uncertainties will be addressed in Sec. 7.2.4. To account for this uncertainty, we perform a simulation for each extreme case. There are 5 in total and the options can be selected using `SetConfig2Ion` from Table 3.4.

The first option is the default option that covers all the setup described in this section so far. This option is assumed if `SetConfig2Ion` is set to any values besides 8 or 9 (indices match Sec. 7.2.3). Options 8 and 9 assume a different ion initial energy configuration. Option 8 assumes the total ion recoil energy to be 1 eV that is shared by two particles kinematically, while Option 9 assumes 50 eV. The recoil energy of 50 eV is a conservative upper bound according to [92] and our data analysis (specifically Fig. 7.27 from Sec. 7.2.4).

This numbering scheme is partly historical; the options will be applied later in the analysis (Table 7.4 of Sec. 7.2.3).

3.1.6 Application: Average Beta TOF

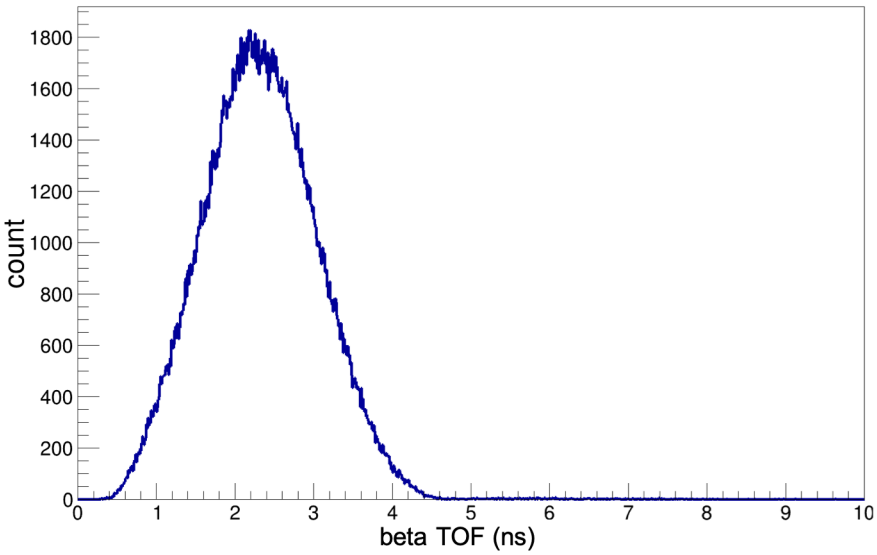

Figure 3.5: Beta-TOF distribution from Geant4 simulation for TRIMS. The mean is 2.3 ns, which will be used to correct the ion TOF (Sec. 6.1.2).

A quick application that can be used in TRIMS data analysis is to obtain the mean beta TOF for the ion-TOF correction. The average beta TOF is difficult to obtain analytically for three reasons. The first is that the initial beta energy follows the Fermi function, which is difficult to integrate. The second is that the initial beta momentum direction is isotropic and so does not align with the electric field most of the time. Because TRIMS does not have the sensitivity to determine the initial beta momentum direction for each event, the averaging requires integrating over all angles. The third is that because of the cyclotron radius, determining the decay location for a coincidence event, i.e. when both beta- and ion-detectors receive hits, is immensely difficult. Fortunately, Geant4 can track the TOF of

particles and provide a distribution of beta TOF for coincidence events as shown in Fig. 3.5. The figure is produced using geometry from Fig. 3.3 and `beta1FirstIncEdep_Exact` from Table 3.8. We assume the radial decay position is limited to within 3 mm from the center of the beta-detector to avoid complications from electron backscattering that our physical detectors cannot resolve. The mean of 2.3 ns and standard deviation of 0.7 ns from the spectrum will be used later to correct the ion TOF in the data (Sec. 6.1.2).

3.2 SRIM

The SRIM (Stopping and Range of Ions in Matter) software was developed to simulate transportation of ions in materials [165, 166]. It applies the Monte Carlo method to track various types of incident ions with an energy range of 10 eV to 2 GeV as they travel through various types of materials. The SRIM GUI makes it easy to select the ion types, the incident ion energy, the target materials, and the depth of the target. In terms of physics, SRIM implements details such as ionization, phonon generation, and electron/nuclear stopping power. The electron stopping power specifically is obtained from fitting the data from a large number of experiments, which makes SRIM a popular tool for studying material response to radiation. For instance, SRIM is the go-to software for simulating ion implantation for semiconductor devices.

Since the TRIMS experiment detects ions at a low energy level of tens of keV, the dead-layer effect from our silicon detectors causes significant energy loss. For this reason, we rely on SRIM to simulate this energy-loss mechanism for our ion-detector. The SRIM results are used both as an input to the Geant4 simulation (Sec. 3.1) and as an empirical correction to the data (Sec. 6.2.2).

Note that the SRIM simulation does not account for the dead-layer effect on the electrons.

3.2.1 SRIM as a Reference for Geant4 Simulation [167]

An example of the results that we can obtain from SRIM is shown in Fig. 3.6. The plot shows on the x-axis the incident ion energy and on the y-axis the detected ion energy by

a silicon detector with 100 nm half-dead layer. The dead layer refers to the inactive silicon layer of the detector; the energy of the particle deposited in the dead layer would be lost from detection (more details in Sec. 5.1.2). Whereas what we call a half-dead layer is a partially dead layer where only half of the energy deposited is lost [168]. In fact, SRIM does not know about the dead layer. What SRIM provides is the energy deposited in a certain thickness of the target material,

$$E_{\text{inc}} = E_{\text{dead}} + E_{\text{col}}, \tag{3.9}$$

where E_{inc} is the incident energy of the particle, E_{dead} the energy deposited in the dead layer, and E_{col} the energy deposited in the active electron-collecting layer (depletion region). Then the detected energy E_{det} can be obtained by,

$$\begin{aligned} E_{\text{det}} &= \frac{1}{2}E_{\text{dead}} + E_{\text{col}} \\ &= E_{\text{inc}} - \frac{1}{2}E_{\text{dead}}. \end{aligned} \tag{3.10}$$

The data points in Fig. 3.6 are simulated using E_{inc} from 10 to 60 keV in 10 keV steps, where each data point is simulated using 1 M events. These data points are then fitted to a 2^{nd}-degree polynomial. Because the dead-layer effect is different for different ions, we did the SRIM simulation for three types of atomic ions: H^+, T^+, and $^3He^+$. As for the molecular ions, their dead-layer effect can be derived from the atomic ions because the molecules are immediately ionized upon detection. For example, when a $^3HeH^+$ incident on the detector at 60 keV, it is ionized to a $^3He^+$ or $^3He^{++}$ and a H^+. Since the two ions have the same incident speed, the $^3He^+$ takes 45 keV and the H^+ 15 keV by energy conservation. As the ions travel through the dead layer, we can independently calculate their detected energies using Fig. 3.6 and combine the resulting energies to obtain the detected energy of the $^3HeH^+$.

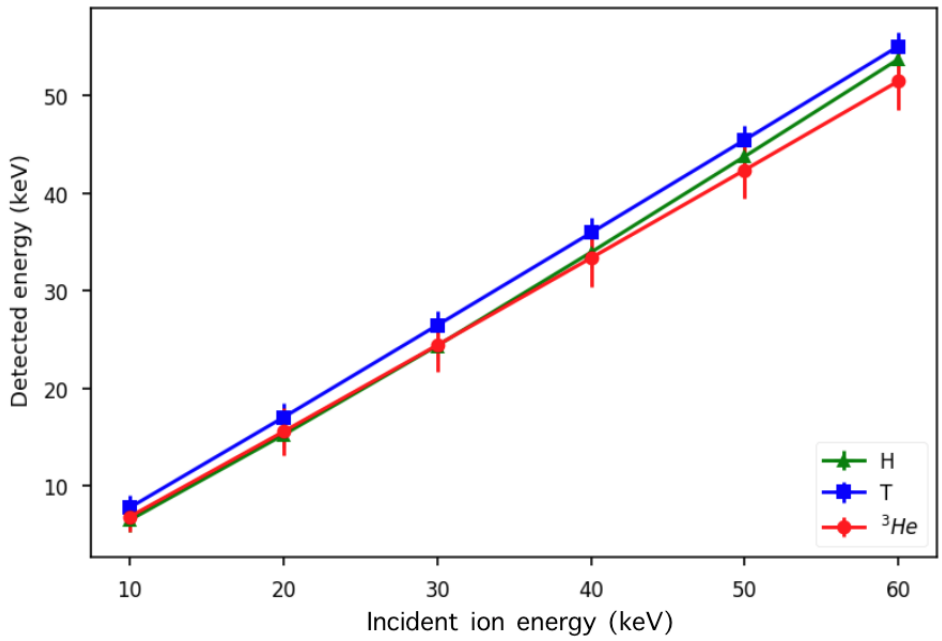

Figure 3.6: SRIM dead-layer simulation for TRIMS [169]. The result shows on the x-axis the incident ion energy and on the y-axis the detected ion energy Eq. 3.10 as the ion is incident normally to a 100 nm half-dead-layer silicon detector. The plot is generated for three types of atomic ions: H^+ (green triangles), T^+ (blue squares), and $^3He^+$ (red diamonds). The uncertainties on the data points are statistical. The data points from each ion type are then fitted to a 2^{nd}-degree polynomial.

Normal incidence of the ions is assumed in our SRIM simulation. The assumption is a good one because the initial decay energies of the ions are of order eV, which is negligible considering our HV of 60 kV; after the acceleration from the HV, the ions are essentially incident normal to the ion-detector. The assumption is also confirmed by the Geant4 simulation.

Because Geant4 is best at simulating high-energy physics where the dead-layer effect is negligible, SRIM is more reliable in terms of simulating the responses from the ion-detector. For this reason, we generated a reference ASCII table for our Geant4 code using the SRIM results shown in Fig. 3.6. We refer to this table as the SRIM-table. Again, this table is made only for H^+, $^3He^+$, and T^+ (^3H). The evaluations for $^3HeT^+$ and $^3HeH^+$ are done inside our

Geant4 code using the method explained in the previous paragraph. In the SRIM-table, the incident energy ranges from 10 keV to 90 keV in 10 keV steps, and dead-layer width ranges from 50 nm to 150 nm in 10 nm steps. Because the SRIM-table has two varying parameters, we apply a 2-D linear interpolation to extract the information in between the data points. As SRIM is based on a Monte Carlo simulation, we can also extract the energy broadening contributed by the dead layer. The broadenings are included in the SRIM-table in the form of the standard deviations of the detected ion energies.

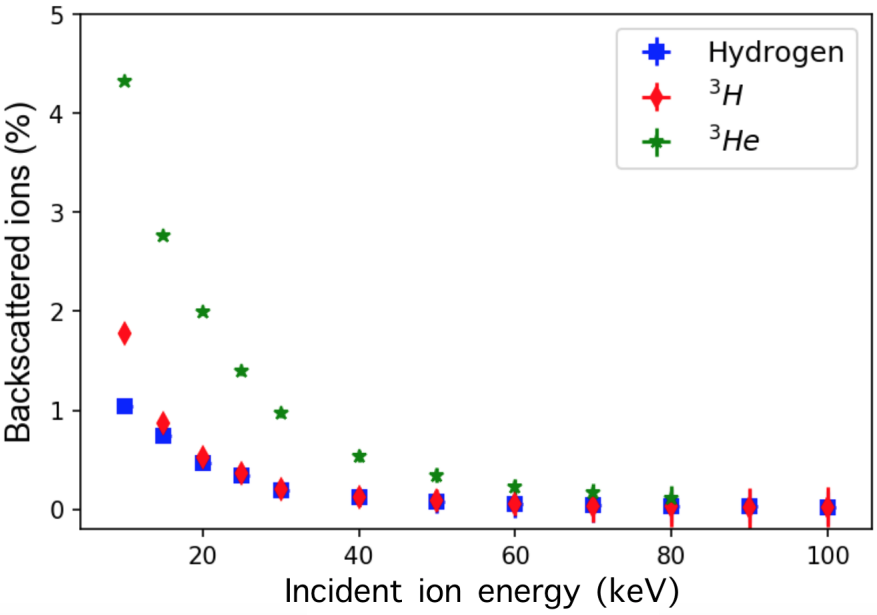

Figure 3.7: SRIM ion-backscattering simulation for TRIMS [169]. The result shows on the x-axis the incident ion energy and on the y-axis the ion-backscattering probability as the ion is incident normal to a silicon detector.

Other than the dead-layer effect, SRIM also incorporates ion backscattering in its simulation. The ion-backscattering probability as a function of incident ion energy is provided in Fig. 3.7. The plot shows that ion backscattering only becomes significant at low ion energy, which will be largely cut out using a fiducial volume cut (Sec. 6.2.3). Furthermore, SRIM has already included the effect as a source of energy broadening. Therefore, thanks to

this SRIM result, the TRIMS Geant4 simulation does not specifically need to simulate ion backscattering.

3.2.2 SRIM for Pulse-Height Defect Correction to the Data [140]

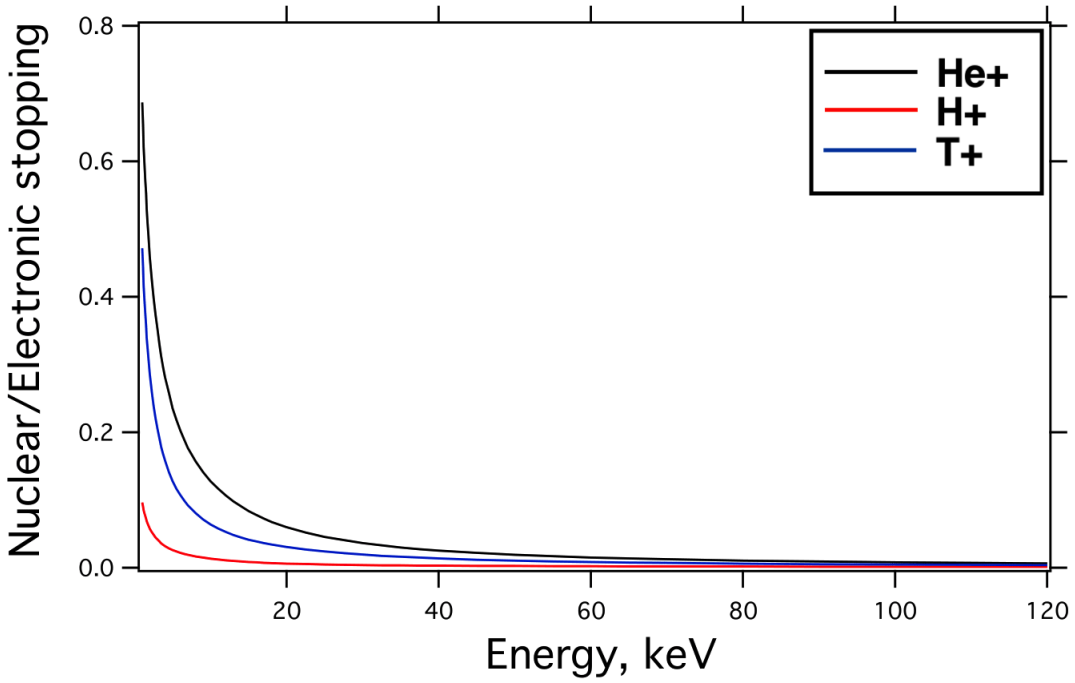

Figure 3.8: The ratio of nuclear versus electronic contribution to stopping power as a function of energy according to a SRIM simulation [41]. The energy here refers to the in-flight energy while the ion travels in a silicon medium.

Unfortunately, the dead-layer effect is not the only contributor to ion energy lost in a silicon detector. We also need to account for the nuclear recoils that cause the so-called pulse-height defect (Sec. 5.1.2). Fortunately, SRIM provides stopping powers, i.e. energy lost per unit distance a particle travels, separately for electronic and nuclear losses. According to a SRIM simulation, the ratio between nuclear and electronic stopping powers is provided in Fig. 3.8. We label the energy deposited in the medium due to the electronic stopping power as the

E_{ele} and that due to the nuclear stopping power as the E_{nucl}. Only the E_{ele} deposited in the active layer of the detector contributes to the detected energy. The E_{ele} deposited in the dead layer is largely lost due to the dead-layer effect, and all the E_{nucl} is lost due to the pulse-height defect. Therefore, we need to update Eq. 3.9 and Eq. 3.10 to the followings,

$$E_{\text{inc}} = E_{\text{ele,dead}} + E_{\text{ele,col}} + E_{\text{nucl}}, \tag{3.11}$$

$$\begin{aligned} E_{\text{det}} &= \frac{1}{2}E_{\text{ele,dead}} + E_{\text{ele,col}} \\ &= E_{\text{inc}} - \frac{1}{2}E_{\text{ele,dead}} - E_{\text{nucl}}. \end{aligned} \tag{3.12}$$

Using the total stopping power from SRIM as a reference, we can actually estimate the dead-layer width of our ion-detector. The idea is to run a SRIM simulation using 60 keV $^3He^+$ ions that are incident to a silicon medium. The E_{ele} here is obtained by multiplying the 1 nm step by the electronic stopping power at that step. Since the SRIM simulation tracks full trajectories, we can trace the trajectories in 1 nm steps and sum up the E_{ele} until the energy matches the high-energy end of the data from channel `c1` of Fig. 7.1. Then, the rest of the distance in the trajectories corresponds to the dead layer. From the data, we figure out that the 60 keV H^+ corresponds to a detected energy of 50±2 keV (shown much later in Fig. B.1 of App B.1). With the pulse-height defect accounted for, this approach estimates a half-dead-layer width of 150±40 nm for our ion-detector.

Assuming this dead-layer width, we repeat the SRIM simulation on $^3He^+$ in an energy range of (0, 120)keV with 1 keV steps, which yields plot similar to the red diamond data points in Fig. 3.6. We then fit the incident energy as a function of the detected energy using a 3$^{\text{rd}}$-degree polynomial to arrive at,

$$E_{\text{ion,inc}} = 2.864 + 1.507E_{\text{ion,det}} - 5.871 \times 10^{-3}E^2_{\text{ion,det}} + 2.895 \times 10^{-5}E^3_{\text{ion,det}}, \tag{3.13}$$

where $E_{\text{ion,inc}}$ is the incident ion energy and $E_{\text{ion,det}}$ to the detected ion energy. Note that all the coefficients have their corresponding units (Table 3.10) such that every term in Eq. 3.13 has an unit of energy. This polynomial is used to correct the ion energy in our tritium-data and provides excellent physical agreement with our experimental setup (Sec. 6.1.2).

	Constant	Linear	Quadratic	Cubic
			10^{-3}	10^{-5}
Units	keV	1	keV^{-1}	keV^{-2}
He				
DtoI	2.864	1.507	-5.871	2.895
ItoD	-1.531	0.605	3.244	-1.209
H				
DtoI	1.122	1.578	-13.644	11.341
ItoD	-0.446	0.560	7.210	-4.273
T				
DtoI	1.488	1.463	-11.444	10.937
ItoD	-0.749	0.605	7.744	-6.160
HeH				
DtoI	2.235	1.895	-20.509	21.559
ItoD	-0.995	0.468	5.797	-3.258
HeT				
DtoI	2.518	1.780	-15.288	13.582
ItoD	-1.298	0.521	4.312	-1.716

Table 3.10: Cubic polynomial fit parameters [140]. Each of the polynomials either converts the detected ion energy to the incident ion energy (DtoI) or the incident ion energy to the detected ion energy (ItoD). The $^3He^+$ coefficients are applicable up to 120 keV, and the rest to 60 keV. The uncertainties and the systematics these polynomials contribute will be addressed in Sec. 8.2.3.

The SRIM simulation with the fixed dead-layer width is also done on H^+ and T^+ in an energy range of (0, 60)keV. To get the results for molecules $^3HeH^+$ and $^3HeT^+$, we

use the same method described in Sec. 3.2.1. These results are provided in Table 3.10. The uncertainties and the systematics these polynomials contribute will be addressed in Sec. 8.2.3.

In our Geant4 simulation, we use these polynomials as the default option. In this option, the broadening information still comes from Sec. 3.2.1. We would not need to vary the dead-layer width in this option, since the polynomial fit incorporates the estimation of the dead-layer widths of the actual ion-detector.

3.3 COMSOL

The COMSOL Multiphysics software is a general physics simulation software developed by COMSOL Inc. [170]. It applies the finite-element method to solve systems of partial differential equations associated with physics found in electrical, mechanical, fluid, and chemical applications. The COMSOL GUI makes it user-friendly to design an apparatus in 3D, manage its material properties, and generate the finite-element mesh for it accordingly. Moreover, the GUI allows the users to choose how they want the final physics results to be displayed, e.g. in heat maps or plots.

For the TRIMS experiment, we use COMSOL (version 5.2) to simulate the electromagnetic fields applied on the TRIMS decay chamber by the HV and the magnets. The basic geometry is provided in Fig. 3.9, which resembles the NEC acceleration chamber from Fig. 2.6. To save development and the simulation time, the S-shaped electrodes and the corona rings are left out. The materials for the simulated parts are provided in Table 3.11. Notice that only the first three parts are showcased in Fig. 3.9. All except two are standard materials whose properties are pre-determined in COMSOL's library. The first exception is the vacuum material, which is customized as air with the electrical conductivity set to 10^{-40} S/m. The other exception is Kovar. For the purpose of the electromagnetic simulation, the three essential properties are electrical conductivity, relative permittivity, and relative permeability, which are correspondingly set to 2.041×10^6 S/m, 1, and 3,000 [171]. The relative permeability does vary for Kovar; we choose a high permeability (assuming standard heat treatment) because we are concerned about whether or not the Kovar rings

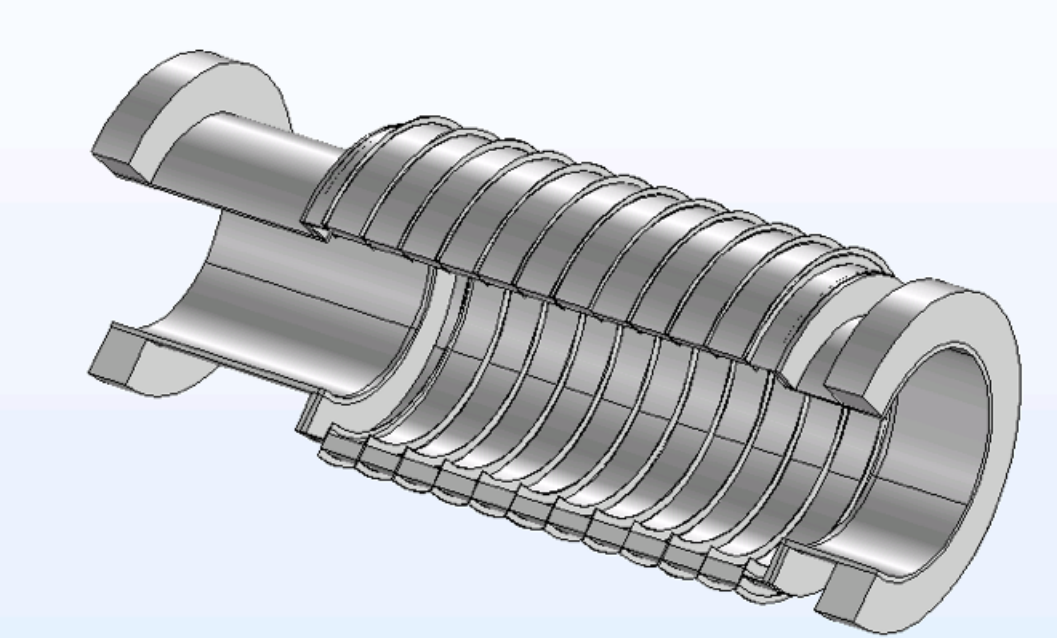

Figure 3.9: COMSOL cutaway geometry for TRIMS's decay chamber. The dimensions follow that of the NEC acceleration chamber in Fig. 2.6.

Part	Material
ConFlat vacuum pipes	Steel AISI 4340
Ceramic rings	Alumina
Kovar rings	Kovar
Volume inside chamber	Vacuum
Volume outside chamber	Air
Beta and ion electrodes	Steel AISI 4340
Quartz tube	Glass (quartz)
Magnets	Copper

Table 3.11: COMSOL materials for parts in TRIMS. Only the first three parts are present in Fig. 3.9. All the parts are present in Fig. 3.10.

would be problematic for our system by creating Penning traps.

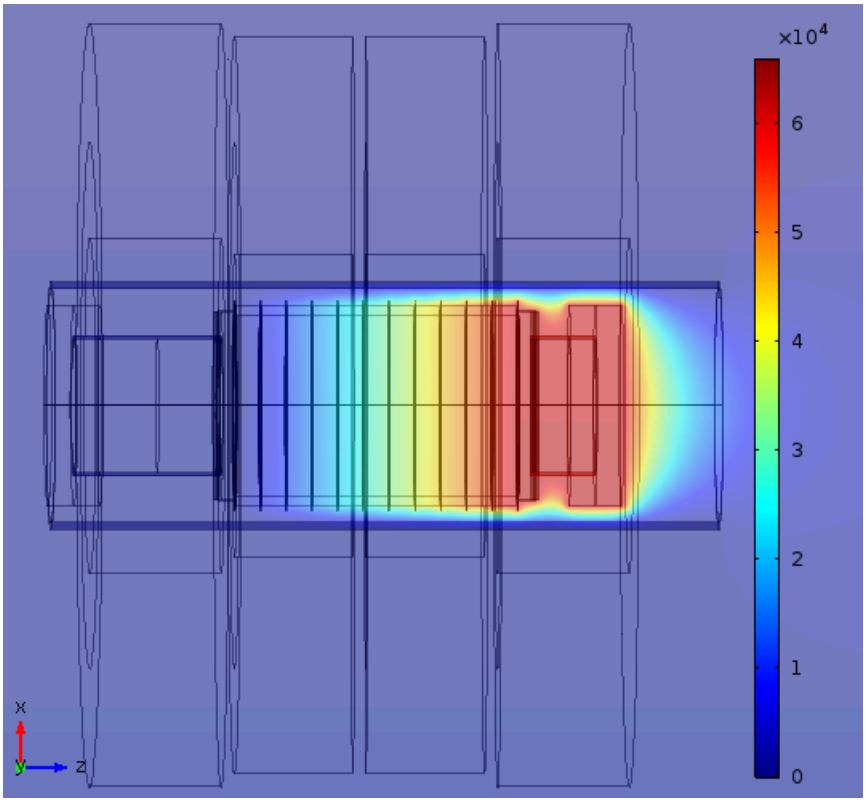

Figure 3.10: COMSOL electric field simulation for TRIMS. The plot shows a 2D heat map (color axis in units of kV) of the electric potential overlaid on the TRIMS decay chamber geometry. The background purple color indicates zero potential.

As a showcase for the COMSOL physics result and graphics, Fig. 3.10 shows a 2D heat map of the electric potential across the decay chamber. Figure 3.10 includes the beta- and ion-electrodes as thin stainless-steel discs placed in positions according to Fig. 2.1. The electrodes are floating in the geometry without making contact with the chamber, so that they are electrically insulated from each other. Each side of the decay chamber is sealed off by a blank ConFlat flange, and the chamber is placed in the quartz tube surrounded by the four magnet coils. To simulate the magnetic field, COMSOL requires running current

around the copper magnet coils. The current is adjusted such that the magnetic field is about 0.25 T uniformly across the chamber; this accuracy is sufficient for our COMSOL studies. To simulate the electric field, the voltages on the Kovar electrodes are set independently according to the voltage division from the divider-chain (Sec. 2.1.3): the voltage starts at ground on the ion-side, increments by 5.5 kV for each Kovar ring, and finally reaches 60.5 kV on the beta-side. The beta electrode is set at 60.5 kV, and the ion-electrode at -100 V.

As for Penning traps, they can accumulate enough ions to cause breakdowns [172]. And if a Penning trap is formed in the middle of the decay chamber, it can cause a delay in beta and ion time of flight, which is an essential physics parameter we are measuring. To check if our system has Penning trap problems, Fig. 3.11 a)* shows a 2D heat map of the magnetic field amplitude. We can see the magnetic field is distorted mostly by the Kovar ring that extends in the Z-direction and not so much by the other three Kovar rings that are thin in the Z-direction. If we zoom in on the Z-extended Kovar ring, the result is shown in Fig. 3.11 b), where the direction and the length of the blue arrows correspond to the direction and the magnitude of the magnetic field. The red curves show the equipotential lines of the electric field. According to the simulation, the magnetic field is strengthened inside the Z-extended Kovar ring and distorts the surrounding magnetic field lines; ideally the magnetic field should be uniform across the chamber. A Penning trap is characterized by a magnetic field line crossing the same electric equipotential line twice. Despite the distortion, the simulation shows that there are no significant Penning traps forming. We can see there are two spots that shows two Penning traps in Fig. 3.11 b) and they are circled in green. By azimuthal symmetry, both traps form a ring shape around the decay chamber's central axis. Nonetheless, the Penning traps are small such they we do not see a breakdown in the actual experiment. Moreover, these Penning traps are behind the beta electrode and so cannot delay the to-be-detected betas and ions. This COMSOL study informs us that our

*Note that the result is not simulated with the full length of the decay chamber. The reason is that the full electromagnetic simulation is computationally expensive, and we do not need a full simulation with repetitive patterns to study the Penning traps.

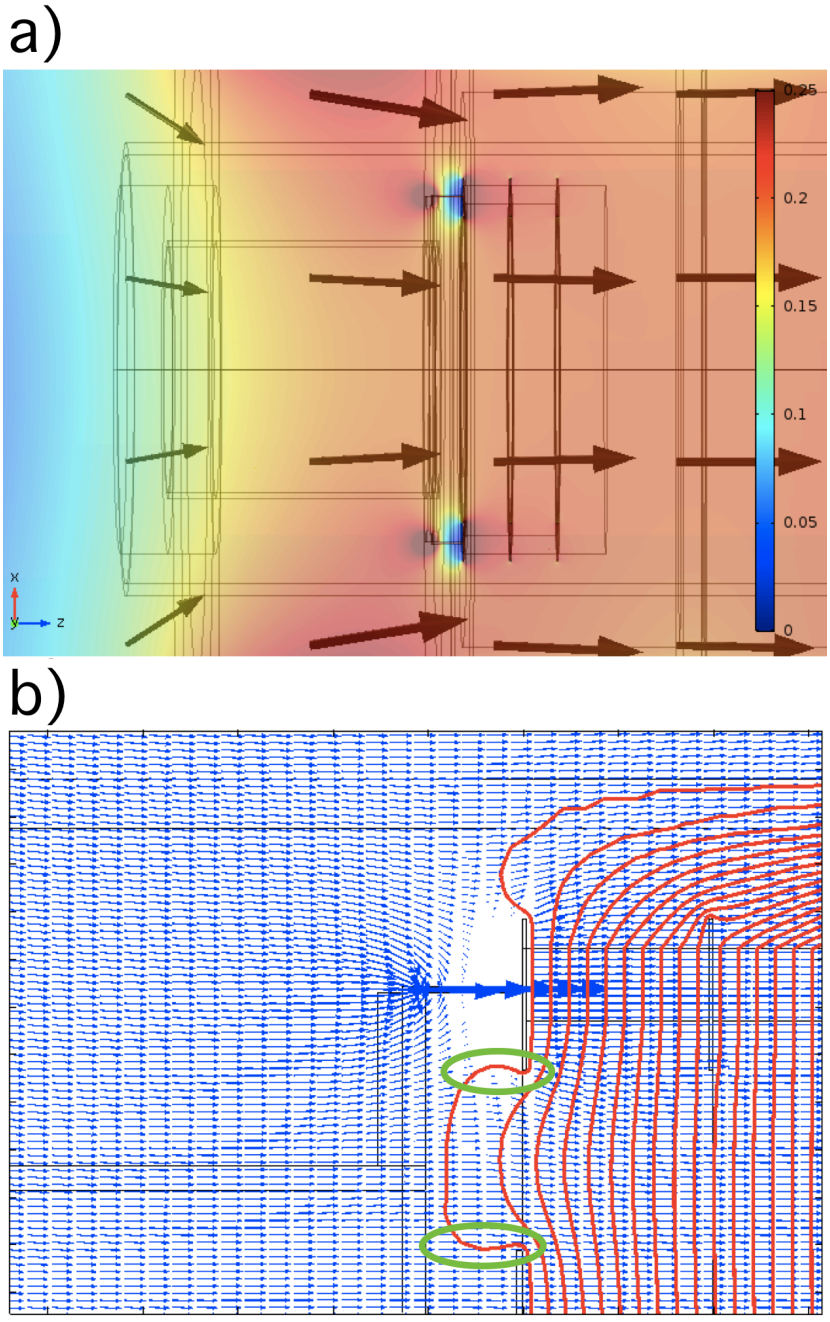

Figure 3.11: COMSOL electric and magnetic field simulation for TRIMS. Plot a) shows a 2D heat map (color axis in units of Tesla) of the magnetic field amplitude. The arrows point in the general magnetic field direction. Plot b) zooms in on the Kovar ring, where the blue arrows point in the direction of the magnetic field at that position (defined by the tail of the arrow) and have length proportional to the log base 10 of the magnetic field amplitude. The red curves show the equipotential lines of the electric field that are 550 V apart. The two spots that show the presence of a weak Penning trap are circled in green.

system is not subject to Penning trap problems.

Chapter 4

DATA-TAKING

This chapter covers how data are collected in the TRIMS experiment. To start off, Sec. 4.1 describes the setup of the data acquisition (DAQ) software we used to convert digitizer signals into computer-analyzable data. Then, Sec. 4.2.1 describes the run procedures for taking tritium data. Finally, Sec. 4.3 describes various items that help us assess the quality of the data we collected.

A note on the terminology is that a "run" here refers to a continuous data-taking period when signals from the silicon detectors are recorded. Our typical run lasts 300 s, and we take a number of them a day at various scan-positions (Sec. 2.5.5).

4.1 Data Acquisition

4.1.1 ORCA

Digitized data from both of the detectors (Sec. 2.5.1) and the slow-control devices (Sec. 2.6) are read out by the Object-oriented Realtime Control and Acquisition (ORCA) [173] software. The ORCA software is a general-purpose data-acquisition program that has been written and maintained by Mark Howe initially at the University of Washington and then at the University of North Carolina, Chapel Hill. It is specifically written for MacOS X operating systems, which is the reason why our DAQ computer is a Mac Pro. The devices read out by ORCA are connected to the DAQ computer via USB connectors. The ORCA software has a GUI, where icons, which are represented by photos of the physical devices, can be dragged and connected to configure the desired DAQ setup. The main ORCA setup for TRIMS is shown in Fig. 4.1. It is worth pointing out that the LabJack U6 interface on the top right of Fig. 4.1 was added to ORCA by Mark at TRIMS's request. The specific ORCA setup

for the CAEN DT5770 digitizer is shown in Fig. 4.2; we are able to configure the digitizer via ORCA. The digitizer configuration shows that the only active channels are channel 0 for the beta-detector and channel 2 for the ion-detector. It also shows that the digitizer trigger comes from an external source as pointed out in Sec. 2.5.2.

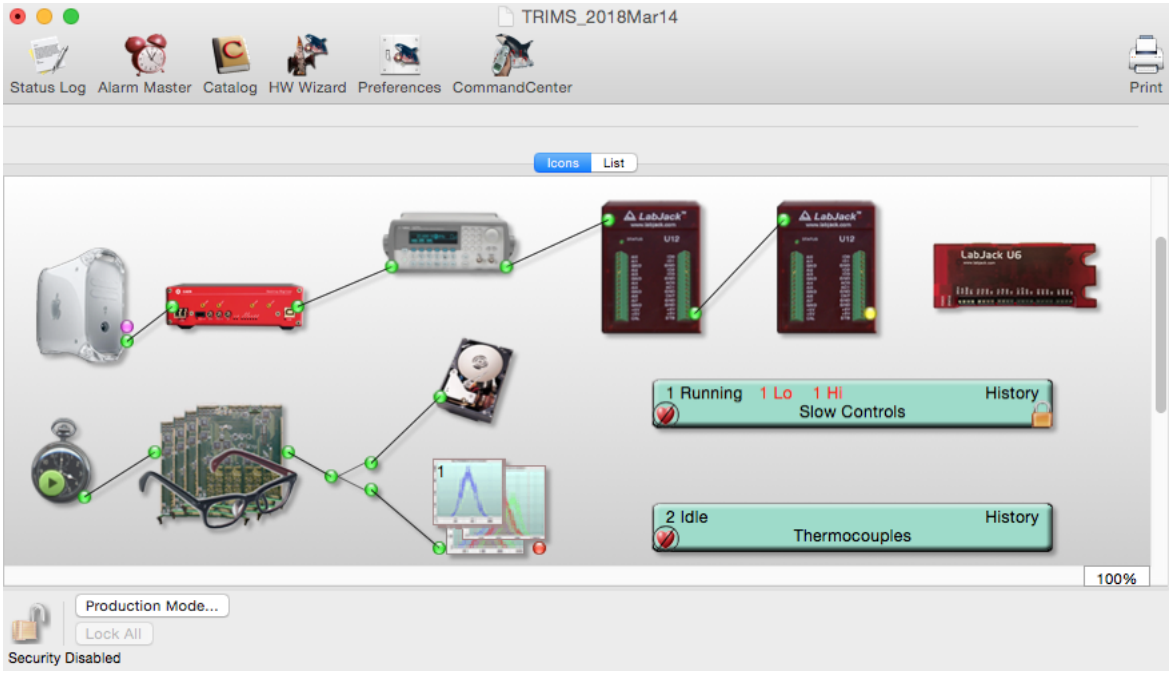

Figure 4.1: Main ORCA setup for TRIMS. This is the general layout of the ORCA GUI. The devices are shown as portrayed; the device icons from left to right show a Mac Pro, a CAEN DT5720 digitizer, an Agilent 33220A pulser, two LabJack U12s, and a LabJack U6. Other icons are basic ORCA setup for DAQ. Further details can be found in [173].

To allow a much wider range of applications, ORCA also has options to script the configurations. But for the TRIMS experiment, the basics settings suffice.

Another feature of ORCA is that it displays live data. For instance, an ORCA waveform, such as the red trace shown in Fig. 4.3, is displayed in real time whenever the digitizer is triggered. In Fig. 4.3, the x-axis shows the time, where each time bin has a length of 4 ns because the digitizer has a 250 MHz sampling rate (Sec. 2.5.2). The digitizer records

4096 time bins both before and after the trigger time, which corresponds to a time range of $(-16,\ 16)\mu$s for each waveform. The y-axis shows the waveform amplitude in analog-to-digital converter units (ADC) for each time bin. And with a 12-bit ADC resolution for each time bin, the waveforms are fine enough that we can see the presence of electronic noise. Notice that the waveform has an exponential tail. The tail comes from the preamps' high-pass filters and serves to reset the signal amplitude to the voltage baseline after each detection. Details of how the waveforms are processed are the subject of Ch 5.

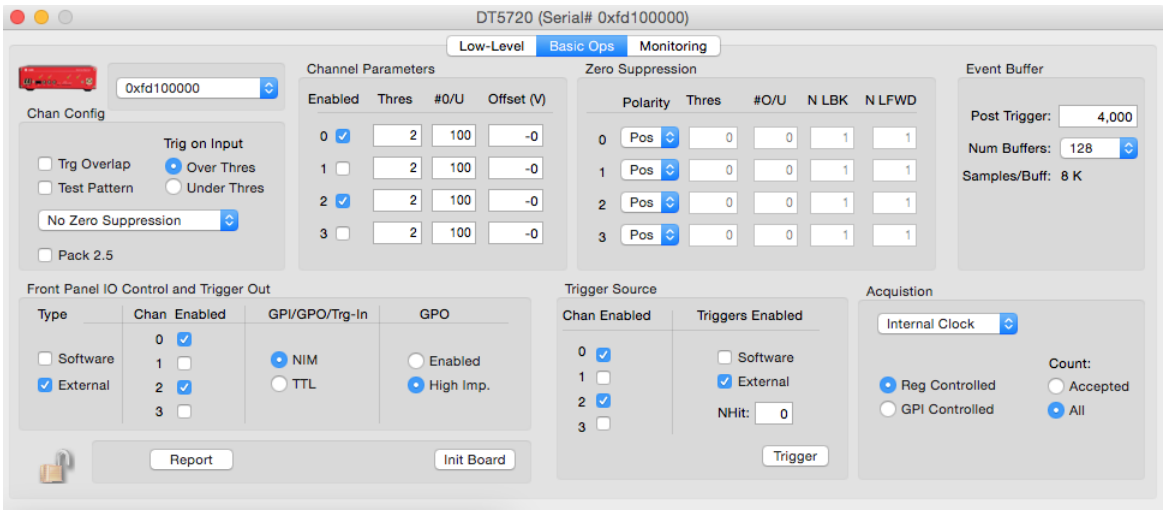

Figure 4.2: ORCA digitizer setup for TRIMS. The setup shows that we only activate digitizer channel 0 and 2 and that we use an external trigger.

While displaying real-time waveforms can be convenient, the oscilloscope does the same thing. To us, the main advantage of ORCA's real-time display is that it provides time traces of the slow-control data. The time trace is updated once every second. The real-time display was how we found out that the micro-discharge events corresponded to pressure spikes, which eventually allowed us to debug our HV system (Sec. 2.1.3). The ORCA software also has an option to set alarms on these slow-control values. The alarms issue pop-up warnings whenever a slow-control value passes a pre-determined threshold. We use the alarms to

make sure our hardware is under normal conditions when we are taking data. More details on the slow-control readout are provided in Sec. 4.3.1.

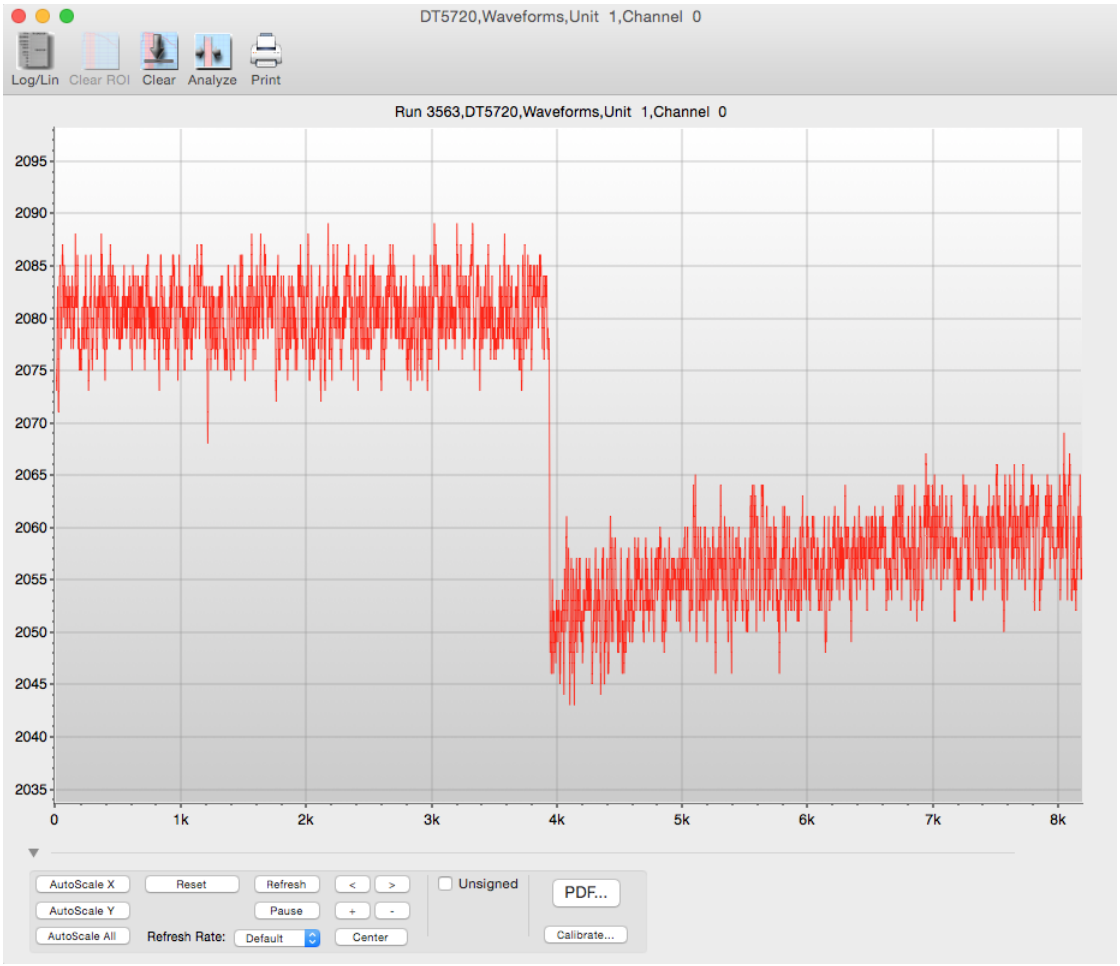

Figure 4.3: Sample ORCA waveform. The red trace represents the waveform received from the digitizer. The x-axis shows time bin, while the y-axis shows the ADC bin. The particular waveform comes from channel 0 for the beta-detector. Further details on the format can be found in [173].

4.1.2 Acquisition Rate and Storage

With two active digitizer channels, the maximum available acquisition rate is 500 waveforms per second from the detectors. This upper limit comes from the USB connection between the DAQ computer and the digitizer; the configuration has a maximum data transmission rate of 30 Mb/s. If the event rate passes the limit, ORCA would display a "buffer full" message while the digitizer would drop the excess events. For this reason, when we are taking tritium-data, we target an event rate of 200 Hz so that we do not trigger "buffer full" due to Poisson statistics.

The signal data are only recorded during a run. Once a run completes, ORCA generates a file that contains the signal waveforms; we call this file a raw-ORCA-file. For a regular 300 s run for collecting tritium-data, the raw-ORCA-file generated is around 3 GB in size. The raw-ORCA-files are first stored in a designated 4 TB WD My Passport HDD hard drive that is connected directly to the DAQ computer (1^{st} column of Fig. 4.4). Then ORCA has a setup that automatically sends these raw-ORCA-files to a designated remote server hosted at CENPA called TRIMPOLINE (2^{nd} column of Fig. 4.4). The hardware of the TRIMPOLINE server is also connected to two 4 TB hard drives that are identical to the one connected to the DAQ computer. Other than the backup raw-ORCA-files saved in hard drives, TRIMPOLINE has a setup that sends the raw-ORCA-files to cloud storage once every 24 hr [174].

There is another remote server hosted at CENPA called ROCKS (3^{rd} column of Fig. 4.4). The ROCKS server is composed of computer clusters and is shared among several experiments at CENPA. However, an 8 TB hard drive was installed on ROCKS for TRIMS and the KATRIN group at UW, which allowed us to run heavy duty data analysis on ROCKS. More specifically, we run the ORCA-to-ROOT converter on ROCKS for the majority of our tritium-data (Sec. 5.4.1). The converted data (raw-ROOT-files) are then downloaded from ROCKS to yet another identical 4 TB hard drive. This hard drive can then be directly used by a personal computer for further analysis (4^{th} column of Fig. 4.4).

For the slow-control data, ORCA stores them in ASCII format on the DAQ computer

once every 10 s. A series of programming scripts have been written to transfer these data to a database hosted on TRIMPOLINE. Details on this topic are covered next in Sec. 4.3.1.

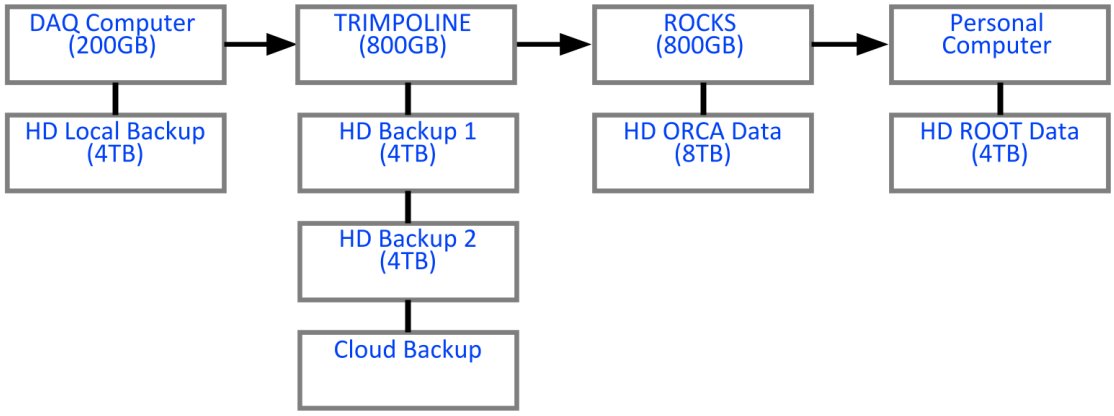

Figure 4.4: TRIMS data storage map. The arrows point in the direction where the data are transferred. Both TRIMPOLINE and ROCKS are remote servers hosted at CENPA that support the TRIMS experiment in terms of data storage and data analysis.

4.2 Tritium Runs

4.2.1 Run Procedures

While the run procedures vary depending on what type of data we are taking, we have standard procedures for taking tritium-data [156]. The procedures start out from the system in its maintenance configuration: the main-vacuum system is being pumped by the getter (or the ion pump) and has its pressure read by the ion gauge. In this configuration, the valves that are opened are AV2 (or AV6), AV3, AV5, and AV8 (Fig. 2.8). The rest of the valves start out closed. Note that with AV8 open, tritium gas has already been released to the region enclosed by valves SV1, CV3, SV2, LV1, and AV7. The preamps are also biased, but their batteries are being charged; the chargers need to be unplugged to avoid ground loops when taking data. The detectors are centered, cooled, and biased. Recall that the ion-detector is centered at the home-position (Sec. 2.5.5), and a micrometer is used to set the X-position of

the ion-detector, i.e. the scan-position. Starting from this initial configuration, the standard tritium data-taking procedures can proceed as follows:

Standard Data-Taking Procedures [156]:

Checking the system:

1. Make sure CO_2 is flowing for the JT-coolers

2. Make sure the ion-detector is centered at the home-position of (0.305 in, 80 mm)

3. Make sure the preamps are charged

Running the system:

4. Unplug the preamps from their chargers

5. Fill the cold trap

6. Turn on the SRG

7. Ramp up the magnets slowly, i.e. tuning the magnet power supplies to 52% each

8. Ramp up HV slowly to 60 kV, while watching the oscilloscope to see if breakdown happens

9. Take a 300 s background-run at the home-position and fill in a row of the manual-entry database (Sec. 4.3.2)

10. (T2-run) Turn off the ion gauge and valve off the gauge tree (close AV5)

11. Valve off the getter (close AV2) to stop it from pumping on the main system

12. Screw open the leak valve (LV1) 2.25 turns. Add T_2 until the detector signal count rate showing up on the oscilloscope is about 200 Hz

13. (HT-run) Turn off the ion gauge, take three 300 s conversion-runs at the home-position, and fill in a row of the manual-entry database for each run. Note that the gauge tree is still open to the main-vacuum system, and the ion gauge is converting T_2 to HT

14. Take a 300 s run at the home-position and fill in a row in the manual-entry database

15. Take a run at the next scan-point ($d = 1$) at (0.315 in, 80 mm), and take a run for every 0.01 in increment of the micrometer until ($d = 10$) at(0.405 in, 80 mm). Each run lasts 300 s and is recorded by a row in the manual-entry database

16. Valve open the getter (open AV2) to pump down. Use this time to top off the cold trap and move the ion-detector back to the home-position

17. Repeat Step 11 to 13

18. Repeat Step 14

19. Take a run at the next scan-point ($d = -1$) at (0.295 in, 80 mm), and take a run for every 0.01 in decrement of the micrometer until ($d = -10$) at (0.205 in, 80 mm). Each run lasts 300 s and is recorded by a row in the manual-entry database

20. Repeat Step 16. There is no need to refill the cold trap after the last run of the day

21. Repeat Step 11 to 20 if time allows to complete all these steps

Shutting off the system:

22. Valve open the gauge tree, and turn on the ion gauge

23. Ramp down HV and the magnets slowly, and then ground the system

24. Reconnect the preamps to their chargers

25. Turn off the SRG

26. Record the activity in the ELOG [175]

We refer to a run using the T_2 source as a T2-run and the HT source as a HT-run. As a quick reminder, the HT source is obtained by introducing T_2 gas to the ion gauge, whose iridium component acts as a catalyst that converts T_2 to HT (Sec. 2.3.2). Whether to valve off the ion gauge or not is what differentiates the procedures for taking a T2-run from a HT-run: Step 10 is only carried out for a T2-run and Step 13 for a HT-run. The conversion-runs taken in Step 13 are the buffer to ensure that the runs taken after the conversion-run have desirable HT purity (later in Fig. 7.10). Note that the T_2 source used for the T2-runs was not pure and the purity dropped over the year of our data-taking. However, the T_2 purity was above 50% for all the T2-runs we took, and we had sufficient statistics for T_2 events. In fact, we never had to open valve CV4 for more T_2; the amount of T_2 gas trapped in between CV3 and CV4 was all we needed for the experiment.

Since we cannot use the ion gauge for the T_2 source, we rely on the SRG to measure the pressure of the main-vacuum system during runs. Once we valve off the getter pump, the pressure starts to rise due to surface outgassing (Fig. 4.10). If the pressure gets too high, we risk HV discharge. So we set a safe practical threshold of 10^{-5} Torr before we pump down with the getter and restart the tritium filling process in Step 12. This set a time limit of around 80 min until each refill (Sec. 2.3.2).

During this 80 min, we need to take a run-scan (same term as defined in Sec. 2.5.5), i.e. a series of runs carried out in Step 14-15 (right-scan) or Step 18-19 (left-scan), where we vary the ion-detector's position. Each run-scan contains 11 runs, covering all scan-points

of either a left- or right-scan. The conversion runs are not included in a run-scan. The scan is required later in the analysis (Sec. 8.1). We scan the ion-detector in the X-direction (Sec. 2.1.2) because we can do that using a micrometer; the micrometer provides more precise positioning and finer scan steps (Sec. 2.5.4). The step size is determined such that we can complete a full half scan (left- or right-scan) in an 80 min period with enough statistics at each scan-position.

The home-position is the reference position shared between the left-scan and the right-scan. Every run-scan must contain a run at the home-position because each tritium fill may not necessarily provide the same event rate. We rely on the so-called ion-incident event counts to normalize the rate (Sec. 7.1.4).

Finally, to document what data we are taking, a manual-entry database is available for recording the configuration for each run (Sec. 4.3.2), and an ELOG [175] server is available for summarizing the overall activities of the day. Also a reference of the run numbers is provided in App. A.

4.3 Data Quality

Other than the signal waveforms from the detectors, we have collected other forms of data for quality control. These data are saved in the slow-control database, manual-entry database, and also in the raw-ORCA-files alongside the waveforms. The data tell us about the conditions of each run so that we know which runs are to be included in the final analysis. The qualified runs are record in a spreadsheet for easy reference.

4.3.1 Slow-Control Databases

Notice that the slow-control data need to be calibrated too. The calibration information is taken from each device's user manual and is manually uploaded to a table different from Table 4.1 that is in the same database. The format of the calibration table is such that we can update the calibration parameters by adding a new row. To illustrate how these simple calibrations are done, take `hv_v` as an example. The recorded `hv_v` readout needs

another factor of 8000 to be converted to a HV reading in kV; this factor of 8000 is what is recorded in the calibration table. The ion gauge pressure is a little special because of its wide available range, but the pressure readout in Torr can be easily obtained by $a \times 10^b$ given `p_ig_coeff` as a and `p_ig_exp` as b. A `C++` script based on ROOT [176] is responsible for reading both of the tables on the slow-control database and generating a time series plot for each calibrated slow-control parameter. One quick note is that, in order to read `PostgreSQL` using ROOT, we need the flag `-enable-pgsql` upon installing ROOT. It enable classes with headers "TSQL" that interface between ROOT and databases on a remote server.

Column Name	LabJack No.	Channel	Description
`time`	Timestamp		
`hv_v`	U12. No.1	AI0/AI1	HV power supply voltage
`hv_i`	U12. No.1	AI2/AI3	HV power supply on/off
`p_ig_coeff`	U12. No.1	AI4/AI5	Ion gauge pressure coefficient
`p_ig_exp`	U12. No.1	AI6/AI7	Ion gauge pressure exponent
`p_cep`	U12. No.2	AI0/AI1	Pirani gauge pressure
`p_ip`	U12. No.2	AI2/AI3	Ion pump pressure
`mag_status`	U12. No.2	AI4/AI5	Magnet on/off
`mag_hall`	U12. No.2	AI4/AI5	Magnet field strength
`diode_v`	U12. No.2	AI6/AI7	HV divider current
`srg`	U6.	AI0/AI1	Spinning rotor gauge pressure
`neg_hv_v`	U6.	AI2	Negative HV power supply voltage
`neg_hv_i`	U6.	AI3	Negative HV power supply on/off

Table 4.1: Slow-control database column names. Refer to Sec. 2.6 for the description of the devices in each entry.

The thermocouple data are stored as yet another table in the slow-control database. This is because we do not need the data other than during bake-outs. The specific calibration for the thermocouples is done using a heuristic linear function fit to the readout voltage versus temperature relation for type-K thermocouples [177]. The calibration is directly done in ORCA because ORCA has a convenient option to apply a fixed scalar multiplir to the readout. Again, the calibrated thermocouple data can be read out by the ROOT script, which in the end generates Fig. 2.9.

4.3.2 Manual-Entry Database

Other than the slow-control database, there is another database on TRIMPOLINE called the manual-entry database. We use this database to record run configuration information that cannot be automatically recorded. After each run, the person who took the data is also responsible for filling in a row of the manual-entry database [156]. To ease the process, we can fill in the entries to a webform hosted by CENPA [174]. Moreover, the webform is set up so that the default value of each entry inherits from the previous submission, which make it convenient to submit multiple runs that have similar configurations. The columns in the manual-entry database are listed in Table 4.2.

Column Name	Description
`id`	ID provided for each row entered into the database
`modtime`	Timestamp when the entry is submitted
`orca_run_number`	Unique ID provided by ORCA for each run, and so it is unique to each raw-ORCA-file

notes	Additional notes to describe unusual observations of the run, e.g. noisy waveforms, or to describe what was misrecorded before the same database row is updated
ion_det_pos_x	Ion-detector scan-point (X-direction)
ion_det_pos_y	Ion-detector scan-Y-point
center_run	The orca_run_number of the home-position run in the same run-scan
beta_detector_position	Whether the beta-detector is centered or hidden
junk_run_checkbox	Check if the run should be abandoned
trims_run_log_number	The ELOG number where the run has been recorded
run_duration	Run duration in seconds
data_source	Source type: T2, HT, Kr, Am, pulser, background, and others.
valve_av1	Valve AV1 is open (=1) or closed (=0)
valve_av2	Valve AV2 is open (=1) or closed (=0)
valve_av3	Valve AV3 is open (=1) or closed (=0)
valve_av4	Valve AV4 is open (=1) or closed (=0)
valve_av5	Valve AV5 is open (=1) or closed (=0)
valve_av6	Valve AV6 is open (=1) or closed (=0)
valve_av7	Valve AV7 is open (=1) or closed (=0)
valve_av8	Valve AV8 is open (=1) or closed (=0)
valve_sv1	Valve SV1 is open (=1) or closed (=0)
valve_sv2	Valve SV2 is open (=1) or closed (=0)

valve_sv3	Valve SV3 is open (=1) or closed (=0)
valve_sv4	Valve SV4 is open (=1) or closed (=0)
valve_sv5	Valve SV5 is open (=1) or closed (=0)
valve_cv1	Valve CV1 is open (=1) or closed (=0)
valve_cv2	Valve CV2 is open (=1) or closed (=0)
valve_cv3	Valve CV3 is open (=1) or closed (=0)
valve_cv4	Valve CV4 is open (=1) or closed (=0)
valve_lv1	Valve LV1 is open (=1) or closed (=0)
cold_trap_status	The cold trap is filled (=1) or not (=0)
jt_cooler_pressure	Pressure of CO_2 applied on the JT-coolers
ion_jt_cooler	JT-cooling the ion-detector (=1) or not (=0)
magnet_ps_1	Magnet power-supply reading for the inner coils
magnet_ps_2	Magnet power-supply reading for the outer coils
and_or_logic	Coincidence trigger logic set to AND (=1) or OR (=0)
mesh_bias_voltage	Mesh ion-electrode bias voltage
ion_detector_bias_voltage	Ion-detector bias voltage
ion_detector_amplifier_gain	Shaping-amplifier gain for the ion-detector trigger
ion_detector_discriminator_threshold	Discriminator threshold in ADC for the ion-detector trigger
beta_jt_cooler	JT-cooling the beta-detector (=1) or not (=0)

beta_detector_bias_voltage	Beta-detector bias voltage
beta_detector_amplifier_gain	Shaping-amplifier gain for the beta-detector trigger
beta_detector_discriminator_threshold	Discriminator threshold in ADC for the beta-detector trigger

Table 4.2: Manual-entry database column names [174, 178]. The detector position scan-points are defined in Sec. 2.5.5. Refer to Fig. 2.8 for the valve labels, and Sec. 2.5.2 for the detector system setup.

If some of the columns are entered incorrectly, they can be corrected by submitting a new webform that is applied to the same `orca_run_number`. Then, if we want to access the manual-entry data for the run, we select the latest row for that run (Sec. 4.3.4). When submitting a correction, we are also required to fill in the column `notes` to describe what the correction is about.

Since we are scanning our ion-detector position (Sec. 4.2.1), the columns `ion_det_pos_x` and `ion_det_pos_y` are the most vital entries in the manual-entry database. Recall that for every scan we do, we always included a run that is at the home-position as a reference between the left- and the right-scans (Sec. 4.2.1). For this reason, we include the column `center_run` so that every run can refer to the `orca_run_number` of the home-position run in the same scan.

After a series of runs, we also record our activities on ELOG. We have a dedicated ELOG logbook for data taking that is different from the ELOG logbook for our general updates. This ELOG server is also set up to have a webform that contains entries similar to that of Table.4.2. Items recorded on ELOG are much more general, which usually describe the activities done in the whole day instead of in a run-to-run basis. The ELOG entry is recorded by the column `trims_run_log_number` in the manual-entry database.

Finally, looking at the column `data_source`, we have 7 options to choose from. Label

"T2" and "HT" refer to runs using the T_2 and the HT source (Sec. 2.3.2). Similarly, "Kr" is for runs using the ^{83m}Kr source (Sec. 2.3.3), "Am" for runs using the ^{241}Am sources (Sec. 2.3.4), "Pulser" for runs using the pulser input (Sec. 2.5.1), and "Background" for HV runs with no sources. The "others" usually refer to test runs.

4.3.3 Timestamp-Table and Voltage-Table

Beside the signal waveforms that take a while to process, the raw-ORCA-files contain other useful data that can be quickly acquired. One such item is the timestamp for each run. We have a code that reads through all the raw-ORCA-files and generates a ACSII file called the timestamp-table, whose columns are provided in Table 4.3. Each row of the timestamp-table corresponds to a run and so a raw-ORCA-file. Based on the column `timestamp_init` and `timestamp_fin`, the timestamp-table tells us when each run is taken and the duration of the runs to an accuracy of a second.

The table also provides in the column `tot_event_number` the accumulated number of events in each run, which helped us track our progress in data collection. Overall, we have collected roughly 4.5 M events for both T2-runs and HT-runs in the year 2018. Nonetheless, the counts are based on OR-logic (Sec. 2.5.2), while we are most interested in coincidence events. And so, counts according to `tot_event_number` are only very rough estimations.

Column Name	Description
`run_number`	Unique ID provided by ORCA for each run
`timestamp_init`	Timestamp recorded for the first event of the run
`timestamp_fin`	Timestamp recorded for the last event of the run
`tot_event_number`	Total number of events in the run

Table 4.3: Timestamp-table column names. The entries to the table are obtained by reading the ORCA-files described in Sec. 4.1.2.

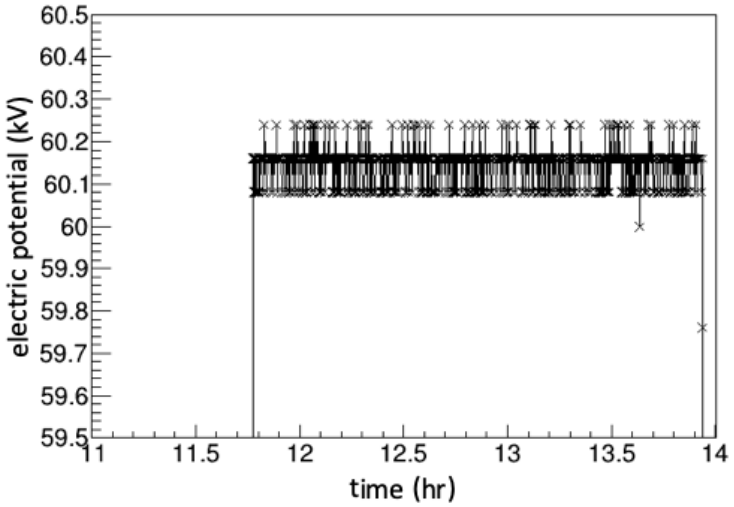

Figure 4.5: Sample slow-control HV voltage. The time window is chosen to include a data-taking session so that we can see the ramped up HV to 60 kV from 11:45am to 2:00pm local time.

Column Name	Description
`run`	Unique ID provided by ORCA for each run
`meanHV`	Average of the entry `hv_v` (kV) from Table 4.1 for the run
`stdHV`	Standard deviation of the entry `hv_v` (kV) from Table 4.1 for the run
`meanNHV`	Average of the entry `neg_hv_v` (kV) from Table 4.1 for the run
`stdNHV`	Standard deviation of the entry `neg_hv_v` (kV) from Table 4.1 for the run

Table 4.4: Voltage-table column names [167]. The values of the entries in this table are derived from referring to both Table 4.1 and Table 4.3.

We find multiple occasions when referencing to the timestamps in the timestamp-table

comes in handy. One such occasion is to relate each run to the slow-control database. Recall that the slow-control database is being filled regardless of whether we start a run or not. But if we know the timestamp of a run, then we can find the corresponding slow-control information on the slow-control database. Figure 4.5 provides an example where the HV voltage (calibrated `hv_v` from Table 4.1) is plotted against time. Based on the timestamp, we are able to find the time window when we ramped up and down the HV, because in between was when we took the runs.

Notice from Fig. 4.5, the HV slow control does not have enough resolution to resolve the noise in voltage; the voltage only fluctuates between 3 different values. This is the reason why we generate the voltage-table, whose columns are provided in Table 4.4. The table records the average voltage in between `timestamp_init` and `timestamp_fin` of the timestamp-table for each run. The voltage-table also includes the standard deviation of these voltage values as well as the data from the negative HV (calibrated `neg_hv_v` from Table 4.1). This voltage information is indispensable in order to correctly implement our energy calibration (Sec. 5.2.2) and the so-called mass-reconstruction (Sec. 6.2.2).

4.3.4 Tritium-Data Spreadsheet

Finally, to determine the quality of each run, we generated a spreadsheet by distilling the tables that have been presented in this section so far. We call it the tritium-data spreadsheet, whose columns are provided in Table 4.5.

Column Name	Description
`data_source`	The entry `data_source` from Table 4.2; the source types are converted into integers: 1: T2, 2: HT, 3: Kr, 4: Am, 5: pulse, 6: background, and 7: others
`orca_run_number`	The entry `orca_run_number` from Table 4.2
`ion_det_pos_y`	The entry `ion_det_pos_y` from Table 4.2
`ion_det_pos_x`	The entry `ion_det_pos_x` from Table 4.2
`center_run`	The entry `center_run` from Table 4.2
`junk_run_checkbox`	The entry `junk_run_checkbox` from Table 4.2
`note`	The entry `note` from Table 4.2
`total_event_number`	The entry `total_event_number` from Table 4.3
`run_duration`	Time duration of the run calculated using (`timestamp_fin` − `timestamp_init`) from Table 4.3
`day_since_2018`	Day since 2018 (Jan 1st, 2018 is day 1) obtained using `timestamp_init` in Table 4.3
`quality`	Quality of the run. This entry is mostly related to the fuzzy runs described in Sec. 6.1.4

Table 4.5: Tritium-data spreadsheet. The spreadsheet includes only the tritium runs that go into the analysis. The spreadsheet has two versions: a Microsoft Excel file that is human-readable and an ACSII file that is intended to be read by the data analysis codes.

The columns are comprised mostly of the entries directly coming from the manual-entry database and the timestamp-table. The only exception is the column `quality`, which shows disqualified runs that we could only identify using the actual tritium-data. As it turns out, the `quality` entry is mostly tagging the so-called fuzzy-runs that will be discussed later in Sec. 6.1.4. These tags are hard-coded run-by-run back to the `Python` codes that generate

the tritium-data spreadsheet. To make it obvious that parts of the code are hard-coded, we isolate the record of the fuzzy-runs to their own `Python` file, which also makes updating the fuzzy-runs much more straightforward.

Filter	Description
`junk_run_checkbox` $\neq -1$	The run is not labeled as a junk run
`data_source` $= 1$ or 2	Choose source T2 or HT only
`ion_det_pos_y` $= 80$	The scan-Y-position is fixed; analyzing only the scan of the ion-detector in the X-direction
`ion_det_pos_x` $= 0.205, 0.215, ..., 0.405$	Only include ion-detector x-position in between 0.205 and 0.405 in with a step size of 0.01 in
scan run	Select only the series of runs where the ion-detector is being scanned

Table 4.6: Filters for the tritium-data spreadsheet. These filters are applied on the manual-entry database to trim out the runs in the spreadsheet.

The spreadsheet is generated using `Python`'s `psycopg2` and `Pandas` package. We use `psycopg2` to query the databases and `Pandas` to manage the data structure of the received data. For instance, we use `Pandas` to convert source types in the column `data_source` into integer values. But more importantly, the versatility of the `Pandas` toolkit allows us to impose the filters from Table 4.6 on the data. The filter in the first row simply filters out all the runs that are marked as "junk-run", while the second focuses our data set on T2-runs and HT-runs only. The choices of `ion_det_pos_y` and `ion_det_pos_x` have already been covered in Sec. 4.2.1. The "scan run" condition excluded the runs when the ion-detector

stayed at the home-position, i.e. when we did not scan the ion-detector. The conversion-runs mentioned in Sec. 4.2.1 are also filtered out in this case. Notice that the fuzzy-runs identified via `quality` in Table 4.5 are still included in the spreadsheet. We will cut them out later (Sec. 6.2.3), but decide to leave them visible in the spreadsheet.

The `Python` code always generates two versions of the tritium-data spreadsheet. The first version is in a Microsoft Excel file that is easily readable by humans. The second version is in an ACSII file that is read by code to include only the qualified runs in the data analysis (Sec. 6.2.3).

4.4 Run Conditions

Aside from the quality of our physics data, we also would like to examine our run conditions that including uniformity and stability of the electric and the magnetic field, and the pressure of our system. Although these run conditions may not directly impact the quality of the data, we need to make sure they are under control.

4.4.1 Field Stability

The electric field stability over time has already been shown in Fig. 4.5 via the HV slow-control reading. The small effect of HV instability on data is also handled in Sec. 4.3.3.

As for the magnetic field stability, we took an overnight measurement using a Hall probe taped onto the radial inner wall of one of the coils. The slow-control `mag_hall` reading (Table 4.1) is shown in Fig. 4.6. The reading shows the stability of the magnetic field is finer than a resolution of 0.01 Tesla (the Hall probe holds 2 significant digits for the slow control) for much longer than our typical data-taking session that lasts 4 hr. This stability is sufficient for our experiment.

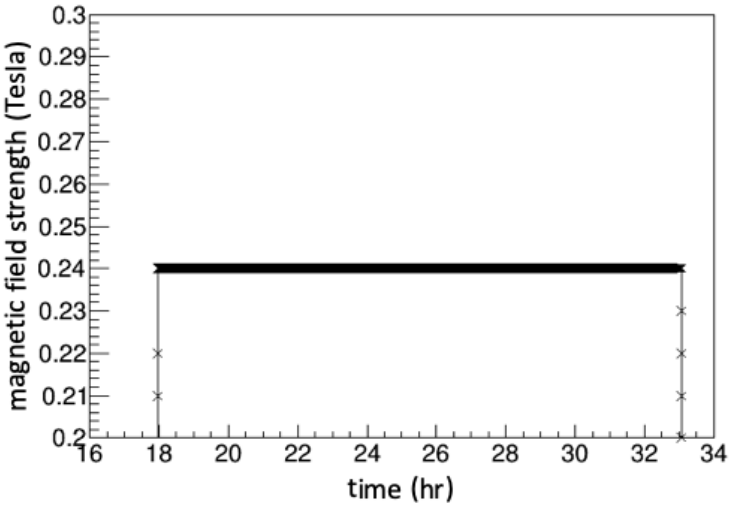

Figure 4.6: Slow-control Hall probe magnetic field strength. This is an overnight stability test; the stability is finer than a resolution of 0.01 Tesla.

4.4.2 Field Uniformity

For the electric field uniformity, we based the result on the COMSOL simulation (Sec. 3.3) as shown in Fig. 4.7. The x-axis of the plot represents the Z-position of the chamber geometry (Sec. 2.1.2). The range of the plot goes from the beta-electrode on the left to the ion-electrode on the right. The blue curve is the electric potential in kV, while the green curve is the electric field strength derived from the potential. The field strength is scaled down such that both curves can be shown in the same plot. However, what matters is that the field strength is roughly constant across the decay chamber. Although the COMSOL simulation is based on an ideal construction, e.g. the mesh ion-electrode is simulated by a solid metal disk, the uniform result gives us confident in our NEC decay chamber setup.

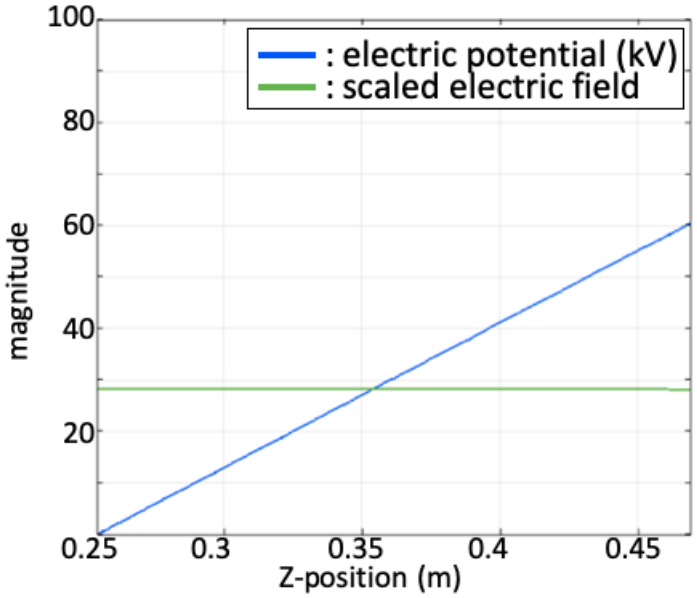

Figure 4.7: COMSOL simulation of the electric field strength across the chamber. The x-axis is the Z-position of the chamber geometry (Sec. 2.1.2), and the range is exactly the length in between the beta-electrode and ion-electrode. The measurement in the simulation is taken at the central axis of the chamber, and the electric potential goes from 0 to 60 kV (blue curve). The electric field strength (green curve) is scaled down such that the two curves can be plotted together; its absolute strength is not what we are looking for. The linearity of the two curves shows the electric field uniformity of our setup.

To assess the magnetic field uniformity, we scan a vertical Hall probe across the bore of our four-coil magnet setup. To do that, we screwed down two metal rulers on the frame of the magnets such that the rulers were attached face to face with the coil on the beta-side. These rulers helped us measure the radial position from where we scanned. Then we set a metal pole through the bore of the magnets. The pole sat on the ruler on the beta-side and was held up on the ion-side by an aluminum stand fixed on the railway stand (Sec. 2.4.2). The pole's vertical alignment was attained using a level, while the horizontal alignment was eye-balled. The Hall probe was fixed inside a solid Teflon pipe that moved along the pole.

The Z-position of the Teflon tube was accessed using a tape measure.

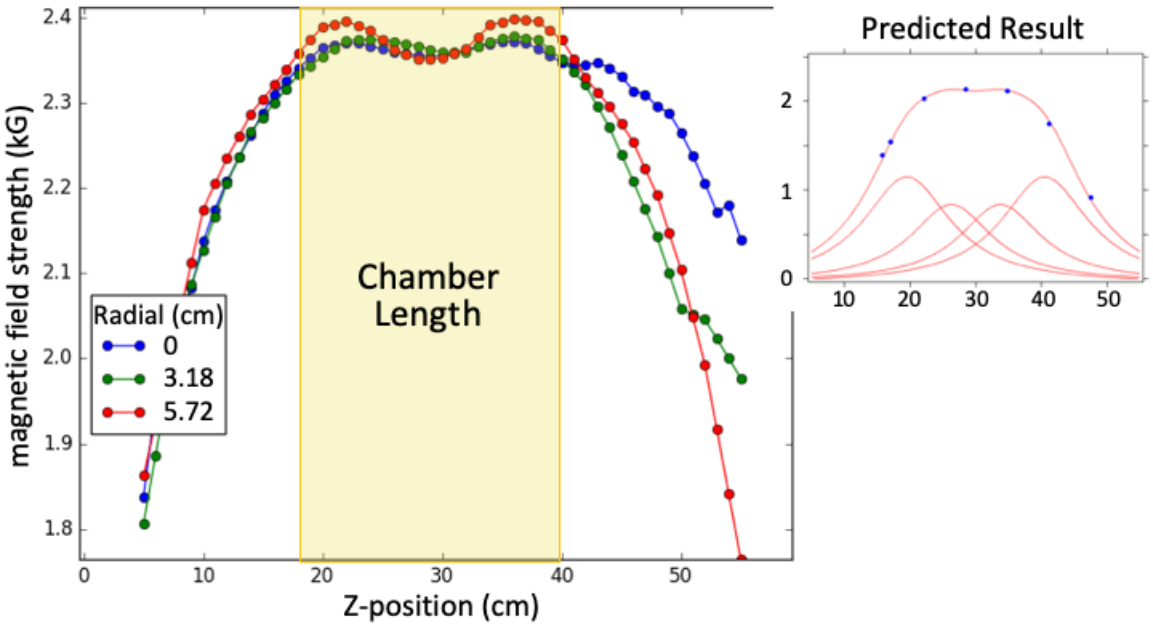

Figure 4.8: Hall probe measurement of the magnetic field strength across the chamber [179, 41]. The x-axis is the Z-position of the chamber geometry (Sec. 2.1.2); the chamber region is shaded in yellow. The y-axis represents the magnetic field strength in kilogauss (1 kilogauss = 0.1 Tesla). The data is collected by scanning a Hall probe across the physical decay chamber. The different color scheme represents the offset in Y-direction from the central axis as we scanned the probe. The top-right plot is the predicted field strength considering our magnet coil setup (Sec. 2.4.2).

Using the setup, the data obtained is given by Fig. 4.8. The x-axis is again the Z-position (Sec. 2.1.2). The region inside the magnet that the decay chamber covers is shaded in yellow. The circle data points are the magnetic field strength measured at each Z-position. Note that the data were taken directly from the readings on the Hall probe, which was stable up to 3 significant digits. The different color of the data points indicates their radial positions as shown in the legend. Recall that we are only scanning our ion-detector up to 10 mm

(Sec. 4.2.1), so the blue data points are the most relevant ones. These blue points are uniform across the decay chamber at 0.237 Tesla up to roughly 1%*. The result matches the analytic prediction given on the top right of Fig. 4.8 that was made based on the current configurations of the 4 magnet coils.

4.4.3 Pressure Stability

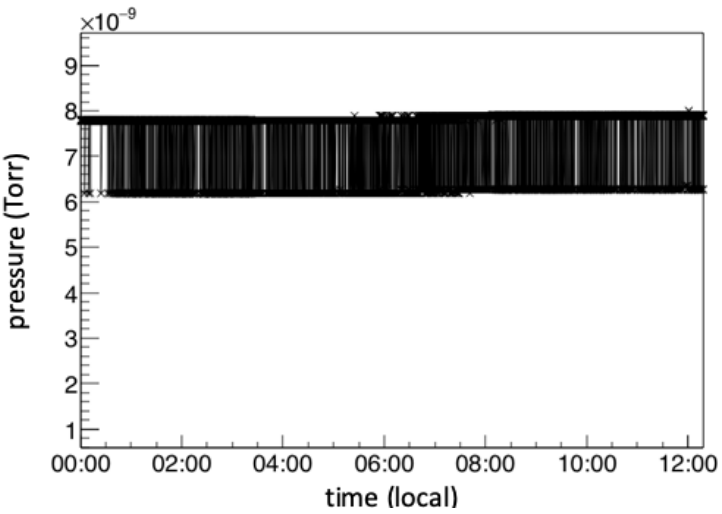

Figure 4.9: Slow-control ion gauge vacuum pressure. The data was taken on the same data as the last day of data taking in December (Fig. 6.9); the data-taking session took place in the afternoon. The pressure is stable at 10^{-9} Torr level when the TRIMS system is in the maintenance configuration (Sec. 4.2.1).

For the pressure stability, Fig. 4.9 shows the slow-control `p_ig` ion gauge pressure reading (Table 4.1). The figure shows the pressure was stable at 10^{-9} Torr level for 12 hr before our last afternoon of data taking. In this maintenance configuration, the main-vacuum system was being pumped by the turbo pump.

*We did not evaluate the exact standard deviation because we do not think this degree of non-uniformity would affect our final systematics.

Because we cannot rely on the ion gauge during data taking (Sec. 4.2.1), Fig. 4.10 shows the slow-control `srg` pressure reading for our SRG. Due to the residual H_2 [†], the pressure started to rise as soon as the main-vacuum system stopped being pumped. The pressure rises are shown by the two slopes in the figure; the slopes correspond to a right-scan followed by a left-scan as expected (Sec. 4.2.1). The pressure never reached 10^{-5} Torr and so never reached the charge-exchange limit that we derived previously (Sec. 2.3.2).

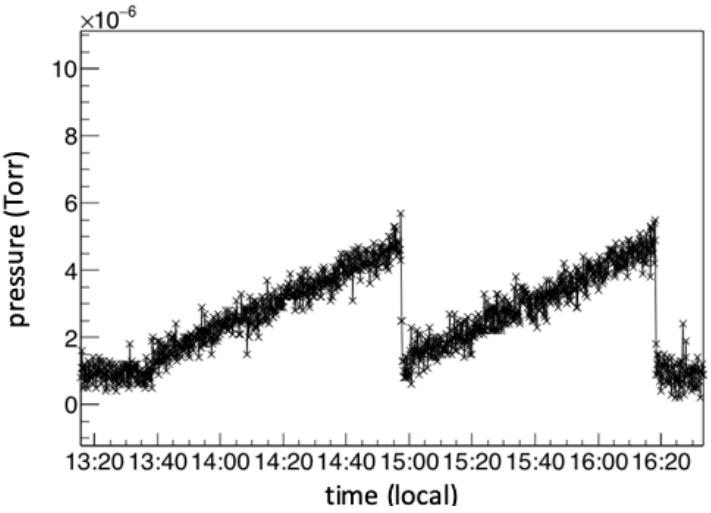

Figure 4.10: Slow-control SRG vacuum pressure. The data was taken during the last day of data-taking in December. The two rises in pressure correspond to a right-scan followed by a left-scan (Sec. 4.2.1).

[†]The residual H_2O is mostly removed by the bakeout Sec. 2.2.1.

Chapter 5
SIGNAL PROCESSING

This chapter covers how we extract physics information from signal pulses, which are the output of the beta- and the ion-detector as they detect incident particles. Since both of the detectors are silicon detectors, Sec. 5.1 gives a short summary about how these semiconductor devices work in general. The rest of the chapter focuses on the software signal-processing chain. Section 5.2 describes the method we used to derive the kinetic energy of an incident particle from the signal pulse, while Sec. 5.3 describes the method to obtain the arrival time. Finally, Sec. 5.4 covers how the overall signal-processing chain is put together, which includes the sequence of when the processes are carried out as well as the plan of how the resulting data are stored.

A note on the terminology is that a "fit" here refers to fitting the data to a function using the least-square method provided by ROOT. The ROOT library also provides the standard errors of the fit parameters as well as the chi-square over DOF (χ^2`/dof`) for the goodness of fit.

5.1 Semiconductor Detector Physics

Semiconductor detector physics is a rich topic on its own. This section only provides a brief overview, while in-depth discussion can be found in [141] and [157].

5.1.1 Charge Signal

A semiconductor detector is essentially a reverse-biased pn-junction, which creates a wide depletion region that extends out from the junction. The electric field is strong inside the depletion region, which results in a limited number of free electron-hole pairs; under reverse

bias, the pn-junction is functionally equivalent to a capacitor [180]. When a particle enters from one side of the junction and reaches into the detection region, it ionizes crystalline lattices, giving electrons enough energy to jump from the valence band to the conduction band of the semiconductor device, and thus creates electron-hole pairs inside the detection region. These electron-hole pairs result in a charge drift across the detection region that produces the electric signal for the detector, similar to the one shown in Fig. 4.3. A strong reverse bias is needed to ensure that these charge carriers drift quickly enough that they are not lost via trapping or recombination. This is important because the number of electron-hole pairs generated (Q_s) is proportional to the kinetic energy of the incident particle (E_{inc}):

$$Q_s = \frac{E_{inc}}{E_i} q, \tag{5.1}$$

where q is the unsigned single electronic charge and E_i is ionization energy. Because the overall signal charge collected corresponds to the signal pulse's amplitude, if we wish to use the amplitude to derive E_{inc}, we want the charge collected to be as close to Q_s as possible. Notice that E_i is not simply the band gap energy of the semiconductor material. Take silicon for example: its E_i is around 3.6 eV, which is significantly greater than its 1.12 eV band gap. The rest of the energy goes into phonon excitation. The statistical fluctuations in the number of charge carriers, which can be described by the uncertainty in E_i due to the uncertainty in phonon excitation, contribute to what is called the Fano noise to the detector resolution. The Fano noise is at a level of 0.1 keV [157], which is small compared to our energy range of interest (Sec. 5.3.5).

Compared to other types of detectors such as gaseous ionization detectors, semiconductor detectors have a number of advantages. Despite the Fano noise, semiconductor detectors have high energy resolution due to their small ionization energy. Semiconductor detectors also have relatively high timing resolution because the signal carriers are electrons that travel fast. Lastly, semiconductor detectors are compact and readily vacuum compatible, which make them the most suitable choice for a small scale experiment like the TRIMS experiment.

The following section covers some of the disadvantages in regard to silicon detectors.

5.1.2 Dead Layer, Pulse-Height Defect, and Radiation Damage

Because we are using silicon detector, we need to concern about the dead-layer effect that affects energy detection. The dead layer is the region outside the depletion region on the side of the pn-junction where particles are incident. Assuming the dead layer is completely dead, i.e. there is no electric field in the region, then the electron-hole pairs generated in the dead layer do not create charge drift. Only when an incident particle penetrates deep enough to reach the depletion region can it start to generate charge signals. In real life, the dead layers are never completely dead. If a dead layer is partially dead, a portion of the charge can still drift to the charge-collection region. Although the dead-layer charge-collection efficiency cannot be measured directly without specialized equipment, by matching the Monte Carlo simulation to the physical detected energy spectrum, it has been shown that the efficiency is roughly 50% for typical silicon detectors [168]. This collection efficiency is what we assumed in our SRIM simulation (Sec. 3.2). For ion detection however, the dead-layer effect has additional complications. Compared to electrons, ions have shallower penetration depth and so lose more energy to the dead layer. Moreover this penetration depth depends on the type of ion, which makes correction difficult because we do not know the type of detected ion a priori.

We also need to be concerned about the pulse-height defect, which is a collection of phenomena that explains why a heavier ion generates smaller signals than a lighter ion of the same energy. The dead-layer effect is only one of three contributors to the pulse-height defect. Another contributor is nuclear recoil at low energy. Because slow ions have larger de-Broglie wavelength, they are more likely to interact with the Si nucleus. And because of the relatively long time scale of the nuclear recoil process, no electrons are emitted while the electrons of the Si atom reconfigure. In other words, nuclear collisions are not ionizing, but they contribute to energy lost to detection*. The final contributor is having a higher

*Notice that the electrons have much larger de-Broglie wavelength then the ions, but considering their mass and momentum, the electrons contribute negligibly to nuclear recoil.

recombination rate along the track of a heavier ion. Because a heavier ion travels slower given the same kinetic energy, it takes the ion a shorter distance to create the same number of electron-hole pairs. Therefore, this heavier ion will have higher electron-hole pair density along its path, which results in a higher recombination rate because the recombination rate increases with electron-hole pair density. This last contributor is insignificant to TRIMS however, because at an ion incident energy as low as 10s of keV, the number of electron-hole pairs generated is only on the order of 10^4. This is a small number compared to the doping level, which is typically much larger than $10^{10}\,/\mathrm{mm}^3$, and so difference in recombination rate is miniscule. To accommodate the other two contributors to the pulse-height defect, we used the SRIM simulation software to study the effect and applied the corresponding correction to the detected ion energy (see Sec. 3.2.2).

Other than issues about energy lost to detection, another concern for these silicon detectors is radiation damage. For these detectors to function under their intended performance, near perfect lattice structure is essential to keep E_i close to a constant and to prevent defects from trapping charge carriers. Creating electron-hole pairs alone does not damage the lattice. However, energetic particles may break the chemical bonds between the silicon atoms and damage the lattice. Moreover, energetic ions are implanted into the lattice and create defects. Over time, the detectors will have significant loss in their energy resolution. According to Canberra, their silicon detector has a threshold dose of $10^9\,/\mathrm{cm}^2$ alpha particles [148] and each of our detector has an active area of $0.5\,\mathrm{cm}^2$. For TRIMS, we had an accumulation of events on the order of 10^7 for tritium data. As for the krypton-data, we took our ^{83m}Kr calibration data without the electric field and only took up to an order of 10^5 events in the -4kV HV Kr setting. So we are significantly below the threshold for radiation damage.

5.2 Energy Measurement

When a particle is detected by one of the silicon detectors, the output electronic signal of the detector is converted into a digital waveform as shown in Fig. 4.3. The immediate first question to ask is, how do we obtain the incident energy from the waveform? Because the

amplitude of the waveform is associated with the energy, we first need a method to extract the amplitude. The method we used is called a double-trapezoidal filter (2TF), which is covered in Sec. 5.2.1. Then we perform a calibration explained in Sec. 5.2.2 to convert the amplitude to energy. Ideally, we would like the scale of this conversion, i.e. the gain, to be independent of the detected energy and to be stable over time. However, gain nonlinearity and gain shift are present in our system and Sec. 5.2.3 describes how we correct for them. Lastly, after some detector noise analysis in Sec. 5.2.4, we arrive at the energy resolution of our detectors in Sec. 5.2.5.

5.2.1 Double-Trapezoidal Filter

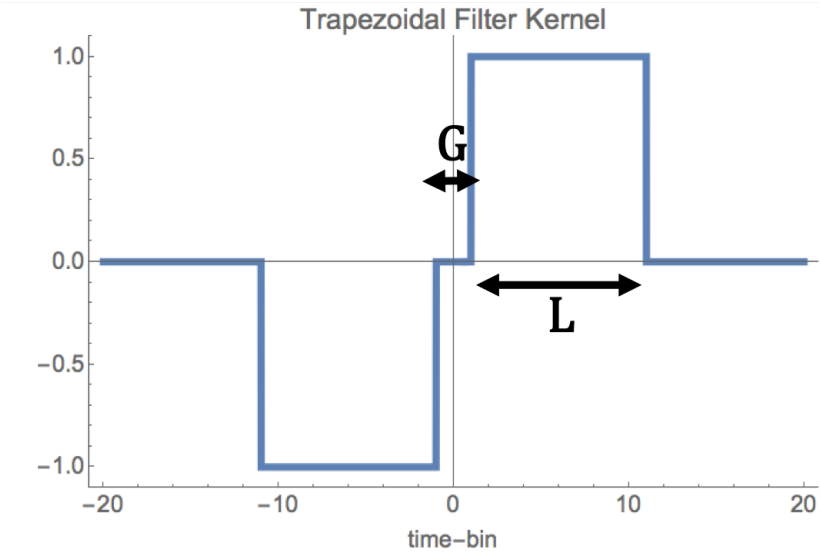

Figure 5.1: Sample trapezoidal filter kernel. The function is anti-symmetric about the origin. The parameter G stands for the gap length and L for the peaking length.

Compared to a CR-RC type analog filter [141], a double-trapezoidal filter (2TF) is a digital filter in the modern digital era that has great signal-to-noise performance. Detailed characteristics of the trapezoidal filter are covered in [181]; in this section, we focus on implementation.

The process starts with the waveform shown in Fig. 5.2 a). The goal is to obtain the amplitude of the pulse near the vertical blue dashed line, knowing that the amplitude is subject to noise. Notice the waveform is identical to the one in Fig. 4.3, but it is in the ROOT format and is inverted. The inversion is to match the sign of the convolution kernel. The convolution kernel we used is shown in Fig. 5.1 and in a formula,

$$S_i = \sum_{j=0}^{L} v_{i-j} - \sum_{k=L+G}^{2L+G} v_{i-k}, \tag{5.2}$$

where v_i is the digitized amplitude of the waveform at time bin i. The essence of the 2TF is to convolve the kernel in Fig. 5.1 with the waveform in Fig. 5.2 a). The kernel function is anti-symmetric about the origin and takes two parameters that have units in time bin. The parameter G (time bins) is the gap length, which should be only as wide as the waveform pulse's rise time, i.e. the number of time bins required only needs to cover the slope of the pulse at the blue dashed line in Fig. 5.2 a). The parameter L (time bins) is the peaking length (or peaking time). The kernel's shape shows that within each L the weight is either 1 or -1, which is designed to subtract off the baseline.

The waveform in Fig. 5.2 b) is obtained by convolving Fig. 5.2 a) with the filter kernel in Fig. 5.1. This is specific to the implementation, but the waveform in Fig. 5.2 b) is delayed by $L/2$; the first $L/2$ of the waveform are padded by 0's. The resulting waveform resembles a triangle more closely than a trapezoid. This is because the upper base length for the trapezoid is determined by G, which is small compared to L. Notice also the big fluctuation at the beginning of the waveform; data from that region cannot be used because they do not cover the entire range of the kernel. Next, a second kernel that has half the peaking length as the first and has no gap length is convolved with Fig. 5.2 b) to obtain Fig. 5.2 c), and thus the name "double-trapezoidal filter". The resulting waveform looks like a sine function and has a zero-crossing indicated by a vertical blue dashed line. If we match the time bin indicated by the vertical blue dashed line to Fig. 5.2 b), that is where the amplitude $A \times L$ of the trapezoid can be extracted. Note that this $A \times L$ needs to be divided by the peaking length L to arrive at the same scale in ADC as in Fig. 5.2 a). In other words, A is the pulse

amplitude we were looking for.

Notice if the zero-crossing is pushed earlier by $2L$, we can estimate the pulse timing shown by the vertical blue dashed line in Fig. 5.2 a). This method does not provide the optimal timing, however. The reason is that the 2TF is an integrating method that remove high-frequency information of the waveform, which is required to extract accurate timing*. An improved method for timing will be discussed in Sec. 5.3.2.

Another note is that there are actually several zero-crossings in Fig. 5.2 c) that correspond to much smaller amplitudes in Fig. 5.2 b). These small pulses were trimmed out by a software threshold of 2 ADC in pulse amplitude because they are coming from electronic noise.

A rule of thumb for trapezoidal filters is the wider the L, the better the filter is at handling noise. The cost of a wide L, however, is that the filter is then affected by the waveforms' exponential tails, which results in the average being smaller than the pulse amplitude*. The optimized values we obtained are $L = 700$ time-bins $= 2800$ ns for the beta-detector and $L = 550$ time-bins $= 2200$ ns for the ion-detector with both having $G = 20$ time-bins $= 80$ ns. This optimization is the subject of Sec. 5.2.5.

---

*The 2TF timing is also limited by the finite time-bin length of 4 ns.

*As we will see later in Sec. 5.2.5, the parallel noise plays a bigger role than the exponential tail in limiting the optimal peaking length.

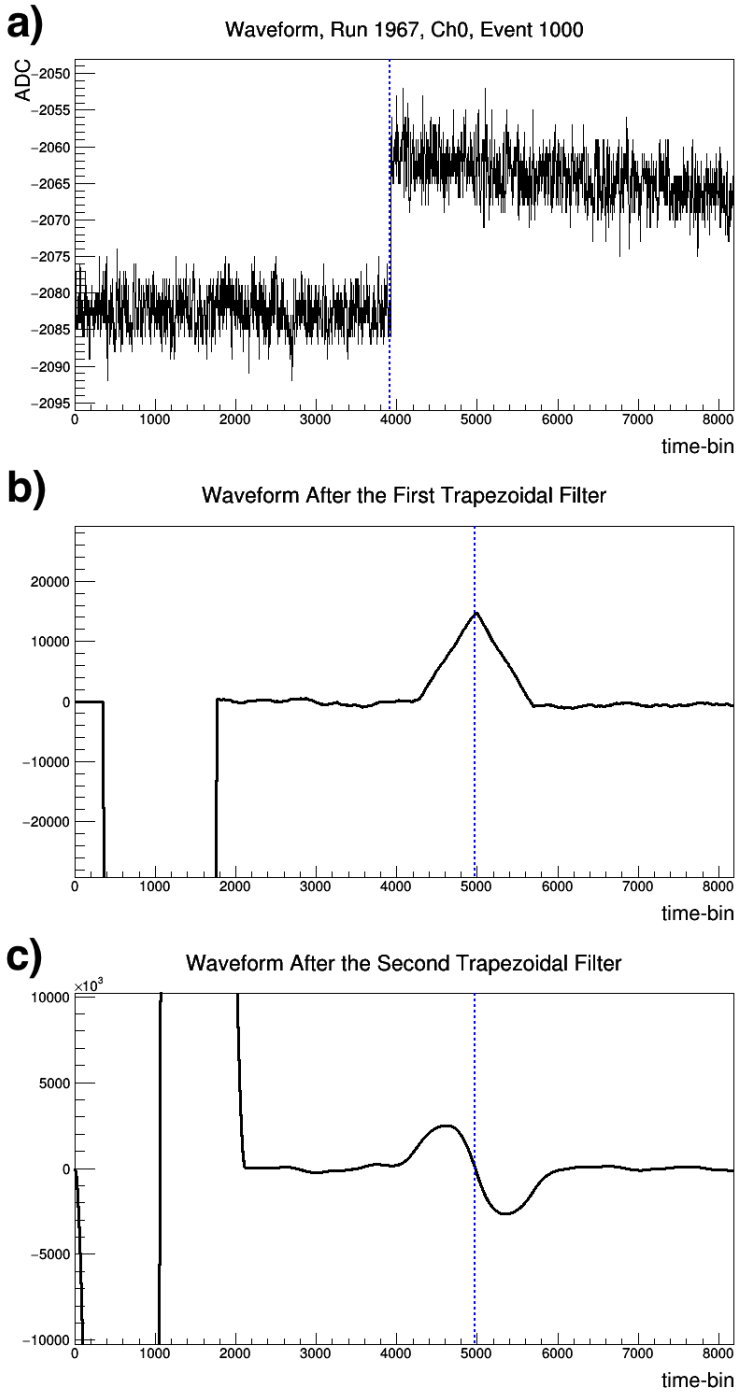

Figure 5.2: Waveform under a double-trapezoidal filter. Plot a) shows the original waveform. Plot b) shows the waveform after the first trapezoidal filter that is also delayed by $L/2$; the first $L/2$ of the waveform are padded by 0's. Plot c) shows the waveform after the second trapezoidal filter. The blue dashed lines indicate the timing from the zero-crossing of plot c). The timing from plot c) needs to be shifted earlier by $2L$ to match the pulse timing in plot a).

Pileups do happen when more than one big pulse passes the software threshold. The 2TF is good at resolving pileup events that are more than L apart from each other. In that case, only the pulse with the maximal amplitude is considered; we do not concern ourselves with these pileup events because TRIMS is not event-rate limited. The data-taking rate of TRIMS is at approximately 200 Hz, making pileup events very unlikely in a digitizer window of 25 µs. On the other hand, we are interested in 2-particle events that happen much closer together than L. Because trapezoidal filters cannot resolve these 2-particle events, we leave the discussion to Sec. 5.3.2.

5.2.2 Energy Calibration

To calibrate our detectors, we use several different sources. In part, they help with cross checking. But the main reason is that not every source is available for both the beta- and the ion-detectors; we use them according to their availability in different situations. As a note for this section, all the energy spectra in this section come from either the beta- or ion-detector alone; no detector coincidence-event selection is imposed. One more note is that none of these sources are sources of heavy ions, and so they cannot calibrate the dead-layer effect. These corrections are done in a later stage of the analysis that is covered in Sec. 6.1.2.

The first calibration source is ^{83m}Kr conversion electrons covered in Sec. 2.3.3. A sample spectrum in ADC unit is shown in Fig. 5.3. The ^{83m}Kr calibration is carried out with only the magnetic field and no electric field. So after an electron is emitted, it can travel to either the beta- or the ion-detector. The spectrum given in Fig. 5.3 comes from the ion-detector, but the beta-detector produces a nearly identical spectrum. The fitted Gaussian gives a mean of 21.98 ADC. The corresponding peak is actually a combination of channels IC L, M, and N from Table 2.2, which our detector cannot resolve. The combined peak has an average energy of 30.69 keV however, which allowed us to calibrate in this case to 30.69 keV/21.98 ADC =

1.396 keV/ADC for the ion-detector. *.

It is disadvantageous to use ^{83m}Kr calibration for taking tritium data however, because we would need to pump out a substantial amount of tritium stored in the gas-handling system to introduce ^{83m}Kr.

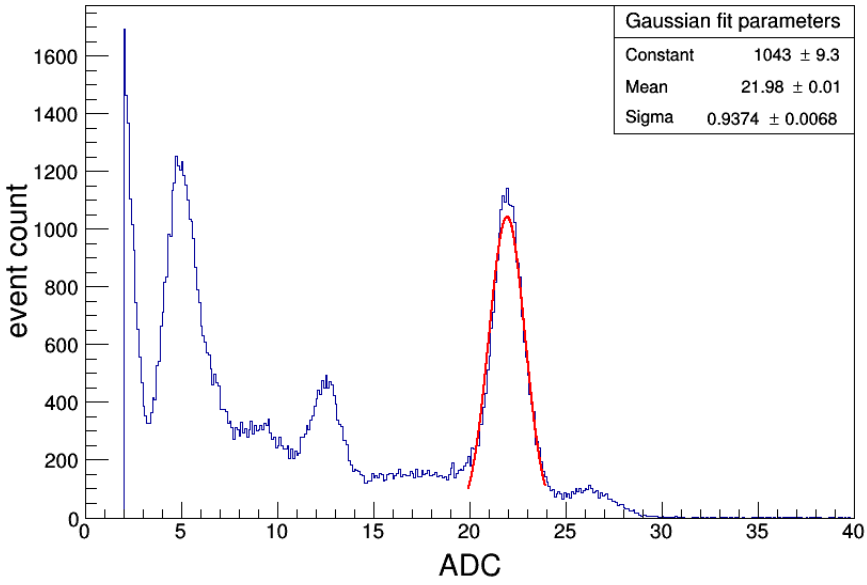

Figure 5.3: Sample ion-detector ^{83m}Kr spectrum histogram. This particular spectrum contains a total of 211,376 events taken in a span of 10 hr. The Gaussian peak is fitted to a combination of several IC electron peaks listed in Table 2.2 that are close to 30 keV. Our silicon detectors cannot resolve these peaks, but they average to 30.69 keV and are sufficient for calibration.

Figure 5.4 shows a sample spectrum of calibration using ^{241}Am gammas as described in Sec. 2.3.4. Neither the electric field nor the magnetic field are turned on for this calibration.

*The error on the calibration can be calculated using the error on the Gaussian mean. It is small compared to the error from the gain shift discussed in the next subsection and so will not be evaluated in this section.

The mono-energetic gammas give a cleaner calibration than electrons because gammas are not affected by the detector dead layer. This is why ^{241}Am was the primary source we used to obtain the intrinsic energy resolution of our detectors; the topic will be discussed shortly in Sec. 5.2.5. The particular spectrum in Fig. 5.4 gives 59.5 keV/47.3 ADC = 1.26 keV/ADC for the beta-detector.

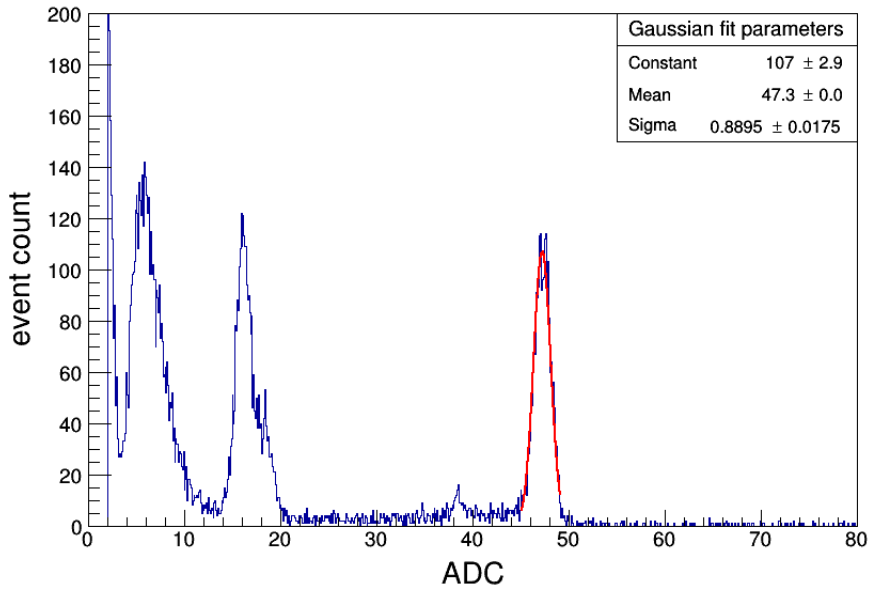

Figure 5.4: Sample beta-detector ^{241}Am spectrum histogram. This particular spectrum contains a total of 14,085 events taken in a span of 11 hr. The Gaussian peak is fitted to the 59.5 keV gamma line.

The trouble with using ^{241}Am is that it is a source external to TRIMS's main system. After the installation of the NEC decay chamber, the only line of sight to a detector is through the UV window. Hence, only the beta-detector could be calibrated via ^{241}Am in the new setup. Even then, the beta-detector is far away from the UV window such that hours are required to collect sufficient events. For instance, data in Fig. 5.4 took 11 hrs. Fortunately, the detectors' resolution was determined before the installation of the NEC chamber.

Both of the next two calibrations use the tritium source.

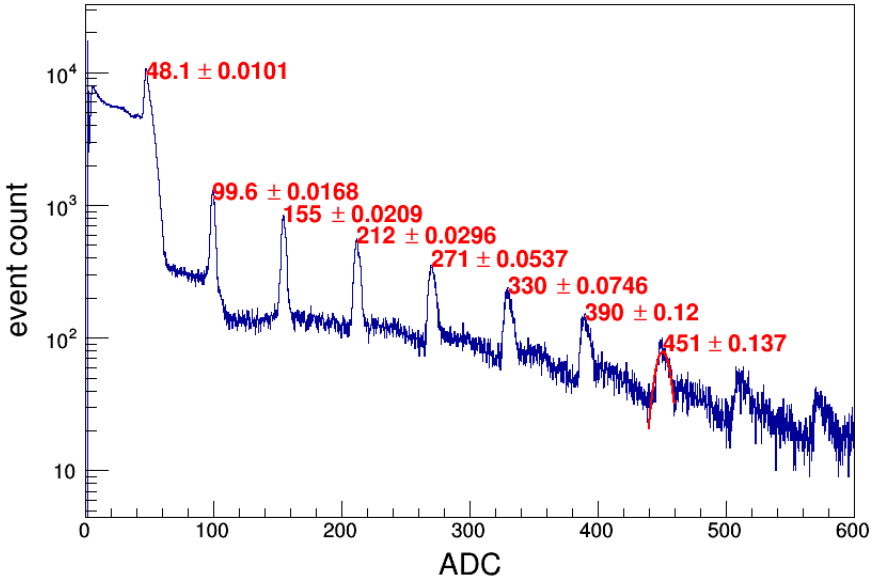

Figure 5.5: Sample beta-detector spectrum histogram from the mesh-electrons. This particular spectrum comes from the single-mode events of our first few tritium runs. The Gaussian peaks are fitted to integer multiples of 60 keV electrons, because the mesh usually emits multiple electrons at the same time. The red numbers show the means of the Gaussian fits and the error of their means.

While we were taking the tritium data, we discovered that the beta-detector spectrum shown in Fig. 5.5 had peaks at integer multiples of 60 keV. These come from groups of secondary electrons emitted from the mesh ion-electrode with small initial energy that reach the beta-detector at close to 60 keV each. The multiplicity can be explained by having multiple electrons emitted from the mesh that travel to the beta-detector at nearly the same time. We refer to these electrons as the mesh-electrons. Since we did not detect mesh-electrons when we were taking background-runs, i.e. runs with HV and magnets ramped up but with no source, we concluded that the mesh-electrons were actually knocked out by the

tritium final-state ions. Although the process results in losing the ions to the mesh and so did not produce coincidence events for our tritium-data, it serves as a valuable calibration source for the beta-detector. In Fig. 5.5, we fit all the mesh-electron peaks that we think are clearly resolvable. We are technically not interested in events that have beta energy higher than 200 keV for our tritium-data, but these peaks can be applied to correct for gain nonlinearity (Sec. 5.2.3). As an illustration, the mesh-electron calibration gives 60.0 keV/48.1 ADC = 1.25 keV/ADC for the beta-detector. In the actual implementation, instead of assuming our HV is at 60 kV, we refer to the slow-control voltage information (Table 4.4).

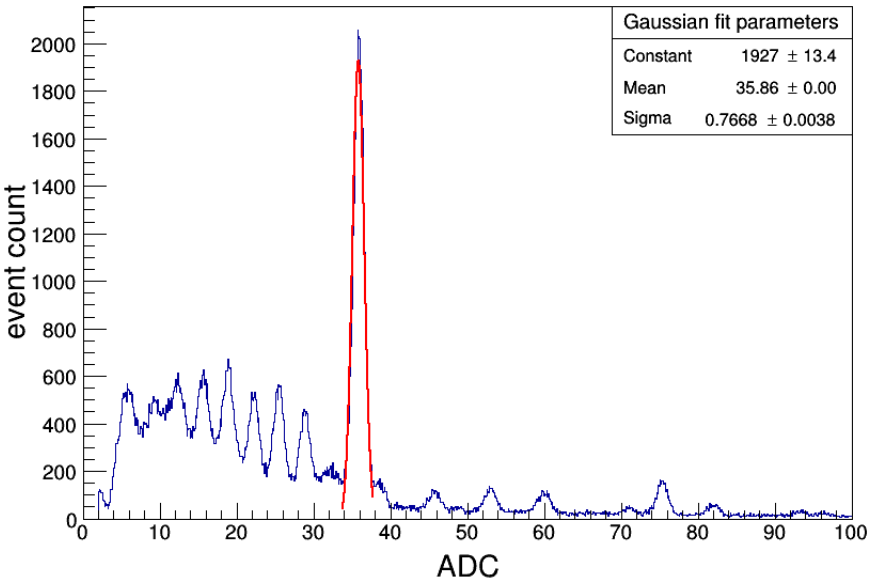

Figure 5.6: Sample ion-detector spectrum histogram from electrons emitted by the gold electrode. This particular spectrum contains a total of 187,817 events taken in a span of 1 hr. The Gaussian peak is fitted to the 48 keV gold-electrons coming from the reverse-biased runs mentioned in Sec. 2.4.1. Each of the smaller peaks come from electrons emitted from a particular Kovar electrode.

An advantage of using mesh-electrons for calibration is that they can be found in the

tritium-data; we have data to calibrate the beta-detector for each run-scan independently. However, to analyze the tritium-data, the calibration on the ion-detector is actually more important, which the mesh-electrons cannot not help.

Since neither ^{241}Am nor mesh-electrons are available for the ion-detector calibration, and ^{83m}Kr calibration is cumbersome, we are driven to use electrons coming from the gold-beta-electrode by applying a reversed bias of $-48\,\mathrm{kV}$ to our decay chamber with no magnetic field. The topic was briefly discussed in Sec. 2.4.1. We call these electrons the gold-electrons. Notice that the inner S-shaped electrodes of the NEC chamber as shown in Fig. 2.6 have a certain orientation; the NEC chamber is not designed to be run in reversed voltage. As a result, without even introducing any tritium to the chamber, a $-48\,\mathrm{kV}$ run generates a sufficient number of electrons to produce a spectrum for the ion-detector as shown in Fig. 5.6. While there are multiple peaks showing up, which are likely coming from each of the S-shaped electrodes, we identify the largest peak as coming from the 48 keV gold-electrons. While this calibration scheme is not ideal, it gives $48.0\,\mathrm{keV}/35.86\,\mathrm{ADC} = 1.34\,\mathrm{keV/ADC}$ for the ion-detector, which again uses voltage information from Sec. 4.3.3 in the actual implementation.

As the last note on the energy calibration, the range of the Gaussian fit in this section is implemented in the following way. First we pick a range that contains the peak that we want to fit. The code finds the ADC bin that has the maximal count $x_{\max}$. Then we set a step size r and a range $R = Nr$, where N is a positive integer. The code then performs a Gaussian fit at each range [$x_{\max}$ - nr, $x_{\max}$ + nr], where $n = 1, 2, ..., N$. Then we pick the range that has the least χ^2`/dof` as our final fit range. We also set a hard 4 ADC threshold for all the histograms in this section, but that would not impact the fit result.

5.2.3 Gain Corrections

The simple linear calibration from Sec 5.2.2 is subject to many sources of errors. For instance, the energy of the calibration electrons from Fig. 5.5 and Fig. 5.6 is voltage-dependent. If our HV is not adjusted exactly to 60 kV or $-48\,\mathrm{kV}$, then the uncertainty would be transferred to the calibration. Moreover, consider the gain defined by keV/ADC such that we can calibrate

an ADC value to an energy. Due to having complicated preamp electronics, this gain can be energy-dependent (gain nonlinearity) or time-dependent (gain shift), both of which would result in inaccurate calibration. Therefore, we address in this section the gain correction.

Voltage Correction

The voltage correction is a simple one, thanks to Sec. 4.3.3. Instead of using a fixed voltage of 60 kV for Fig. 5.5 and −48 kV for Fig. 5.6, we can just refer to the averaged voltage from Table 4.4 for the corresponding runs. Notice again that we are assuming the dead-layer effect is small for electrons with energy as high as 60 keV or 48 keV [163], so the mesh-electrons under x kV have a detected energy of x keV.

Ion-detector Gain-nonlinearity Correction

To correct for the gain nonlinearity of the ion-detector, we use a series of pulser-data that have different input voltages. The pulser was set up to produce 1-ms-wide square pulses at a burst rate of 100 Hz and a run duration of 30 s for each pulser voltage. The pulser voltages were set from 30 to 330 mV with a 10 mV step size, but with three additional points being 400, 500, and 600 mV, where the last point roughly corresponds to 60 keV after ^{241}Am calibration. These data were also taken in a non-sequential order to avoid potential correlation. The spectrum of the pulser-data will look like Fig. 5.3 but with a single clean peak, whose peak location is associated with in the pulser voltage. For each pulser voltage, we fit a Gaussian to the pulser spectrum. The means of the Gaussians are the blue square data points shown in Fig. 5.7. The error bars of the means are too small to be shown. In addition to these data points from the pulser, we also place a point at the origin with no error bar because 0 ADC should corresponds to 0 keV. These data points are then fitted to the following function:

$$f(x) = ax + \frac{b}{x+c} - \frac{b}{c}, \tag{5.3}$$

where a, b, and c are the fit parameters, whose fit values and the χ^2/dof are given on the top left of the plot. The percentage residuals from the fit are given in the bottom plot. The ADC to keV values we can obtain from this fit function then give our ion-detector gain-nonlinearity-corrected energy calibration.

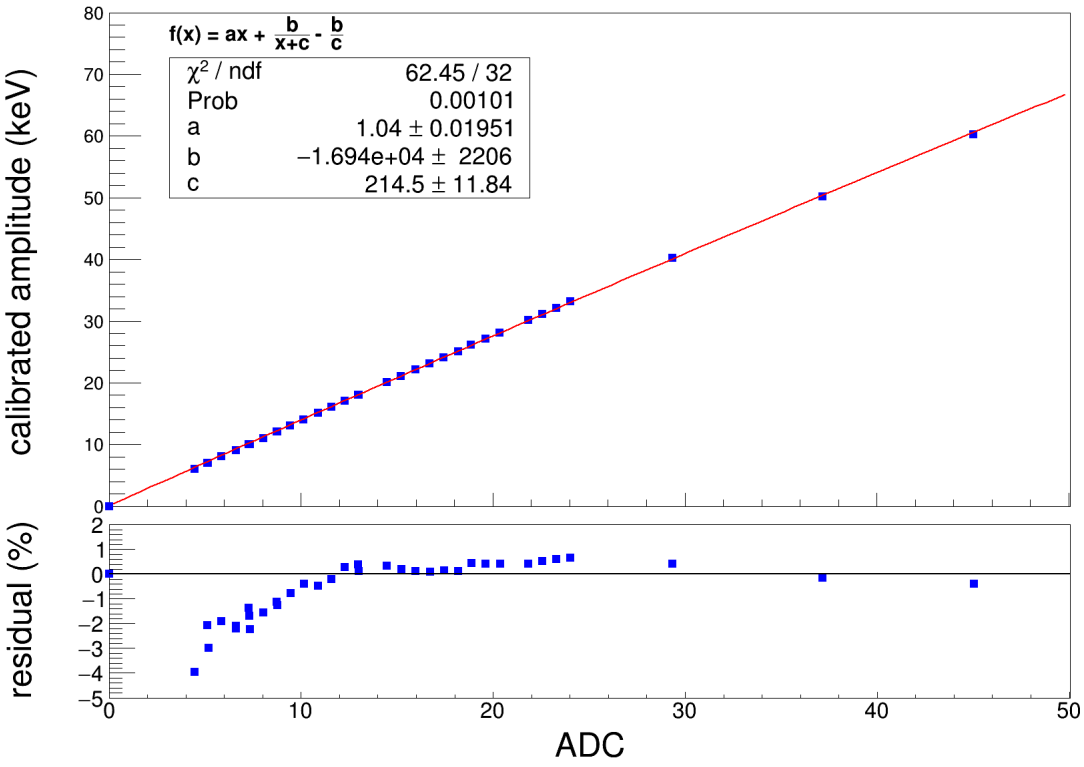

Figure 5.7: Ion-detector gain nonlinearity. The data points are collected using the pulser with various amplitudes. The error bars are obtained from the uncertainty of the Gaussian mean fitted to the ADC peaks; they are present but are too small to be visible in the plot. The x-axis gives the ADC value of each pulse amplitude, while the y-axis is the linearly calibrated amplitude using the ^{241}Am source. The data are fitted using ROOT to the function given on the top left with parameters a, b, and c. The y-value of the fit function gives the gain-nonlinearity-corrected detected energy. The bottom plot provides the percentage residuals of the fit.

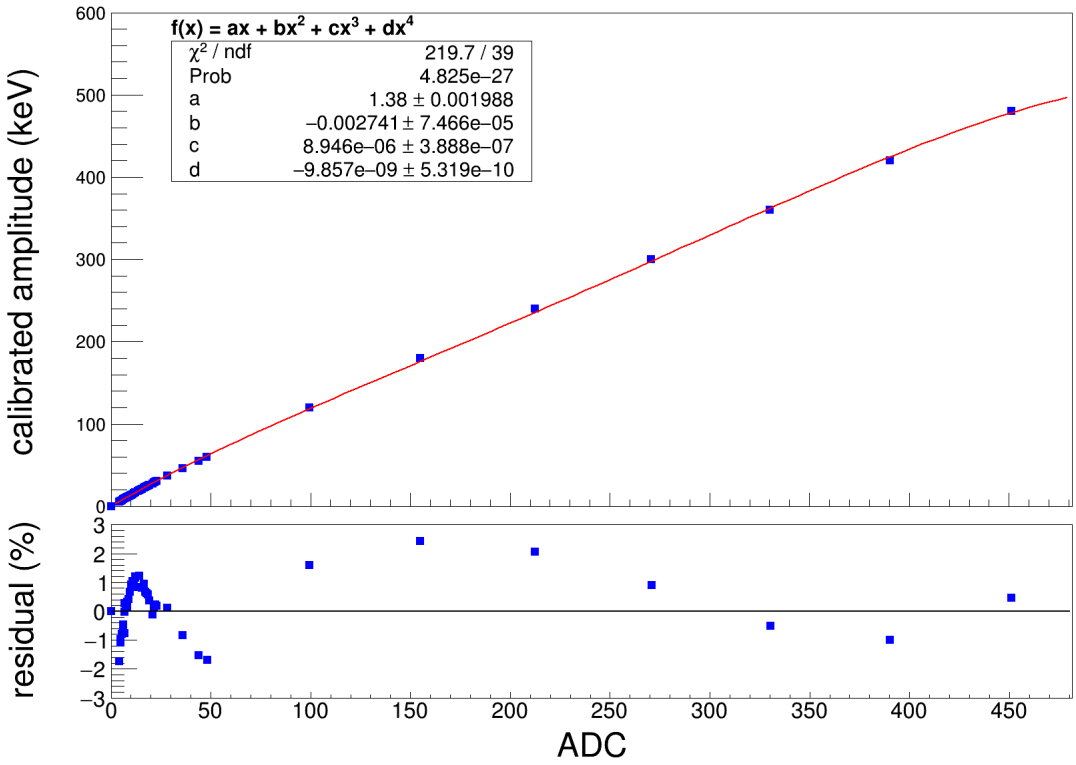

Figure 5.8: Beta-detector gain nonlinearity. The data points are collected using a combination of the pulser with various amplitudes and the mesh-electron peaks from Fig. 5.5. The error bars are obtained from the uncertainty of the Gaussian mean fitted to the ADC peaks; they are present but are too small to be visible in the plot. The x-axis gives the ADC value of each pulse amplitude and mesh-electron peak, while the y-axis is the linearly calibrated amplitude. For the linear calibration, the pulser-data use the ^{241}Am source, while the mesh-electron data follow the "Voltage Correction" in this subsection. The data are fitted using ROOT to a 4^{th} order polynomial given on the top left with parameters a, b, c, and d. The y-value of the fit function gives the calibration with the gain-nonlinearity correction. The bottom plot provides the percentage residuals of the fit.

The particular functional form is used instead of our initial attempt with a polynomial so that we can extrapolate the fit function up to 120 keV (Sec.5.3.5); polynomials are not great for extrapolation because of their oscillatory behavior. At the time when we took the pulser-data, we were not expecting an energy range greater than 60 keV.

Beta-detector Gain-nonlinearity Correction

As for the beta-detector gain-nonlinearity correction, all the data points below 50 keV in Fig. 5.8 are obtained in the same way as in Fig. 5.7. Fortunately for the beta-detector however, we also have data from the mesh-electron peaks in Fig. 5.5. Because the energy range is extended to 400 keV, we only need the fit function for interpolation. Hence, we used a 4^{th} order polynomial given on the top left of Fig. 5.8, as well as their fit values and the corresponding χ^2/`dof`. The ADC-to-keV values we can obtain from this polynomial is then our beta-detector calibration with the gain-nonlinearity correction.

One caveat is that the polynomial reaches its turning point at roughly 500 ADC. This means that the noise events with high ADC values can be wrongly calibrated into our energy range of interest. For this reason, we apply the B3 cut later in Table 6.5.

One additional comment is that this kind of pulser test is how we decided to switch the digitizer channel from 1 to 0 for the beta detector because the latter is much more linear.

Beta-detector Gain-shift Correction

The detector gaisn also drift over time. For the beta-detector, we can track the drift using again the mesh electrons from Fig. 5.5. Because our trigger setup uses to the OR-logic (Sec. 2.5.2), the tritium-data records all the singles event. As a result, the mesh-electrons are present in every tritium-data, we group all the runs on the same day, and Gaussian fit the mesh-electron peak that corresponds to 360 keV. The choice of which peak to use is a tradeoff between sensitivity and statistics. The higher the peak ADC values, the more sensitive they are to gain change because the gain is multiplied directly by the ADC value to produce the calibrated amplitude in keV. One the other hand, the statistics drop exponentially with

increasing peak ADC values as shown in Fig. 5.5; if we take the maximum point of the peaks in Fig. 5.5, they follow a straight line in a log plot.

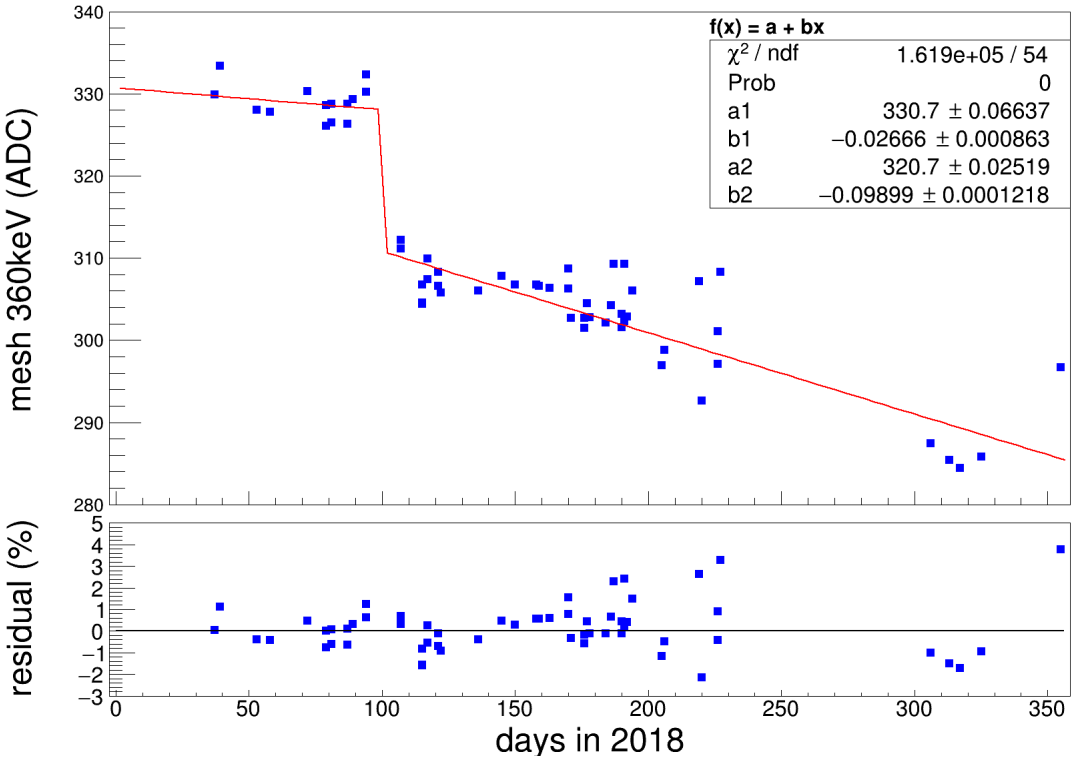

Figure 5.9: Beta-detector gain shift. The data points come from the tritium-data, all of which provide mesh-electron data like Fig. 5.5; the peak corresponding to 360 keV mesh-electrons is chosen. The error bars are obtained from the uncertainty of the Gaussian mean fitted to the ADC peaks; they are present but are too small to be visible in the plot. The x-axis gives the days when were taking our data, which are extracted from column `day_since_2018` of Table 4.6. The y-axis gives the mesh-electron peak value in ADC. The data are separated into two parts, each of which is independently fitted using ROOT to a line given on the top right. The steep line around day 100 is a ROOT artifact; there are no data in that region. The bottom plot provides the percentage residuals of the fit.

The blue square data points in Fig. 5.9 are obtained from the 360 keV mesh-electron

peaks, and are plotted over days in 2018 during our entire data-taking session. They are grouped into two parts, one before day 100 and one after. Then we fit each group independently using a linear function given on the top right of the plot. The subscripted of 1 on the fit parameter corresponds to the group before day 100 and 2 to after. The intermediate line at day 100 is just an artifact of the ROOT fit. The percentage residuals from the fit are given on the bottom. Once we get the fit function, we normalize the function value to 360 keV for the beta-detector calibration with the gain-shift correction. The reason for the gain shift is presently unknown.

As for the ion-detector, although it's more important to our analysis, we have no accurate way to do a shift correction unfortunately. Unlike the beta-detector that detects mesh-electrons, the ion-detector has no monoenergetic source in the tritium data for such correction. However, by inspecting near 60 keV H^+ events, we know no substantial shifts occurred.

5.2.4 Noise and Energy Resolution

According to [141, 157], there are in general three types of noise that affect the energy resolution of a silicon detector. They are series noise, parallel noise, and $1/f$ noise. The classification of series and parallel is effectively guided by whether the noise source is in series or in parallel to the signal input.

The series noise is contributed mostly by Johnson noise, which is caused by thermal agitation of charge carriers in the FET channel. But in a RC circuit like that of a silicon detector, Johnson noise also depends on capacitance: the noise increases with increasing capacitance. This is why our preamp was designed in the way described in Sec. 2.5.1 that minimized the capacitance of the detector circuitry at its biasing stage.

The parallel noise is contributed mostly by shot noise. Shot noise is caused by discrete electrons spontaneously passing through supposedly insulating barriers such as capacitors and pn-junctions. These passing electrons create the so-called leakage current. For capacitors, leakage current is caused by imperfect insulation. In our case, low detector leakage

current from the detectors is promised by Canberra's design (Sec. 2.5). As for the reverse biased pn-junctions in our circuitry, their leakage current can be reduced by lowering the temperature. This is why a Joule-Thomson cooler as described in Sec. 2.5.3 was implemented to cool our detector circuitry. The performance of the cooling will be shown in Sec. 5.2.5.

The $1/f$ noise, or the flicker noise, is intrinsic to electronic devices like FETs. The noise is inversely proportional to the frequency of the input signal f and is categorized as pink noise as a way to distinguish it from other noise sources. The origin of the $1/f$ dependence, however, is not yet well-understood. Nonetheless, using FETs is a common preamp design choice because FETs have the best overall noise performance, which is mainly attributed to having small leakage current. As a side note, FETs are very sensitive to overcharge; care must be taken to prevent them from being damaged by static charges.

And of course, there are also the microphonic noises from mechanical devices in the lab and the 60 Hz noise from electronic devices that run on alternating current. These noise sources were not the major concern for us because the trapezoidal filter is excellent in filtering out low-frequency noise. As for the ground-loop noise, its effect should be minimized by using fiber optics.

5.2.5 Energy Resolution

We characterize the energy resolution by the full width at half maximum (FWHM) of a Gaussian fit to the spectrum of a calibration source. Take the ^{241}Am 59.5 keV gamma calibration from Fig. 5.4 as an example, the FWHM can be obtained by,

$$\text{FWHM} = \frac{59.5}{47.3} \times 2\sqrt{2\ln(2)} \times 0.890 = 2.64\,\text{keV}, \tag{5.4}$$

where the 59.5 keV is the known ^{241}Am gamma energy, the 47.3 ADC is the mean of the Gaussian fit to the gamma energy, and the 0.890 ADC is the standard deviation of the Gaussian fit. The fraction converts the unit of the standard deviation from ADC to keV, while the $2\sqrt{2\ln(2)}$ factor converts the standard deviation to the FWHM.

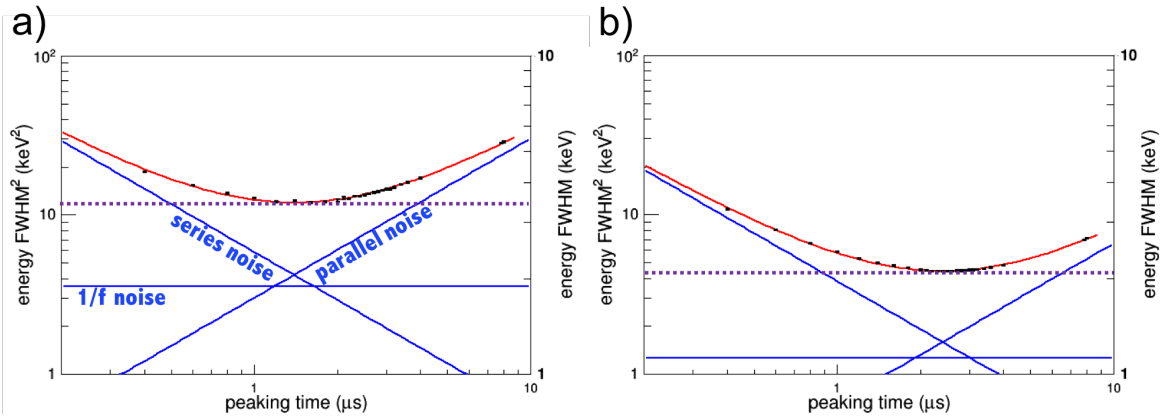

Figure 5.10: Energy resolution versus peaking length (L) log-log plots. The plot a) data were taken without cooling, and the plot b) were taken after Joule-Thomson cooling. The data points (black dots) are the FWHM^2 obtained using different peaking lengths. The red curves are fitted to the data points via Eq. 5.5. The three noise contributions are represented by the three blue lines in each plot. The data points are chosen to be concentrated in three regions, i.e. the low ($\approx$ 500 ns), the intermediate ($\approx$ 2000 ns), and the high ($\approx$ 8000 ns) region to cover the essential structure of the curve. The optimal energy resolutions are thence indicated by the purple dashed horizontal lines according to the fitted curves. For convenience, the FWHM is shown in the right y-axis for each plot. This particular data set came from our ion-detector.

According to [141], the "noise" can be characterized by the square of FWHM and depends on the peaking length of the trapezoidal filter. In fact, the FWHM^2 depends on the peaking length* in the following way: let peaking length (or peaking time) be L, then the contribution from the series noise $\sim 1/L$, the 1/f noise $\sim$ const, and the parallel noise $\sim L$, i.e.

$$\mathrm{FWHM}^2(L) = \frac{a}{L} + b + cL, \tag{5.5}$$

*The term shaping time is more often used to be associated with FWHM instead of the peaking length. However, while these two terms have different meaning for analog filters, they are interchangeable when describing a digital filter.

where a, b, and c are fit parameters that determine the contribution from each term. Now, an advantage of a digital filter is that it allows us to vary the peaking length offline, so that we could to find the optimal peaking length for the best energy resolution. The black data points shown in Fig. 5.10 are the FWHM^2 (log y-axis) obtained using different peaking lengths (log x-axis). Notice that each of the three components forms a straight line in a log-log plot as shown by the labeled blue lines in Fig. 5.10a). The red curve is then the sum of these three components as in Eq. 5.5 that is fitted to the data. Having a theoretical fitted curve allowed us to extract the optimal peaking length and the minimal FWHM^2 as indicated by the purple dashed horizontal lines in Fig. 5.10.

Compared to Fig. 5.10a), Fig. 5.10b) shows the data taken after the detector was cooled by the Joule-Thomson cooler described in 2.5.3. We can see an improved energy resolution by comparing the location of the purple dashed lines. And as expected, cooling most significantly reduces the parallel noise because of how leakage current depends on temperature, but all three components are reduced.

Detector	Optimal Peaking length	Energy Resolution
beta-detector	2800 ns = 700 time-bins	2.46 keV (FWHM) 1.05 keV (sigma)
ion-detector	2200 ns = 550 time-bins	2.05 keV (FWHM) 0.87 keV (sigma)

Table 5.1: Detector optimal peaking length and energy resolution. The detectors are under Joule-Thomson cooling. These results are substantially better than the 5 keV Canberra specification.

The resulting energy resolutions of our detectors are given in Table 5.1 along with their corresponding optimal peaking lengths. These results are substantially better than the 5 keV Canberra specification. These sets of data are taken using the ^{241}Am gamma source, and so the broadening from the dead-layer effect and the pulse-height defect are not accounted

for. Furthermore, the energy resolution also does not address the uncertainties associated with the gain corrections (Sec. 5.2.3). Fortunately, our analysis scheme indirectly accounts for these uncertainties (Sec. 6.1.2).

5.3 Timing Measurement

The signal processing step that comes next is called a digital constant fraction discriminator (dCFD), which we use to extract pulse timing. To see the strength of a dCFD, we first discuss the noise that can affect the timing measurement.

5.3.1 Noise and Timing Resolution

The two main noise sources to the timing are time walk and time jitter [157].

Time walk is caused by the amplitude-dependence of the timing extraction. As an example, consider a naive method that determines the timing by the time point when the pulse signal passes a fixed voltage threshold V_T. In this case, if pulses have a fixed rise time, which is defined by the time required for the pulse to reach its full amplitude from the baseline, then given a small and a large pulse that start at the same time, the small pulse reaches V_T later than the large pulse. This means this method provides more delayed timing measurement the smaller the pulse amplitude is. Hence, the time "walks" for the small pulse. Naively, we can also ask why we cannot use the exact point when pulse voltage just starts to rise, i.e. set V_T to the voltage baseline. The problem is that the starting point is buried in electronic noise.

Time jitter is caused by electronic noise that can randomly bump up the signal voltage to pass V_T. These jitters happen in the digitizer, the pulser, and the preamp. Our digitizer has an internal jitter smaller than 1 ns between the channels; its four channels share a single clock [152]. Our pulser has an internal jitter of 1 ns between the pulses it generates as well [182]. However, we will see in Sec. 5.3.3 that the electronic noise from the preamps is the dominant source of noise to the timing measurement.

5.3.2 Constant Fraction Discriminator

While 2TF is excellent in amplitude extraction, following it with a constant fraction discriminator (CFD) improves our timing extraction. The basic idea is improving the naive method from Sec. 5.3.1: instead of using a fixed voltage threshold, we can use a threshold determined by a fraction C of the pulse amplitude. If both C and the rise time are fixed, the timing determined will be independent of the amplitude. This fixed fraction C explains the "constant fraction" in the CFD. In cases where the rise time does vary, we need to obtain the rise time for each pulse by the rising slope of the waveform pulse. We apply the CFD as usual, but then we correct the CFD timing by subtracting it with C times the rise time to obtain the so call zero-constant-fraction timing. This corrected timing resolves both aspects of the time walk.

To use the CFD on digitized waveforms (dCFD), linear or spline interpolation is usually the choice to extract the CFD timing from discrete time bins. In TRIMS however, we fit the waveforms using a Woods-Saxon (WS) function[†], which can be thought of as a smoothed step function. Despite the method taking significantly more processing time, we find that fitting the waveform gives us the best performance. More importantly, fitting the waveform helps mitigate the time jitter, especially for low-amplitude pulses.

The specific function that we use to fit the waveforms (1WS-fit) is the following,

$$f(t) = \frac{A}{1 + e^{-(t-t_0)/a}} e^{-bt} + A_0. \tag{5.6}$$

An example of such a function is shown as the red curve in Fig. 5.11. The waveform behind the red curve is the same waveform as from Fig. 5.2 a), but the time window is zoomed-in to the pulse. To implement the procedures that correctly fit every waveform, determining viable initial values is crucial, so these initial values will be provided here for each parameter. Units for the parameters are given inside the parentheses. The parameter A (ADC) is the amplitude and is initialized by the pulse amplitude obtained by the 2TF (Sec. 5.2.1). The

[†]The function is also called a logistic function. It is a commonly used sigmoid function, and it is not associated with the nucleon model that uses the Woods-Saxon function except the function itself.

parameter t_0 (time bins) is the trigger location, i.e. the timing right in the middle of the WS-function. It is initialized by the timing T_0 (time bins) that is also obtained by the 2TF. The T_0 is indicated by the blue dashed vertical line in the plot. The parameter A_0 (ns) is the waveform's baseline. Knowing the gap length G and peaking length L of the 2TF, the baseline is initialized by,

$$A_0 = \frac{1}{2L}\left(\sum_{j=T_0-G/2-L}^{T_0-G/2} v_j - \sum_{k=T_0+G/2}^{T_0+G/2+L} v_k\right) - \frac{A}{2}. \tag{5.7}$$

The first term is the difference in the average voltage values in the range $(T_0 - G/2 - L, T_0 - G/2)$ and $(T_0 + G/2, T_0 + G/2 + L)$. The second term is half of the pulse amplitude. These windows match exactly the non-zero values of the TF2 kernel. At the end of the average, the formula also subtracts half of the pulse amplitude to arrive at the baseline. The positive parameter a (time bins) determines the width of the WS-function; it can be understood as the rise time up to a scale. Because the rise time is considered fixed for our preamps, we fixed a as well, but in the following specific way. The parameter is first initialized by $a = 1.0$, but can vary in a range of $a \in [0, 5]$. Because T_0 is actually not an ideal initialization for t_0, having a variation in a allowed t_0 to converge to the correct location. A second fit is then performed immediately after the first; the initializations of the second fit directly come from the results of the first fit, except $a = 1$ is fixed this time. Finally, the parameter b (1/time bins) is always fixed at $b = 10,000$ and is there to better fit the exponential tail described in Sec. 4.1.1; it is technically not a part of the WS-function. If we set the constant fraction $C = 0.5$, then the parameter t_0 is exactly the dCFD timing we are looking for. The result of t_0 is indicated by the red dashed vertical line in Fig. 5.11.

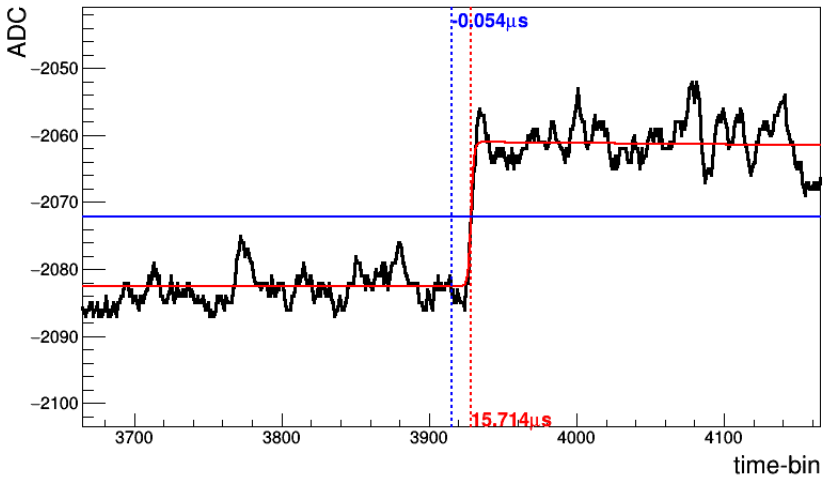

Figure 5.11: Waveform and dCFD. The waveform is the zoomed-in version of Fig. 5.2 a). The red curve is the WS-function Eq. 5.6 fitted to the waveform (1WS-fit). The blue dashed vertical line is the timing determined by the 2TF. The blue solid horizontal line goes through half an amplitude across the fit function to make up a constant fraction of $C = 0.5$. The red dashed vertical line is the dCFD timing determined by the crossing point of the blue horizontal line and the WS-function. We can see the 2TF timing errs by $0.054\,\mu s = 54\,ns$ for this waveform.

Two caveats are worth mentioning. The first is that the 1WS-fit does not cover the entire range of the waveform because that would be too time consuming. Instead, the fit range we used is $(T_0 - L, T_0 + L)$, and was confirmed to make little difference in result from using the full range. The second is that, as mentioned previously, $C = 0$ is a common choice because it also accounts for variation in rise time. However, when we plot out the distribution of the parameter a before we fix its value, it is close to a constant of 1. That is why we set $a = 1.0$ in the second fit, because then a different choice of C would only shift a constant timing shared by every waveform. This global shift will then be canceled when we calculate the timing difference between ions and betas in a coincidence event; the timing difference

is independent of the choice of C. This explains why we used the most convenient fraction $C = 0.5$, so that the dCFD timing is given by the parameter t_0.

5.3.3 Timing Resolution

To obtain the timing resolution of our detectors, we use the pulser route in our trigger setup Fig. 2.16. The pulser signals go to the test input on the preamp shown in Fig. 2.15 region 1c), which provides signals that mimic detector signals up to the dead-layer effect. The same pulser output was teed to the beta- and the ion-preamp, so that the same signal was received at the same time up to electronic delays. The electronic delays between the two paths can be caused by the difference in cable lengths or the NIM devices not being completely identical. The delay, i.e. the time-zero correction, does not affect the timing resolution measurement because it only gives a constant time shift to all the events. To avoid ground-loop noise, the pulser was connected to the preamps via fiber optics. Due to the power required for the pulser to drive the fiber optics, the input range could only go as high as 80 keV in pulse amplitude. Fortunately, this range is sufficient because the timing resolution is excellent with large-amplitude pulses as we will see. The pulser was programmed to give 1-ms-wide square pulses at a burst rate of 100 Hz. We varied the pulse amplitude and took data for 10 s at each amplitude point.

With this test setup, we estimated the timing resolution using the FWHM obtained from standard deviation of the Gaussians fitted to the histograms of the beta-detector timing subtracted from ion-detector timing. This means the FWHM contains contributions from both the beta- and the ion-detector, cancelling the pulser's internal jitter noise of 1 ns. The resulting timing resolution at different input amplitudes is shown in Fig. 5.12. The red and blue points are showing the same data set. The difference, however, is that the red triangles were obtained using the 2TF timing, while the blue diamonds were obtained using the dCFD timing. Timing resolution is improved as promised by dCFD.

Even after fitting the waveforms to the WS-function, the timing resolution for low-amplitude pulses still had much to be desired. As a result, we would like to filter out

these low-amplitude events in a later stage of the analysis (filters B1 and B2 in Table 6.5).

We did a few other tests. The first was to test if the timing resolution was improved by JT-cooling; no significant improvement was found. The second was to test if the timing resolution depends on the relative delay between the beta and ion signals; the test showed no dependence. And lastly, notice the setup that produced Fig. 5.12 sent the same pulse amplitude to the beta- and the ion-detector. To test if time resolution depends on these two amplitudes independently, we attenuated the pulser input amplitude to one detector at a time (3 dB to 18 dB in 3 dB step). We found the statistical independence is true, such that if we divide the FWHM in Fig. 5.12 by $\sqrt{2}$, we arrive at the time resolution for each detector.

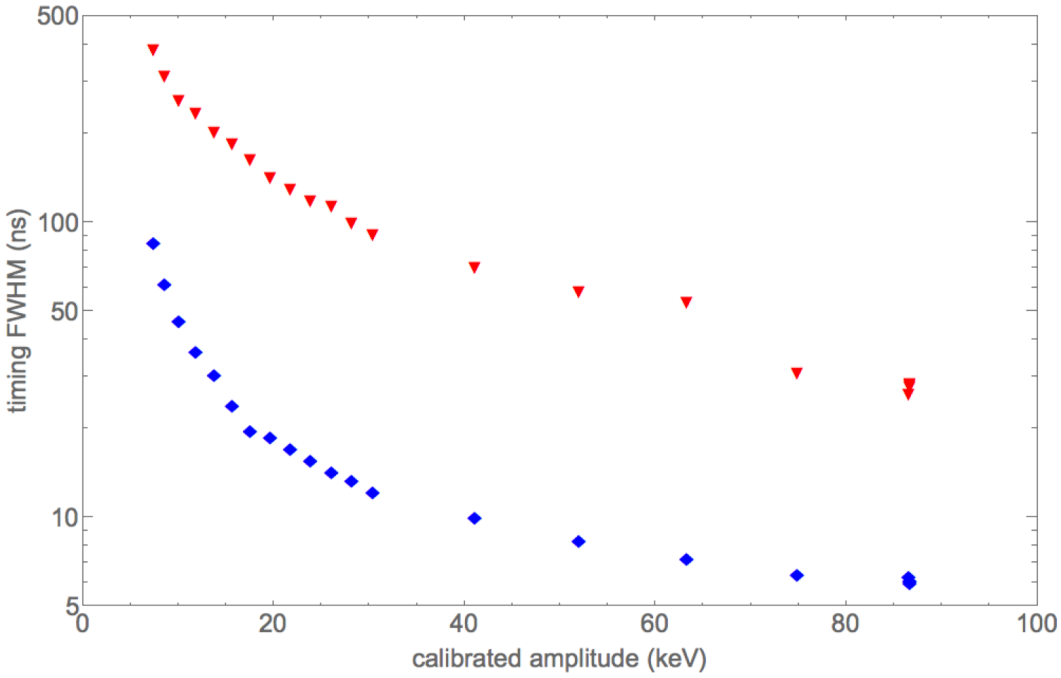

Figure 5.12: Timing resolution versus energy. The x-axis shows the ^{241}Am calibrated beta-detector amplitude, while the y-axis for the timing FWHM is in log-scale. The data were collected using a pulser. The red and the blue points comes from the same data set, but the red triangles use the 2TF timing, while the blue diamonds use the dCFD timing. The error bars are smaller than the data points.

5.3.4 Double Woods-Saxon Fit for Two-Particle Events

While we were inspecting the tritium-data, we found events whose waveforms consisted of two pulses that were close to each other. We call these events the 2-particle events, and they are the signature of tritium beta decay resulting in two ions and two electrons instead of one each. A more complete description of these events is given in Sec. 6.1.1; this section focuses on the method that extracts the timing information from both of the pulses in a 2-particle event. Notice that these two pulses may be as close together as tens of nanoseconds. Because these time differences are much shorter than the peaking length, the 2TF cannot resolve them, let alone determine them. Fortunately, a variation of the dCFD using the WS-function does the job well.

The variation is a simple one, we fitted the 2-particle event waveforms using a double Woods-Saxon (2WS) function instead of the single-WS function in Eq. 5.6,

$$f(t) = \frac{A_1}{1+e^{-(t-t_1)/a_1}}e^{-bt} + \frac{A_2}{1+e^{-(t-t_2)/a_2}}e^{-bt} + A_0. \tag{5.8}$$

The fit parameters are A_1, A_2, t_1, t_2, a_1, a_2, A_0, and b. An example of the function is shown as the red curve in Fig. 5.13. The parameters A_1 and A_2 (ADC) are initialized by half the pulse amplitude from the 2TF. The parameters t_1 and t_2 (ns) are subjected to a constraint that $t_1 < t_2$. To get the correct initialization for various cases, the fit is performed three times using t_1 and t_2 initializations of $(t_0 \pm 3G)$, $(t_0 \pm G)$, and $(t_0 \pm G/2)$. Out of the three fits, the one with the smallest χ^2`/dof` is chosen. These initial values were decided via trial and error; we reviewed the various 2-particle waveforms and checked how well each initialization fit the waveforms. The parameters a_1 and a_2 (ns) are fixed to be 1 from the beginning. Finally, the parameters A_0 (ADC) and b (ns) are initialized by the same parameters from the 1WS-fit that we performed on the waveforms before the 2WS-fit.

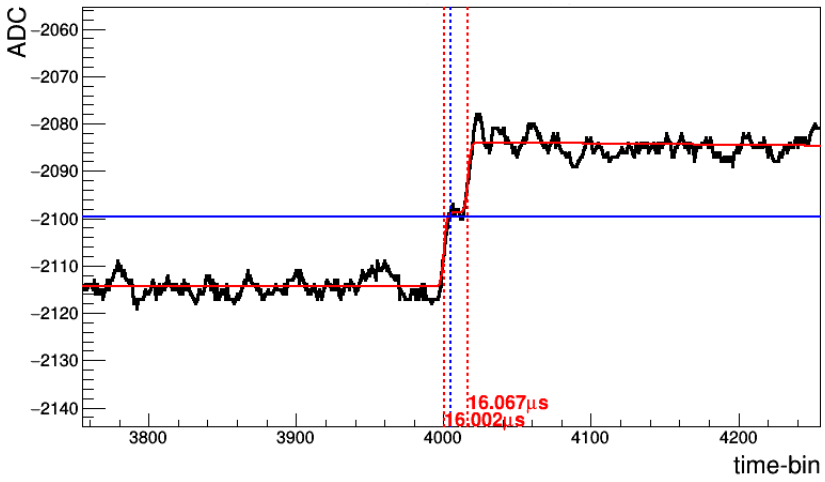

Figure 5.13: Waveform and 2WS dCFD. As compared to Fig. 5.11, there are two pulses that are very close to each other; they are only 65 ns apart. The red curve is now a 2WS-function fitted to the waveform. The timings of the two pulses provided by the 2WS are indicated by the two red dashed vertical lines. The blue dashed vertical line is again the timing determined by the 2TF. The blue horizontal line is no longer helpful because the fraction $C = 0.5$ amplitudes are at different locations for the two WS-functions.

We always start the dCFD by applying 1WS-fit to the waveform. To determine whether we should invoke the 2WS-fit or not, i.e. whether the waveform comes from a 2-particle event or not, we follow the following three conditions. The first is when χ^2/dof> 20. For the second condition, recall that in the single-WS case, the 1WS-fit is done twice with the parameter a fixed in the second fit (Sec. 5.3.2). Let a_0 be the width parameter obtained from the first 1WS-fit, then the second 2WS-fit condition is such that $a_0 > 2$ time-bins. The last is when the χ^2/dof for the first 1WS-fit is greater than the χ^2/dof for the second 1WS-fit. The 2WS-fit is invoked when any of these three conditions apply. However, if the χ^2/dof of the 2WS-fit is greater than that of the 1WS-fit, then the fit goes back to using 1WS-fit. All the input numbers for these conditions were obtained empirically. For instance,

the condition $a_0 > 2$ time-bins was chosen after examining the distribution of a_0 to balance the event selection efficiency and run-time. Performing 2WS on every waveform would take a significant amount of time to process. Over all, for waveforms that have amplitude larger than a 20-keV detector signal, this waveform selection scheme performs at near 100% efficiency for over 2000 waveform samples*. For smaller waveforms however, these conditions are not reliable and must be used with care.

If a waveform passes the three conditions, then the parameters t_1 and t_2 of the 2WS-fit are the dCFD timings of the two pulses both with the fraction $C = 0.5$. The timings are indicated by the two red dashed vertical lines in Fig. 5.13. The amplitudes for the pulses are also updated to A_1 and A_2 instead of the single amplitude obtained from 2TF.

5.3.5 TRIMS Energy Range of Interest

Using the information provided thus far, we can more concretely determine the energy range of interest for the TRIMS experiment.

Because our basic setup runs under a HV of 60 kV, and we detect mostly singly charged particles, our primary energy range of interest is [0, 60]keV. However, due to 2-particle events (Sec 5.3.4), it should be extended to [0, 120]keV. Moreover, considering that the tritium betas have a Q-value of roughly 20 keV, a conservative range should be [0, 150]keV with an extra 10 keV to account for various sources of noise. As for the lower bound, recall we have a hardware threshold of roughly 3 ADC from our discriminators (Sec 2.5), which corresponds to roughly 4 to 5 keV in detected energy (Sec. 5.2.3). So we finally arrive at a functional TRIMS energy range of interest of [5, 150]keV.

An even more careful determination of the energy range is to consider Fig. 5.12. Because we cannot tolerate waveforms that have timing resolutions much worse than 20 ns*, we cannot rely on the events with smaller than 10 keV detected energy. Considering this requirement

*Half of them are used for tuning and another half for testing. The tuning was done heuristically via visual inspection, so it was not perfect.

*This heuristic value comes from a qualitative inspection of the TRIMS Geant4 simulation result.

should be placed for both the ion and the beta, what we are looking for is a fiducial volume that will be covered in Sec 6.2.3 (filter B6 of Table 6.5). Additionally, we also need to consider the energy lost due to the dead-layer effect. In the end, the [5, 150]keV range is rather inaccurate, but it gives us a general sense of what data we should use.

5.4 Signal-Processing Chain

While Sec. 5.2 and 5.3 describe the signal-processing methods, this subsection focuses on how the TRIMS signal-processing chain is put together. This chain covers all the processes starting from taking in raw detector waveforms to outputting energy and TOF information of the incident particles.

The chain starts out with the raw data, i.e. the direct voltage signal from the detectors. These raw data are processed by the digitizer, recorded by ORCA, and stored in ORCA-files. Then we run a program called an ORCA-to-ROOT converter that converts the ORCA-files into files in ROOT format. We call the output files the raw-ROOT-files. Both the 2TF and the dCFD are carried out in the ORCA-to-ROOT converter. Next, we run another program called a ROOT-to-ANA converter to converts the raw-ROOT-files into what we call the analysis-ROOT-files. Processes such as energy calibration and coincidence event selection are parts of the ROOT-to-ANA converter. This section basically covers the implementation of these two digital converters.

5.4.1 ORCA-to-ROOT Converter

The ORCA-to-ROOT converter was written based on a small part of BEANS (Building ... Analysis ... Sequence), which was software developed by Sanshiro Enomoto for the KATRIN experiment. Since the waveforms obtained from ORCA are initially stored in an ORCA-file, the primary functionality of the ORCA-to-ROOT converter is to translate the ORCA-file to a ROOT file. We call this ROOT file a raw-ROOT file to distinguish it from all the different ROOT files generated later in the analysis. In fact, the ORCA-to-ROOT conversion is important because the majority of TRIMS data analysis codes are developed

based on ROOT's framework.

As mentioned in the introduction, the ORCA-to-ROOT converter does not just store the same data in a different format, it also carries out signal processing steps on the waveforms. The derived values are also stored in the raw-ROOT-file; a list of these values are provided in Table 5.2. The two main steps are the 2TF (Sec. 5.2.1) that extracts pulse amplitudes "`ADC`" in ADC units and the dCFD (Sec. 5.3.2) that extracts pulse timing "`Time`" in nanoseconds. A note for all the `TriggerPosition` entries is that while their units are in time bins, their values are not necessarily integers multiple of time bins; the timing resolutions can be better than a time bin size. Other supplementary parameters from the signal processing steps are also recorded for the purpose of debugging and applying event cuts.

The slow control data from the LabJacks described in Sec. 4.3.1 are also recorded in the ORCA-file. In addition to recording once every 10 s in an ASCII file, the LabJack values are recorded three times a second into the ORCA-file. However, the 3 Hz rate is still much smaller than the event rate of roughly 200 Hz, so the following strategy is implemented: the events record the same LabJack values until the recorded LabJack values are updated. For example, if there is a LabJack reading at 1.1 s and another at 1.4 s, then every event happening in between 1.1 and 1.4 s records the LabJack value at the 1.1 s. While Table 5.2 only displays `LabJack1Timestamp` and `LabJack1Channel0`, all the entries from Sec. 4.3.1 are saved in the same manner. These LabJack values are used in situations such as when we wish to access the timestamp of the event or to correct for the changes in HV we applied to the system.

Entry Name	Description
Waveform	The array of the entire waveform that contains the voltage amplitude for each time bin and is ordered in time. This is the array showcased in Fig. 5.2 and Fig. 5.13. Note that this array is obtained from the raw waveform multiplied by its polarity P_W so that the pulse is positive for 2TF to analyze.
RunNumber	The unique run ID from ORCA described in Sec. 4.2.1
EventNumber	The event ID given to each event of the same run. The ID is ordered by trigger.
Channel	The digitizer channel from which the event is detected
AcquisitionTime	The timing (ns) since the beginning of the run. Given the digitizer acquisition window for an event, this is the time of the first time bin
LabJack1Timestamp	The timestamp (s). It's recorded by the LabJack U12 No.1 in Table 4.1
LabJack1Channel0	The LabJack1 channel that records the hv_v value in Table 4.1. The value is updated three times a second
...	The rest of the LabJack channels from Sec. 4.3.1
GapLength($G_{2\mathrm{TF}}$)	The gap length (time bins) of the 2TF
ShapingLength ($L_{2\mathrm{TF}}$)	The peaking length (time bins) of the 2TF
SoftThreshold	The software threshold (ADC units) of the 2TF; the default value is 2 ADC
ADC	The pulse amplitude (ADC units) obtained by the 2TF
TriggerPosition	The pulse timing (time bins) obtained by the 2TF
NumberOfTriggers	The number of triggers within the same acquisition window as found by the 2TF

`CFDFraction`	The constant fraction used in dCFD
`CFDRange`	The fit range (time bins) of the WS-function used in dCFD
`CFDThreshold`	The χ^2/`dof` threshold for a 1WS-fit. Passing this threshold invoked 2WS-dCFD
`TriggerPositionCFD`	The timing (time bins) indicated by dCFD in time bin unit. For 2WS-dCFD, this is the timing of the first pulse.
`TriggerPositionCFD2ND`	The timing (time bins) of the second pulse in case of 2WS-dCFD. Otherwise, the value is set to be the same as `TriggerPositionCFD`
`Time`	The timing (ns) of the first pulse obtained by converting `TriggerPositionCFD` to nanoseconds and adding it to `AcquisitionTime`
`Time2ND`	The timing (ns) of the second pulse obtained by converting `TriggerPositionCFD2ND` to nanoseconds and add it to `AcquisitionTime`
`Chi2overDOF`	The χ^2/`dof` of the WS-fit.
`Parameter_y0`	The fit parameter A_0 from Eq. 5.6 and Eq. 5.8
`Parameter_x1`	The fit parameter t_1 from Eq. 5.8, which is set to t_0 from Eq. 5.6 in case of 1WS-fit
`Parameter_a1`	The fit parameter a_1 from Eq. 5.8, which is set to a from Eq. 5.6 in case of 1WS-fit
`Parameter_A1`	The fit parameter A_1 from Eq. 5.8, which is set to A from Eq. 5.6 in case of 1WS-fit
`Parameter_x2`	The fit parameter t_2 from Eq. 5.8, which is set to -1 from Eq. 5.6 in case of 1WS-fit

`Parameter_a2`	The fit parameter a_2 from Eq. 5.8, which is set to -1 from Eq. 5.6 in case of 1WS-fit
`Parameter_A2`	The fit parameter A_2 from Eq. 5.8, which is set to -1 from Eq. 5.6 in case of 1WS-fit
`Parameter_b`	The fit parameter b from Eq. 5.6 and Eq. 5.8
`WaveformLength` (L_w)	The size of the array for the raw waveform
`WaveformMin` ($A_{\min}$)	The minimum of the raw waveform within time bin window ($L_w - L_c$, $L_w + L_c$)
`WaveformMax` ($A_{\max}$)	The maximum of the raw waveform within time bin window ($L_w - L_c$, $L_w + L_c$)
`fWaveformBase` (A_{b})	The average amplitude of the raw waveform within time bin window (10, $L_c + 10$).
`fWaveformPol` (P_W)	The waveform polarity. The polarity equals 1 when ($A_{\max} - A_{\mathrm{b}}$) $>$ ($A_{\mathrm{b}} - A_{\min}$), and -1 otherwise.

Table 5.2: Essential entries saved in the raw-ROOT-files. The provided entries are saved twice for every event, populated once by the beta-detector, and once by the ion-detector. The variable L_c stands for characteristic length and is defined by $L_c \equiv (3L_{2\mathrm{TF}} + G_{2\mathrm{TF}})/2$ rounded to the nearest integer.

As the entire array of the waveform is also stored for each event, the size of a raw-ROOT-file is larger than the corresponding ORCA-file. This is the reason why the ORCA-to-ROOT conversion is typically performed on a dedicated server, i.e. the ROCKS server (Sec. 4.1.2). The additional information stored in the raw-ROOT-file is necessary for us have an overall understanding of the data. However, not all information is necessary for analyzing the tritium data and the sheer size of the files would become a burden. This is where the ROOT-to-ANA converter comes in, which serves to distill the data.

5.4.2 ROOT-to-ANA Converter

Filter-No.	`TCut` Name	Condition
A1	`negPolarity`	$P_W == -1$
A2	`notSaturated`	$A_{\min} > 400$
A3	`singleSoftTrig`	`NumberOfTriggers` $== 1$
A4	coincidence	`ADC` >`SoftThreshold` for both waveforms that have the same `eventID`. This filter cannot be implemented using `TCut`.

Table 5.3: Waveform filters. The variables are adapted from Table 5.2.

The ROOT-to-ANA converter translates a raw-ROOT-file into an analysis-ROOT-file, picking only the necessary entries from Table 5.2 for the tritium analysis, as well as applying filters to filter out the irrelevant events. The programming description of these filters is provided in Table 5.3. The first of the filters (filter A1) is that the waveform must have the correct polarity, i.e. the event pulse coming from the digitizer should be a negative pulse as shown in Fig. 4.3*. Otherwise, the pulse would not be a signal coming from the detectors. The second (filter A2) is that the waveform must not be saturated; a saturated waveform has an amplitude larger than the range of the digitizer. Since the voltage information beyond the digitizer range cannot be correctly recorded, there is no way to retrieve the amplitude of a saturated waveform. Fortunately, the saturation corresponds to a pulse height of 2 MeV, which is an order of magnitude higher than the upper bound of our range of interest (Sec. 5.3.5). The third (filter A3) is that the waveform must have a trigger number of 1. At our event rate, multi-trigger events are rare. Since writing code to properly handle

*All the waveforms in this chapter have been flipped to be positive to simplify the signal processing.

multi-trigger events would be burdensome, we simply drop these rare events.

The fourth (filter A4) and the most important of them all is the coincidence filter. Since the digitizer records the waveforms from both the beta- and the ion-detectors under OR-logic, there are plenty of waveforms recorded that have no signal. This filter simply requires waveforms from both detectors to have signal in them, i.e. a signal amplitude greater than the software threshold of 2 ADC. Notice that the software threshold is to prevent the 2TF from picking up noise from the recorded waveform; it is functionally different from the hardware threshold of 3 ADC (Sec 2.5). Finally, we note that ORCA records the beta- and the ion-detector events as two separate events that share the same `eventID`, but from now on we will refer to an event as a coincidence event that passes all four filters[†].

Table 5.4 provides all the entries recorded in an analysis-ROOT-file. These entries are made specifically for coincidence events in that the amplitudes and the timing have both the beta- and the ion-detector counterparts. Since the ROOT-to-ANA converter is specifically developed for the tritium analysis, it only makes sense to apply the conversion to tritium runs. The run selection is done via the spreadsheet described in Sec. 4.3.4.

Other than the filters, the ROOT-to-ANA converter also runs the energy calibration described in Sec. 5.2.2. In other word, both `beta_edep` and `ion_edep` are calibrated to have units of keV. The gain correction from Sec. 5.2.3 has also been implemented when evaluating `beta_edep` and `ion_edep`. Note that `ion_edep` is the detected ion energy instead of the incident energy. A correction for the dead-layer effect on top of `ion_edep` will be covered in Sec. 6.1.2.

It is also worth emphasizing that (`time2ND` = `time`) for the cases in which the 2WS-fit is not invoked. This is "inherited" by `Time2ND` and further upstream by `TriggerPositionCFD2ND` in Table. 5.2. This is a convenient choice for defining the ion TOF for the 1-ion and the 2-ion cases under the same expression (Sec. 6.1.2 and Sec. 7.1.2).

For clarification purposes, we refer to the calibrated signal amplitude from the beta-

[†]We will refer to the events taken in the OR-logic mode specifically as the singles events.

detector as beta-energy, even in the cases when the incoming particle is not a beta-particle, and similarly for ion-energy. Both the beta- and ion-energy have been gain corrected (Sec. 5.2.3) at this stage.

Entry Name	(Unit)	Description
`runID`		The unique run ID from ORCA described in Sec. 4.2.1
`eventID`		The event ID from `EventNumber` in Table 5.2
`beta_amp`	(ADC)	The beta-detector event amplitude from `ADC` for digitizer channel 0. For 2WS-dCFD, it is taken from `Parameter_A1`
`ion_amp`	(ADC)	The ion-detector event amplitude from `ADC` for digitizer channel 2. For 2WS-dCFD, it is the sum of `Parameter_A1` and `Parameter_A2`
`beta_edep`	(keV)	The beta-energy (keV), i.e. the calibrated `beta_amp`.
`ion_edep`	(keV)	The ion-energy, i.e. the calibrated `ion_amp`.
`beta_time`	(ns)	The beta incident time from `Time` for digitizer channel 0
`ion_time`	(ns)	The ion incident time from `Time` for digitizer channel 2
`beta_time2ND`	(ns)	The beta incident time from `Time2ND` for digitizer channel 0
`ion_time2ND`	(mm)	The ion incident time from `Time2ND` for digitizer channel 2
`ion_detposY`		The ion-detector scan index in vertical direction from the manual-entry database (scan-Y-point)
`ion_detposX`		The ion-detector scan index in horizontal direction from the manual-entry database (scan-point)
`voltage`	(V)	The HV voltage from Table 4.4

`sourceType`		The indicator of whether the run is a T_2 or HT run from the manual-entry database. The T_2 source is recorded as 1 and the HT source as 2
`day`	(day)	The day since 2018 (Jan 1^{st}, 2018 is day 1) obtained using `LabJack1Timestamp`

Table 5.4: Entries saved in the analysis-ROOT-files. The provided entries are saved for every pair of events that forms a coincidence event. The scan-points are defined in Sec. 2.5.5.

The ROOT-to-ANA converter also matches the run number from the manual-entry database described in Sec. 4.3.2 and records entries from Table. 4.2 to Table. 5.4. These entries include the ion-detector scan indices (scan-point "`ion_detposX`" and scan-Y-point "`ion_detposY`") as defined in Sec. 2.5.5 and the source-type ("`sourceType`"). A note about the "`sourceType`" entry is that the tritium-data contain only two source-types, and they are identified by integer 1 for T_2 and 2 for HT. The same manual-entry values are saved for each event; the repetition helps when it comes to using the "`TCut`" functionality in ROOT.

5.4.3 KAFFEE

The signal-processing chain can be automated by KAFFEE (Katrin Automation Framework ...), which is software developed by Sanshiro Enomoto. The KAFFEE software is a workflow automation framework that can launch any software tasks automatically based on the contents of the incoming data. Furthermore, the output from KAFFEE is directed to the BEANS GUI that allows interactive ROOT-file-based data analysis on a web browser. Even though KAFFEE was originally developed for KATRIN, its versatile input, task, and output configurations made it readily applicable to the TRIMS experiment.

For TRIMS, the BEANS GUI web browser was hosted by the remote server TRIMPOLINE from Sec. 4.1.2. An example of the web interface is shown in Fig. 5.14. The KAFFEE software allowed a near-time data monitor from TRIMS, which was especially valuable dur-

ing detector performance tests. Unfortunately, because TRIMPOLINE was not designed to handle hundreds to thousands of GB-sized ORCA-files and raw-ROOT-files, the signal-processing chain is manually executed by a local computer for tritium runs.

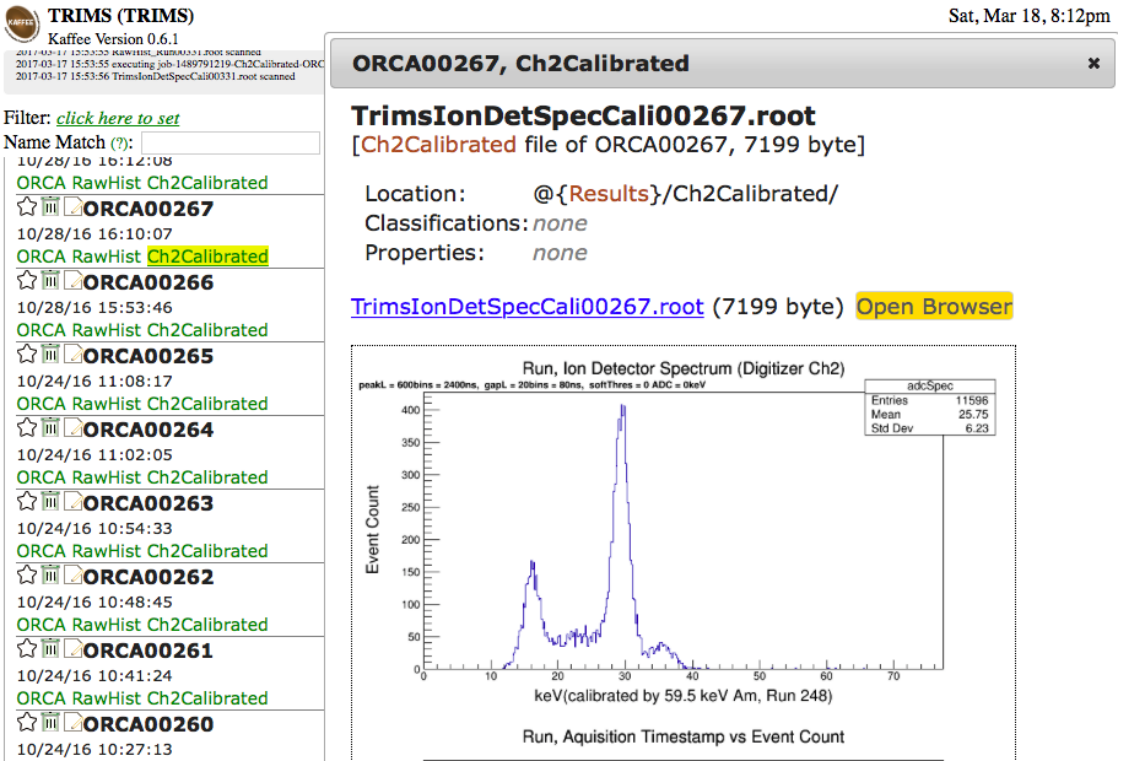

Figure 5.14: Example of BEANS GUI web interface that runs KAFFEE. The KAFFEE software automatically invokes the signal-processing chain discussed in this section to process the newest run as soon as data taking finishes. Once the process is complete, a few selected histograms of the run are posted on the webpage. The figure displays an example of a histogram from an earlier run using ^{83m}Kr source. Notice that the ^{83m}Kr spectrum shown has already been calibrated.

Chapter 6

DATA ANALYSIS: CHARGE AND MASS RECONSTRUCTION

This chapter covers how we can reconstruct the charge and mass information based on the energy and timing information obtained from analyzing the waveforms (Ch. 5). The charge and mass information will then allow us to systematically separate different branches of the beta-decay final states (Ch. 7).

Before doing the charge and the mass reconstruction, Sec. 6.1 studies the tritium-data using ion-energy versus ion-TOF 2D-histograms as well as applying corrections to the ion-energy and TOF. The charge and the mass reconstruction is done in Sec. 6.2. Finally, Sec. 6.3 describes a procedure called “charge-mass boxing" that categorizes all the final state branches.

It is worth emphasizing that we are scanning our ion-detector for a reason that can best be stated later in Sec. 8.1.1. However, we will rely on the terminologies introduced in Sec. 2.1.2 and Sec. 2.5.5 to better explain how our we organize our tritium-data. When we finally obtain the analysis-ROOT-files described in Sec. 5.4.2, they contain all the tritium-data that consist of a number of run-scans. But then we separate these data into the raw-T2-data and the raw-HT-data based on the binary source-type tag (`sourceType` in Table. 5.4); we only have source-types T_2 and HT in our tritium-data. We then further separate them into the left- and the right-scans. These are the 4 main categories of the tritium-data as will be shown in Fig. 6.9 in this chapter. Be aware that a left-scan raw-T2-data still contains multiple run-scans; before we apply any filters, it contains all the T_2 data we took when we scanned the ion-detector to the negative X-direction. Moreover, when we say the left-scan raw-T2-data at the home-position, we are referring to a combination of all the runs that used the T_2 source, belonged to a left-scan, and were taken at the home-position. And as

a reminder, each run-scan for either a left- or a right-scan must contain a run at the home-position for reference (Sec. 4.2.1), and the home-position is the only scan-position shared between a left- and a right-scan.

One last reminder is that the analysis-ROOT-files contain only coincidence events (Sec. 5.4.2).

6.1 Data in Energy versus Time of Flight

This section lists the beta final state branches that are observable by the TRIMS experiment in Sec. 6.1.1. In Sec. 6.1.2, we apply corrections to both the ion-energy and ion-TOF. In Sec. 6.1.3, we show how the physical branches appear in the resulting 2D histograms. And finally in Sec. 6.1.4, we use these histograms to isolate problematic runs that we were not able to capture using just the data-quality check from Sec. 4.3. A final layout of TRIMS data collection is also provided (Fig. 6.9).

6.1.1 Physical Branches

Before looking at the data, we need to figure out what beta-decay final state branches there are that are physically available. A list of these branches for T_2 in Table 6.1 and HT is provided in Table 6.2. Focusing first on Table 6.1, the "Decay-Branch" column lists the possible product particles produced by the T_2 beta decay. The anti-neutrinos are neglected because we cannot detect them. The "-" symbols indicate that the particle is negatively charged, e.g. "e-" for an electron, while the "+" symbols indicate the particle is positively charged and "++" doubly positively charged. The overall charge is neutral for each decay-branch. Decay-branch $\{^3\text{He}, \text{T}\}$ happens when the beta is captured by the ion; it produces no charged particles, so we cannot detect it. Decay-branches $\{^3\text{HeT}^+, \text{e}^-\}$, $\{^3\text{He}^+, \text{T}, \text{e}^-\}$, and $\{^3\text{He}, \text{T}^+, \text{e}^-\}$ are the most common cases where the beta decay produces an ion and an electron. Decay-branch $\{^3\text{He}, \text{T}\}$ happens when the beta is captured by the ion; it produces no charged particles, so we cannot detect it. The "2e-" cases are when the decay produces not only a beta but also a shake-off electron.

Decay-Branch	Detection-Channel	Detection-ID
$\{^3He, T\}$		
$\{^3HeT^+, e^-\}$	$\{^3HeT^+, e^-\}$	`T2_mainM6`
$\{^3He^+, T, e^-\}$	$\{^3He^+, e^-\}$	`T2_mainM3`
$\{^3He, T^+, e^-\}$	$\{T^+, e^-\}$	`T2_mainM3`
$\{^3He^+, T^+, 2e^-\}$	$\{^3He^+, T^+, 2e^-\}$	`T2_2I2eM32`
	$\{^3He^+, T^+, e^-\}$	`T2_2I1eM32`
	$\{^3He^+, 2e^-\}$	`T2_1I2eM3`
	$\{T^+, 2e^-\}$	`T2_1I2eM3`
	$\{^3He^+, e^-\}$	`T2_1I1eM3`
	$\{T^+, e^-\}$	`T2_1I1eM3`
$\{^3He^{++}, T, 2e^-\}$	$\{^3He^{++}, 2e^-\}$	`T2_2I2eM34`
	$\{^3He^{++}, e^-\}$	`T2_2I1eM34`
$\{^3He^{++}, T^-, e^-\}$	$\{^3He^{++}, T^-, e^-\}$	
	$\{^3He^{++}, T\text{-}\}$	
	$\{^3He^{++}, e^-\}$	
$\{^3He^{++}, T^+, 3e^-\}$	$\{^3He^{++}, T^+, 3e^-\}$	
	$\{^3He^{++}, T^+, 2e^-\}$	
	$\{^3He^{++}, T^+, e^-\}$	
	etc., but small	

Table 6.1: Physical-branches for T_2 beta decay. The symbol “e" stands for electron. The decay-branches of HT beta decay are given in the first column. The commas indicate having multiple particles as the decay products. The second column provides possible detector-coincidence combinations for each decay-branch; the listed charged particles are detected by either the beta- or the ion-detector. The third column provides the labeling system that will be relevant in the analysis (Sec. 6.3.1).

Decay-Branch	Detection-Channel	Detection-ID
$\{^3He, H\}$		
$\{^3HeH^+, e^-\}$	$\{^3HeH^+, e^-\}$	`HT_mainM4`
$\{^3He^+, H, e^-\}$	$\{^3He^+, e^-\}$	`HT_mainM3`
$\{^3He, H^+, e^-\}$	$\{H^+, e^-\}$	`HT_mainM1`
$\{^3He^+, H^+, 2e^-\}$	$\{^3He^+, H^+, 2e^-\}$	`HT_2I2eM32`
	$\{^3He^+, H^+, e^-\}$	`HT_2I1eM32`
	$\{^3He^+, 2e^-\}$	`HT_1I2eM3`
	$\{H^+, 2e^-\}$	`HT_1I2eM1`
	$\{^3He^+, e^-\}$	`HT_1I1eM3`
	$\{H^+, e^-\}$	`HT_1I1eM1`
$\{^3He^{++}, H, 2e^-\}$	$\{^3He^{++}, 2e^-\}$	`HT_2I2eM34`
	$\{^3He^{++}, e^-\}$	`HT_2I1eM34`
$\{^3He^{++}, H^-, e^-\}$	$\{^3He^{++}, H^-, e^-\}$	
	$\{^3He^{++}, H^-\}$	
	$\{^3He^{++}, e^-\}$	
$\{^3He^{++}, H^+, 3e^-\}$	$\{^3He^{++}, H^+, 3e^-\}$	
	$\{^3He^{++}, H^+, 2e^-\}$	
	$\{^3He^{++}, H^+, e^-\}$	
	etc., but small	

Table 6.2: Physical-branches for HT beta decay. The table is very similar to Table 6.1.

As for the "Detection-Channel" column, it lists the combinations of the particles in a particular decay-branch that are detected by either the beta- or the ion-detector to form a coincidence-event. In other words, for each detection-channel, the beta-detector must detect at least 1 negatively charged particle and the ion-detector 1 positively charged ion to form

a coincidence. However, a valid TRIMS event does not require the detectors to capture all the product particles . For example, detection-channel $\{^3He^+$, e-$\}$ means out of the original decay-branch $\{^3He^+$, T^+, 2e-$\}$, the beta-detector detects 1 electron and the ion-detector detects the $^3He^+$; the other electron and the T^+ miss the detectors.

The "Detection-ID" column labels the detection-channels of interest to the TRIMS experiment; these detection-channels turn out to receive significant counts in the tritium-data (Sec. 7.4.1). As for the other branches, decay-branch $\{^3He, T\}$ cannot be detected by TRIMS, whereas decay-branch $\{^3He^{++}, T^-, e^-\}$ and $\{^3He^{++}, T^+, 3e^-\}$ are rare (Sec. 8.3.2, Sec. 8.3.3). Therefore, for convenience, when we refer to an ion, we assume it to be a positively charged ion.

Moreover, we refer to the branches whose decay produces 1 singly charged ion as the main-bands, and whose decay produces either 2 ions or 1 doubly charged ion as the minor-bands. In case of T_2, $\{^3HeT^+, e^-\}$, $\{^3He^+, T, e^-\}$, and $\{^3He, T^+, e^-\}$ belong to the main-bands, while $\{^3He^+, T^+, 2e^-\}$ and $\{^3He^{++}, T, 2e^-\}$ to the minor-bands.

Notice that many of the detection-channels are degenerate, e.g. both detection-channels $\{^3He^+, e^-\}$ and $\{T^+, e^-\}$ share the same detection-ID `T2_mainM3`. This is reflecting that TRIMS does not have the resolution to distinguish a T^+ from a $^3He^+$ because their masses are too close together. This mass degeneracy will follow through the rest of the analysis. Another note is about the `M34` $\left(\text{mass-}\frac{3}{4}\right)$ and the `M32` $\left(\text{mass-}\frac{3}{2}\right)$ labels in some detection-IDs, as will be explained in Sec. 7.1.1.

As for Table 6.2, it is nearly identical to Table 6.1. However, because a H^+ is much lighter in mass than a $^3He^+$, there is no detection-ID degeneracy problem for HT beta decays.

6.1.2 Ion-TOF and Ion-Energy

Before trying to identify the detection-channels in our data, we would like to apply two post-signal-processing corrections to improve our event reconstruction. The first is on the ion TOF (ion-TOF T_{ion}) and the second on the ion incident energy (ion-energy E_{ion}).

As for the beta incident energy (E_β), we just use `beta_edep` from Table 5.4.

Timing corrections

We can first approximate the ion-TOF by,

$$T'_{\text{ion}} \equiv \texttt{ion\_time2ND} - \texttt{beta\_time}, \tag{6.1}$$

where variables `ion_time2ND` and `beta_time` come from Table 5.4 in Sec. 5.4.2.

As a quick example to justify Eq. 6.1, consider a singly charged particle of mass m that is accelerated under a full potential of $V = 60\,\text{kV}$ from rest:

$$E = \gamma mc^2 = \sqrt{\frac{1}{1+\beta^2}}mc^2 = mc^2 + \text{KE} = mc^2 + qV, \tag{6.2}$$

where "KE" stands for kinetic energy. Suppose this particle is an ion with a mass of 3 atomic mass units, then,

$$\beta_{ion} = \sqrt{1 - \frac{1}{(1+\frac{qV}{m_{\text{ion}}c^2})^2}} \approx \sqrt{1 - \frac{1}{(1+\frac{60\,\text{keV}}{2\,808\,000\,\text{keV}})^2}} \approx 0.0065, \tag{6.3}$$

which is not quite relativistic. On the other hand, if the particle is an electron, then,

$$\beta_e = \sqrt{1 - \frac{1}{(1+\frac{qV}{m_e c^2})^2}} \approx \sqrt{1 - \frac{1}{(1+\frac{60\,\text{keV}}{511\,\text{keV}})^2}} \approx 0.45, \tag{6.4}$$

which is relativistic. This means that the beta-TOF is negligible compared to the ion-TOF. And so, we can treat the betas as if they arrive at the beta detector instantly after the decay,

$$\text{TOF}_{ion} - \text{TOF}_{\beta} \approx \text{TOF}_{ion} \approx t_{ion} - t_{\beta}, \tag{6.5}$$

where the t's are the arrival times.

One other important note is that from Sec. 5.4.2, (`ion_time2ND` = `ion_time`) for the cases when the ion-detector 2WS-fit is not invoked (Sec. 5.3.4). This applies to the majority of the cases, except for ion-detector events that detect both $\{^3\text{He}^+, \text{H}^+\}$ of a 2-ion event. The exception case will be covered in Sec. 7.1.2.

However, further corrections can be applied to Eq. 6.1,

$$T_{\text{ion}} \equiv \texttt{ion\_time2ND} - (\texttt{beta\_time} - \texttt{beta\_TOF}) - \texttt{time\_zero}, \tag{6.6}$$

where T_{ion} is the ion-TOF we are looking for. Compared to Eq. 6.1, Eq. 6.6 contains two additional terms, `beta_TOF` and `time_zero`.

The `beta_TOF` is the average TOF of the betas produced by the decays that take place in the decay chamber. This value is obtained using the Geant4 simulation. From Fig. 3.5, we get `beta_TOF` = 2.3 ns. The standard deviation of `beta_TOF` is as large as 0.7 ns, but we do not consider it for a reason we will discuss at the end of this subsection.

The `time_zero` is the intrinsic electronic timing difference caused by the setups for the beta-detector and ion-detector being slightly different; this correction is often referred to as the time-zero correction. To obtain `time_zero`, we inspect the ^{83m}Kr coincidence events (Sec. 2.3.3). Recall that when we took the krypton-data, the HV was off and only the magnets were on. In this case, the two electrons from each decay are guided by the magnetic field to either the beta- or the ion-detector. Because the electric field is absent, the Kr electrons provide symmetric coincidence events between the two detectors, and so their average TOF difference should be zero. This implies that the shift in (`ion_time` - `beta_time`) should give us an approximated value for `time_zero`.

The distribution of the krypton-data coincidence is given by Fig. 6.1, whose x-axis represents (`ion_time` - `beta_time`). The mean of the distribution should be the time zero we are looking for. The distribution has a sharp peak at the mean, which are the coincidence events between the IC electron and the prompt Auger electron. The distribution also has long tails toward both directions, which are the coincidence events between the IC electrons from the first and the second internal conversion. The second ^{83m}Kr internal conversion has a noticeable half-life, which explains the exponential tails. Because of the tails, the mean value of the distribution heavily depends on our choice of range. In order to avoid bias, we fit the distribution to an empirical function Eq. 6.7.

$$f(t) = Ae^{-\lambda_1(t-t_0)}\Theta(t-t_0) + Ae^{\lambda_2(t-t_0)}\Theta(t_0-t) + \frac{B\Gamma/2\pi}{(t-t_0)^2+(\Gamma/2)^2} + b, \qquad (6.7)$$

where the fit parameters are t_0, A, λ_1, λ_2, B, Γ, and b. The Θ's are Heaviside step functions. The fit function is basically two exponential decay functions whose exponents have different

signs; the parameters λ_1 and λ_2 are associated with the half-life of the second ^{83m}Kr internal conversion. The Θ functions ensure exponential decay on both sides of t_0. The function that has B and Γ as the parameters is a Lorentzian function. The function is symmetric and smoothes the connection of the two exponential functions at t_0. The b parameter is there to handle the flat background. The parameter in question is t_0 which roughly gives the "center" of the distribution, which is the time zero we are looking for. The fit of t_0 gives `time_zero` $= 9.46 \pm 0.07$ ns.

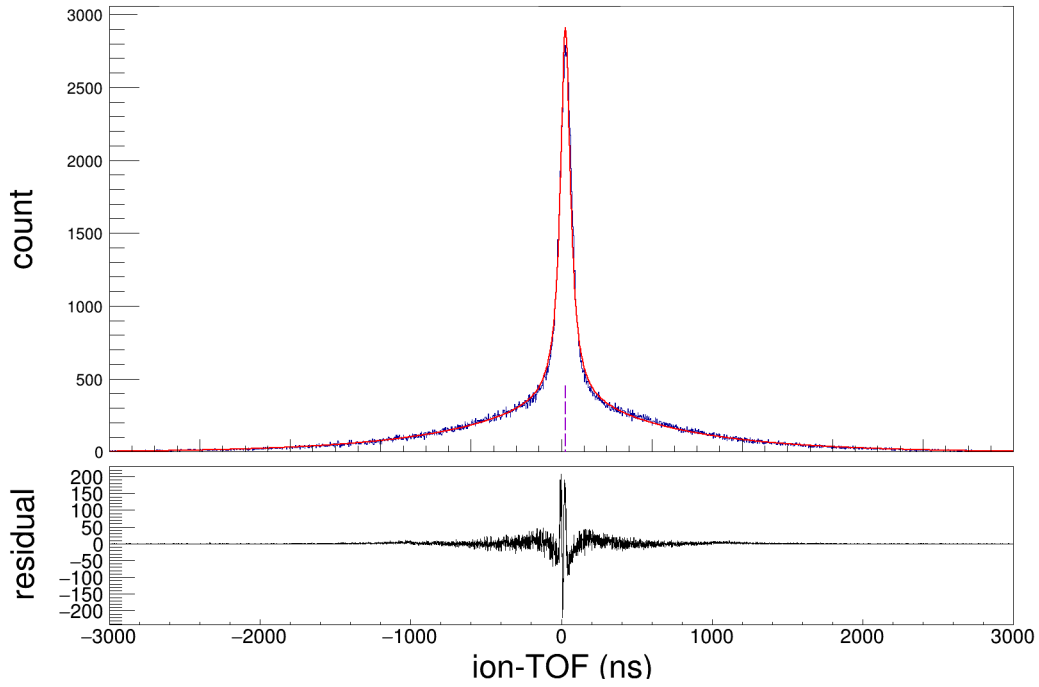

Figure 6.1: Electronics time-zero shift as obtained from ^{83m}Kr coincidence events. The ion-TOF on the x-axis represents T'_{ion} from Eq. 6.1, while the y-axis on the top plot represents the events count, and the maximum should locate at the time zero of our detector read out. We fit it to an empirical function Eq .6.7 to extract time zero and find $t_0 = 9.46 \pm 0.07$ ns from the time-origin. The position of the time zero is indicated by a shortened vertical dashed purple line. The χ^2`/dof` is 1.46. The bottom plot shows the absolute residual of the fit function to the data.

We plug in the `beta_TOF` and the `time_zero` in Eq. 6.6 as constants to complete the ion-TOF correction.

Energy corrections

For ion-energy, we have `ion_edep` from Table 5.4. But we also want to correct for the dead-layer effect as well as the pulse-height defect, which was discussed in Sec. 3.2.2. Fortunately, we already have a correction formula Eq. 3.13,

$$E_{\text{ion}} \equiv 2.864 + 1.507\texttt{ion\_edep} - 5.871 \times 10^{-3}\texttt{ion\_edep}^2 + 2.895 \times 10^{-5}\texttt{ion\_edep}^3, \quad (6.8)$$

where the coefficients have units as determined in Table. 3.10. Note that Eq. 6.8 treats every ion as if it is a $^3He^+$. This assumption will create biases with our fiducial-volume cut (Sec. 6.2.3), but they will be handled in Sec 8.2.3.

Notation and systematics discussion

For convenience, when we refer to ion-TOF, we will be referring to T_{ion} from Eq. 6.6 unless otherwise noted. Similarly, we refer to ion-energy as E_{ion} from Eq. 6.8 and beta-energy as $E_\beta = \texttt{beta\_edep}$.

These physics corrections technically do not factor into our ability to separate out the bands to get their branching ratios. However, these corrections give us the confidence that we do understand our data and improve out resolution.

On a related note, the energy resolution with gain corrections and the timing resolution are also not directly included in our systematics. Their effects are difficult to translate into branching ratio estimation. However, for the rest of the analysis, keep in mind that our approaches to the systematics indirectly take into account these broadenings.

6.1.3 Physics Data

Extracting from the analysis-ROOT-files (Sec. 5.4.2), we will now refer to these analysis tritium-data obtained using the T_2 source (Sec. 4.2.1) as the raw-T2-data and data from

using the HT source as raw-HT-data. As a reminder, the raw-T2-data uses the gas directly from our T_2 source, while raw-HT-data uses the gas that has undergone catalytic conversion with hydrogen (Sec. 2.3.2). A histogram of the raw-T2-data is given in Fig. 6.2. This histogram contains all the qualified T_2 run-scans. Notice that after the correction from Eq. 6.8, we can see band-No. a2) from Fig. 6.2 extends to 60 keV as expected.

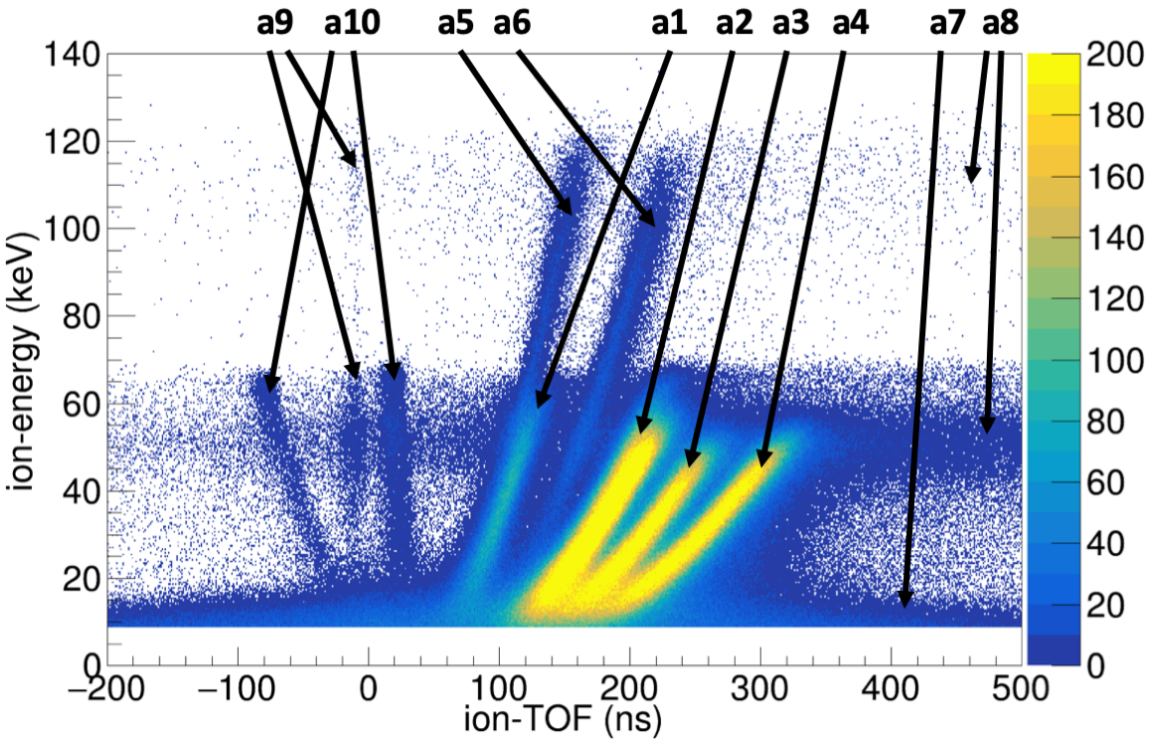

Figure 6.2: Ion-energy versus ion-TOF histogram for the raw-T2-data. The z-axis represents the event count. The bands are pointed out by the arrows and their descriptions are provided by Table 6.3 as identified by their band-ID.

Band-No.	Band Label	Description
a1	`M1`	Main-band detecting a mass-1 ion and an electron
a2	`M3`	Main-band detecting a mass-3 ion and an electron
a3	`M4`	Main-band detecting a mass-4 ion and an electron
a4	`M6`	Main-band detecting a mass-6 ion and an electron
a5	`M32`	Minor-band detecting a $^3He^{++}$ with either 1 or 2 electrons
a6	`M34`	Minor-band detecting either $\{^3He^+, T^+\}$ or $\{^3He^+, H^+\}$ with either 1 or 2 electrons
a7		Events that have low ion-energy, which likely originate from decays close to the ion-electrode
a8		Events that have low beta-energy, which likely originate from decays close to the beta-electrode
a9		Events that miss the beta but detect secondary electrons coming from ions hitting the ion-detector
a10		Events that miss the beta but detect secondary electrons coming from the ion hitting the mesh ion-electrode. These events require 2 ions because while 1 ion hits the mesh, the other ion needs to be detected (Sec. 7.1.1).

Table 6.3: Band identification of Fig. 6.2. The masses are provided in unit of amu. The "Band Label" covers one aspect of the detection-ID in Table 6.1 and 6.2.

The corresponding labels in Fig. 6.2 are described in Table 6.3. Band-No. a1), a2), a3), and a4) correspond to the main-bands, i.e. detection-ID m1, m3, m4, and m6 in Sec. 6.1.1. We can see the band-No. a2) that corresponds to $^3He^+$ stretches to 60 keV under Eq. 6.8 as expected as from us running 60 kV HV. Note that, as discussed in Sec. 2.3.2, the T_2 source

used for the raw-T2-data was not pure; the T_2 source had more than 30% HT contamination that was slowly increasing over time [132]. This is the reason why band-No. a1) and a3) that come from HT decay products H^+ and $^3HeH^+$ can be spotted in the raw-T2-data. The ion-energy versus ion-TOF histogram for the raw-HT-data is given in Fig. 6.3, where band-No. a4) for $^3HeT^+$ is less prominent as expected.

If we skip band-No. a5) and a6) for a moment, band-No. a7) and a8) most likely come from the decays close to the electrodes whose product charged particles spend a substantial amount of time in a region of low electric field. Having in addition either low beta- or ion-energy, those events end up having low timing resolution (see Fig. 5.12), and so a very broad T_{ion}. These events can also come from randomly triggered noise events for we set a low software threshold (`SoftThreshold` from Table 4.2). Band-No. a9) are the events when the beta-detector misses the beta, but detects the secondary electrons that are knocked out when the ion or the ions are incident on the ion-detector*. These undesirable events will be removed by further event cuts (Sec. 6.2.3).

As for band-No. a10) events, they are events when the beta-detector misses the beta but detects the mesh-electrons, which are the secondary electrons that are knocked out when an ion is incident on the mesh ion-electrode. The ion that hits the mesh will be lost from the detection, so this type of events requires 2 ions from the decay. These events have a surprising application in terms of determining the HT purity of our source (Sec. 7.1.1).

Band-No. a5) and a6) come from the minor-bands where the ion-detector detects 2 ions, i.e. the detection-channels that have "2i"'s in Table 6.3. Notice that, as shown in Fig. 6.2, the minor-bands are overlapping with the main-bands, e.g. the lower ion-energy portion of band-No. a5) is overlapping with band-No. a1). To separate out the minor-band events properly, we need to include the information of the beta-energy (`beta_edep` from Table 5.4).

---

*These knocked out electrons must have greater than 100 eV to pass the mesh that is set at -100 V (Sec. 2.1.1). This is confirm when we took data using a mesh voltage of -25 V instead that result in a much more prominent band-No. a9).

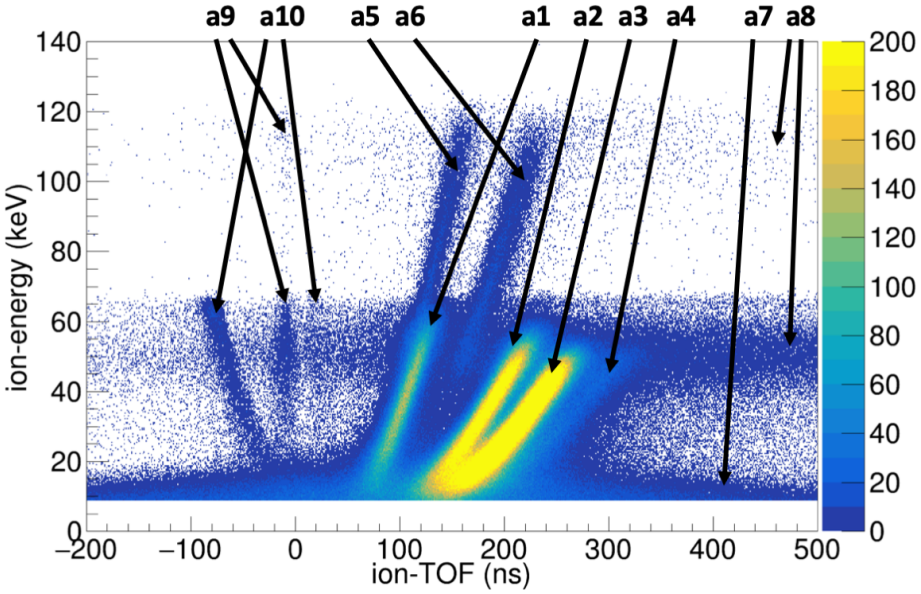

Figure 6.3: Ion-energy versus beta-energy histogram for the raw-HT-data. Compared to Fig. 6.2, the mass-6 band-No. a4) becomes much less prominent.

This leads to the ion-energy versus beta-energy histogram shown in Fig. 6.4, whose band labels are described in Table 6.4. All the four main bands are joined as band-No. b1). The minor bands however, are separated into 3 categories. Band-No. b2) `2I1e` events include `2I1em34` and `2I1em32` from Sec. 6.1.1, band-No. b3) `2I2e` events include `2I2em34` and `2I2em32`, and band No. b4) `1I2e` events include `1I2em1` and `1I2em3`. The `1I1em1` and `1I1em3` events are buried in band-No. b1), which requires assistance from the Geant4 simulation to separate out (Sec. 7.2.3).

Band-No. b5) events are the electron-backscattering events that result in beta-energy loss (see Sec. 3.1.3). Handling beta-backscattering events also requires assistance from the Geant4 simulation (Sec. 7.2.3).

Band-No. b6) events correspond to band-No. a9) and a10) events. From Fig. 6.4 we can see that mesh-electrons provide beta-energies in integer multiples of 60 keV, which is expected because electrons generated at the mesh must go through the entire 60 kV potential to reach

the beta-detector. Moreover, an ion can knock out more than one electron at a time. These electrons arrive on the beta-side so close in time that the beta-detector would register one single large signal with an amplitude that equals 60 keV multiplied by the number of captured electrons. This multiple mesh-electron detection does occur quite frequently according to the data.

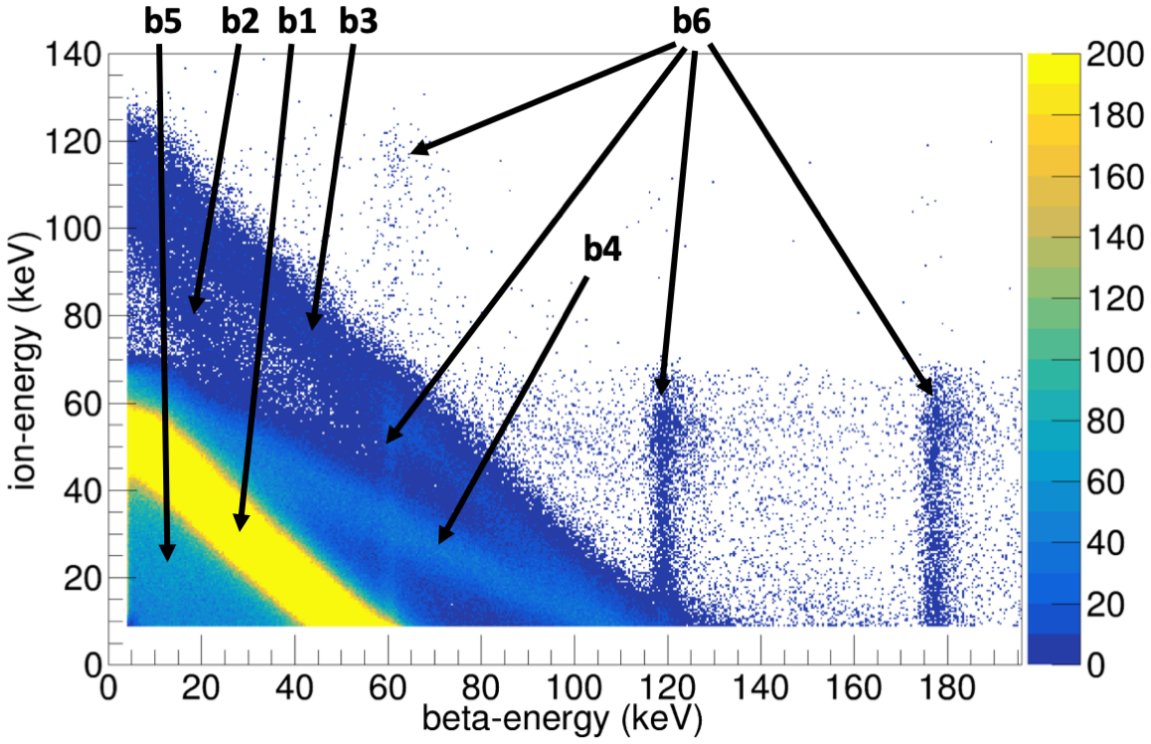

Figure 6.4: Ion-energy versus beta-energy histogram for the raw-T2-data. The z-axis represents the event count. The bands are pointed out by the arrows and their descriptions are provided by Table 6.4 as identified by their band-ID.

Band-No.	Band Label	Description
b1	`main, 1I1e`	Main-band or the `1I1e`-band. The `1I1e`-band is a minor-band where 2 ions are produced but the ion-detector detects only 1 ion and the beta-detector detects 1 electron
b2	`2I1e`	Minor-band where the ion-detector detects 2 ions or 1 doubly charged ion, and the beta-detector detects 1 electron
b3	`2I2e`	Minor-band where the ion-detector detects 2 ions or 1 doubly charged ion, and the beta-detector detects 2 electrons
b4	`1I2e`	Minor-band where the ion-detector detects 1 ions, and the beta-detector detects 2 electrons
b5		Events when electrons backscatter from the beta-detector
b6		Events coming from band-No. a9) and a10) in Table 6.3

Table 6.4: Band identification of Fig. 6.4. The "Band Label" covers one aspect of the detection-ID in Table 6.1 and 6.2.

6.1.4 Exceptional Runs and Overall Data Collected

At this stage of the analysis, we are picking up a number of undesirable runs from the tritium-data that escape our data quality control (Sec. 4.3). These exceptional runs can be categorized into fuzzy-runs, deficit-runs, and excess-runs. This section will briefly discuss each of them.

For the fuzzy-runs, their ion-energy vs ion-TOF histogram is shown in Fig. 6.5. Compared to Fig. 6.2, no band structure is evident in a fuzzy-run. Eventually, we figured out the

problem was caused by digitizer glitches in the waveform as shown in Fig. 6.6. These glitches can happen before (Fig. 6.6.a)) or after (Fig. 6.6.b)) the signal waveform. In the two cases shown in Fig. 6.6, the WS-functions from dCFD (Sec. 5.3.2) are fitted correctly. However, in many other cases, the glitches happen too close to the signal, create "fuzziness" in the timing, and render the data unusable.

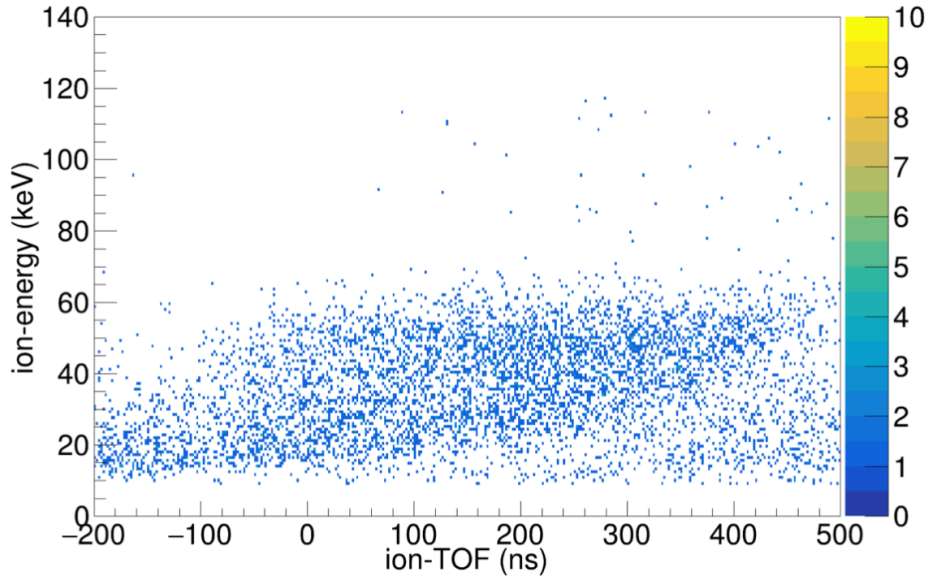

Figure 6.5: Ion-energy versus ion-TOF histogram of a fuzzy-run. The plot should be compared to Fig. 6.2.

The glitches in a fuzzy-run affect both the beta and the ion-detector on all of their waveforms within the run. Curiously, the glitch is confined in one run, and the chance of a run being a fuzzy-run appears to be independent from all the other runs. Nevertheless, in order to correctly perform the normalization between run-scans (Sec. 7.1.4), once we identify a fuzzy-run, we need to drop the entire run-scan that contains the run. A normalization scheme that allow us to drop individual runs has not yet been developed at the time of this thesis.

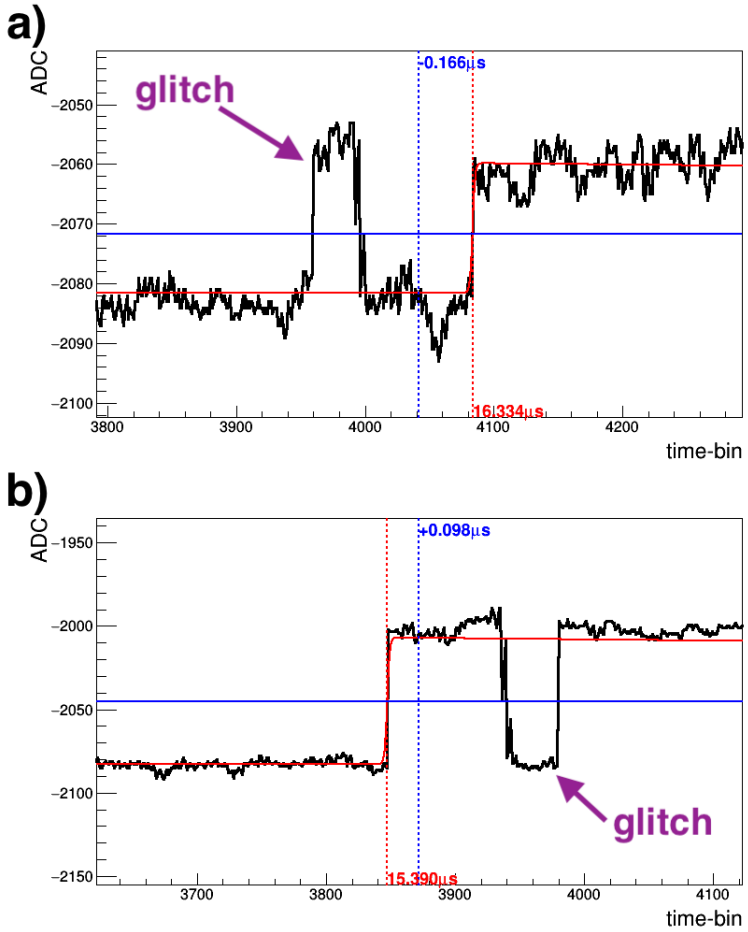

Figure 6.6: fuzzy-run waveforms. The digitizer glitches are pointed out by the purple arrows. Plot a) shows the case when a glitch happens before the physical pulse and plot b) after. For either of the cases, the dCFD mis-fits the WS-function to the glitch in many of these events, even though they are not mis-fit for the two waveforms shown.

For the deficit-runs, we found them when we plotted the event rate of every run in the tritium data as shown in Fig. 6.7. In a normal run, the event rate should be flat across its 300 s run period. However, runs in Fig. 6.7 are showing a deficit in event rate at a certain period of the run duration. The data in the deficit-runs are otherwise of good quality.

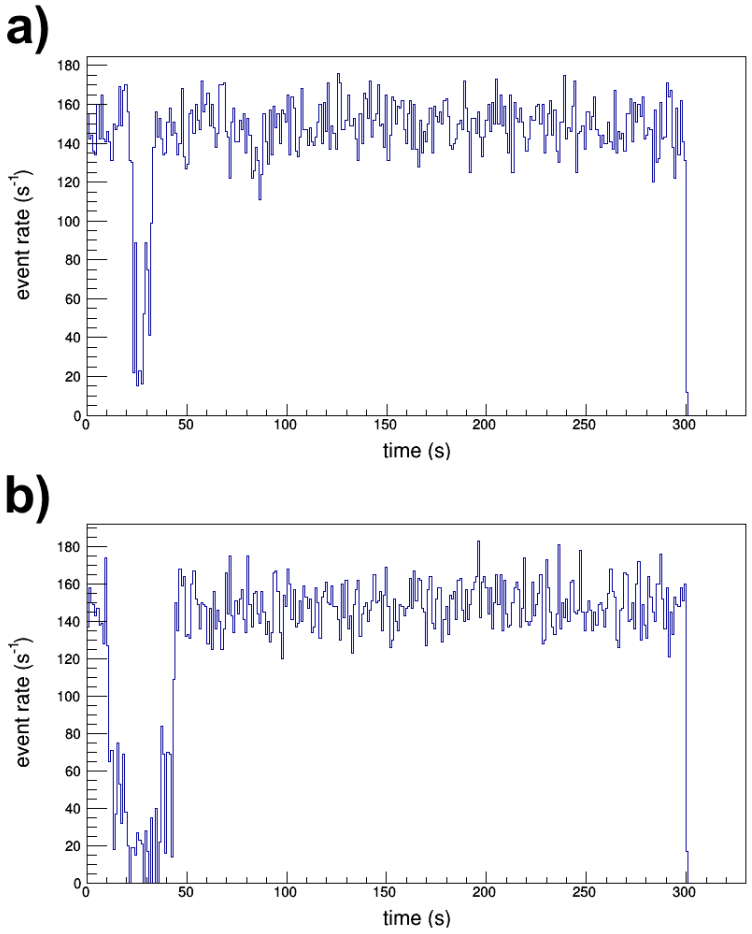

Figure 6.7: Deficit-run event rate over time. The x-axis represents the acquisition time since the start of the run, while the y-axis represents the ion-detector event rate in count per second. In plot a), we can see a deficit in event rate at the 25 s mark for the run, while plot b) shows a much more severe case in a different deficit run.

For the excess-runs, they only stand out when we compare the number of counts of other runs at the same scan-position (Sec. 5.4.2), which is shown in Sec. 6.8. The excess-runs appear to have over twice as many events as the other runs. Moreover, this excess is not present when comparing other runs in the run-scan that contains an excess-run. The data in the excess-runs are otherwise of good quality.

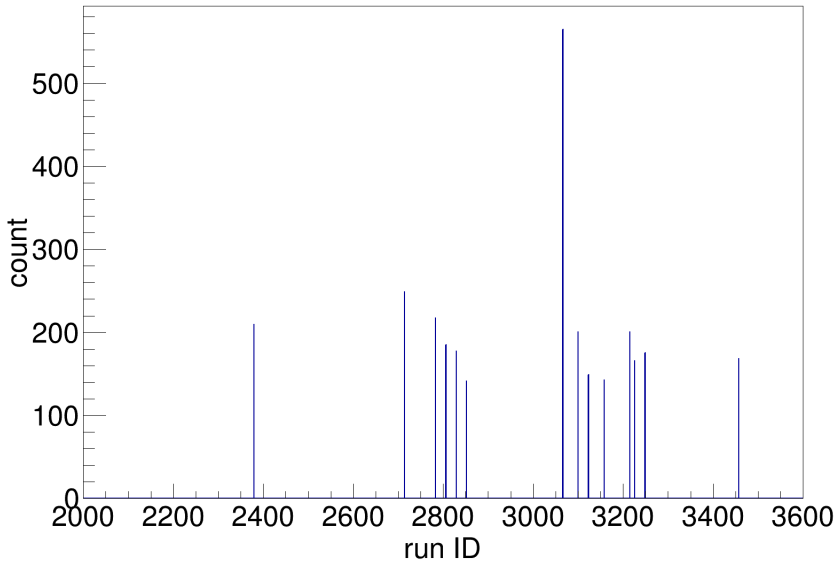

Figure 6.8: Cumulative count for each run at scan-point ($d = -7$). The x-axis represents the run-ID of the runs present, while the y-axis represents the event count per run. We can see there is one run that stands out, which we refer to as the excess-run.

Considering that the deficit- and the excess-runs do not seem to have a significant impact on the analysis*, we do not drop these runs. Otherwise, we would need to drop the entire run-scan, which would drastically impact our statistics. For this reason, the `quality` entry in the tritium-data spreadsheet Table 4.5 mostly tags the fuzzy-runs as well as all the runs that belong to the same run-scan†. After dropping all the fuzzy-runs and keeping the deficit- and excess-runs, Fig. 6.9 shows the accumulated count in the tritium-data that we include in our final analysis. The systematics associated with including the deficit- and the excess-runs is considered in Sec. 7.1.4.

The corresponding run numbers associated with these exceptional runs are given in the App. A. At the time of this thesis, we do not understand what causes the glitch in the

*related to the source-activity normalization in Sec. 7.4.1.

†The only odd exception is provided in the App. A.2.

fuzzy-runs, nor the deficit and the excess in the otherwise good quality runs. However, we are continuing to investigate the cause and the impact of these exceptional runs past the completion of this work (Sec. 9.2.1).

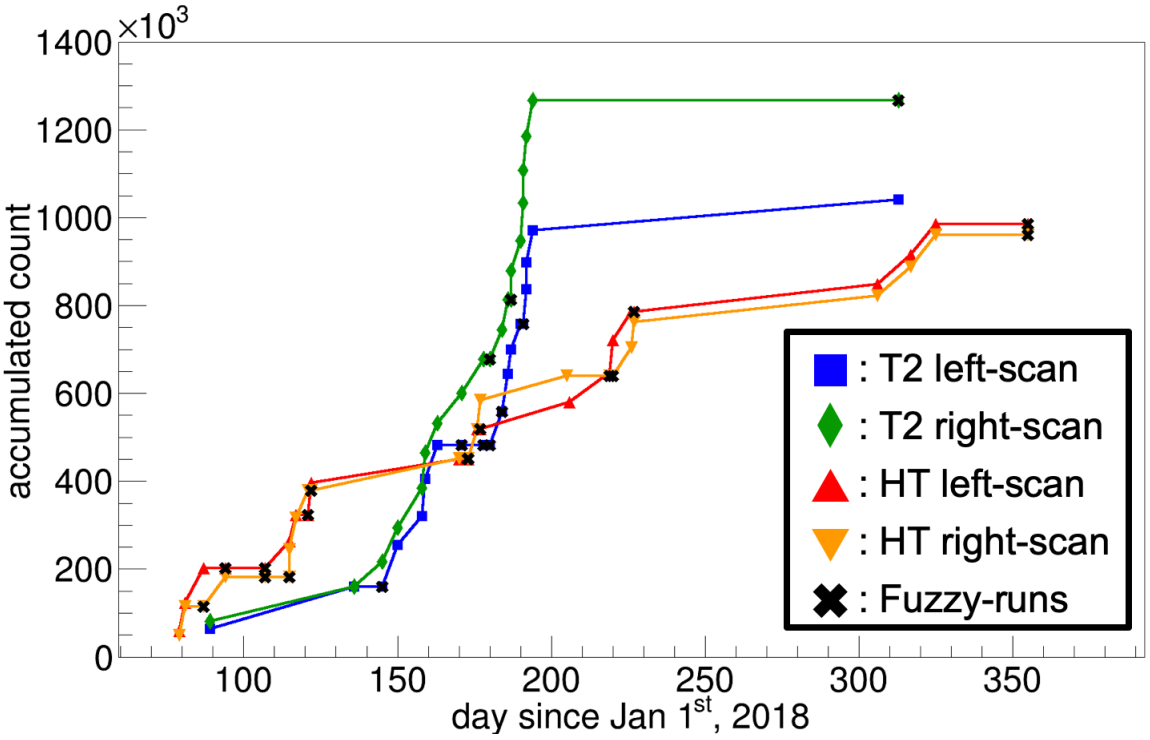

Figure 6.9: The total data collected that goes into our final analysis. The x-axis represents the days in 2018 when we were taking our data, while the y-axis represents the data counts accumulated up to that day in the x-axis. The counts include both the coincidence and the single events at the home-position. The data are separated into 4 categories: left- and right-scan of raw-T2-data and raw-HT-data as shown in the legend. The black crosses indicate that there is a fuzzy-run in at least one of the run-scans collected that day; the run-scans that contain fuzzy-runs do not go into the count accumulation.

6.2 Charge and Mass Reconstruction

It is difficult to separate out the bands according to different detection-IDs from Table 6.1 and Table 6.2 directly using Fig. 6.2 and Fig. 6.4. For this reason, in this section, we are empirically reconstructing the charge information to better separate out minor-bands from the main-bands and the mass information to better separate out the bands with different ion masses.

6.2.1 Charge Reconstruction

For the charge reconstruction, we apply the following formula,

$$Q_{ie} \equiv \frac{E_{\text{ion}} + E_{\text{beta}} - 3\,\text{keV}}{60\,\text{kV}}, \tag{6.9}$$

where the ion-energy E_{ion} and beta-energy E_{β} come from Sec. 6.1.2. The "$-3\,$keV" comes from the tritium beta spectrum that has a maximum at $3\,$keV*. The subtraction is done so that the beta is assumed to be at rest initially after the decay. Then the formula is divided by $60\,$kV corresponding to our HV potential, which gives Q_{ie} a unit of charge.

Notice that Q_{ie} is a pseudo-charge defined in a way that such that if 1 ion and 1 electron (thus the subscript ie) are detected in our system, Q_{ie} gives the value of an electron charge ($Q_{ie} = 1\,\text{e}$). The ($Q_{ie} = 1\,\text{e}$) can be thought of as a line in Fig. 6.4 that connects the $60\,$kV beta-energy on the y-axis to the $60\,$keV ion-energy on the x-axis; the line is along the main-band and is parallel to the `2I2e`-band (Table 6.4). The line corresponds to the `2I2e`-band should ideally give ($Q_{ie} = 2\,\text{e}$).

---

*The choice is historical; the beta spectrum average of $5.7\,$keV should be a more reasonable choice. However, this additional constant only shift Q_{ie} by a constant, which would not influence the result of the analysis.

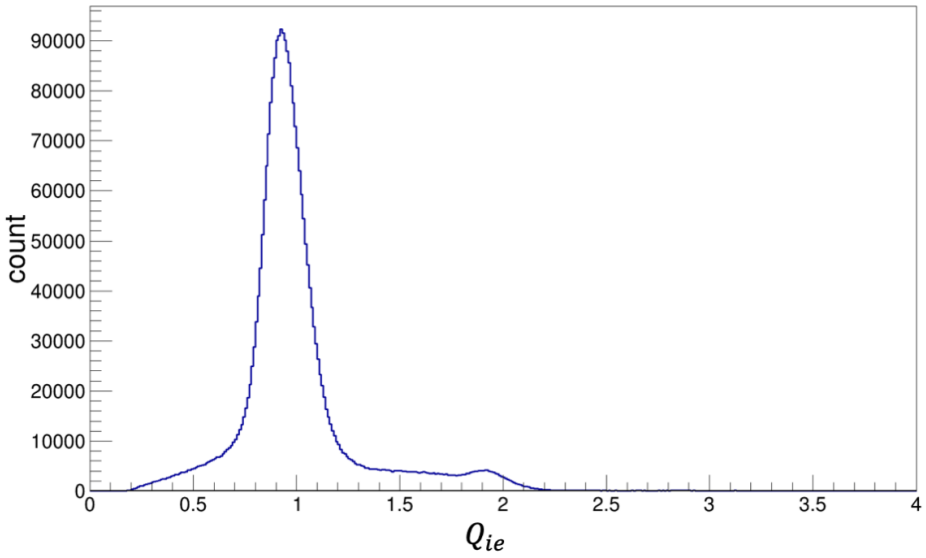

Figure 6.10: Charge histogram for the raw-T2-data. The x-axis represents the reconstructed charge based on Eq. 6.9, while the y-axis represents the event count.

The charge histogram for the raw-T2-data is given in Fig. 6.10. We can see that the main-band forms the largest peak around a charge of ($Q_{ie} = 1\,\mathrm{e}$) as expected, while the `2I2e`-band forms another peak at around ($Q_{ie} = 2\,\mathrm{e}$). The `2I1e`- and the `2I2e`-band do not form any peaks; they form a flat plateau that connects the two peaks. Notice that these peaks do not center perfectly at an integer charge. Many complications may have caused the deviation, but this deviation does not adversely affect our ability to separate the bands as long as the charge reconstruction is applied consistently to all events.

6.2.2 Mass Reconstruction

The mass in this context refers to the ion mass. Because TRIMS is doing an ion-TOF measurement, the bands with different ion masses are separated out from one another in our data as shown in Fig. 6.2. To more accurately address the separation, we reconstruct the ion mass for each event using the ion's kinematic information.

Several assumptions are in place to simplify the derivation. According to Eq. 6.3, we

can safely assume the ions are non-relativistic. We also assume the mesh voltage was small compared to the 60 kV HV. Moreover, we assume that the initial kinetic energy of the ions is negligible because the recoil energy is in the tens-of-eV range.

Under the assumptions, suppose we have a singly positively charged ion that starts out at rest in the region between the two electrodes of the TRIMS experiment (see Fig. 2.1). Then referring back to Table 2.1, the ion receives a constant acceleration of $qV/m_{\rm ion}L$, where the extra parameter q is one positive electron charge and $m_{\rm ion}$ the mass of the ion. Suppose the decay happens D_{ion} away from the ion-electrode, and suppose that it takes the ion Δt_D to traverse across D_{ion} under the constant acceleration and Δt_L across $L_{\rm ion}$ under constant speed $v_{\rm ion}$. The parameter $v_{\rm ion}$ is the final ion speed after it crosses the acceleration region. Then given the incident ion energy $E_{\rm ion}$, we have,

$$D_{ion} = \frac{E_{\rm ion}L}{qV}, \text{ and } v_{\rm ion} = \sqrt{\frac{2E_{\rm ion}}{m_{\rm ion}}}, \tag{6.10}$$

which can be used to evaluate Δt_D and Δt_L,

$$D_{ion} = \frac{E_{\rm ion}L}{qV} = \frac{1}{2}\frac{qV}{m_{\rm ion}L}(\Delta t_D)^2 \quad \Rightarrow \Delta t_D = L\sqrt{\frac{2m_{\rm ion}E_{\rm ion}}{(qV)^2}}, \tag{6.11}$$

$$v_{\rm ion} = \sqrt{\frac{2E_{\rm ion}}{m_{\rm ion}}} = \frac{L_{\rm ion}}{\Delta t_L} \quad \Rightarrow \Delta t_L = L_{\rm ion}\sqrt{\frac{m_{\rm ion}}{2E_{\rm ion}}}. \tag{6.12}$$

And so,

$$T_{\rm ion} = \Delta t_D + \Delta t_L = \sqrt{m_{\rm ion}}\left(L\frac{\sqrt{2E_{\rm ion}}}{qV} + L_{\rm ion}\frac{1}{\sqrt{2E_{\rm ion}}}\right) \tag{6.13}$$

$$\Rightarrow M_m \equiv m_{\rm ion} = 2E_{\rm ion}\left(\frac{T_{\rm ion}}{\frac{2E_{\rm ion}}{qV}L + L_{\rm ion}}\right)^2. \tag{6.14}$$

Since we already have L, $L_{\rm ion}$, and V from Table 2.1 as well as $T_{\rm ion}$ and $E_{\rm ion}$ from Sec. 6.1.2, we can evaluate this reconstructed ion mass M_m from Eq. 6.14 for every event in our data. The subscript m stands for main as in the main-band because Eq. 6.14 only approximates the ion mass correctly in atomic mass unit (u) if the ion-detector detects only 1 singly charged ion.

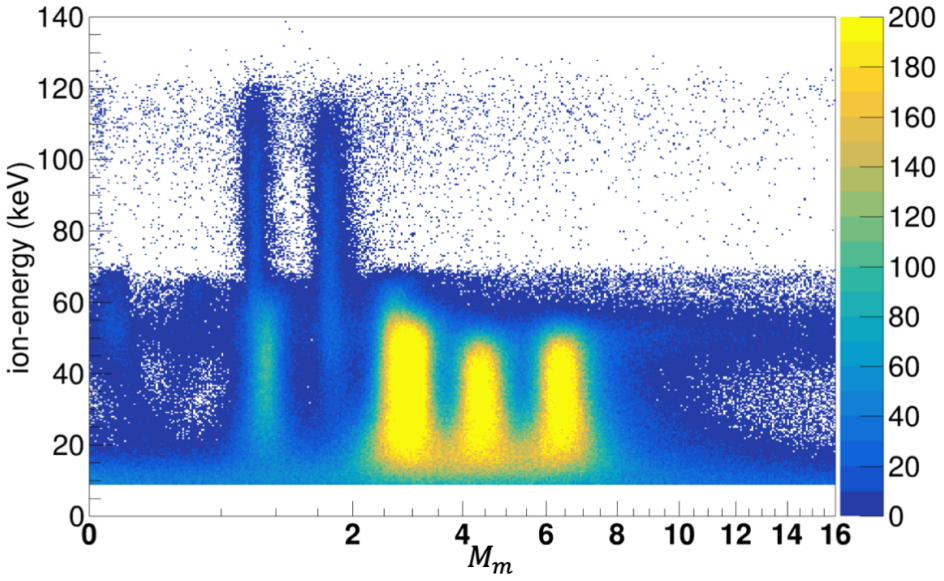

Figure 6.11: Ion-energy versus mass histogram for the raw-T2 data. The y-axis represents the ion-energy, while the x-axis represents reconstructed ion mass based on Eq. 6.14 and is in the square-root scale. The z-axis represents the event count.

The histogram of ion-energy versus the mass is given by Fig. 6.11. Notice that the x-axis is M_m in the square-root scale. The variable $\sqrt{M_m}$ will be a convenient choice for us because it scales linearly with T_{ion}, and so the mass peak broadening contributed by T_{ion} stays comparable between different mass species. The structure of Fig. 6.11 is similar to that of Fig. 6.2. However, the $\sqrt{M_m}$ values are largely independent of ion-energy, which allows us to separate the bands by setting cuts on the $\sqrt{M_m}$.

One caveat is that the negative ion-TOF events have their mass reconstructed using the absolute value of their T_{ion}. These undesirable events are filtered out using cuts described in Sec. 6.2.3.

Notice that similar to the charge reconstruction, the mass peaks are not exactly centered at integer atomic mass. Many detailed corrections can be placed on top of Eq. 6.14 to obtain a more accurate mass estimation. However, once again, the mass reconstruction is an

empirical tool that helps us separate the bands; small deviations do not impact our ability to separate the bands.

6.2.3 Basic Event Cuts and the Main Fiducial Volume Cut

Filter-No.	`TCut` Name	Equation/Description
B1	`ionEThres`	4 <= `ion_edep`; 4 keV ion deposited energy threshold
B2	`betaEThres`	4 <= `beta_edep`; 4 keV beta deposited energy threshold
B3	`betaNonlinADCCut`	`beta_amp` < 400; 400 ADC beta amplitude cut to prevent inaccurate values from beta nonlinear calibration
B4	`RUNCUT`	Cutting out the runs tagged by `quality` entry in the tritium-data spreadsheet Table 4.5, which mostly cut out the fuzzy-runs and the runs in the same run-scan (Sec. 6.1.4)
B5	`timeCut`	50 <= T_{ion} < 400; [50, 400)ns ion-TOF cut to remove irrelevant/noise events
B6	`FVCut`	20 <= E_{ion} < 40; [20, 40)keV ion-energy fiducial volume cut based on the corrected ion-energy

Table 6.5: Basic spectrum filters.

To remove some undesirable events from the data, we apply several cuts as given in Table 6.5. Filters B1 and B2 are energy threshold cuts on top of the software threshold filter A4 in

Table 6.5. Filter B3 is added to filter out the high beta-energy events that can appear to have low beta-energy because of the polynomial fit from the beta-detector calibration (Fig. 5.8); the polynomial reaches its maximum around 500 ADC and start decreasing afterward. Filter B4 cuts out the fuzzy-runs that were discussed in Sec. 6.1.4. Filter B1 to B4 are basic cut that remove only the noise and unphysical events and they are applied to all the plots starting from Ch. 6, including the plots before this section.

Filter B5 removes all the negative ion-TOF (Eq. 6.6) events as well as all the noise events with large ion-TOF that are most likely random coincidence events (later in Fig. 7.37). The main- and the minor-bands from Table 6.3 contain the physics events in question. These events are well-contained in this time window, especially when we apply it at the same time with the next filter, filter B6.

The most important filter that we applied is filter B6 the fiducial volume (FV) cut. The cut is set to be [20, 40)keV on the ion-energy E_{ion} from Eq. 6.8. This energy range of interest (compared to Sec. 5.3.5) allows us to ignore the events close to the electrodes that either have low ion- or low beta-energy, and so have bad timing-resolution (see Fig. 5.12). The cut essentially limits our study to the decays that happen in the fiducial volume (FV) near the center of the decay chamber. As the branching ratio is independent of where the decay happens, having a fiducial volume would not alter our physics results. The FV-cut was originally implemented using the beta-energy. However, due to the concern that the beta backscattering would shift the beta-energy, we updated to using the ion-energy. Using ion-energy has its concern too, in that the dead layer affects different ion species differently, and we need to perform a fiducial volume correction at the later stage of the analysis (Sec. 8.2.3).

Filter B5 and B6 are often applied together, and we refer to it as the main-FV cut.

Figure 6.12, 6.13, 6.14, and 6.15 shows how the main-FV filter affects the raw-T2-data.

The one feature that is most worthy to point out is the third charge peak that appears in between the ($Q_{ie} = 1$) and ($Q_{ie} = 2$) peaks in Fig. 6.15. This third peak corresponds to the `1I2e`-band ((band-No. b4) of Fig. 6.4), which is isolated out by the FV-cut as shown in Fig. 6.13.

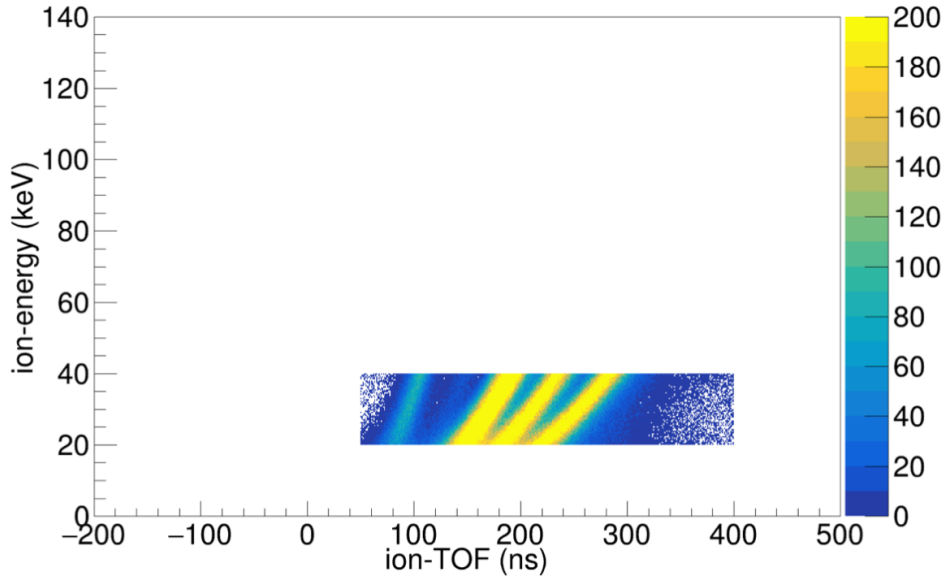

Figure 6.12: Events inside the main-FV for the ion-energy versus ion-TOF histogram Fig. 6.2.

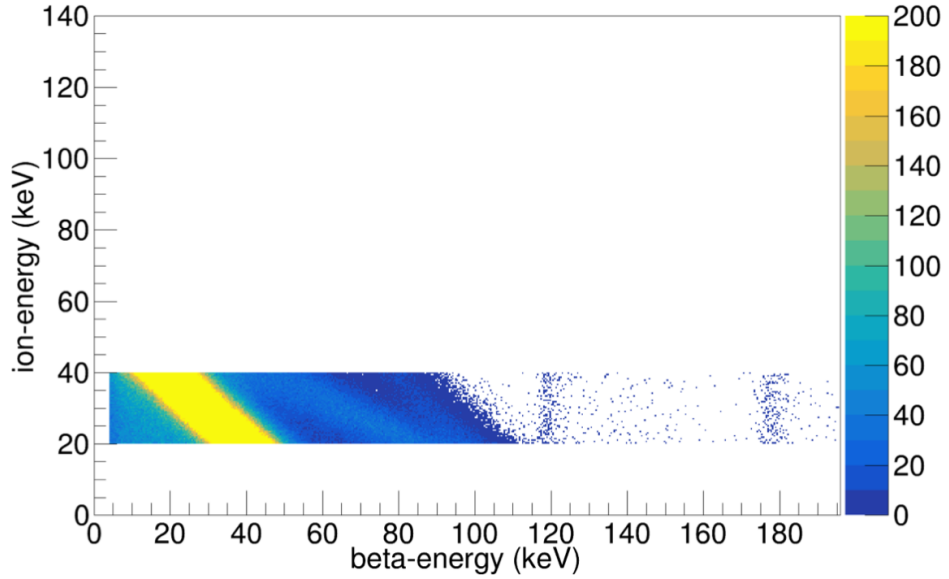

Figure 6.13: Events inside the main-FV for the ion-energy versus beta-energy histogram Fig. 6.4.

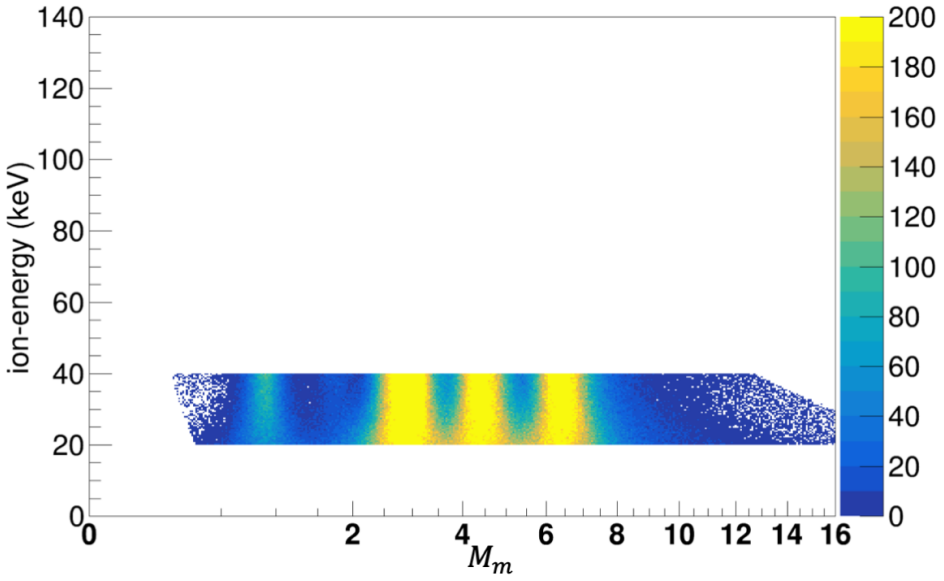

Figure 6.14: Events inside the main-FV for the ion-energy versus mass histogram Fig. 6.11.

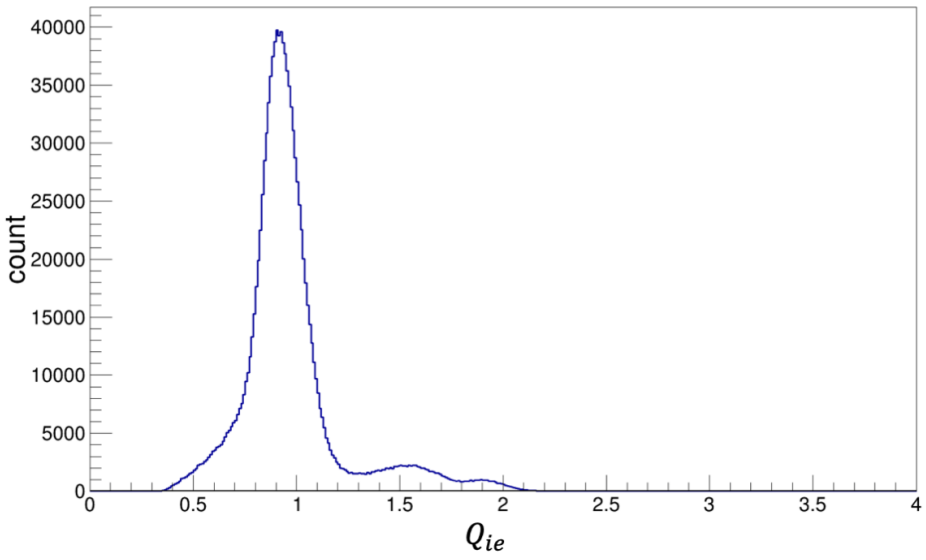

Figure 6.15: Events inside the main-FV for the charge histogram Fig. 6.10.

6.2.4 Charge-Mass Plane

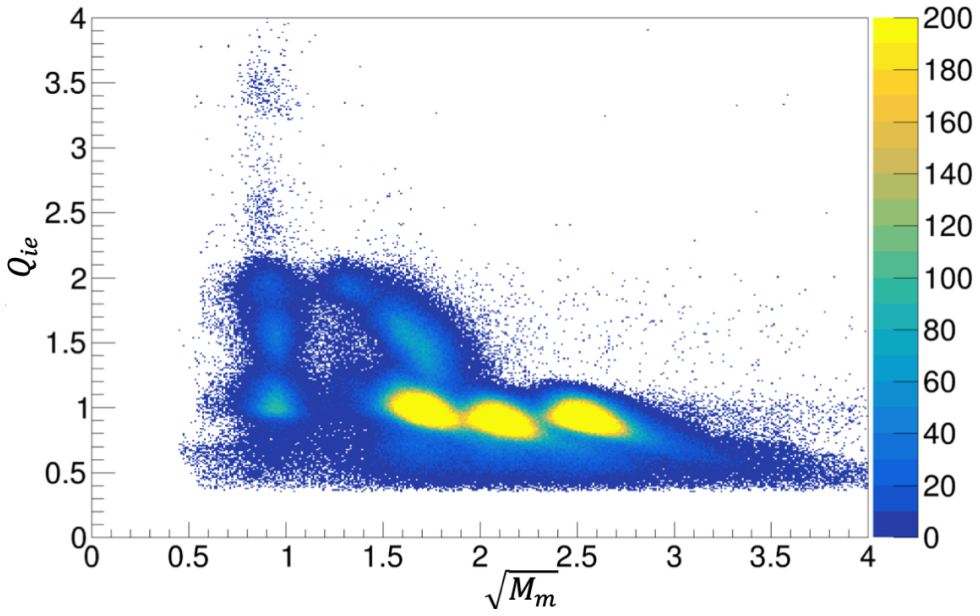

Figure 6.16: Charge versus mass histogram for the raw-T2-data under the main-FV cut.

Finally, by combining the charge and mass reconstruction, the charge versus mass histogram is given in Fig. 6.16. This is the point when we can start to separate out the main- and minor-bands.

6.3 Charge-Mass Boxing

6.3.1 Charge and Mass Cuts

To separate out the physical bands in Table 6.1 using Fig. 6.16, we partition the raw-T2-data into 8 regions as shown in Fig. 6.17. We refer to each of the 8 regions as a charge-mass box or a CM-box. The get the CM-boxes, we applied three charge cuts, which is represented by the horizontal purple lines in Fig. 6.17. From bottom to top, the lines are located at ($Q_{ie} = 1.3\,\mathrm{e}$), ($Q_{ie} = 1.7\,\mathrm{e}$), and ($Q_{ie} = 2.3\,\mathrm{e}$). The region that falls in charge range of [0, 1.3)e is referred to as charge-box `c1`, range of [1.3, 1.7)e as `c2`, and range of [1.7, 2.3)e as `c3`. Similarly,

we applied three mass cuts, which are represented by the vertical green lines in Fig. 6.17. From left to right, the lines are at ($\sqrt{M_m} = 1.2\,\sqrt{\text{u}}$), ($\sqrt{M_m} = 2\,\sqrt{\text{u}}$), and ($\sqrt{M_m} = 2.3\,\sqrt{\text{u}}$). The region that falls in $\sqrt{M_m}$ range of $[0,\ 1.2)\sqrt{\text{u}}$ is referred to as mass-box `m1`, range of $[1.2,\ 2)\sqrt{\text{u}}$ as `m3`, range of $[2,\ 2.3)\sqrt{\text{u}}$ as `m4`, and range of $[2.3,\ 4)\sqrt{\text{u}}$ as `m6`. Notice however that only charge-box `c1` is further partitioned into 4 separate mass-boxes; CM-box `c2` and `c3` are only partitioned into 2 separate mass-boxes. In this way, we have 8 CM-boxes: `c1m1`, `c1m3`, `c1m4`, `c1m6`, `c2m1`, `c2m346`, `c3m1`, and `c3m346`.

The basic idea is to have a dominant physics band from Table 6.1 in each CM-box, and address the "leakage" of the dominant-bands to other boxes in the later analysis (Ch. 7); we refer to the leakage as cross-contamination (CC). The dominant-bands in each of the CM-boxes are provided in Table 6.6. Many of the CM-boxes do not have a dominant-band because the CM-boxes are actually shared between raw-T2- and raw-HT-data. The raw-HT-data counterpart of Fig. 6.17 is given by Fig. 6.18, and the corresponding dominant-band in CM-boxes by Table 6.7.

There are no `1I1e`- or `2I1e`-bands in Table 6.6 and 6.7. The `1I1e`-bands are absent because they are physically indistinguishable from the main-bands, i.e. the `m1`, `m3`, `m4`, `m6` bands. The `2I1e`-bands are absent because due to the FV-cut, the "leftover" of the `2I1e`-bands is completely overlapping with the main-bands (see where band-No. b2) in Fig. 6.4 ends up in Fig. 6.13). This issue will also be addressed as a part of the cross-contamination; specifically, we need to rely on a factor called the 1eV2e ratio from the Geant4 simulation (Sec. 7.2.4).

One note about the reduction of data from Fig. 6.16 to Fig. 6.6. In order to have a better comparison with the later results, we focus on the left-scan data at the home-position. Much of the analysis work done in Ch. 7 will be scan-position dependent.

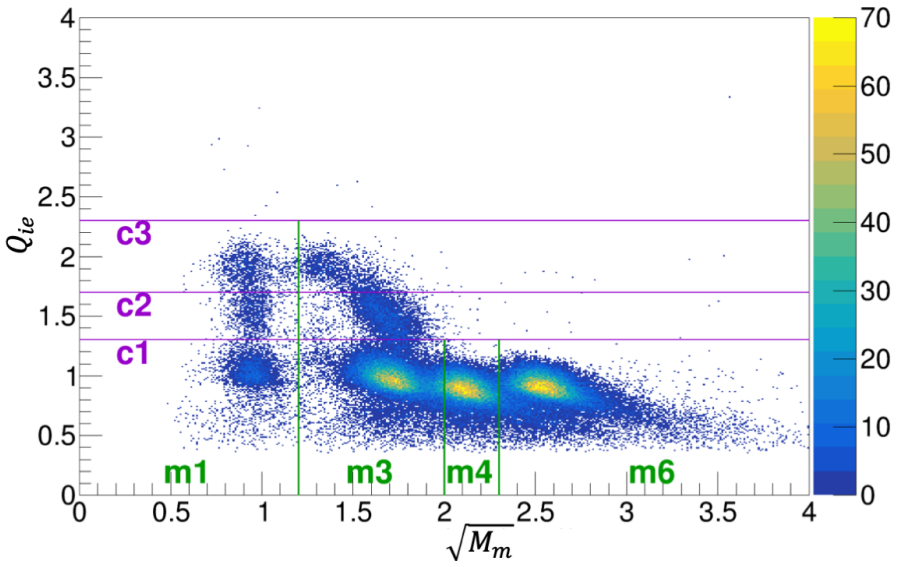

Figure 6.17: Charge-mass boxing for the left-scan raw-T2-data at the home-position in the main-FV. The boxing partitions Fig 6.16 into 8 regions. The dominant-band in each box is provided by Table 6.6.

Box-No.	Box-ID.	Dominant-Band
1	c1m1	none
2	c1m3	T2_mainM3
3	c1m4	none
4	c1m6	T2_mainM6
5	c2m1	none
6	c2m346	T2_1I2eM3
7	c3m1	T2_2I2eM34
8	c3m346	T2_2I2eM32

Table 6.6: CM-boxes and their corresponding dominant-bands for the raw-T2-data in the main-FV. The band labels can be traced back to Table 6.1.

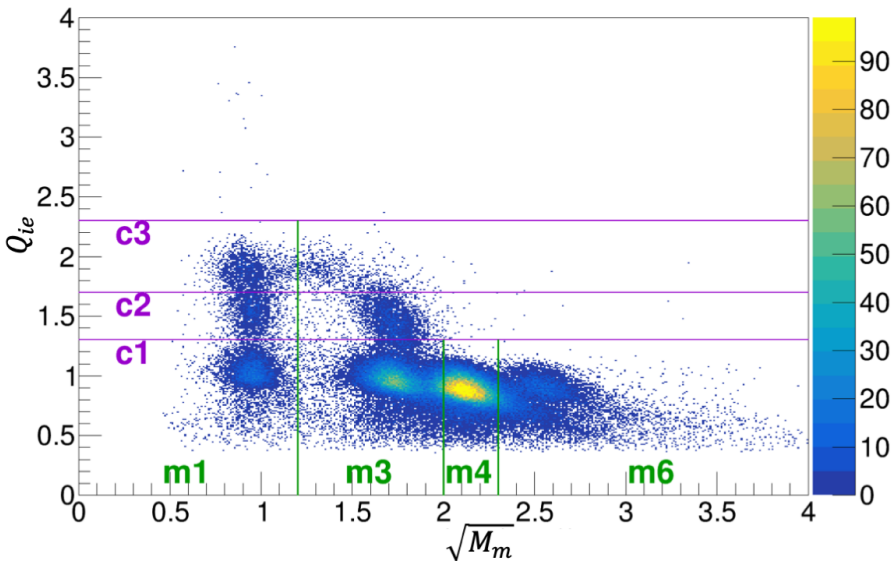

Figure 6.18: Charge-mass boxing for the left-scan raw-HT-data at the home-position.

Box-No.	Box-ID.	Dominant-Band
1	c1m1	HT_mainM1
2	c1m3	HT_mainM3
3	c1m4	HT_mainM4
4	c1m6	none
5	c2m1	HT_1I2eM1
6	c2m346	HT_1I2eM3
7	c3m1	HT_2I2eM34
8	c3m346	HT_2I2eM32

Table 6.7: CM-boxes and their corresponding dominant-bands for the raw-HT-data in the main-FV. The band labels can be traced back to Table 6.2.

6.3.2 Charge and Mass Cuts in Other Views

To relate back to the charge definition from Sec. 6.2.1, we draw the three charge cut lines from Sec. 6.3.1 on top of Fig. 6.13 to obtain Fig. 6.19. But of course, now the data is limited to the left-scan raw-T2-data at the home-position. These constant charge lines indeed correspond to the diagonal lines in the ion-energy versus beta-energy plane.

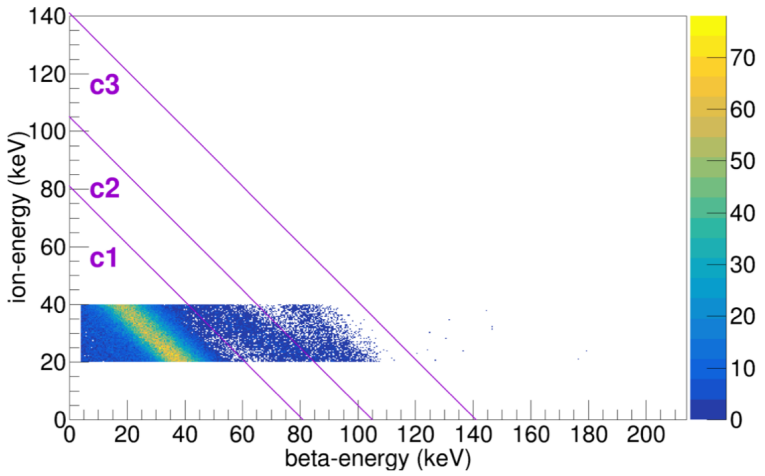

Figure 6.19: The three charge-boxes in the ion-energy versus beta-energy histogram for the left-scan raw-T2-data at the home-position in the main-FV. The purple diagonal lines are the ($Q_{ie} = 1.3\,\mathrm{e}$), ($Q_{ie} = 1.7\,\mathrm{e}$), and ($Q_{ie} = 2.3\,\mathrm{e}$) lines from Sec. 6.3.1.

It is also helpful to look at the mass projection spectrum for each charge-box, which is shown in Fig. 6.20 for the raw-T2-data. The task of separating out the bands that have different ion masses is essentially separating out the mass peaks from the mass projection. And to do that, Fig. 6.20 is going to be the referential starting point. We also draw the three mass cut lines from Sec. 6.3.1 in Fig. 6.20.

One last note is that from Fig. 6.20.a), the mass line ($\sqrt{M_m} = 2\sqrt{\mathrm{u}}$) does not seem like the optimized choice to box the `mainM4` peak; ($\sqrt{M_m} = 1.9\sqrt{\mathrm{u}}$) looks like a better choice. Looking at Fig. 6.6 however, the reason behind this choice is made specifically minimize the `1I2eM3` band contamination in box.ID `c1m4`.

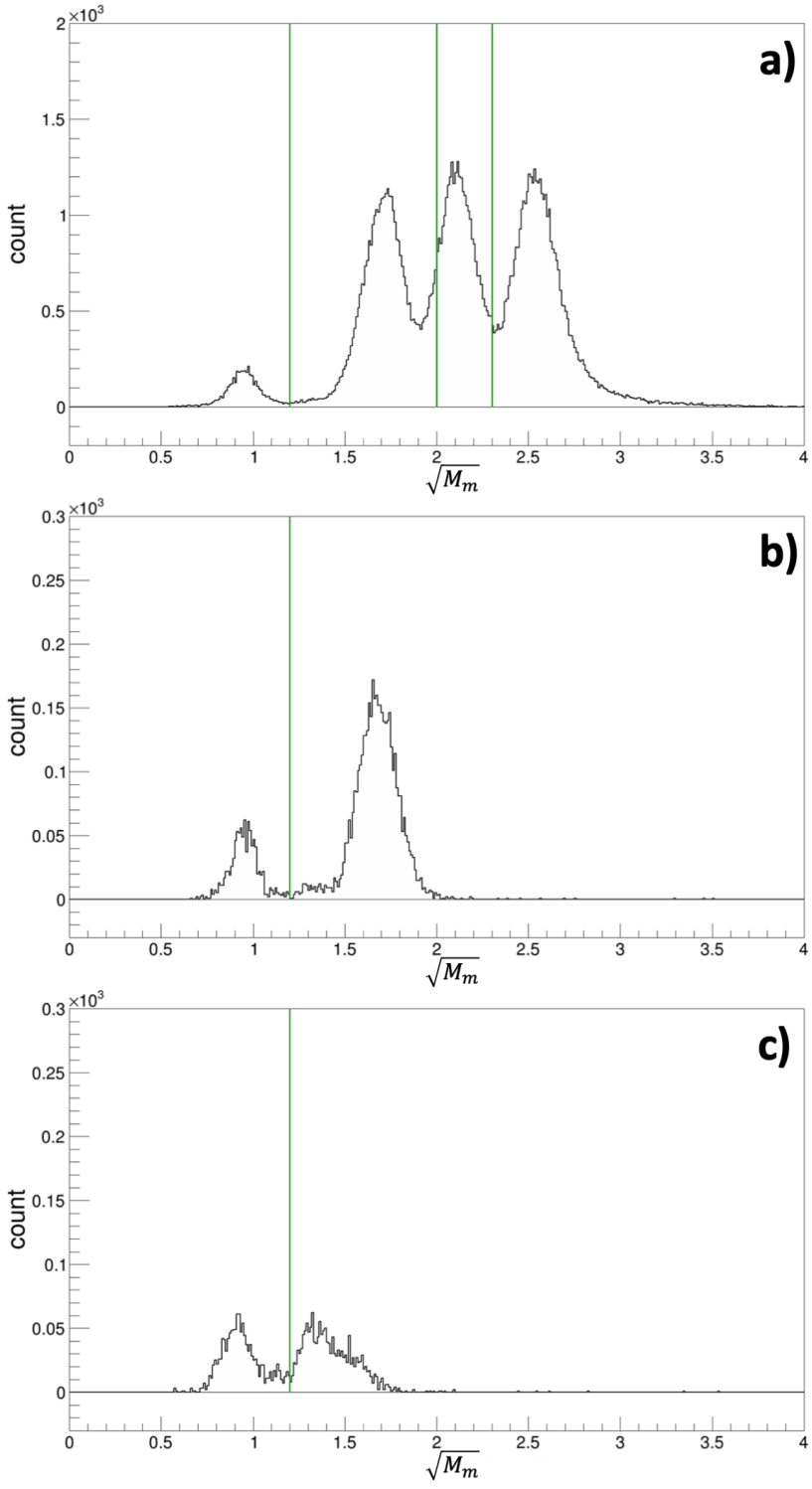

Figure 6.20: Mass spectrum for the left-scan raw-T2-data at the home-position in the main-FV. Referring to Fig. 6.17, plot a) is the reconstructed ion mass under `c1`-cut, plot b) under `c2`-cut, and plot c) under `c3`-cut. The y-axis now represents the count. The green vertical lines are the ($\sqrt{M_m} = 1.2\,\sqrt{\text{u}}$), ($\sqrt{M_m} = 2\,\sqrt{\text{u}}$), and ($\sqrt{M_m} = 2.3\,\sqrt{\text{u}}$) lines from Sec. 6.3.1.

Chapter 7

DATA ANALYSIS: CROSS-CONTAMINATION CORRECTION

This chapter covers how we handled the cross-contamination (CC), or the "leakage" of the dominant-bands from their corresponding CM-boxes (Table 6.6 and Table 6.7) to other CM-boxes (see Fig. 6.17 and Fig. 6.18). We separate the CC contribution into 3 categories: source-CC, charge-CC, and mass-CC.

The source-CC describes how our T_2 source and HT source are not pure; they are both a mixture of T_2 and HT gas. The methods that we developed to estimate the HT-purity and source activity in each source to obtain "pure" T_2 and HT data are discussed in Sec. 7.1. The charge-CC refers to the "leakage" vertically in the charge axis of Fig. 6.17 and Fig. 6.18, and mass-CC horizontally in the mass axis. Obtaining the charge-CC will require using the Geant4 simulation as will be discussed in Sec. 7.2, and obtaining the mass-CC will require information from both the source-CC and the charge-CC as will be discussed in Sec. 7.3. Combining all three contributions, Sec. 7.4 will describe how we perform the overall CC-correction to the data as well as how we handle the corresponding error propagation. An important note is that, for TRIMS, we need to perform the CC-correction at every ion-detector scan-point (Sec. 2.5.5).

As a recap of the notation we introduced so far, refer back to Sec. 2.5.5 again because we are scanning the ion-detector, but the discussion of the reason is delayed until Sec. 8.1.1. In this chapter, we further define a far scan-point as an index d such that the corresponding scan-position X_d is far from the home-position, e.g. $(d = -9)$ or $(d = 10)$. As items introduced in Ch. 6, we defined the ion-TOF, ion-energy, and beta-energy based on the "Notation and systematics discussion" of Sec. 6.1.2. We also defined the pseudo-charge Q_{ie} in Sec. 6.2.1 and the reconstructed main-band square-root ion mass $\sqrt{M_m}$ in Sec. 6.2.2. However, for

convenience, we often refer to Q_{ie} as charge in units of an electron charge (e) and $\sqrt{M_m}$ as mass in the square-root of the atomic mass unit ($\sqrt{\text{u}}$).

7.1 Source Contamination Subtraction Ratio

This section covers how we estimate the HT-purity within the raw-T2- and raw-HT-data, and perform a so-called source-subtraction to get "pure" T_2 and HT data. We investigate two types of events present in our data that can help us extract the source purity information: the "3-finger" events will be covered in Sec. 7.1.1 and the 2-ion events in Sec. 7.1.2. The method to obtained the HT-purity based on the two types of events is covered in Sec. 7.1.3. Section. 7.1.4 cover the so-called ion-singles events, from which we can derive the relative source-activity to our data. Finally, Sec. 7.1.5 covers the methods we used to obtain the ratios required for the source contamination subtraction.

An addition note is on the definition of HT-purity. For our convenience, it is defined based on the event purity, i.e. the percentage of the overall events that are coming from the HT decays. This definition is different from the percentage of HT molecules among our tritium gas because T_2 is twice as likely to decay as HT because it has more tritium nuclei. The same definition applies to the function `HT_Level` in the Geant4 simulation (Sec. 3.1.1).

7.1.1 Three-Finger Events for Source Purity

The first type of events that can tell us about the source HT-purity are the beta-detector double-Woods-Saxon (beta2WS) events. The beta2WS events occur when the beta-detector receives two signals in each event (Sec. 5.3.4). The 2D histograms of the beta2WS events are shown in Fig. 7.1. Figure 7.1.a) and .b) are the beta2WS counterparts of Fig. 6.2 and Fig. 6.4. Those previous plots from Ch. 6 contain both beta1WS and beta2WS events; beta2WS events are only a small portion of the overall raw-T2-data. Also, be aware that a beta and its shake-off electron would not in fact produce a beta2WS event because their timing would be too close together to resolve. Instead, a single signal would be produced having a combined energy from the two electrons. Other mechanisms are required to produce

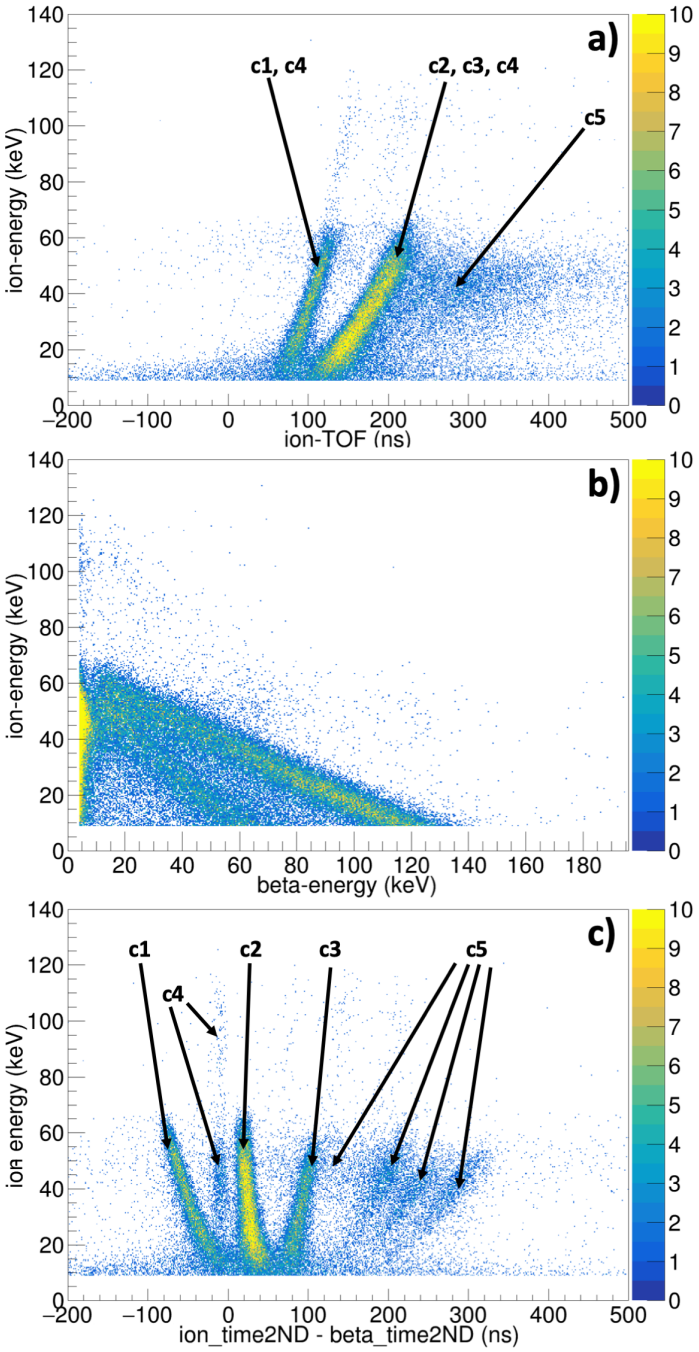

Figure 7.1: Spectrum of beta2WS events for the raw-T2-data (all scan-points combined). Plot a) is to be compared to Fig. 6.2, which includes both the beta1WS and beta2WS events. Similarly, plot b) is to be compared to Fig. 6.4. The x-axis in plot c) shows a specific timing: the timing difference between when the ion-detector detects its first signal and the beta-detector detects its second signal. The description of each band as labeled is in Table 7.1, and band-No. c1), c2), and c3) are what we refer to as the 3-finger bands.

a beta2WS event.

The beta2WS events we care about are referred to as the 3-finger events, and they are most likely coming from the physical process that is illustrated in Fig. 7.2 [41]. In a 3-finger event, the decay starts out with 2 ions and 2 electrons (a beta and a shake-off). The beta-detector first detects either the beta or the shake-off electron or both. Then one of the ions is detected by the ion-detector, while the other ion hits the mesh and creates a shower of electrons. Some of the mesh-electrons are then detected by the beta-detector to form a second signal.

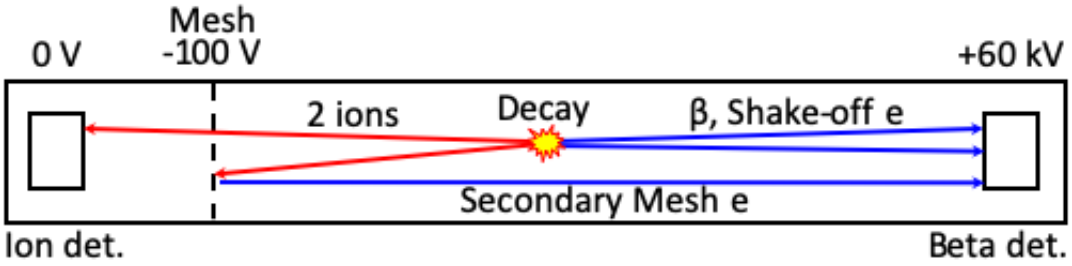

Figure 7.2: Diagram illustration of the 3-finger events [41]. The ion trajectories are indicated by red arrows, while the electron trajectories by blue arrows. In a `beta2WS 3-finger` event, the decay produces 2 ions, 1 beta electron, and 1 shake-off electron. One of the ions is detected by the ion detector, while the other hits the mesh and produces secondary mesh-electrons. In this case, the beta-detector detects the mesh-electrons hundreds of nanoseconds after it detects the beta electron or the shake-off electron.

To have a better view of the 3-finger events, we modify the x-axis of Fig. 7.1.a) from the normal (T_{ion} = `ion_time2ND - beta_time`) to (`ion_time2ND - beta_time2ND`) to incorporate the second beta-detector signal timing (Table 5.4). The resulting new histogram is provided in Fig. 7.1.c), whose band descriptions are given in Table 7.1. The 3-fingers refer to the band-No. c1), c2), and c3). While they overlap in Fig. 7.1.a) inside either the mass-1 or the mass-3 band (band-No. a1) and a2) from Fig. 6.2), these 3 "fingers" are isolated from one

another in Fig. 7.1.c), and thus the name.

Band-No.	Band Label	Description
c1	`beta2WSH`	event from HT decay, where $^3He^+$ knocks out mesh electrons and H^+ passes through the mesh to be detected by the ion-detector
c2	`beta2WSMid`	event from T_2-decay, where either $^3He^+$ or T^+ knocks out mesh electrons and the other passes through the mesh to be detected by the ion-detector
c3	`beta2WSHe`	event from HT decay, where H^+ knocks out mesh electrons and $^3He^+$ passes through the mesh to be detected by the ion-detector
c4	`beta2WSFalse`	misidentified beta2WS events due to their pulses being relatively wide in their waveforms
c5		event when either the beta or the mesh electrons are first detected by the beta-detector, and then the ion hits and knocks out more electrons from the ion-detector, where the electrons are again detected by the beta-detector (compared to a9 in Table 6.3)

Table 7.1: Band identification of Fig. 7.1.

The leftmost finger band-No. c1) belongs to the H^+ events from HT decay, where the $^3He^+$ hits the mesh. The way to understand why is to realize that mesh-electrons, just like the betas, travel to the beta-detector in a negligible amount of time. In other words, the mesh-electron detection time is essentially the same time when the $^3He^+$ reaches the mesh. The `ion_time2ND` is just the time when the H^+ reaches the ion-detector. And because H^+

has smaller mass, the H^+ reaches the ion-detector sooner than the $^3He^+$ can reach the mesh. Therefore, the H^+ 3-finger band is the one that has negative x-values in Fig. 7.1.c). If we switch the roles of the H^+ and the $^3He^+$ in this scenario, we obtain the rightmost finger band-No. c3).

As for the case of the T_2 decay, either detecting $^3He^+$ or T^+ produces the middle finger band-No. c2). The reason is that in a 3-finger event, one ion hits the mesh and the other hits the ion-detector. But given $^3He^+$ and T^+ have similar masses, the ion always hits the mesh sooner than the other ion hits the ion-detector. This means that the middle finger will always have a positive time in Fig. 7.2.

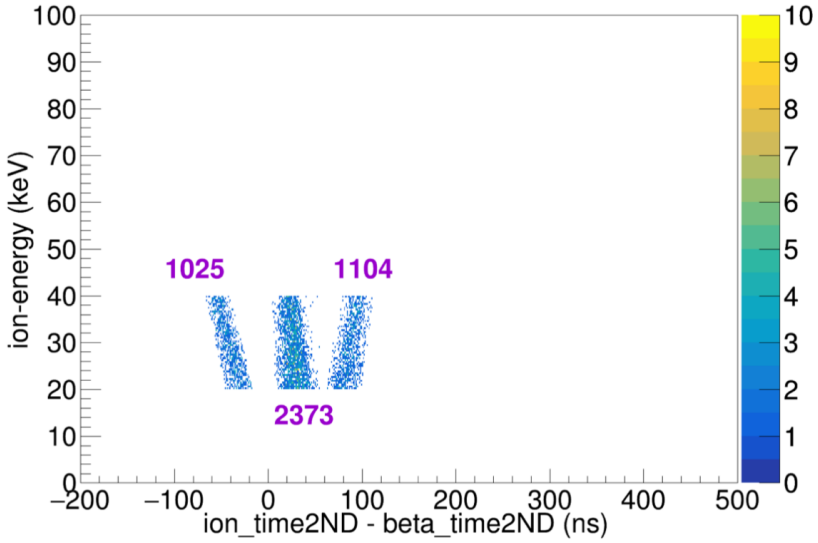

Figure 7.3: Isolated `3-finger` spectrum from the raw-T2-data in the main-FV. However, compared to Fig. 7.1, only the left-scan home-position data is present. The counts for each finger are shown by the purple numbers in the plot; these counts provide information about the source purity of the data.

Thence, by comparing the abundance of the middle finger to the left and the right finger, we can tell what proportion of the events come from the HT versus from the T_2 decay and derive the HT-purity. As a start to this derivation, we applied the main-FV cut to Fig. 7.1

to arrive at Fig. 7.3 for the raw-T2-data. We also manually trim out band-No. c4) and c5) events from Fig. 7.1 c) and assume those noise events contribute negligible error given how well separated the fingers are. The counts of each finger are provided in the plot. These counts will be used to evaluate the HT-purity in Sec. 7.1.3.

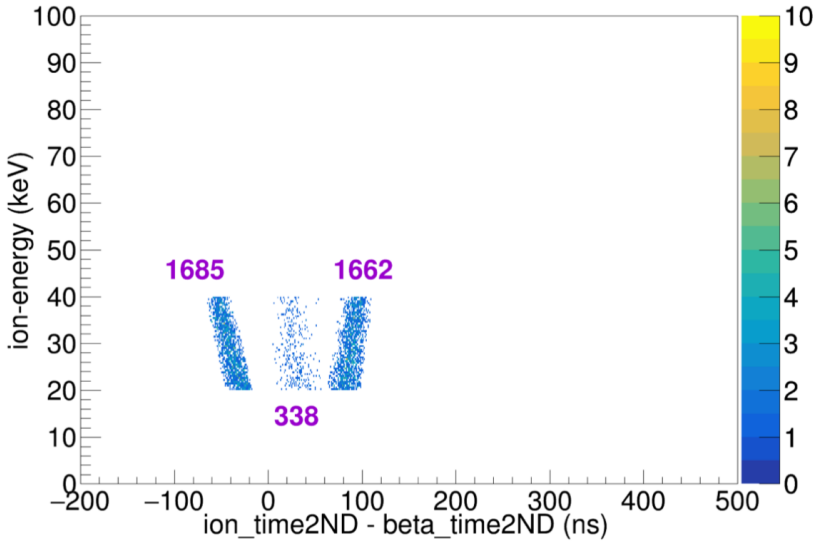

Figure 7.4: Isolated `3-finger` spectrum from the left-scan raw-HT-data at the home-position in the main-FV. Compared to Fig. 7.3, we can see a deficit in band-No. c2) as expected.

Similarly, we have Fig. 7.4 for the raw-HT-data. We can see the deficit in the middle finger, which is an indicator that T_2 contributes little to the events in raw-HT-data.

This demonstrates that the 3-finger events do contain information about the source composition. The quantitative treatment will be covered in Sec. 7.1.3.

7.1.2 Two-Ion Events for Source Purity

Another type of events are what we call the high ion-energy cut fiducial volume (high-FV) events. As shown in Fig. 7.5, instead of the regular main-FV cut, we apply a [75, 95)keV ion-energy cut on Fig. 6.2. The high-FV cut cuts out all the main-bands, leaving only 2-charge events, i.e. the `2I2e-` and the `2I1e`-bands (Table 6.4). According to Table 6.3, the

only possible events are $^3He^{++}$ or the events when the ion-detector detects two ions (2-ion event). We refer to the combination of the $^3He^{++}$ events and the 2-ion events as the 2-charge events.

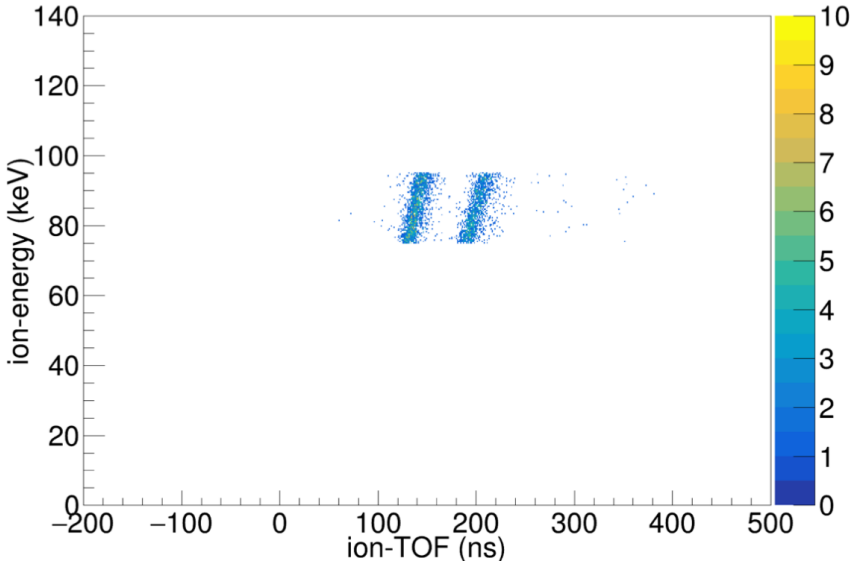

Figure 7.5: Ion-energy versus ion-TOF histogram Fig. 6.2 in the high-FV. Compared to Fig. 6.12, there are no main-band events.

The mass projection of the 2-charge events in the raw-T2-data is given in Fig. 7.6. In order to get the correct mass of $^3He^{++}$, instead of Eq. 6.14, in principle we should assume the electric potential well is twice as deep,

$$m_{\text{ion,He++}} \equiv 2E_{ion}\left(\frac{T_{\text{ion}}}{\frac{2E_{\text{ion}}}{2qV}L + L_{\text{ion}}}\right)^2 \approx 4m_{\text{ion}}. \tag{7.1}$$

By using the $m_{\text{ion,He++}}$ formula on the $^3He^{++}$ events, we should obtain the mass of the ^3He that is 3 amu.

As for the 2-ion case, nothing is changed except the ion-energy is doubled. So the correct mass formula is,

$$m_{2\text{ion}} \equiv 2(E_{\text{ion}}/2)\left(\frac{T_{\text{ion}}}{\frac{2(E_{\text{ion}}/2)}{qV}L + L_{\text{ion}}}\right)^2 \approx 2m_{\text{ion}}. \tag{7.2}$$

However, we need to watch out that the T_{ion} is defined in Eq. 6.6 using `ion_time2ND` instead of `ion_time`. Recall that (`ion_time2ND` = `ion_time`) unless 2WS-fit is invoked on the ion-detector, which only happens when the ion-detector detects both $\{^3\text{He}^+, \text{H}^+\}$ from a 2-ion event. This is because $^3\text{He}^+$ is heavier in mass than H^+, which means the $^3\text{He}^+$ will arrive slightly later than the H^+ and form 2 pulses that are close in time. This explains why we fit a 2WS-function to the 2-pulse waveform. In an $\{^3\text{He}^+, \text{H}^+\}$ 2-ion event, this means that the T_{ion} is capturing the TOF of the slower of the 2 ions, i.e. the $^3\text{He}^+$ out of $\{^3\text{He}^+, \text{H}^+\}$. And so m_{2ion} is also describing the mass of the ^{3}He. As for the $\{^3\text{He}^+, \text{T}^+\}$ 2-ion event, no 2WS-function would be invoked on the ion-detector because our detector cannot resolve the difference in the arrival time of the $^3\text{He}^+$ and the T^+. However, even in this case, the same mass m_{2ion} formula should describe the mass of the ^{3}He, or T, which are both 3 amu.

Since we cannot distinguish the ion species ahead of the time, we have to use the same mass reconstruction formula Eq. 6.14 for every case. And because both $m_{\text{ion,He++}}$ and m_{2ion} are describing the mass of the ^{3}He that is 3 amu, we have,

$$m_{\text{ion}} = \frac{1}{4} m_{\text{ion,He++}} = \frac{3}{4}, \tag{7.3}$$

and,

$$m_{\text{ion}} = \frac{1}{2} m_{\text{2ion}} = \frac{3}{2}. \tag{7.4}$$

This is consistent with Fig. 7.6 of having a mass peak at $\sqrt{M_m} = \sqrt{3/4} \approx 0.87\sqrt{\text{u}}$ and another at $\sqrt{M_m} = \sqrt{3/2} \approx 1.23\sqrt{\text{u}}$. For this reason, we sometimes refer to these two bands as the mass-$\frac{3}{4}$ and the mass-$\frac{3}{2}$ band.

One caveat about Eq. 7.1 and Eq. 7.2 is that their approximations hold only if we assume $L_{ion} \ll L$. The assumption is not technically true, but it is sufficient to justify the 2-charge events' mass peak locations.

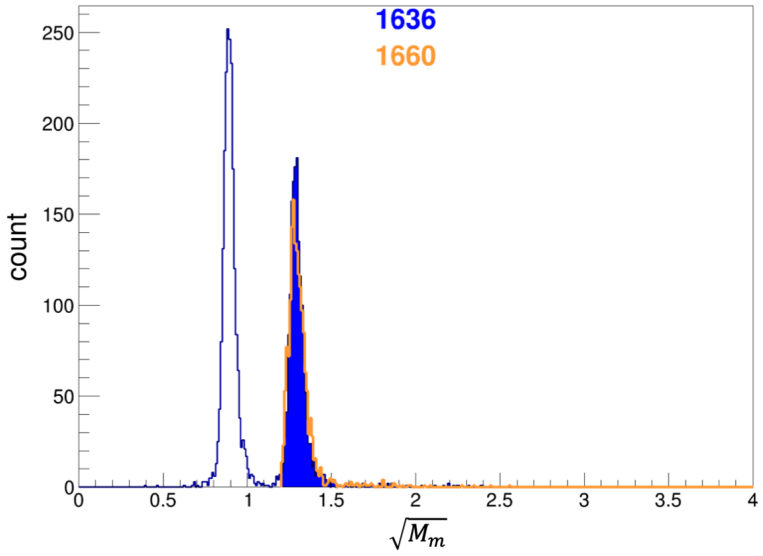

Figure 7.6: Mass spectrum for the raw-T2-data at the home-position in the high-FV. Similar to Fig. 6.20, the left peak is associated with the $^3He^{++}$ events and the right 2 peaks the 2-ion events. The focus is on the 2-ion events, and so a ($\sqrt{M_m} > 1.2\sqrt{\text{u}}$) cut is applied. The ion1WS events form the blue peak and the ion2WS form the orange peak. The corresponding count in each peak is provided in the plot in matching color; the counts provide information about the source purity of the data.

There is more to the story about the high-FV events. An event in the 2-ion peak either comes from the decay that produces $\{^3He^+, T^+\}$ or $\{^3He^+, H^+\}$. The latter appears amoung the ion-detector double-Woods-Saxon (ion2WS) events, because H^+ arrives at the ion-detector significantly earlier than the $^3He^+$. Using this information, we divide the mass-$\frac{3}{2}$ peak in Fig. 7.6 into into a blue peak for the ion1WS events and an orange peak for the ion2WS. Both of the peaks are at mass-$\frac{3}{2}$ as if the ion received is a 3 amu ion. This is because Eq. 6.1 picks the second timing `ion_time2ND`, and so the ion-TOF evaluated in a ion2WS event is always the slower ion, i.e. $^3He^+$ among $\{^3He^+, H^+\}$. The counts for the two 2-ion peaks are provided in the plot in the matching color. Because $\{^3He^+, T^+\}$ can only come from the T_2 source, and $\{^3He^+, H^+\}$ from the HT source, these counts can be

used to evaluate the HT-purity as will be demonstrated in Sec. 7.1.3.

For the HT-purity evaluation, we are not interested in the $^3He^{++}$ events, so an additional ($\sqrt{M_m} > 1.2\sqrt{\text{u}}$) cut is applied to isolate the 2-ion event. A small portion of the 2-ion events leak below $1.2\sqrt{\text{u}}$. However, the leakage does not matter for the HT-purity evaluation as long as the 2-ion peaks are not contaminated by other events such as $^3He^{++}$.

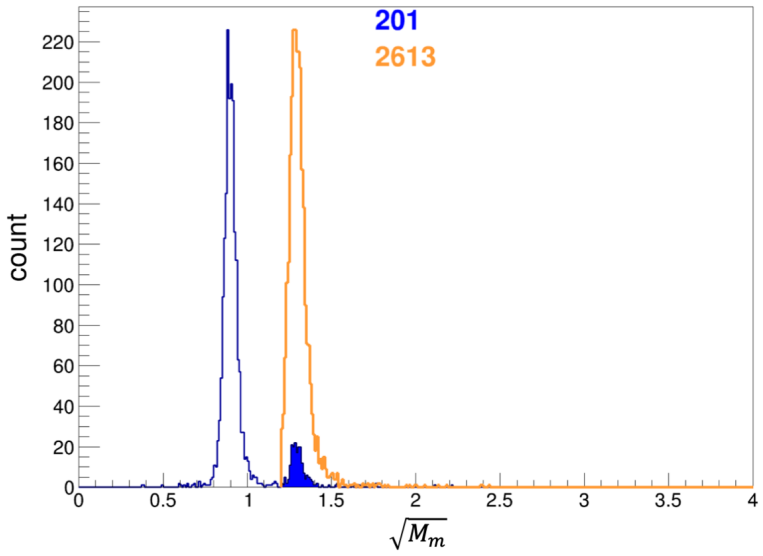

Figure 7.7: Mass spectrum for the raw-HT-data at the home-position in the high-FV. Compared to Fig. 7.6, we can see a deficit in the blue 2-ion mass-$\frac{3}{2}$ peak from T_2 decays as expected.

The raw-HT-data counterpart of Fig. 7.6 is provided in Fig. 7.7. And we can see that the blue $\{^3He^+, T^+\}$ peak is lacking, which is again an indicator that T_2 contributes little to the events in raw-HT-data as expected.

7.1.3 Source Purity Estimation

To obtain the HT-purity correctly using counts found in Sec. 7.1.1 and Sec. 7.1.2, we apply the result of the following derivation [140]. Suppose the source activities for T_2 and HT are

$A(\mathrm{T2})$ and $A(\mathrm{HT})$, then the HT-purity can be defined by,

$$P(\mathrm{HT}) = \frac{A(\mathrm{HT})}{A(\mathrm{T2}) + A(\mathrm{HT})}. \tag{7.5}$$

To obtain information about $A(\mathrm{T2})$ and $A(\mathrm{HT})$, suppose the counts for the 3-finger events from Sec. 7.1.1 are f_1, f_2, and f_3, corresponding to the counts of the left, middle, and the right finger. Take Fig. 7.3 for example, $f_1 = 1025$, $f_2 = 2373$, and $f_3 = 1104$. Because f_2 contains only the events that are coming from T_2 decays, and f_1 and f_3 from HT decays, the following proportionality relations hold,

$$\begin{aligned} f_1 + f_3 &= p_f A(\mathrm{HT}), \\ f_2 &= q_f A(\mathrm{T2}), \end{aligned} \tag{7.6}$$

where p_f and q_f are the proportionality scales. And so we have,

$$\begin{aligned} f_1 + f_2 + f_3 &= p_f A(\mathrm{HT}) + q_f A(\mathrm{T2})) \\ &= p_f \left(A(\mathrm{HT}) + A(\mathrm{T2})\right) + (q_f - p_f) A(\mathrm{T2}) \\ &= p_f \left(A(\mathrm{HT}) + A(\mathrm{T2})\right) + \left(1 - \frac{p_f}{q_f}\right) f_2 \\ &\equiv a_f + b_f f_2, \end{aligned} \tag{7.7}$$

and,

$$\begin{aligned} P(\mathrm{HT}) &= \frac{A(\mathrm{HT})}{A(\mathrm{T2}) + A(\mathrm{HT})} \\ &= \frac{(f_1 + f_3)/p_f}{(f_1 + f_3)/p_f + f_2/q_f} \\ &= \frac{f_1 + f_3}{f_1 + f_3 + \frac{p_f}{q_f} f_2} \\ &= \frac{f_1 + f_3}{f_1 + f_3 + \left(1 - \left(1 - \frac{p_f}{q_f}\right)\right) f_2} \\ &= \frac{f_1 + f_3}{f_1 + f_3 + (1 - b_f) f_2}. \end{aligned} \tag{7.8}$$

So if we can get $b_f \equiv \left(1 - \frac{p_f}{q_f}\right)$, we can obtain $P(\mathrm{HT})$. To get b_f, we fit $f_1 + f_2 + f_3$ as a linear function of f_2 as shown in the right plot of Fig. 7.8. Notice that if the HT-purity does

not change over time, the data points in the $f_1 + f_2 + f_3$ versus f_2 plot will be the same exact point, which will prevent our effort to apply a linear fit to the data. Fortunately, we do have conversion-runs for the HT source (Sec. 4.2.1), whose HT-purity over time changes because the time scale of the catalytic conversion is on the order of minutes. We have 4 data points in total for the fit, 3 come from the conversion-runs, and the fourth is the home-position runs that immediately follow. We cannot add the other data points taken when the ion-detector was not at the home-position, because that would change the p_f and q_f in the proportionality relation Eq. 7.6.

One important note is that in order for the linear fit using Eq. 7.7 to work, the parameter a_f needs to be constant for all the data points. In other words, the total activity $(A(\mathrm{HT}) + A(\mathrm{T2}))$ must not change over time. However, we know this is true because the total number density of tritium atoms does not change during the catalytic conversion: the number of tritium atoms is independent of the tritium's molecular form, and the half-life of tritium is much longer than our data-taking time.

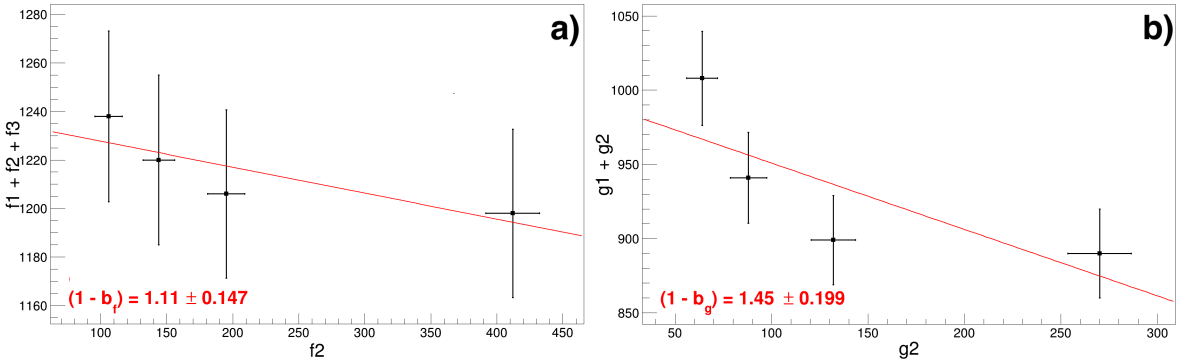

Figure 7.8: Linear fit to the right-scan raw-HT-data to evaluate the HT-purity of the data. Plot a) is fitted using Eq. 7.7 to the `3-finger` events (Sec. 7.1.1), while plot b) is fitted using Eq. 7.10 to the `2-ion` events (Sec. 7.1.2). The χ^2`/dof` is 0.113 for plot a) and 1.83 for plot b). The error bars come from the Poisson error of the counts, treating them as if $f_1 + f_2 + f_3$ is independent of f_2 and $g_1 + g_2$ is independent of g_2. There are only 4 data points present for the fit, and 3 of them come from the conversion-runs.

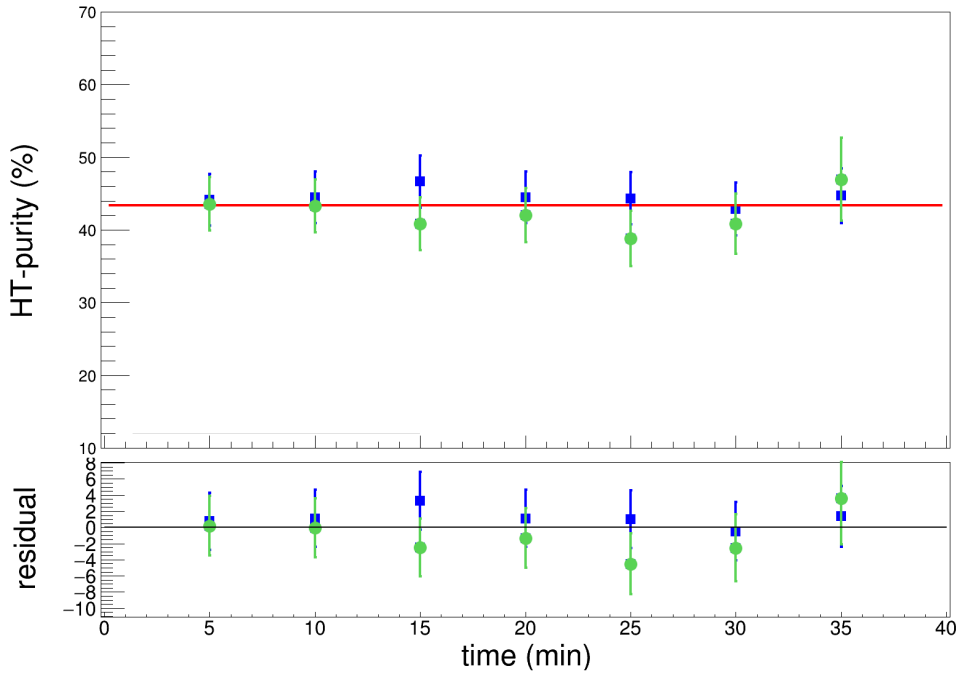

Figure 7.9: HT-purity over time for the right-scan raw-T2-data. The blue data points come from the 3-finger events derived using Eq. 7.8, while the green data points are the 2-ion events derived using Eq. 7.11. The HT-purities are independent of time for the raw-T2-data as expected because the T_2 gas is not exposed to the catalyst. For this reason, we apply a horizontal line fit to the data to extract the expected HT-purity. The χ^2/dof is 4.132/13. The evaluation of the error bars can be found in the text, and the residual of the fit is given on the bottom plot.

A similar linear fit is applied using the 2-ion events from Sec. 7.1.2, whose counts are defined by g_1 for the ion1WS events and g_2 for the ion2WS events. Take Fig. 7.6 as an example, $g_1 = 1636$ and $g_2 = 1660$. The corresponding proportionality relations are,

$$\begin{aligned} g_1 &= p_g A(\mathrm{HT}), \\ g_2 &= q_g A(\mathrm{T2}), \end{aligned} \tag{7.9}$$

$$g_1 + g_2 \equiv a_g + b_g g_2, \tag{7.10}$$

$$P(\mathrm{HT}) = \frac{g_1}{g_1 + (1 - b_g)g_2}. \tag{7.11}$$

Using Eq. 7.8 and Eq. 7.11, we derive the HT-purity of the raw-T2-data as shown in Fig. 7.9. The blue data points come from the 3-finger events, and the green from the 2-ion events. The x-axis represents the time knowing that we took 300 s runs at every scan-point. However, each data point consists of all the runs taken at that scan-point given a source-type and scan-direction. For the run-scans using the T_2 source, the T_2 gas is not exposed to the catalyst, and so their HT-purity is independent of time as expected. We fit the data to a horizontal line to extract the expectation value for the HT-purity. The fit is done on the combination of the 3-finger and 2-ion data at the same time. We do not include the data for all the scan-points in HT-purity estimation because the statistics plummet for the scan-positions far from the home-position. The error bars come from error propagating Poisson errors for the counts in Eq. 7.8 and Eq. 7.11 along with the error of the b_f and b_g from the fits in Eq. 7.8. The error of the m's are propagated to each data point independently, which overestimates the error bars since every data point uses the same m's.

As for the HT-purity of the raw-HT-data, the result is shown in Fig. 7.10, whose HT-purity is time-dependent as expected. In fact, the first 3 data points are conversion runs; the 4^{th} data point is when the run-scans start. We fit the data points to the dynamic equilibrium function commonly used in chemistry [183],

$$P(\mathrm{HT}, t) = 100 + \frac{k_{\mathrm{T2}} + k_{\mathrm{HT}} e^{-(k_{\mathrm{T2}} + k_{\mathrm{HT}})t}}{k_{T2}} \left(P(\mathrm{HT}, \infty) - 100\right), \tag{7.12}$$

where the fit parameter k_{T2} is the T_2-to-HT conversion rate and k_{HT} the HT-to-T_2 rate. The parameter $P(\mathrm{HT}, \infty)$ is also a fit parameter, and it describes the HT-purity at the equilibrium given infinitely long conversion time. The structure of this formula is such that the output $P(\mathrm{HT}, t)$ is directly the HT-purity in percentage at time t. Note that this formula is only an approximation because the real dynamic equilibrium needs to take into account the partial pressure of H_2 that we are not able to observe. Moreover, the dynamic equilibrium obtained by averaging the run-scans is not exactly identical to that obtained

from the combined run-scan data. However, according to the fit residual, the function fits the data well.

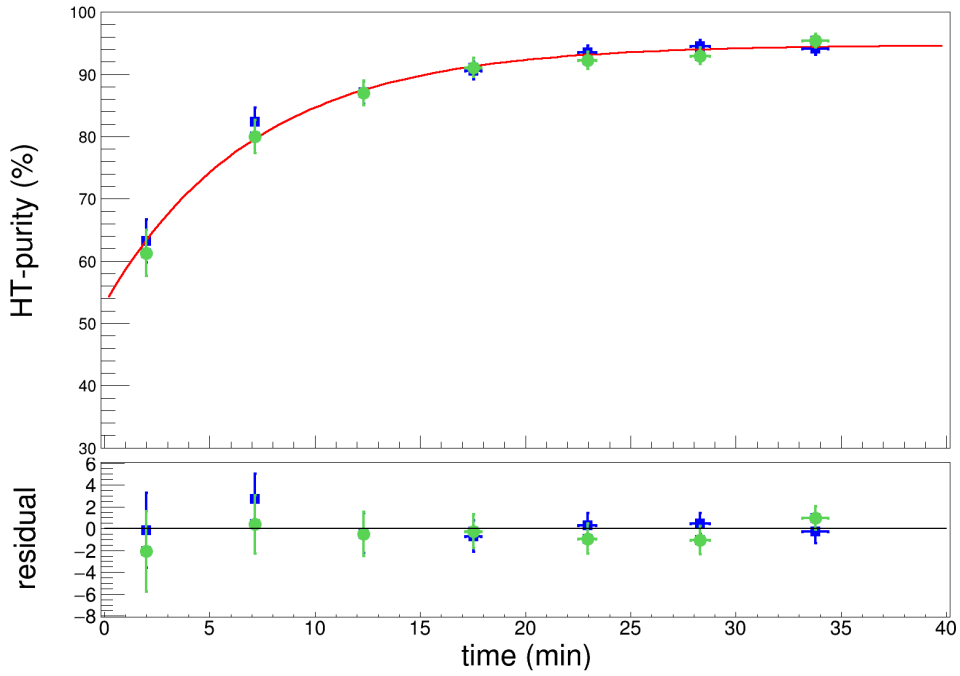

Figure 7.10: HT-purity over time for the right-scan raw-HT-data. Compared to Fig. 7.9, these data are time-dependent and are fit to the dynamic equilibrium function Eq. 7.12. The χ^2/dof is 4.541/11. The first 3 data points come from the conversion-runs. The 4^{th} point come from the home-position runs and is when the run-scans start.

The error bars of Fig. 7.10 on the y-axis are obtained in the same manner as for Fig. 7.8. The error bars on the x-axis come from the start time variation of all the runs taken for that scan-point. Because adjusting the ion-detector position was done manually, there are time gaps between runs. And the accumulation of these time gaps explains why the error bar becomes larger as we scan out from the home-position. This time error is assumed to be 0 for the first conversion run. Notice the time between opening the system to the ion gauge and the start of the first conversion run does not matter. The reason is that we are

estimating the dynamic equilibrium of the combined HT-purity, i.e. the HT-purity in the combined data of all the runs with the same source-type at a particular scan-point. The runs already do have different HT-purities at the beginning, so their starting points do not matter. *. Because our left- and right-scan data are spread quite evenly in days (Fig. 6.9), the HT-purities for them are very similar.

We also shifted the time backward by 3.01 min, e.g. the first data point is at $(5 - 3.01) = 1.99$ min, to incorporate the time integration. The correction can be understood by realizing that the HT-purity is changing during the 300 s run period because the catalytic conversion is ongoing. So the y-axis value for each data point is more of an average HT-purity within the 300 s. Fortunately, because the time-dependent part of Eq. 7.12 is an exponential function, it turns out the correction is simply a constant time shift for every data point [140].

Lastly, instead of counting the 3-finger and the 2-ion events, the most obvious choices are actually counting the mass-1 or the mass-6 main-bands. Unfortunately, mass-1 main-band actually has significant contamination from the minor-bands, while the mass-6 main-band is very close to the mass-4 main-band such that they largely overlap with each other. For these reasons, it is difficult to disentangle the events such that we get clean mass-1 and mass-6 main-bands, which is required to perform a precise HT-purity estimation.

7.1.4 Ion-Singles Events For Source-Activity

Another important reference other than the HT-purity is an amplitude that is proportional to the overall source-activity. We call it the activity-amplitude, and it is used to compare the source-activity between run-scans. Using coincidence events to estimate the activity-amplitude would be problematic because the coincidence count drops to nearly zero at far scan-points. Fortunately, we recorded the data using OR-logic (Sec. 2.5.2), so that we could estimate the activity-amplitude using the counts from the ion-detector alone, which we call

*One caveat is that no time errors are applied to Fig. 7.8; we drop the error because it does not affect the horizontal line fit.

the ion-singles events. The ion-singles events include all the ion-detector events, regardless of whether the events are in coincidence with the beta-detector events or not. To prevent noise events, we also applied the main-FV cut to the ion-singles events, and the estimated activity-amplitudes are given in Fig. 7.11.

Recall from Fig. 6.9, we separate our data into 4 categories: left-scan raw-T2-data, right-scan raw-T2-data, left-scan raw-HT-data, and right-scan raw-HT-data. Within each category, all the runs at the same scan-point are combined together. The raw-T2-data data points are colored in red in Fig. 7.11, and the raw-HT-data in blue. We can see that both the left- and the right-scan share the home-position as expected (Sec. 4.2.1).

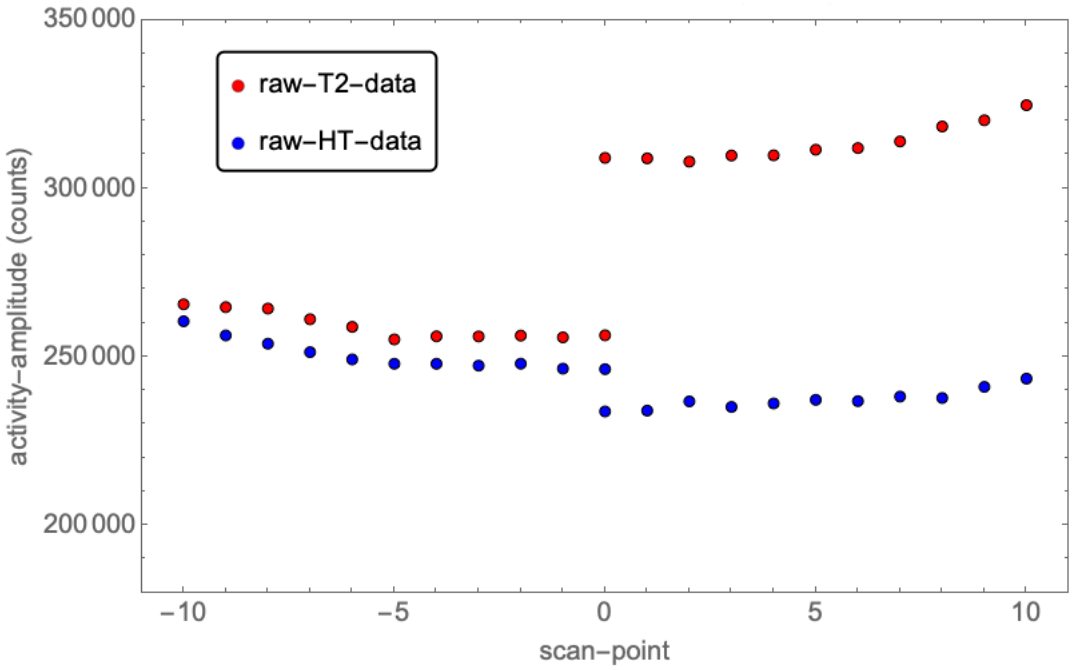

Figure 7.11: The activity-amplitudes for left- and right-scans of the raw-T2-data (red data points) and the raw-HT-data (blue data points). The conversion-runs for the raw-HT-data are dropped.

Within each of the 4 categories, the source-activity should be the same because we sealed

off the T_2 source using the leak valve before we proceeded to take data (Sec. 4.2.1). And since we are talking about the event rate, the catalytic conversion should not change the source-activity because the process does not remove tritium from the gas. However, according to Fig. 7.11, the activity-amplitudes are rising at far scan-points. We believe these events are caused by the proton ions coming from the gold electrode. Despite the deviation being rather small, we used the average activity-amplitudes within a scan-point d in integer range of $[-5,\ 0]$ for the left-scan and $[0,\ 5]$ for the right-scan as our final reference. In other words, each of the 4 categorizes receive only one activity-amplitude as a reference for any scan-point. We denote the reference activity-amplitude as A(rawT2, L), A(rawT2, R), A(rawHT, L), and A(rawHT, H). Their errors are taken to be the standard deviation of the six points included in the average, which incorporates the contribution from including the deficit- and the excess-runs.

One may wonder why we do not combine the beta-singles events with the ion-singles events to get more statistics for estimating the activity-amplitudes. The reason is that the entire main-vacuum system (Sec. 2.2.1) is facing the beta-detector. Decays that happen in the volume behind-the-mesh ion-electrode can produce electrons that fall into the HV potential and be detected as a beta-detector single event. This would not be a problem if the beta-detector singles rate is scan-position independent. Unfortunately, it is dependent because the ion-detector itself blocks most of the electrons from the main-vacuum system, especially when the ion-detector is at the home-position. In other words, the behind the mesh electrons causes the beta-detector singles rate to increase at the far scan-points [140].

7.1.5 Source Contamination Subtraction Ratios

Just knowing the HT-purity from Sec. 7.1.3 is not enough. We want to obtain "pure" T_2 and HT charge-mass distribution (CM-distribution) from Fig 6.17 and Fig 6.18. Notation-wise, we denote the CM-distributions in Fig 6.17 as N(rawT2) with HT-purity P(rawT2, HT) in percentage and Fig 6.18 as N(rawHT) with HT-purity P(rawHT, HT). A fair note about N(rawT2) is that it does not just contain one count, but it is a distribution of counts in the

8 CM-boxes. To obtain the pure CM-distributions, we cannot just scale the spectrum using the source purity. For example,

$$N(\text{incorrect pure } \mathrm{T}_2 \text{ data}) = \frac{100 - P(\text{rawHT, HT})}{100} \times N(\text{rawT2}), \tag{7.13}$$

does not give us a pure T_2 spectrum because doing so does not remove, for instance, the mass-1 band from HT contamination in box-ID `c1m1`. Instead, we need,

$$N(\text{T2\_HT}) = N(\text{rawT2}) - R(\text{T2\_HT}) \times N(\text{rawHT}), \tag{7.14}$$

where N(T2_HT) is the estimated pure T_2 CM-distribution, and R(T2_HT) is what we call the source contamination subtraction (source-CC) ratio. We use the label "T2_HT" to emphasize that our T2_HT-data is obtained by subtracting the raw-HT-data from the raw-T2-data; the T2_HT-data is an estimation of the true pure T_2 data.

Ideally, suppose we have the same amount of the raw-T2-data and the raw-HT-data, i.e. N(rawT2) and N(rawHT) have the same counts. Then for example, given their HT-purities are 40% and 90% respectively, or,

$$\begin{aligned} N(\text{rawT2}) &= 0.6N(\text{rawT2, T2}) + 0.4N(\text{rawT2, HT}), \\ N(\text{rawHT}) &= 0.1N(\text{rawHT, T2}) + 0.9N(\text{rawHT, HT}), \end{aligned} \tag{7.15}$$

where the counts of N(rawT2, T2) and N(rawT2, HT) are chosen to be the same as N(rawT2) and similarly for N(rawHT). And given N(rawT2) and N(rawHT) have the same count, N(rawT2, T2) = N(rawHT, T2) and N(rawT2, HT) = N(rawHT, HT). We can obtain the pure T_2 CM-spectrum by,

$$\begin{aligned} N(\text{T2\_HT}) &= N(\text{rawT2}) - \frac{0.4}{0.9}N(\text{rawHT}) \\ &= 0.6N(\text{rawT2, T2}) + 0.4N(\text{rawT2, HT}) - 0.4\frac{0.1}{0.9}N(\text{rawHT, T2}) - 0.4N(\text{rawHT, HT}) \\ &= 0.6N(\text{rawT2, T2}) + \cancel{0.4N(\text{rawT2, HT})} - 0.044N(\text{rawT2, T2}) - \cancel{0.4N(\text{rawT2, HT})} \\ &= (0.6 - 0.044)N(\text{rawT2, T2}). \end{aligned} \tag{7.16}$$

In this case, $R(\text{T2\_HT}) = \frac{0.4}{0.9}$. Despite losing a portion of $N(\text{rawT2, T2})$ in the process, the derived $N(\text{T2\_HT})$ is pure in T_2.

Nonetheless, as we can see from Sec. 7.1.4, we do not have the same amount of raw-T2-data and raw-HT-data. To avoid the difficulty, we can directly use the 3-finger or the 2-ion events to obtain the source-CC ratio. Take the 3-finger events for example, suppose the 3-finger counts are f_1, f_2, and f_3 for the raw-T2-data and F_1, F_2, and F_3 for the raw-HT-data. Then because $(f_1 + f_3)$ is proportional to $N(\text{rawT2, HT})$ under the same constant as $(F_1 + F_3)$ is proportional to $N(\text{rawHT, HT})$. Assume the same HT-purities as the previous example, the proportionality gives,

$$\frac{f1 + f3}{F1 + F3} = \frac{0.4M(\text{rawT2, HT})}{0.9M(\text{rawHT, HT})}, \tag{7.17}$$

where M's are the total counts of the CM-distribution. So even if $N(\text{rawT2, HT}) \neq N(\text{rawT2, HT})$, let,

$$R(\text{T2\_HT}) = \frac{f1 + f3}{F1 + F3}. \tag{7.18}$$

Inserting it to Eq. 7.14, we get,

$$\begin{aligned}
N(\text{T2_HT}) &= N(\text{rawT2}) - \frac{f1 + f3}{F1 + F3} N(\text{rawHT}) \\
&= N(\text{rawT2}) - \frac{0.4M(\text{rawT2, HT})}{0.9M(\text{rawHT, HT})} N(\text{rawHT}) \\
&= 0.6N(\text{rawT2, T2}) + 0.4N(\text{rawT2, HT}) \\
&\quad - \frac{0.1 \times 0.4M(\text{rawT2, HT})}{0.9M(\text{rawHT, HT})} N(\text{rawHT, T2}) - \frac{\cancel{0.9} \times 0.4M(\text{rawT2, HT})}{\cancel{0.9}M(\text{rawHT, HT})} N(\text{rawT2, HT}) \\
&= 0.6N(\text{rawT2, T2}) + \cancel{0.4N(\text{rawT2, HT})} \\
&\quad - \frac{0.1 \times 0.4M(\text{rawT2, HT})}{0.9M(\text{rawHT, HT})} N(\text{rawHT, T2}) - \cancel{0.4N(\text{rawT2, HT})} \\
&= \left(0.6 - \frac{0.1 \times 0.4M(\text{rawT2, HT})}{0.9M(\text{rawHT, HT})}\right) N(\text{rawT2, T2}),
\end{aligned} \tag{7.19}$$

where,

$$\frac{M(\text{rawT2, HT})}{M(\text{rawHT, HT})} N(\text{rawT2, HT}) = N(\text{rawHT, HT}), \tag{7.20}$$

because N(rawT2, HT) and N(rawHT, HT) have the same distribution and differ up to the activity-amplitude scale. Thence, $R(\text{T2\_HT}) = \frac{f1+f3}{F1+F3}$ is a valid strategy to obtain pure T_2 CM-distribution. Notice that we do not need to know the HT-purity in this subtraction scheme.

The source-CC ratio R(T2_HT) obtained using the 3-finger and 2-ion events are given in Fig. 7.12 as the red square and the orange triangle data points. According to the error bars shown in the figure, a major problem with these two approaches however, is that the statistics of the 3-finger and the 2-ion events fall off very quickly at far scan-points. For this reason, we need another approach.

The idea for the third approach is really quite simple. Recall from Sec. 7.1.4, we do have the activity-amplitude available to obtain the scale between N(rawT2, T2) and N(rawT2, HT). In other words, take activity-amplitudes A(rawT2) and A(rawHT), then,

$$\frac{A(\text{rawT2})}{A(\text{rawHT})} = \frac{M(\text{rawT2, HT})}{M(\text{rawHT, HT})}. \tag{7.21}$$

And by using the HT-purity found in Sec. 7.1.3, we can derive the source-CC ratio,

$$R(\text{T2\_HT}) = \frac{P(\text{rawT2, HT})A(\text{rawT2})}{P(\text{rawHT, HT})A(\text{rawHT})}, \tag{7.22}$$

which can be justified in the same way as Eq. 7.19.

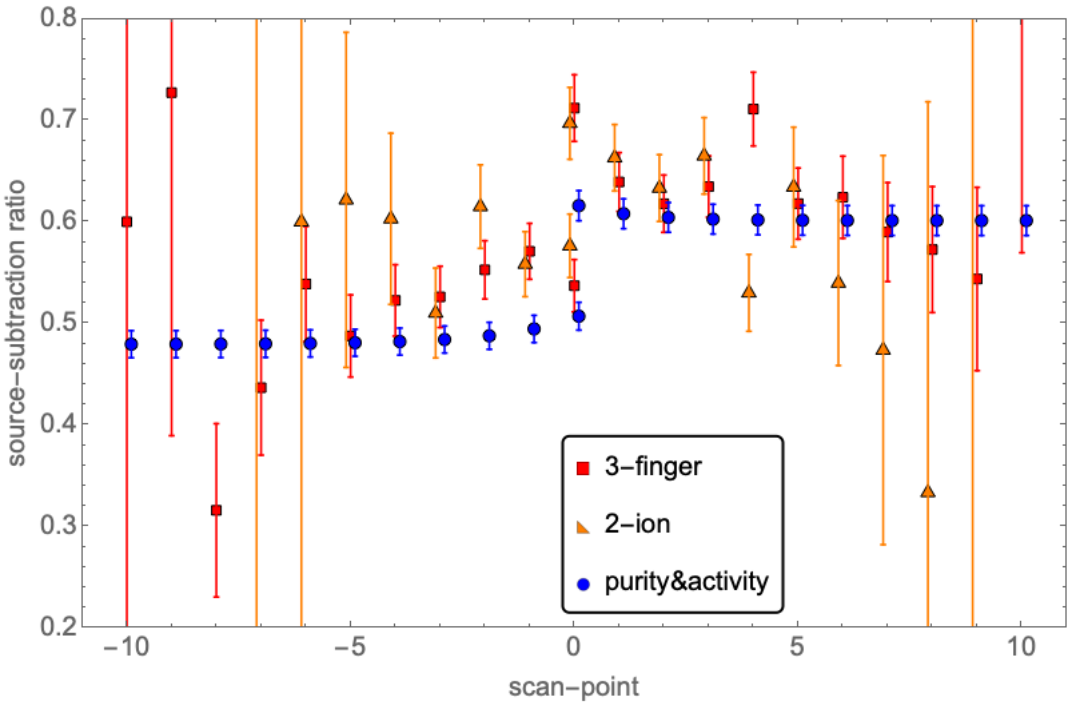

Figure 7.12: The source-CC ratio to subtract the raw-HT-data from the raw-T2-data. The resulting T2_HT-data should contain only T_2 events. The red square data points come directly from the `3-finger` events (Sec. 7.1.1), while the orange triangle points from the 2-ion events (Sec. 7.1.2). The blue circle data points are obtained using Eq. 7.22, using information from Sec. 7.1.4 and Sec. 7.1.5.

The source-CC ratio obtained using Eq. 7.22 is shown as the blue circle data points in Fig. 7.12*. The source-CC ratio now has much smaller error bars, which are mostly contributed by the error on purity. Moreover, the ratio is much better defined at far scan-points, which makes it a desirable option for us.

Lastly, the source-CC ratios R(HT_T2) for obtaining the pure HT CM-distribution are plotted in Fig. 7.13. The plot is obtained in exactly the same manner as Fig. 7.12. There

*The error are correlated because the data points in either the left- or right-scan share the same pair of activity-amplitudes in Eq. 7.22.

is a noticeable variation of the ratios close to the home-position. This variation is expected because the HT-purity does vary in those scan-points due to the catalytic conversion not being completely stabilized (Sec. 7.10).

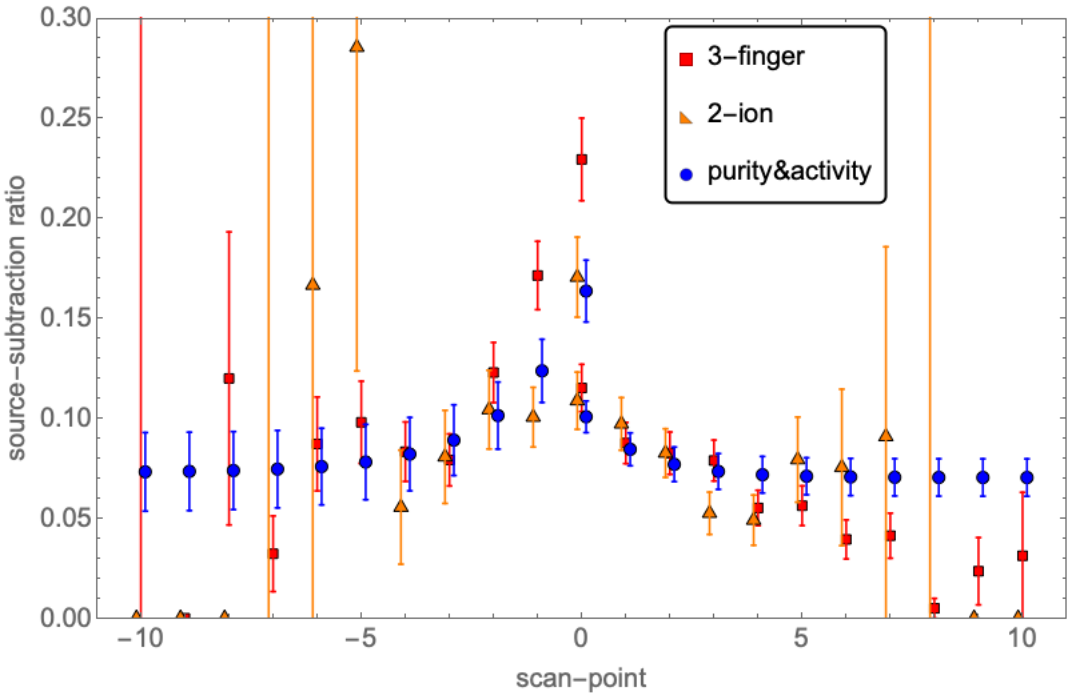

Figure 7.13: The source-CC ratio to subtract the raw-T2-data from the raw-HT-data. The resulting HT_T2-data should contain only HT events.

7.2 Charge Cross-Contamination Ratios

This section covers how we estimate the so-called charge cross-contamination (charge-CC) based on the TRIMS Geant4 simulation (Sec. 3.1). The charge-CC ratios describe the percentage leakage of the dominant-bands to the other CM-boxes along the y-axis of Fig. 6.17 and Fig. 6.18. To obtain the charge-CC ratios, we first need to align the charge peaks between data and simulation (Sec. 7.2.1) and figure out the ion-detector's home-position shift from the origin (Sec. 7.2.2). Then we evaluate the charge ratios as well as another important ratio

called the one-electron versus two-electron (1ev2e) ratio in Sec. 7.2.4, which also covers the way we estimate the corresponding systematics for these ratios.

7.2.1 Beta-Energy Matching and Geant4 Simulation Showcases

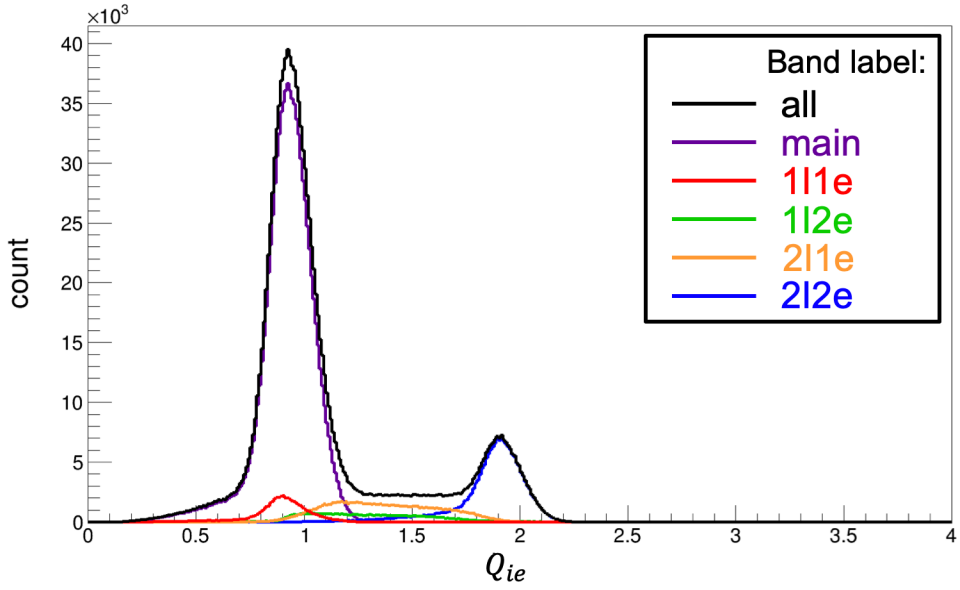

Figure 7.14: Simulated charge histogram using TRIMS Geant4 (Sec. 3.1) at the home-position. This histogram is to be compared to Fig. 6.10. The charge is reconstructed using Eq. 6.9, but with the beta-energy having been corrected by Eq. 7.23.

Before comparing the TRIMS Geant4 simulation (Sec. 3.1) result to the data, we would like to do an empirical adjustment first to match the beta-energy. The reason is that, although electron backscattering and generic Gaussian broadening are included, other detector response physics, such as the dead-layer effect, are not simulated for the beta-detector. To do the matching, we inspect the simulated charge histogram Fig. 7.14 and compare it with Fig. 6.10. The idea is to adjust the beta-energy, such that both of the simulated ($Q_{ie} = 1\,\mathrm{e}$) and ($Q_{ie} = 2\,\mathrm{e}$) peaks match in location with the data. The peak locations are indicated using Gaussians. Although the peaks are not truly Gaussian, by limiting the range of the

fit, the Gaussian fit suffices to point out the peak locations.

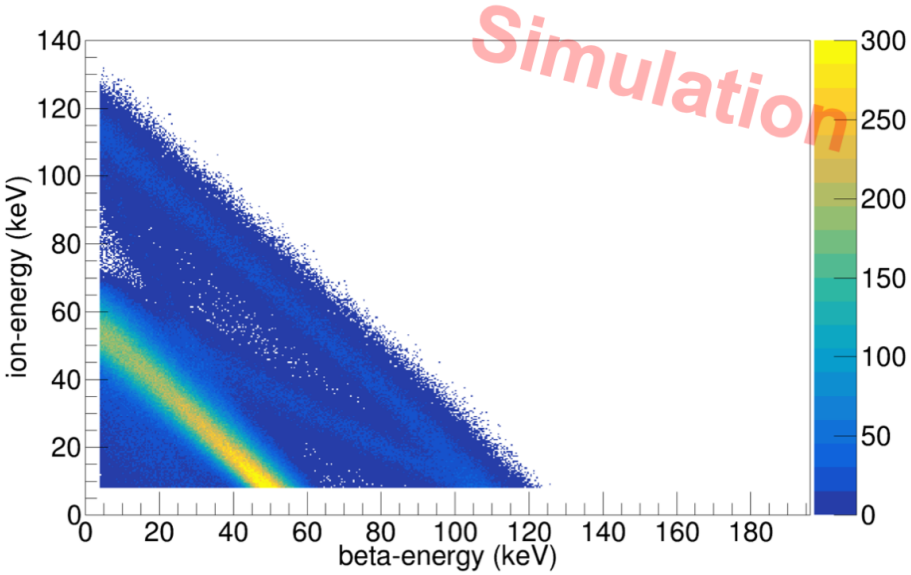

Figure 7.15: Simulated ion-energy versus beta-energy histogram at the home-position. This histogram is to be compared to Fig. 6.4.

The empirical beta-energy matching formula is given by Eq. 7.23,

$$E_\beta = 0.985 E_{\beta,\mathrm{sim}} - 5.45\,\mathrm{keV}, \tag{7.23}$$

where $E_{\beta,\mathrm{sim}}$ is the direct beta-energy output from the simulation, and E_β is the matched beta-energy that will be used for all the following derivations. The error handling associated with the beta-energy matching will be discussed in Sec. 7.2.3.

The charge spectrum in Fig. 7.14 is decomposed into individual bands as shown in the legend. This can only be done in a simulation because we know the decay-branches ahead of time.

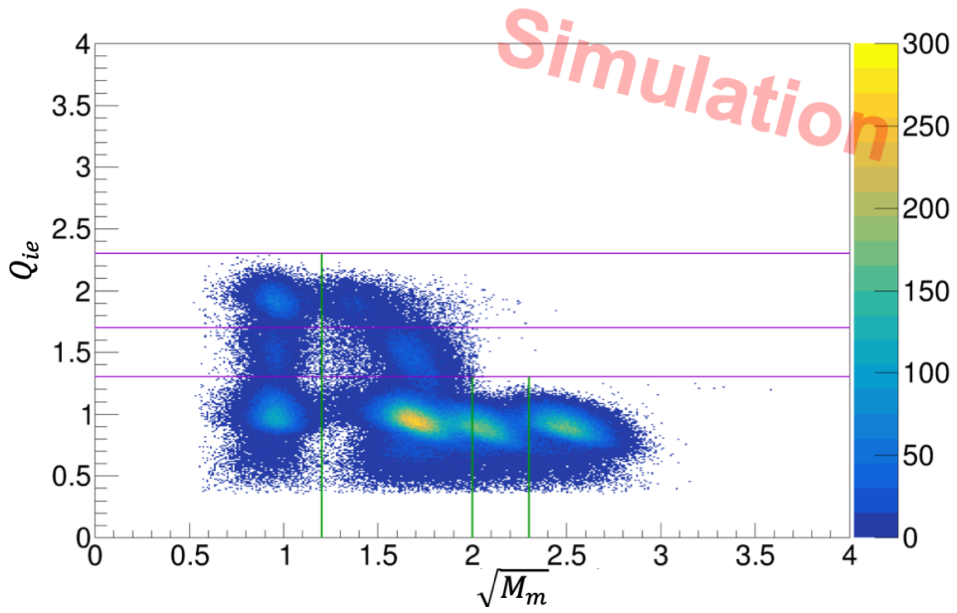

Figure 7.16: Simulated charge versus mass histogram at the home-position in the main-FV. This histogram is to be compared to Fig. 6.16

The simulation uses the default setting (Sec. 3.1.1) with 100 M total events and a week of run time. And after the beta-energy matching, the simulated beta-energy versus ion-energy histogram is given in Fig. 7.15, as compared to the data in Fig. 6.4. The ion-energy is simulated with the dead layer effect using the polynomials from Sec. 3.2.2, but the output ion-energy is again corrected using Eq. 6.8. As for the ion-TOF, there is a slight modification of Eq. 6.6 in that `time_zero` is set to 0 because the simulation does not experience electronic delays.

In the main-FV, the simulated charge versus mass histogram is given in Fig. 7.16 along with the CM-boxes. The electron backscattering, if it occurs, reduces the beta-energy and therefore reduces the charge value while keeping the mass value the same for those events. It results in the minor-bands "smearing" downward in Fig. 7.16, e.g. from CM-box `c3m1` to CM-box `c1m1`. The resulting overlaps in the bands cannot be resolved from data alone and require the simulation to provide the charge-CC. On the other hand, comparing it to

Fig. 6.17, we can see the similarity between the simulation and the data for the main-band mass peak locations are not very compelling, especially for mass-4. This is why the simulated results are used to obtain the charge-CC ratios and not the mass-CC ratios (Sec. 7.3).

7.2.2 Offset in Home-Position

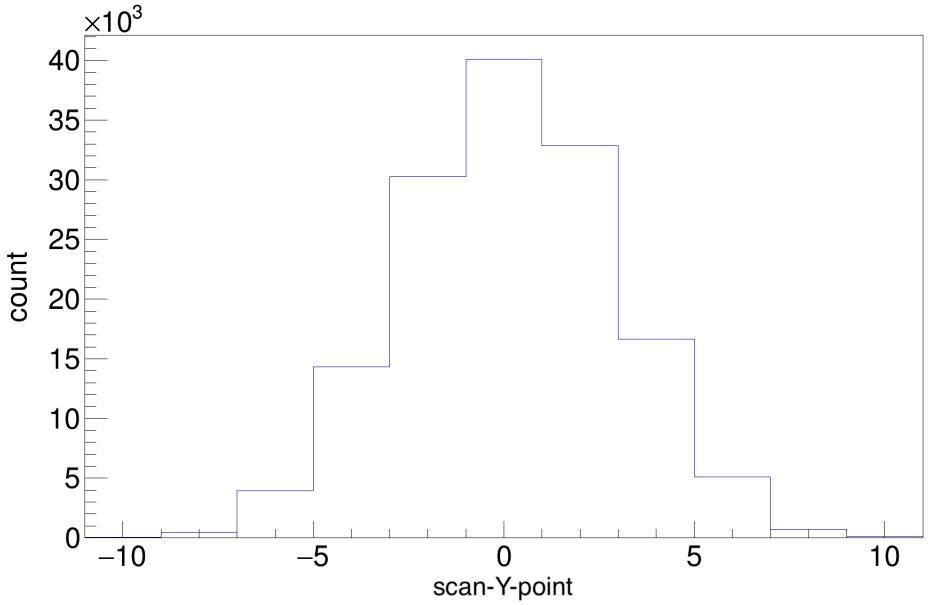

Figure 7.17: Coincidence counts over the scan-Y-point under charge-`c1` cut. The centroid gives the Y-offset of the home-position.

One item that the previous section did not mention is all figures presented in that section assume the ion-detector is placed at the home-position in the simulation. Recall from Sec. 3.3 that we are assuming the ion-detector to have a radius of 50 mm in the simulation. With the large ion-detector we can cut based on `CapturePosX,Y,Z` in Table 3.5, 3.8, and 3.9 on the ion-detector side to select coincidence events with any given scan-position. This is also how we determine the `1I` or `2I` events from Fig. 7.14.

However, there is one problem. Recall from Sec. 2.5.4, the home-position does not locate at the center-position and we need to estimate these offsets.

For the Y-offset, we inspect the run-scans in the Y-direction, and plot out the coincidence count at each scan-Y-point (Sec. 2.5.5) as shown in Fig. 7.17. Because the coincidence rate drops when the two detectors are misaligned, we expect the scan-Y-position that corresponds to the maximum rate to be the Y-component of the center-position. Hence, we take the centroid of the coincidence counts as the Y-offset. Additionally, to avoid distortion from the noise events, we applied a charge-`c1` cut (Sec. 6.3) to Fig. 7.17. The error is simply taken to be the standard error of the centroid estimation. The result is given in Table 7.2, which has been corrected using the correct step size (Sec. 2.5.4).

For the X-offset, there is one additional complication that the left- and the right-scans are taken in separate tritium fills, so the coincidence counts need to be normalized according to Sec. 7.1.4. Otherwise the process is the same, and the result is also provided in Table 7.2

Direction	Offset	Error
X-axis	0.9 mm	0.1 mm
Y-axis	0.18 mm	0.12 mm

Table 7.2: Home-position offsets in the X- and Y-direction. Note that these offsets are signed. Positive X-direction points to the right-scan direction and positive Y-direction points up toward the translation stage (Sec. 2.1.2).

These offsets are incorporated for all the simulation results in this section. We will also use these offsets to estimate the error of the scan-deconvolution (Sec. 8.2.2).

7.2.3 Charge Cross-Contamination Ratios

The main purpose of the charge cross-contamination (charge-CC) ratios is to access the band leakage across the charge-boxes (Sec. 6.3). According to the purple charge-spectrum in Fig. 7.14, the main-bands all reside in the charge-box `c1`. Hence, we only need to focus on the leakage of the minor band. For this reason, the rest of this chapter, we apply the simulation using 50 M total events, but with only 2-charge events, i.e. with a setting shown in Table 7.3. Everything else follows the default setting in Sec. 3.1.1. The run time is also about a week. And the resulting charge spectrum with the main-FV cut is given in Fig. 7.18.

Function Name	Default Value	Function Name	Default Value
		`HT_Level`	0.5
`T2_T_BranchRatio`	0.0	`HT_H_BranchRatio`	0.0
`T2_3He_BranchRatio`	0.0	`HT_3He_BranchRatio`	0.0
`T2_3HeT_BranchRatio`	0.0	`HT_3HeH_BranchRatio`	0.0
`T2_3He2p_BranchRatio`	0.5	`HT_3He2p_BranchRatio`	0.5
`T2_3He_T_BranchRatio`	0.5	`HT_3He_H_BranchRatio`	0.5

Table 7.3: The minor-band only TRIMS Geant4 simulation setting referring to Table 3.4.

Each spectrum in Fig. 7.18 has a tail on the left-hand side. These tails come from the electron backscattering, which is precisely what we are looking for in the simulation. Then to get the leakage, we mark down the percentage of each charge spectrum lying in each charge-box. As an example, Fig. 7.19 shows the case of the charge-box `c2`. The corresponding percentages are also printed out in the plot. Their band names follow the detection-ID in Table 6.1 and Table 6.2. For example, `c2R1I2eM1` says that 78.4% of the `1I2eM1` band lies in the charge-box `c2`. There are two additional bands `1I2eM3T+` and `1I2eM3He+` because the tags in the simulation allow us to separate out T^+ from $^3He^+$ ion. We record these

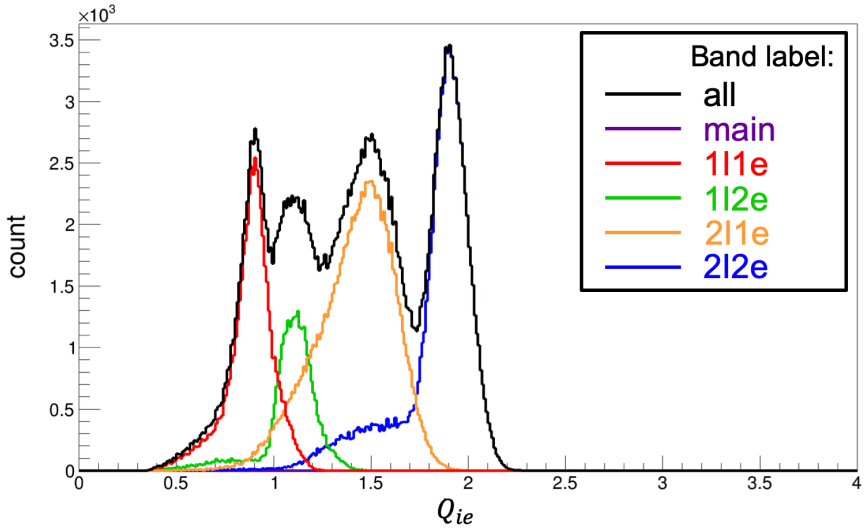

Figure 7.18: Simulated minor-band charge histogram at the home-position in the main-FV. The tail to the left of each spectrum is contributed by the electron backscattering.

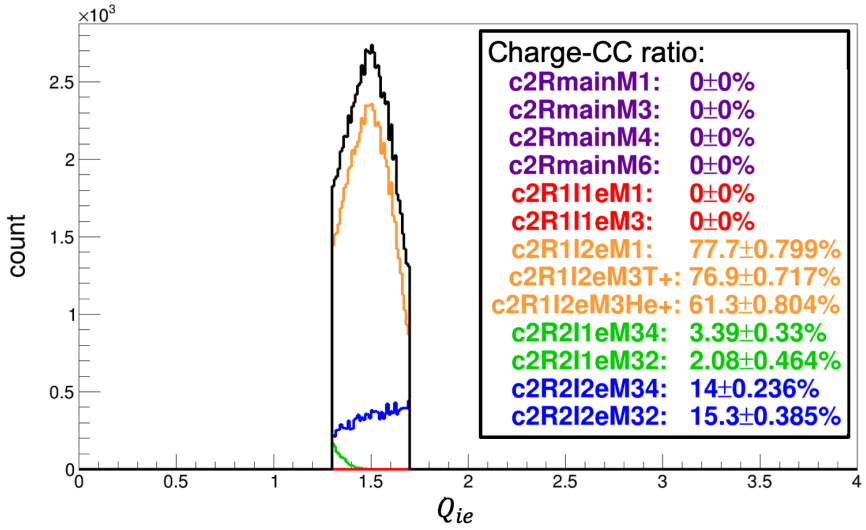

Figure 7.19: Simulated charge histogram in the main-FV and charge-`c2` cut at the home-position, where percentages of each band lying inside the charge interval are also given.

Simulation-ID	Description
s1	default
s2	$E_\beta = 0.98E_{\beta,\text{sim}} - 5.45$, for beta-energy correction
s3	$E_\beta = 0.99E_{\beta,\text{sim}} - 5.45$, for beta-energy correction
s4	$E_\beta = 0.985E_{\beta,\text{sim}} - 5.4$, for beta-energy correction
s5	$E_\beta = 0.985E_{\beta,\text{sim}} - 5.5$, for beta-energy correction
s6	shift the scan-Y-positions by 0.12 mm
s7	shift the scan-positions by 0.1 mm
s8	set initial two-ion total energy to be 1 eV; option 8 in Sec. 3.1.5
s9	set initial two-ion total energy to be 50 eV; option 9 in Sec. 3.1.5

Table 7.4: Simulation-ID for the charge-CC ratio systematics and their descriptions.

percentages for charge-boxes `c1`, `c2`, and `c3`. These percentages converted to ratios are the charge-CC ratios we are looking for.

The error bars shown in Fig. 7.19 are only the Poisson errors based on the counts. These statistical errors are small because of how many events we used. Nevertheless, the systematic errors are much more vital at this interface between the simulation and the experiment. To estimate the complete error bars on these charge-CC ratios, we assume the simulation configurations listed in Table 7.4 are the major contributions. These configurations are labeled using the simulation-IDs (sim-IDs). The default setting described the simulation setup up until now and is labeled by sim-ID. s1). Sim-ID. s2) to s5) describe the error of the beta-energy matching (Eq. 7.23). The errors on these parameters are derived in that when using $aE_{\beta,\text{sim}} - b$, between a in a range of [0.98, 0.99] and b in a range of [5.4, 5.5], we can find values such that both ($Q_{ie} = 1\,\text{e}$) and ($Q_{ie} = 2\,\text{e}$) peaks are matched for either the raw-T2-data or the raw-HT-data. Item sim-ID. s6) and s7) are to account for the detector home-position offset uncertainty (Table 7.2). Finally, item sim-ID. s8) and s9) are related

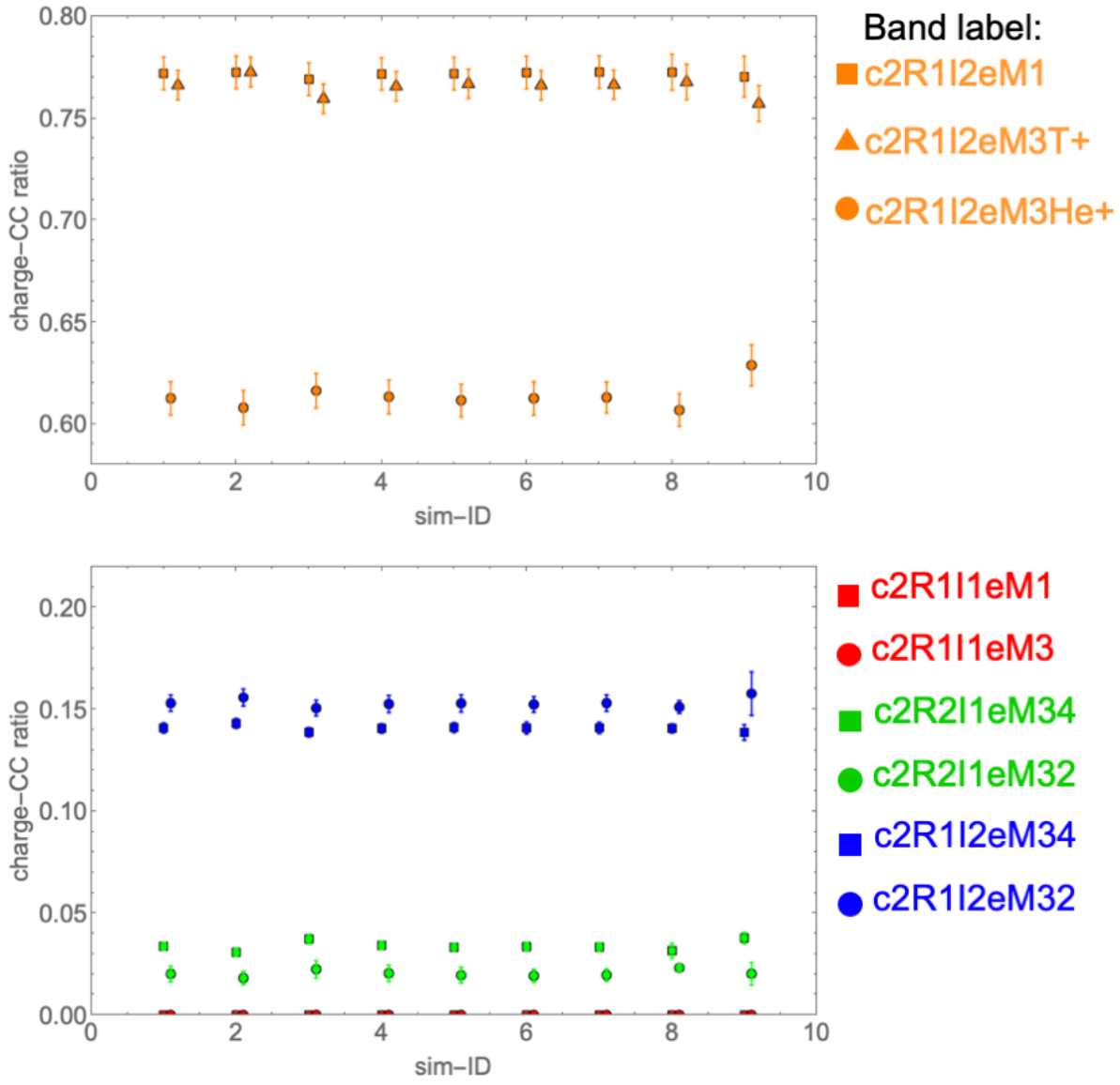

Figure 7.20: The charge-CC ratios under charge-`c2` cut at the home-position, but the ratios are obtained using different simulation configurations whose sim-IDs (Table 7.4) are provided on the x-axis. The slight shifts in x-axis position are just there to avoid the data points from overlapping. The error bars come from the Poisson error of the counts inside the charge interval.

to loosely bounded ion-initial energies (Sec. 3.1.5). Only item sim-ID. s8) and s9) requires redoing the Geant4 simulation; the others can be done in the post simulation analysis on the default Geant4 setting (Sec. 3.1.1 with the Table 7.3 modification).

Once we obtain the charge-CC ratios for all the configurations in Table 7.4, we can plot out the charge-CC ratios versus the sim-ID. The charge-box `c2` example is shown in Fig. 7.20. The percentages shown in Fig. 7.19 basically correspond to the values at (`sim_ID = 1`) along with their error bars. Thence, to obtain the systematics, we conservatively define an effective error s_i at (`sim_ID = i`) by,

$$s_i \equiv \max\left(\left|(\mu_i + \sigma_i) - \mu_1\right|, \left|(\mu_i - \sigma_i) - \mu_1\right|\right), \tag{7.24}$$

where μ_i and σ_i corresponds to the charge-CC ratio and its statistical error at (`sim_ID = i`). Then the total systematics S is obtained by summing s_i's in quadrature,

$$S \equiv \sqrt{\sum_i s_i^2}. \tag{7.25}$$

We use the default μ_1 for our charge-CC ratios. And the charge-CC ratio with systematics for each band is given in Fig. 7.21.

Up until now, all the results are obtained when the ion-detector is placed at the home-position. The apparent next step is to scan the ion-detector. An example of charge-CC ratio versus the scan-point is given in Fig. 7.22 for the `1I2eM3T2` band. The `1I2eM3T2` band is actually a special band that is not present in Fig. 7.19, whose charge-CC ratio μ_{M3T2} is evaluated by,

$$\mu_{\mathrm{M3T2}} \equiv \frac{\mu_{\mathrm{M3T}+} + \mu_{\mathrm{M3He}+}}{2}, \tag{7.26}$$

where $\mu_{\mathrm{M3T}+}$ and $\mu_{\mathrm{M3He}+}$ are the charge-CC ratios from the orange-triangle and -circle data-points in Fig. 7.21. The systematics of these two charge-CC ratios are $S_{\mathrm{M3T}+}$ and $S_{\mathrm{M3He}+}$ obtained using Eq. 7.25. The `1I2eM3T2` charge-CC ratio error S_{M3T2} is then conservatively taken to be,

$$\begin{aligned} S_a &\equiv \max\left(\left|(\mu_{\mathrm{M3T}+} + S_{\mathrm{M3T}+}) - \mu_{\mathrm{M3T2}}\right|, \left|(\mu_{\mathrm{M3T}+} - S_{\mathrm{M3T}+}) - \mu_{\mathrm{M3T2}}\right|\right), \\ S_b &\equiv \max\left(\left|(\mu_{\mathrm{M3He}+} + S_{\mathrm{M3T}+}) - \mu_{\mathrm{M3T2}}\right|, \left|(\mu_{\mathrm{M3T}+} - S_{\mathrm{M3He}+}) - \mu_{\mathrm{M3T2}}\right|\right), \end{aligned} \tag{7.27}$$

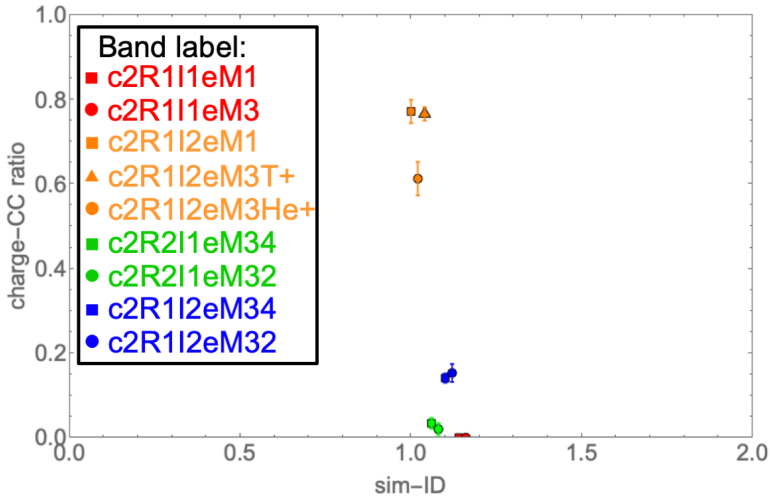

Figure 7.21: The home-position charge-CC ratios the systematics error bars. The slight shifts in x-axis position are to avoid the data points from overlapping. The description of how the error bars are obtained is given in the text.

$$S_{\mathrm{M3T2}} = \sqrt{S_a^2 + S_b^2}. \tag{7.28}$$

As for `1I2eM3HT`, its value and error are taken to be the same as that of `1I2eM3He+`.

In Fig. 7.22, the error bars get large at the far scan-points. The statistical errors are dominating in those cases.

Because the scan-position does not change the beta- and the ion-energy for the charge reconstruction (Eq. 6.9) nor the electron-backscattering probability, we expect the charge-CC ratios to be scan-position independent. For this reason, we fit Fig. 7.22 with a horizontal line and use the value of the fit parameter as well as the fit standard error as the final charge-CC ratios to be referred to. The same horizontal fit is done to all the other charge-CC ratios; the uncertainties for the other bands are much smaller than that of `1I2eM3T2`.

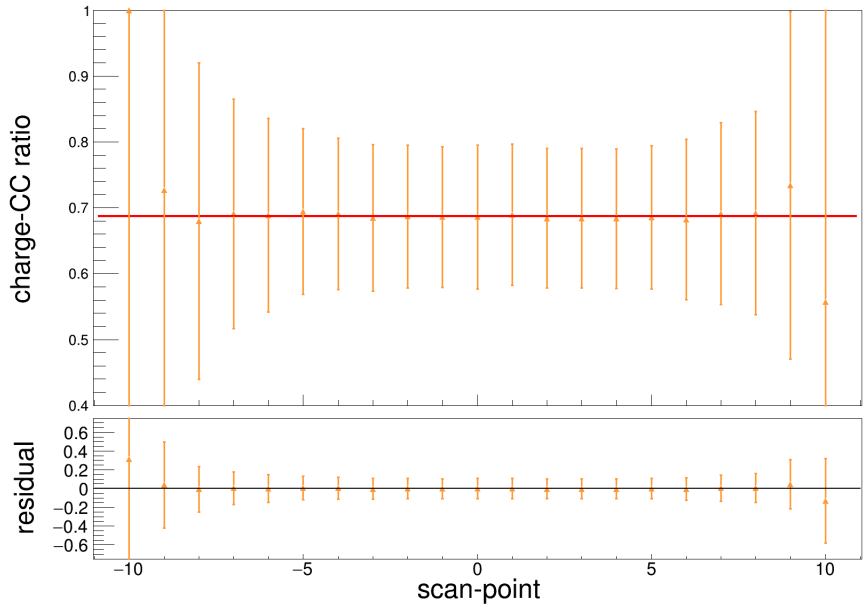

Figure 7.22: The `1I2eM3T2` charge-CC ratio across the scan-points. The ratios are fitted to a horizontal line because the charge-CC ratio should be scan-position independent. The bottom plot shows the absolute fit residual.

7.2.4 One-Electron Versus Two-Electron Ratios

Even if we have the charge-CC ratios for all the minor-bands as shown in Fig. 7.19, we cannot use half of them, because both the `1I1e` and the `2I1e`-bands are indistinguishable from the main-bands in the main-FV. In other words, no CM-boxes contain `1I1e`- or `2I1e`-bands as their dominant-bands (Sec. 6.3.1). In order to resolve this issue, we also need another ratio called the 1eV2e ratio from the simulation. The basic idea is to derive the `1I1e`- and the `2I1e`-band intensities from the `1I2e`- and the `2I2e`-bands. Given an ion-detection configuration C, we can define the 1eV2e ratio as the following,

$$R_{\text{1eV2e}} \equiv \frac{I(\text{the beta-detector detects 1 electron given } C)}{I(\text{the beta-detector detects 2 electrons given } C)}, \tag{7.29}$$

where I stands for intensity. The intensity can be thought of as the number of this specific type of event given a fixed decay number. Hence, if we know the counts of the `2e`-bands

as well as the corresponding 1eV2e ratio, then we can derive the counts for the `1e`-bands as well. And according to this definition, a 1eV2e ratio can range from 0 to positive infinity.

The ion-detection configurations we considered for the 1eV2e ratio evaluation are provided in Table 7.5.

Ion-Detection-ID	Description
`1IM1`	Detecting only H^+ for a 2-ion event
`1IM3T2`	Detecting either T^+ or $^3He^+$ for a 2-ion event given T_2 ion initial condition
`1IM3HT`	Detecting only $^3He^+$ for a 2-ion event given HT ion initial condition
`2IM34T2`	Detecting $^3He^{++}$ for a 2-charge event given T_2 ion initial condition
`2IM34HT`	Detecting $^3He^{++}$ for a 2-charge event given HT ion initial condition
`2IM32T2`	Detecting both T^+ and $^3He^+$ for a 2-ion event
`2IM32HT`	Detecting both H^+ and $^3He^+$ for a 2-ion event

Table 7.5: Description of the ion-detection configuration of each 1eV2e ratio.

We obtain the 1eV2e ratios and their error bars in the same manner as for the charge-CC ratios (Sec. 7.2.3). The first thing to note is that the 1eV2e ratios do not depend on the charge-boxes `c1`, `c2`, or `c3`. Moreover, unlike the charge-CC ratios that should be scan-position independent (Fig. 7.22) however, the 1eV2e ratio depends on the scan-position as illustrated in Fig. 7.23 that shows the `1IM1`-1eV2e ratio. The reason is that the 1eV2e ratios ultimately come down to kinematics and detector geometry. For example, in Fig. 7.23, we can see that the error bars are larger at the home-position than for instance at scan-point ($d = -3$). This is caused by `1IM1` having less statistics because a 2-ion event most likely would have both of the ions detected when the ion-detector is at the home-position, i.e. `2I` is more likely than `1I` in this case. The detection efficiency is primarily a result of how wide our detectors are as compared to the gyroradii of the ions (Sec. 2.4.2). Thus the 1eV2e ratios

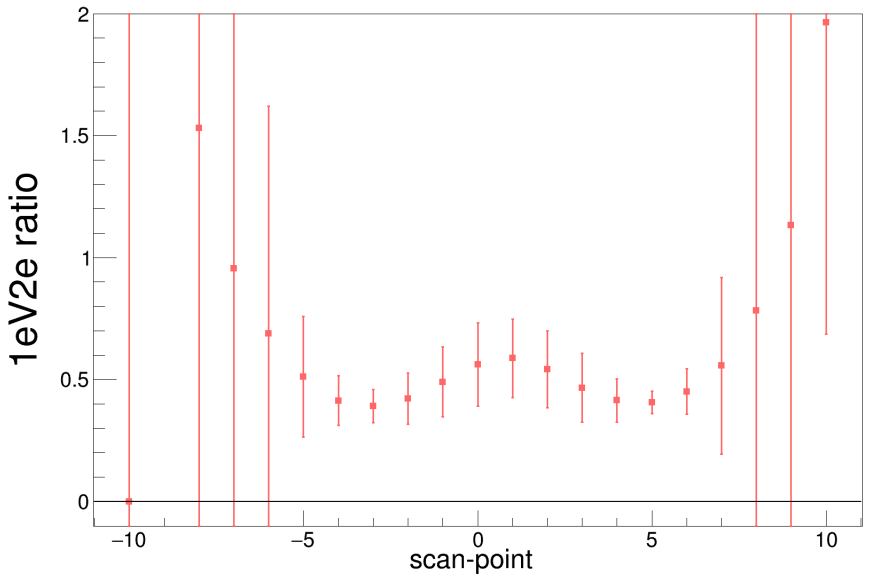

Figure 7.23: The `1IM1` 1eV2e ratios across the scan-points.

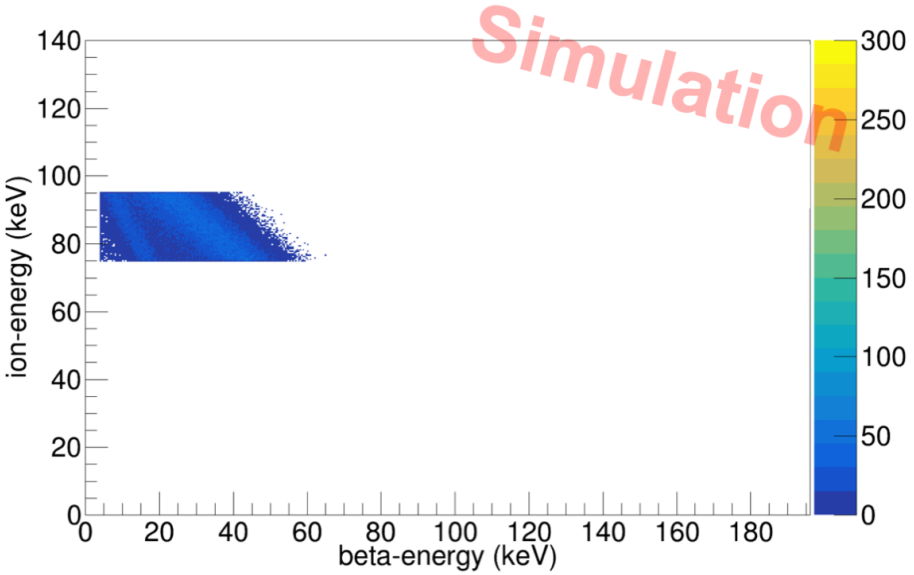

Figure 7.24: Simulated ion-energy versus beta-energy histogram in the high-FV like in Fig. 7.5. According to Fig. 6.4, the two bands remaining are `2I1e` and `2I2e`.

are also sensitive to the initial ion configuration (Sec. 3.1.5) we included in Table 7.4*. The difference in the ion initial condition is also the reason why many 1eV2e ratios are defined separately for the T_2 and the HT source-type in Table 7.5.

Nevertheless, there is an underlying question that has not been answered: since `1I` events are not "observable" to be compared with the simulation, how do we know the simulation is accurate?

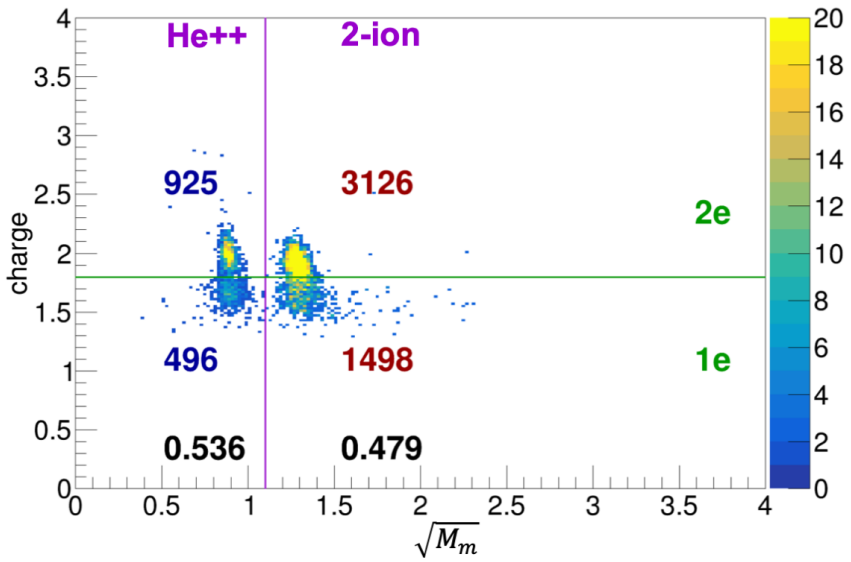

Figure 7.25: Charge vs mass histogram in the high-FV for the left-scan raw-T2-data at the home-position. The purple vertical line is at ($\sqrt{M_m} = 1.1\,\sqrt{\mathrm{u}}$), which cleanly separate the `2IM34` band on the left from the `2IM32` band on the right (Sec. 7.1.2). The green horizontal line is at ($Q_{ie} = 1.8\,\mathrm{e}$). Above the green line, the counts should be `2I2e` dominated, and below `2I1e` dominated. By comparing the `2I1e` count to the `2I2e` count that are provided for each of the 4 boxes under dark blue and dark red, we obtain the effective 1eV2e ratio given on the bottom in black.

To test the accuracy of the simulation, we once again move to the high-FV (Sec. 7.1.2),

*The initial ion configurations have negligible influence on the charge-CC ratios.

where the bands consisted of only 2I1e- and 2I2e-bands as shown in Fig. 7.24. According to Fig. 6.4, we do indeed see these two bands in the data too. In other words, we can access the 1eV2e ratio for the 2I ion-detection configuration from the data, which cover 4 out of 7 ion-detection-IDs from Table 7.5. Thence, we plot out the charge versus mass histograms in the high-FV for the data in Fig. 7.25 and for the simulation in Fig. 7.26.

The data shown in Fig. 7.25 comes from the raw-T2-data. The purple vertical line at ($\sqrt{M_m} = 1.1\sqrt{\mathrm{u}}$) gives a clean separation of the ion-detection-ID. 2IM34 that consist of $^3He^{++}$ events to the left and 2IM32 that consist of 2-ion events to the right. The green horizontal line at ($Q_{ie} = 1.8\,\mathrm{e}$) separates the spectrum further to the 2I2e-dominated boxes on the top and the 2I1e-dominated boxes on the bottom. We can see the charge 1eV2e separation is far from clean however.

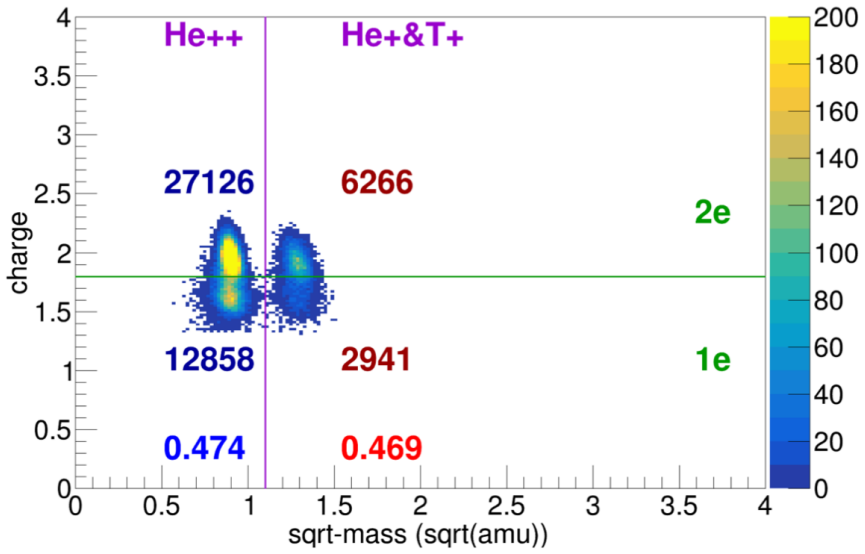

Figure 7.26: Simulated charge vs mass histogram in the high-FV for the T_2 source at the home-position. This has the same idea as Fig. 7.25, but is instead using simulation. The 1eV2e ratios are on the bottom in bright blue and bright red.

To make the comparison between the data and the simulation more readily available, we

compare their effective 1eV2e ratio instead. That is, instead of trying to obtain the clean 1eV2e ratio from the data that requires multiple steps and so accumulates systematic errors, we work backward on the simulation. First of all, the simulation shown in Fig. 7.26 is taken to have 50% T_2 and 50% HT to approximate the isotopic composition of the raw-T2-data (Fig. 7.9). Then we derive the effective 1eV2e ratios directly from the upper and lower charge boxes in Fig. 7.25 and Fig. 7.26. Because the counts are given in the figures, an example of the 1eV2e ratio is $925/496 = 0.536$ for the `2IM34` band in Fig. 7.25. These effective ratios are given in black on the bottom of Fig. 7.25 and in blue and red on the bottom of Fig. 7.26.

Now we have the effective 1eV2e ratios for the `2I` bands in data and in simulation, and we plot them together across the scan-positions as shown in Fig. 7.27. Figure 7.27.a) is evaluated for the `2IM34`, and Fig. 7.27.b) for the `1IM32`. The data points are the black circles, while the simulation points are either blue or red squares. The difference between the data and the simulation is given at the bottom of each plot.

The error bars in Fig. 7.27 are propagated using only Poisson errors from the counts. The ratios in which the denominators are 0 are set to 0 as well; the 0 denominator is set to 1 for error calculation however. If both the numerator and denominator are 0, then the ratio and the error are set to 0 for Fig. 7.27. However, when this happens in the 1eV2e ratios that will be used in the analysis, e.g. Fig 7.23, they are conservatively set to 50 ± 50. Obtaining the accurate 1eV2e ratio far from the home-position has always been the difficulty of this subsection's approach.

Despite the difficulty, the data and the simulation are qualitatively similar to each other, which boosts our confidence in the simulation. The same procedures are also followed for the raw-HT-data, and the results also agree well. Thence, even though we cannot separate out the `1I` bands from the main-bands, we are relying on the simulation to give us the 1eV2e ratio for the `1I` bands. Further systematics on the disagreement in the data versus the simulation should be addressed by a strategy in the later stage of the analysis (Sec. 7.4.4).

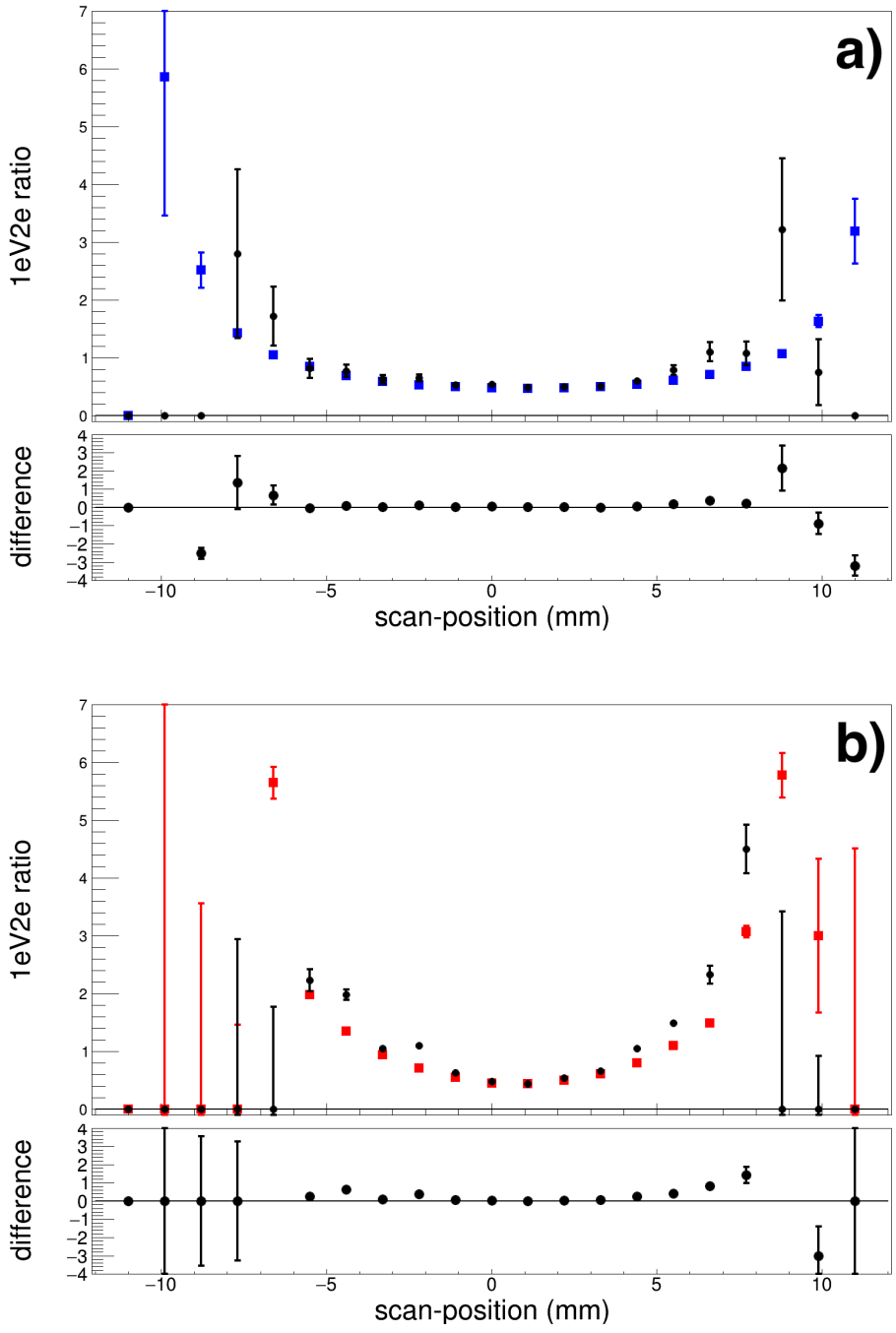

Figure 7.27: Comparing the 2-charge 1eV2e ratios in Fig. 7.26 with Fig. 7.25 across the scan-positions. The colored square points are from the simulation, while the black circle points are from the data. Plot a) is using the 1eV2e ratio from the `M34` band, and plot b) from the `M32` band. A point is set to 0 if the denominator of the 1eV2e ratio receives no counts. The relative difference of the data to the simulation points are given on the bottom of both plots a) and b).

7.3 Mass Cross-Contamination Ratios

This section covers the last ratios we are looking for; they are called the mass cross-contamination (mass-CC) ratios. The mass-CC ratios described the percentage leakage of the dominant-bands to the other CM-boxes along the x-axis of Fig. 6.17 and Fig. 6.18. However, in order to obtain the mass-ratios, we must use the clean mass peaks that contain only one detection-channel (Sec. 6.1.1); the mass peaks should not be cross-contaminated. As described in Sec. 7.3.1, the first step is to remove the source contamination (Sec. 7.1) and the charge (Sec. 7.2) by means of charge- and source-subtraction. Then to derive the mass-CC ratios, Sec. 7.3.2 handles the mass separation for the main-bands from the T_2 events, while Sec. 7.3.3 handles the main-bands from the HT events. Finally, the mass-CC for the minor bands are discussed in Sec. 7.3.4.

7.3.1 Charge-Subtraction and Source-Subtraction

Before deriving the mass-CC ratios, we first need to get clean mass spectra from Fig. 6.20 such that their charge and source contaminations are subtracted out.

The charge-subtraction in this context can be more easily explained using Fig. 6.20. There are three charge-boxes `c1`, `c2`, and `c3`, each of which corresponds to a type of dominant-band `main`, `1I2e`, and `2I2e`. So the goal of the charge-subtraction is to subtract the mass spectrum content of the charge-boxes from each other such that what remain after the subtraction are only the dominant-bands in their corresponding charge-boxes. To perform the charge-subtraction, we refer to the charge-CC ratios (Sec. 7.2.3) to figure out the leakage between each charge-box. We start from charge-box `c2` and `c3` because they only have contamination coming from one another, i.e. from `1I2e`- and `2I2e`-bands, where we can apply a similar technique to Eq. 7.16. Once we obtain the pure `1I2e`- and `2I2e`-bands, we can subtract them out from charge-box `c1`. We also need to apply the 1eV2e ratios (Sec. 7.2.4) to estimate the components of `1I1e`- and `2I1e`-bands in charge-box `c1` as well and subtract them out to get the clean `main`-band. The subtracted out charge contamination is shown in solid magenta

color in Fig. 7.28 for the raw-T2-data.

Next, we need to apply the source-subtraction on top of the charge-subtraction. The method of the source-subtraction has already been covered in Sec. 7.1.5 from where we can refer to the source-CC ratio directly. The subtracted out source contamination is shown in solid green color in Fig. 7.28.

The order of doing the charge-subtraction before the source-subtraction is historical. Because many of the 1eV2e ratios actually depend on the source-type, the opposite order would have actually simplified the subtraction process.

The remaining white histograms from Fig. 7.28 are the clean mass spectrum we are looking for, and we refer to this data as the T2_HT-data. We use the T2_HT-data as an estimation for the true data coming from a pure T_2 source. Similarly, we also performed the charge- and mass-subtraction on the raw-HT-data to get the HT_T2-data as shown in Fig. 7.29.

Compared to Fig. 6.20, we can see in Fig. 7.28.a) that both the main-bands `M1` and `M4` are subtracted out. This is a desirable result because there are no H^+ and $^3HeH^+$ contributions in the main-band for a pure T_2 source. Similarly, for Fig. 7.28.b), the `1I2eM1` is subtracted out because there are no H^+ detection from pure T_2 2-ion events either. As for the estimated HT mass spectrum in Fig. 7.29, the main-band `M6` is also subtracted out as desired, even though the mass-6 peak is not really intense to begin with*.

*The is due to the near 90% HT-purity in the raw-HT-data even for the home-position (Fig. 7.10).

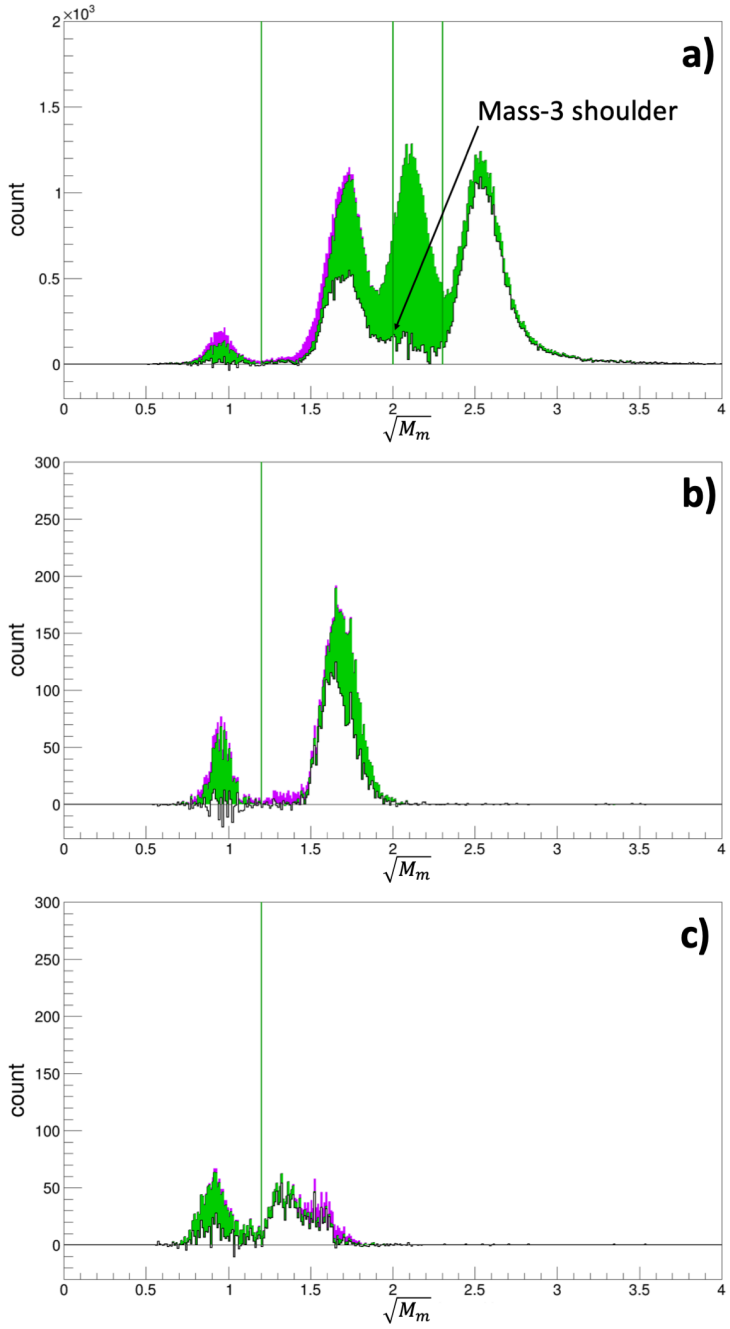

Figure 7.28: Mass spectrum for the left-scan T2_HT-data at the home-position in the main-FV. This plot comes from performing subtractions on top of Fig. 6.20. The magenta portion of the peak is subtracted out using the charge subtraction, while the green portion is subtracted out using the mass subtraction on top of the charge subtraction. The T2_HT-data is the remaining white colored histogram. The green lines are associated with the mass-boxes defined in Sec. 6.3.1.

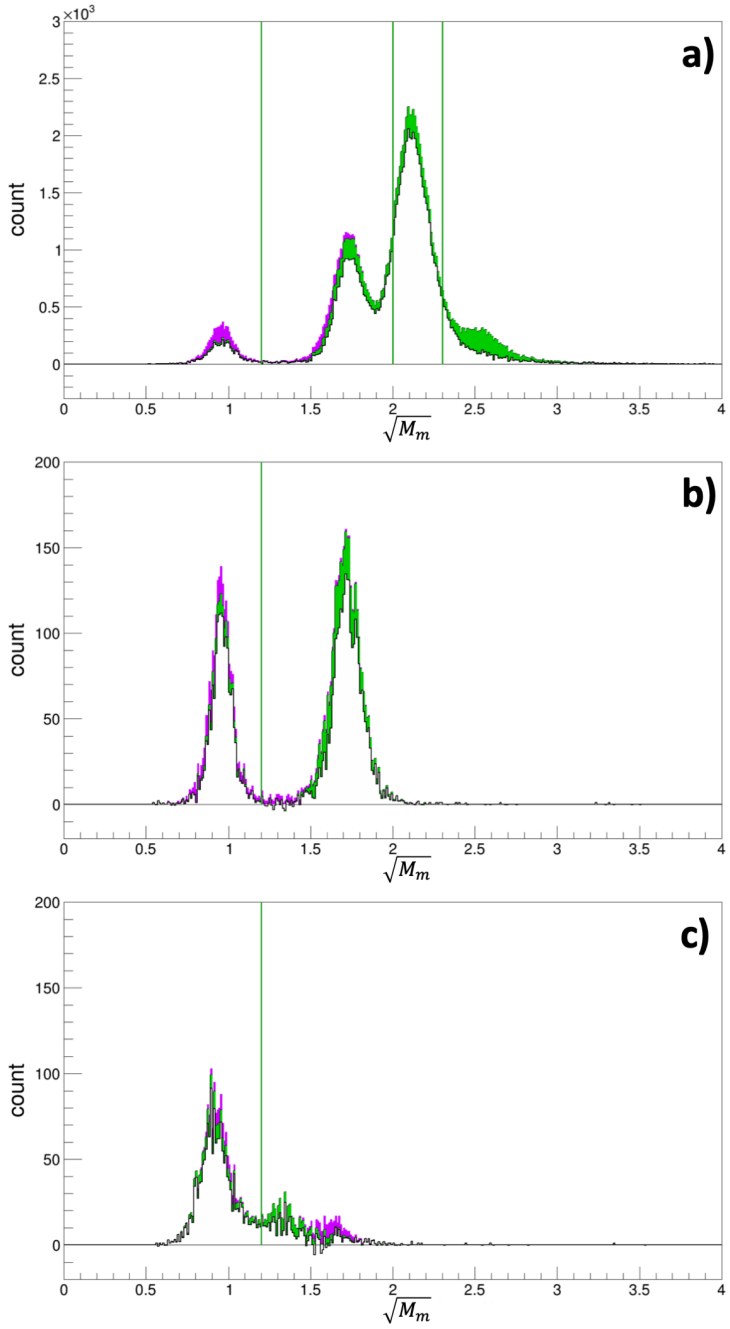

Figure 7.29: Mass spectrum for the left-scan HT_T2-data at the home-position in the main-FV. This plot is to be compared to Fig. 7.28.

7.3.2 Main-band T2_HT Ratios and the Mass-3 Shoulder

The main purpose of the mass cross-contamination (mass-CC) ratios are to access the band leakage across the mass-boxes. Once we get the clean mass spectrum, the next task in obtaining the mass-CC ratios is to separate the mass peaks from one another. This section starts with the T2_HT main-bands. But to do that, we need to look at one puzzle first.

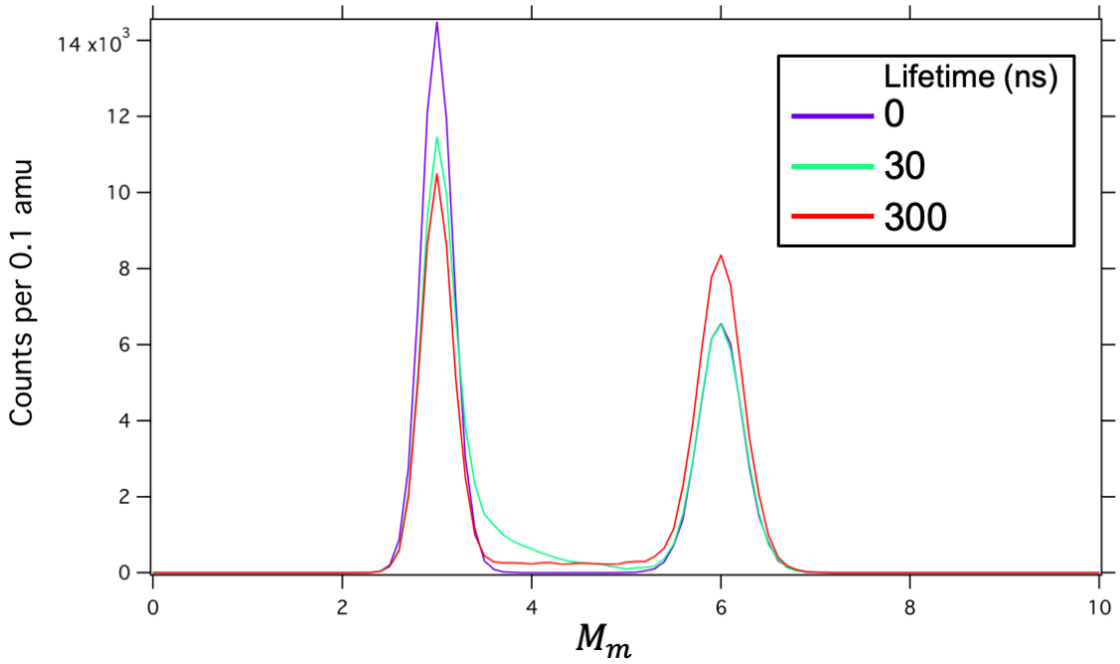

Figure 7.30: Simulated T_2 main-band mass peaks with different dissociation lifetime [41]. The legend lists the lifetime in ns for each peak. The 30 ns lifetime produces a mass-3 shoulder like we observe in the data (Fig. 7.28.a)).

Although the majority of the `M4` events are subtracted out in Fig. 7.28.a), there are counts remaining in that region. We refer to the excess as the mass-3 shoulder. We do not have a direct method to figure what physics events the mass-3 shoulder corresponds to, but to our understanding, they are related to the finite dissociation lifetimes of the molecular ions during the ions' time of flight. Figure 7.30 [41] shows a Monte Carlo simulation of the T_2

mass spectrum given different dissociation lifetime. As shown by the simulation, a 30 ns dissociation lifetime gives the mass-3 shoulder similar to that of the data. Although delayed, the mass-3 shoulder still corresponds to dissociated states. We treat the mass-3 shoulder as part of the mass-3 peak.

With the knowledge of the mass-3 shoulder, we set the ($\sqrt{M_m} = 2.2\sqrt{\text{u}}$) line as a hard separation between the mass-3 and the mass-6 peaks. In other words, in our estimation, we assume every count under $\sqrt{M_m}$ range of $[1.2, 2.2)\sqrt{\text{u}}$ are assumed to be belong to `T2_mainM3` and $\sqrt{M_m}$ range of $[2.2, 4)\sqrt{\text{u}}$ to `T2_mainM6`. In Fig. 7.31, it shows a copy of the charge- and source-subtracted mass spectrum from Fig. 7.28 a). The `T2_mainM3` mass spectrum that we just defined is colored in blue for its part that lies inside mass-box `m3` and orange inside mass-box `m4`. Similarly, the `T2_mainM6` spectrum is in blue for its part that lie inside mass-box `m4` and orange inside mass-box `m6`. The corresponding count for each part is provided on the top of the plot. Notice these counts are not integers due to the charge- and the source-subtraction. Based on these counts, we can determine the ratios of the mass spectra in each mass-box, which are the mass-CC ratios we are looking for. These mass-CC ratios are given on the top left of the plot. For instance, `m3RmainM3T2` means that 86.7% of the `T2_mainM3` mass spectrum is present in the mass-box `m3`. Other than the four ratios listed, the other T2_HT main-band mass-CC ratios are assumed to be 0 including, for instance, `m1RmainM3T2` and `m3RmainM6`.

The errors on these ratios can be derived from error propagating Poisson errors of the counts. However, that would be insufficient in accounting for the errors from the charge and source-subtraction. A more complete treatment will be covered in Sec. 7.3.5.

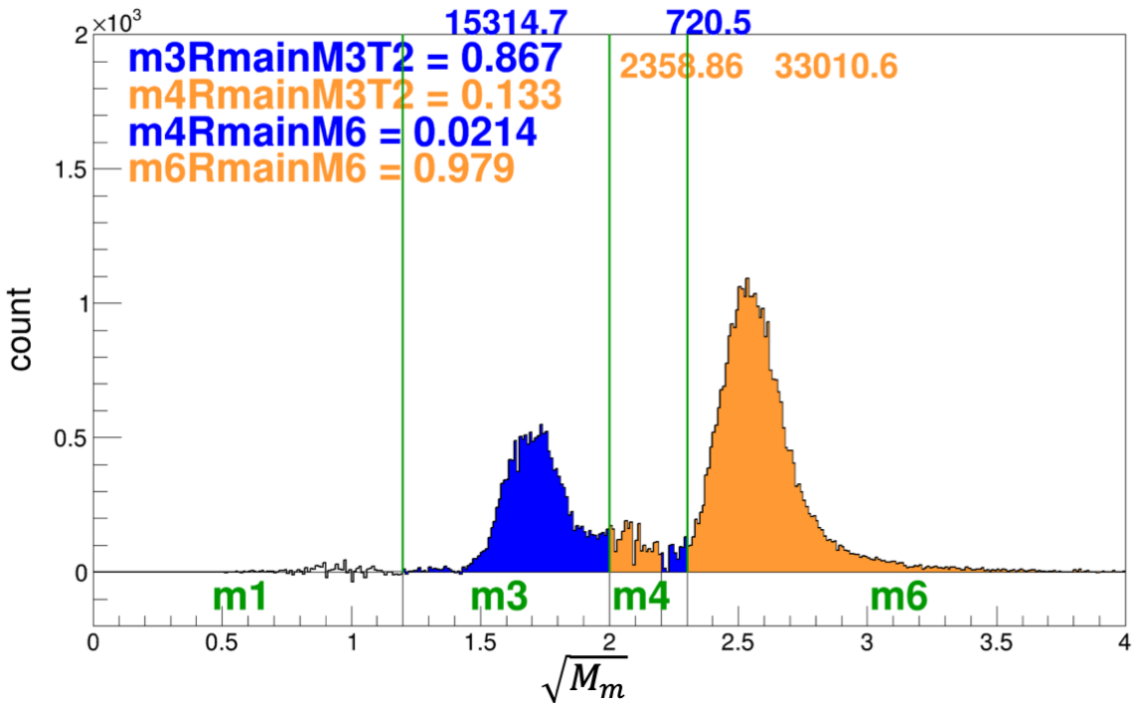

Figure 7.31: Mass-CC ratios for the main-band T2_HT data. The mass spectrum comes from Fig. 7.28 a). In this estimation, every event under $\sqrt{M_m}$ range of [1.2, 2.2)$\sqrt{\text{u}}$ are assumed to belong to `T2_mainM3`, while $\sqrt{M_m}$ range of [2.2, 4)$\sqrt{\text{u}}$ to `T2_mainM6`. The part of the `T2_mainM3` lying in mass-box `m3` is colored in blue and in mass-box `m4` in orange. Similarly, the part of the `T2_mainM6` lying in mass-box `m4` is colored in blue and in mass-box `m6` in orange. Their corresponding counts are provided on the top of each part. The mass-CC ratios as derived from the counts are provided on the top left.

7.3.3 Main-band HT_T2 Ratios Using the Three-Gaussian Fit

As for the HT_T2 main-bands from Fig. 7.29 a), there is a different challenge in separating the mass spectrum. That is, the mass-3 and the mass-4 peaks heavily overlap with each other. To more accurately separate the peaks, we fit the two peaks each with the following three-Gaussian (3-gaus) function:

$$f_{3gaus}(x) \equiv A_1 e^{\frac{-(x-\mu_1)^2}{2\sigma_1}} + A_2 e^{\frac{-(x-\mu_2)^2}{2\sigma_2}} + A_3 e^{\frac{-(x-\mu_3)^2}{2\sigma_3}}, \tag{7.30}$$

under the following global restrictions,

$$\begin{aligned} A_2 &= a_2 A_1, & A_3 &= a_3 A_2, \\ \mu_2 &= \mu_1 + b_2\sigma_1, & \mu_3 &= \mu_2 + b_3\sigma_2, \\ \sigma_2 &= c_2\sigma_1, & \sigma_3 &= c_3\sigma_2. \end{aligned} \tag{7.31}$$

The variable x is parametrized using $\sqrt{M_m}$. The parameters a_2, μ_2, σ_2, a_3, μ_3, and σ_3 are the global fit parameters. In other words, each of the two mass peaks has its own fit parameters A_1, μ_1, and σ_1, but they share their global fit parameters; there are $2 \times 3 + 6 = 12$ fit parameters in total. The global parameters fix the basic shape for the 3-Gaussian functions. The empirical origin of the 3-gaus function comes from the energy dependence of the timing resolution (Fig. 5.12). We infer that each mass peak is built up from Gaussian peaks with different widths; the worse the time resolution, the wider the Gaussian. However, we also observe from Fig. 6.11 and Fig. 6.16 that the broadening appears to be more pronounced toward the high-mass end. This is why we are also shifting the means of the 3-gaus function to match the empirical observation. As the timing broadening should affect the mass peaks equally in the $\sqrt{M_m}$ space (Sec. 6.2.2), we assume the 3-gaus shape to be the same for for the mass-3 and the mass-4 peaks.

This nonlinear fit with the 3-gaus function is done using ROOT, and the result is shown in Fig. 7.32. The fit is done in the $\sqrt{M_m}$ interval of $[1.2,\ 4)\sqrt{\text{u}}$ to isolate the mass-1 peak. Every count in $[0,\ 1.2)$ is assumed to be from `HT_mainM1` and it receives a mass-CC ratio of 1 in the mass-box `m1`. For the other two peaks, the blue 3-gaus function from the fit is assumed to be the true `HT_mainM3` and orange the `HT_mainM4`. After analytically evaluating the area using error functions for the 3-gaus, the derived mass-CC ratio is given on the top left of Fig. 7.32. For instance, `m3RmainM4` means that 13.5% of the orange 3-gaus peak's area is inside the mass-box `m3`.

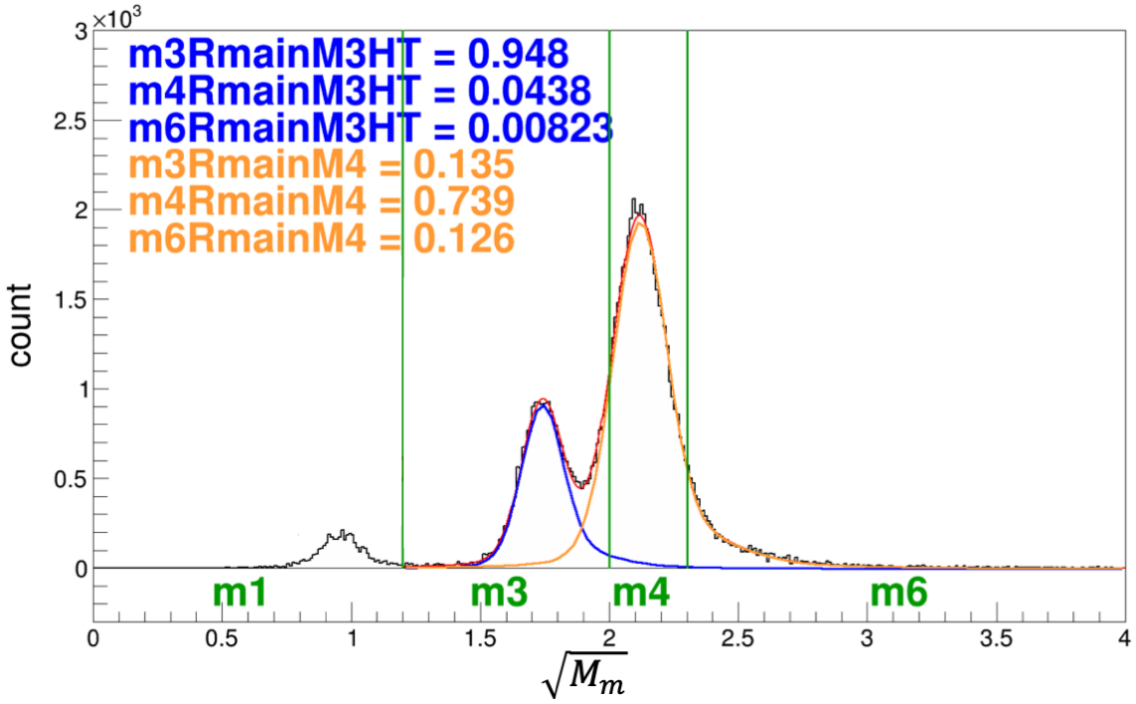

Figure 7.32: Mass-CC ratios for the main-band T2_HT data. The mass spectrum comes from Fig. 7.29 a). Because the mass-3 and the mass-4 peaks do not have a clear separation, they are fitted by the combination of two 3-gaus functions (Eq. 7.30). This particular fit receives χ^2/dof of 2.67. The blue function from the fit is assumed to be HT_mainM3 and the orange HT_mainM4. The mass-CC ratios as derived from the fit functions are given on the top left. The fit is actually performed in a $\sqrt{M_m}$ range of [1.2, 4)$\sqrt{\text{u}}$ to isolate out the mass-1 peak. Every event under the interval [0, 1.2) is assumed to belong to HT_mainM1.

The errors for the mass-CC ratios from the fit is not shown. They are evaluated however in the following way. The fit gives us the errors for the fit parameter and the associated covariance matrix. Since the areas of the 3-gaus functions are just a combination of error functions, we can analytically evaluate the areas' partial derivatives over any of its parameters as well (App. C.1). Then, assume the area is A, the error on the area is given by [184],

$$\sigma(A) = \sqrt{\sum_{i,j} \frac{\partial A}{\partial p_i} \text{Cov}[p_i, p_j] \frac{\partial A}{\partial p_j}}. \tag{7.32}$$

The error of the area can then be easily propagated to get the error of the mass-CC ratios. Lastly, the error for the `HT_mainM1` is assumed to be negligible.

7.3.4 Minor-Band Ratios and Ion Double Woods-Saxon Efficiency

For the minor-bands, because their contributions are relatively small compared to the main-bands, we are simply assuming they are perfectly separated by the ($\sqrt{M_m} = 1.2\sqrt{\text{u}}$) line that defines mass-box `m1` and `m346` (Sec. 6.3.1). Take Fig. 7.29.b) as an example, we are assuming the mass-CC ratios to be 1 for `HT_1I2eM1` in mass-box `m1` and `HT_1I2eM3` in mass-box `m346`.

One benign note for the `2I2e`-band is that, we can see the charge-subtraction in Fig. 7.28.c) and Fig. 7.29.c) result in an obscure mass spectrum shape. This can be understood by inspecting Fig. 6.17 and Fig. 6.18, the shape of the dominant-bands `1I2eM3` in CM-box `c2m346` are tilted in shape. So when charge-subtracting the `1I2eM3` contamination in CM-box `c3m346`, the magenta area subtracted out is actually too high up in $\sqrt{M_m}$. Despite the obscure shape, this does not hurt our analysis, since once we can incorporate all the counts, we do not care about the spectrum shape in each mass-box.

A more serious correction is regarding specifically the `HT_2I2eM32` band, which comes from the 2-ion $\{^3\text{He}^+, \text{H}^+\}$ events. Recall from Sec. 7.1.2, these events should ideally result in ion-2WS events. Unfortunately, while the ion-2WS identification efficiency is nearly 100% in the high-FV, the efficiency is far from great in the main-FV. Figure 7.33 shows all the ion-2WS events from the raw-HT-data. We can see that the band-ID. a6) from Table 6.3 appears to be dimming out under an ion-energy of 40 keV as circled in purple [†]. Not only that, but the main-bands under 40 keV ion-energy are also starting to show up as ion-2WS events. This is caused by the increased false positive and false negative rate of ion-2WS identification with small-amplitude waveforms. The low ion-energy ion-2WS efficiency is a small problem to the main-bands. However, it is one serious problem for the `HT_2I2eM32` band because for a

[†]The $\{^3\text{He}^+, \text{T}^+\}$ contribution to band-ID. a6) is absent because these events are always ion-1WS events (Sec. 7.1.2).

2-ion event, the ion-1WS can be fitted to either the first or the second pulse, and we have no way to find out which. Moreover, the ion-1WS fitting to the first waveform pulses would throw an `HT_2I2eM32` event to CM-box `c3m1`, mixing the 2-ion events with the $^3He^{++}$ events (Sec. 7.1.2). Hence, in order to correctly derive the mass-CC ratios of `HT_2I2eM32`, we need to estimate how many `HT_2I2eM32` events leak out from CM-box `c3m346` to CM-box `c3m1`

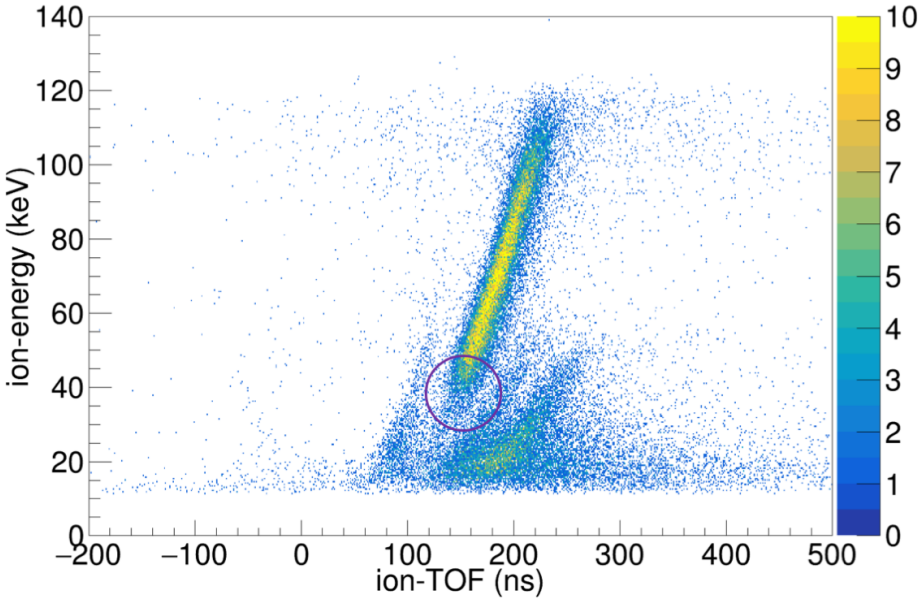

Figure 7.33: Ion-energy versus ion-TOF histogram with only ion-2WS events for the raw-HT-data. The purple circle shows that the ion-2WS band-ID. a6) from Table 6.3 is dimming out below the ion-energy of 40 keV due to the reduction in the ion-2WS identification efficiency. This histogram can be compared to Fig. 6.2, but keep in mind that this histogram comes from the ion-2WS raw-HT-data and Fig. 6.2 from the full raw-T2-data.

To estimate the leakage, we again inspect the 2-charge events in the high-FV (Sec. 7.1.2) and compare them to those in the main-FV. The mass spectrum of the high-FV events is given by Fig. 7.34, and main-FV by Fig. 7.35. They are also under an additional ($Q_{ie} > 1.9$ e) cut, so that we can avoid doing the charge-subtraction and only do the source-subtraction to remove the roughly 10% of T_2 contribution (Fig. 7.10). This is also why Fig. 7.35 looks

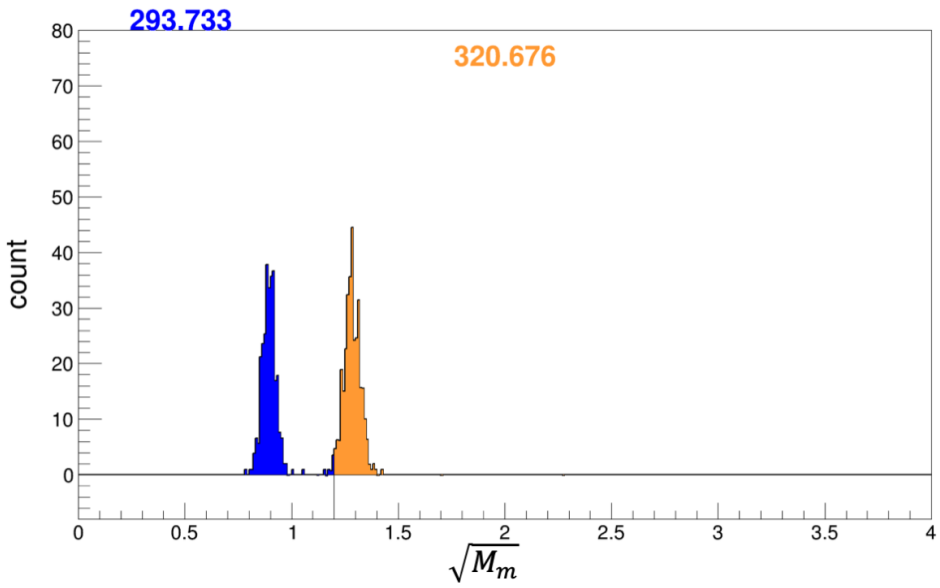

Figure 7.34: Mass spectrum for the left-scan raw-HT-data at the home-position under the high-FV cut with the ($Q_{ie} > 1.9\,\mathrm{e}$) cut. The spectrum in the $\sqrt{M_m}$ interval of $[0,\ 1.2)\sqrt{\mathrm{u}}$ is colored in blue, and $[1.2,\ 4)$ in orange. The corresponding counts are also provided in the plot.

different from Fig. 7.29.c). For both of the plots, the mass spectra in the $\sqrt{M_m}$ interval of $[0,\ 1.2)\sqrt{\mathrm{u}}$ are colored in blue, and $[1.2,\ 4)\sqrt{\mathrm{u}}$ in orange. For Fig. 7.34, the blue portion is rather clean in `HT_2I2eM34` and orange clean in `HT_2I2eM32`. Now, we make an assumption the ratio between `HT_2I2eM34` and `HT_2I2eM32` stays the same in the high-FV as in the main-FV, which should be true as long as the bands are uniform in ion-energy. In other words, if we have M_{34} count of `HT_2I2eM34` events and M_{32} count of `HT_2I2eM32` events in the high-FV, and m_{34} and m_{32} for the events in the main-FV, the assumption is saying,

$$\frac{M_{34}}{M_{32}} = \frac{m_{34}}{m_{32}}. \tag{7.33}$$

But since we have $M_{34}/M_{32} \approx 293.7/320.7$ from Fig. 7.34, suppose $100 \times p$ percent of the

HT_2I2eM32 events are in CM-box c3m1, Fig. 7.35 tells us that,

$$\frac{(1-p)m_{34}}{m_{32}+pm_{34}} = \frac{1-p}{\frac{m_{32}}{m_{34}}+p} = \frac{1-p}{p+\frac{M_{32}}{M_{34}}} \approx 741.5/116.073. \tag{7.34}$$

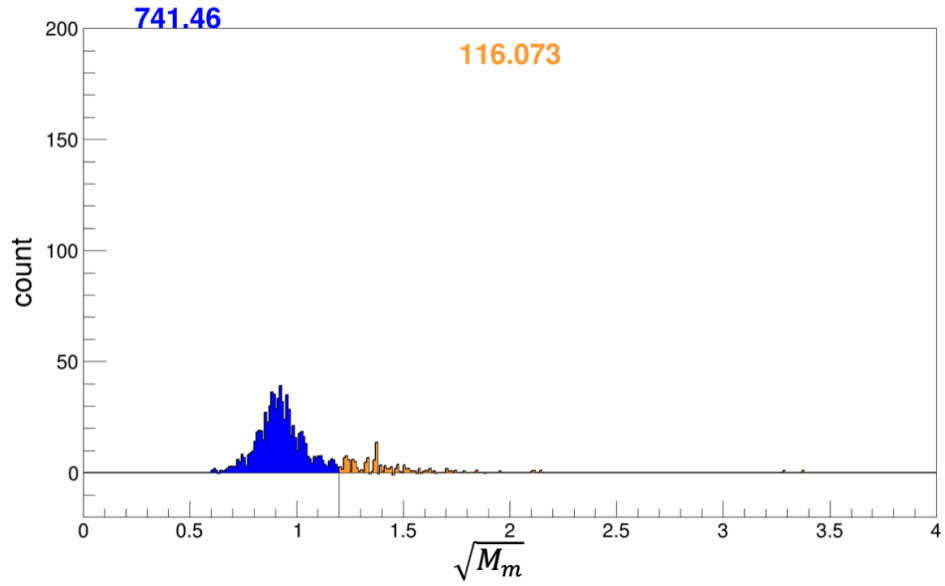

Figure 7.35: Mass spectrum for the left-scan T2_HT-data at the home-position in the main-FV with the ($Q_{ie} > 1.9\,\mathrm{e}$) cut. The spectrum in the $\sqrt{M_m}$ interval of $[0,\ 1.2)\sqrt{\mathrm{u}}$ is colored in blue, and $[1.2,\ 4)\sqrt{\mathrm{u}}$ in orange. The corresponding counts are also provided in the plot.

We can solve for p from Eq. 7.34 and get,

$$p_{\mathrm{HT,2ion,m1}} = 0.743 \pm 0.025, \tag{7.35}$$

which also gives us the mass-CC ratio of the HT_2I2eM32 band in CM-box c3m1. The error comes from error propagating the Poisson errors. And as what one would expect, we also set the HT_2I2eM32 in CM-box c3m346 mass-CC ratio to be $(1-p)$ and the HT_2I2eM34 in CM-box c3m1 mass-CC ratio to be 1 with negligible error.

One more remark about the band uniformity assumption for Eq. 7.33. We incorporate the FV-correction (Sec. 8.2.3) into evaluating the $p_{\mathrm{HT,2ion,m1}}$, and the result makes no noticeable change.

7.3.5 Main Cross-Contamination Error Handling

So far, we have evaluated the "basic error" for each of the mass-CC ratios by means of Poisson error or covariance matrix, but we have not included error coming from the charge- and source-subtraction. Fortunately, the charge- and source-subtraction use the parameters from Sec. 7.2 and Sec. 7.1. The parameters are the source-CC ratios, the charge-CC ratios, and the 1eV2e ratios, whose errors have already been determined. Then to determine the error of a mass-CC ratio induced by these parameters, we vary each parameter by one sigma one at a time, sum in quadrature the changes in the resulting mass-CC ratio including the basic error, and take the square-root of the sum. To explain it in more detail, suppose the mass-CC ratio in question is R and the parameters are p_i with their corresponding errors $\sigma(p_i)$, where $i = 1, ..., N$. Moreover, suppose when we go though the whole mass-CC evaluation after changing one single parameter p_i to $(p_i + \sigma(p_i))$ and keeping all other parameters the same, the resulting mass-CC ratio turns out to be R_i. Then the complete error of R is evaluated by [184],

$$\sigma(R) = \sqrt{\sigma_R^2 + \sum_{i=1}^{N} (R_i - R)^2}, \tag{7.36}$$

where σ_R is the basic error of R. Note that this approach assumes the correlated errors between the parameters to be small, but it is generally a conservative approximation.

Further systematic errors for the mass-CC ratios should be handled by means of Sec. 7.4.4.

One last remark is that since the mass is determined using the ion-energy and ion-TOF information, the mass spectrum should be scan-position independent. For this reason, we only evaluated the mass-CC ratios at the home-position. We formed the weighted average each left-right-scan pair of the mass-CC ratios and apply the same final mass-CC ratio across all scan-points.

7.4 Cross-Contamination Correction

As a reminder, the goal of the TRIMS analysis is to figure out the branching ratio of each physical decay-branch, which can be figured out by comparing the intensity of each of the physical branches relative to the others. We call these intensities the band-intensities. In reality of course, we can only determine the band-intensity up to the detection-channels (Sec. 6.1.1). Now that we have the source-CC ratios (Sec. 7.1), the charge-CC ratios (Sec. 7.2), the 1eV2e ratios (Sec. 7.2), and the mass-CC ratios (Sec. 7.3), we are ready to estimate the band-intensity of each dominant-band (Sec. 6.3.1) from the event count in each CM-box.

The event counts are covered in Sec. 7.4.1. As we will see, these counts undergo several corrections to arrive at what we call the box-intensity. Then in Sec. 7.4.2, we combine the ratios to form a so-called cross-contamination matrix. Using the matrix, we apply a method we called box-fitting in Sec. 7.4.3 to obtain the correct band-intensities that take into account the leakage of the dominant-band to the other CM-boxes. Lastly in Sec. 7.4.4, we globally normalize the χ^2`/dof` to account for the unknown systematics in evaluating the ratios.

7.4.1 Box-Intensity

To first order, the event count in each CM-box that has a dominant-band tells us the band-intensity of that dominant-band. So, we take Fig. 6.17 and just count the number of events we find in each CM-box as labeled in Fig. 7.36. It is worth emphasizing that these charge and mass plots we obtained at this point are all under the main-FV. We call these counts N_i for the CM-box associated with box-No. i (Sec. 6.3.1). To get more accurate band-intensity of the bands however, several corrections are in place. For this section, we apply the following formula [140] to obtain what we call the box-intensity I for box-No. i at scan-point d,

$$\begin{aligned} I_i(\text{T2\_HT}, d) = 1000 \times & \frac{D_i(\text{rawT2}, d) - R(\text{T2\_HT}, d) D_i(\text{rawHT}, d)}{A(\text{rawT2}, d)} \\ & \times \left(\frac{P(\text{rawHT, HT}, d)}{P(\text{rawHT, HT}, d) - P(\text{rawT2, HT}, d)} \right). \end{aligned} \tag{7.37}$$

As the name suggests, this particular case applies the T2_HT source-subtraction (Sec. 7.3.1). To get the HT_T2 version, we only need to swap T2 and HT.

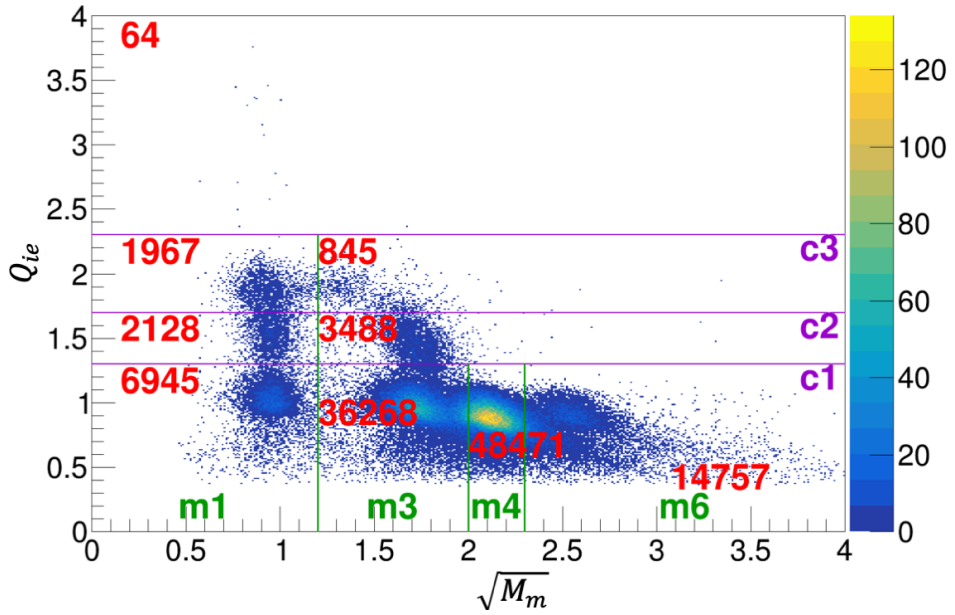

Figure 7.36: Counts in each CM-box of the left-scan raw-T2-data at the home-position in the main-FV from Fig. 6.17. The counts are colored in red and are displayed inside each box. The counts on the top left are for the outlier events that do not enter any of the 8 CM-boxes (Sec. 6.3.1).

There are three corrections that have been performed in Eq. 7.37. They are source-subtraction, random coincidence event correction, and source-activity normalization.

To incorporate source-subtraction as the1st correction, we use the source-CC ratio R(T2_HT) from Eq. 7.22. Then the numerator of the middle factor in Eq. 7.37 is essentially Eq. 7.14.

However, for the 2nd correction, we implement a random coincidence event correction to get D_i's from N_i's,

$$D_i \equiv N_i - n_i, \tag{7.38}$$

where n_i is the count of how many random coincidence noise events fall into CM-box i. At

an event rate of 200 Hz (Sec. 4.1.2) and an acquisition window of 25 µs (Sec. 5.2.1) though, these random pileups are rare. Their rate is estimated by taking all the event in an ion-TOF range of [-1050, -700)ns where there can be no physics events, shifting their timing by +1100 ns so that their timing ends up in our `timeCut` interval of [50, 400)ns (Sec. 6.2.3), and reconstructing their charge and mass normally. We then arrive at Fig. 7.37. And because the random coincidence rate is scan-position independent, what is shown in Fig. 7.37 is actually the count from all the raw-T2-data combined. Hence, to obtain the n_i in Eq. 7.38 that is for a single scan-position, we divide the counts in Fig. 7.37 by 22*.

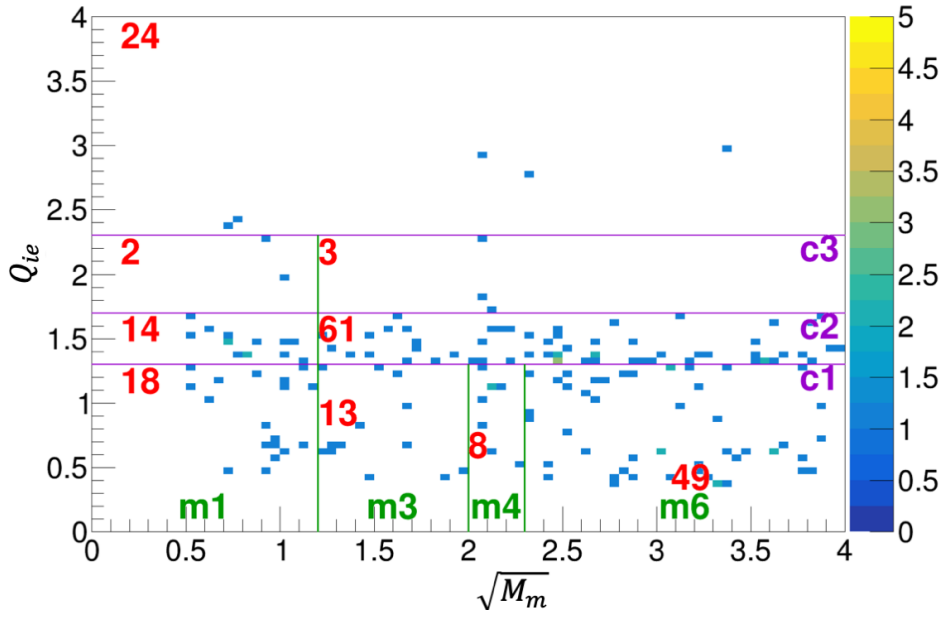

Figure 7.37: Random counts in each CM-box of the raw-T2-data in the main-FV. Note that the 24 count shown on the top left includes all events outside the 8 CM-boxes, not just limited to the events shown in this plot.

The 3rd correction is that, in the denominator of the first factor in the box-intensity

*The scan-positions are integer points in [-10, 0] for the left-scan and [0, 10] for the right-scan, making it 22 points in total.

formula Eq. 7.37, we have the activity-amplitude $A(\text{rawT2}, d)$ from Sec. 7.1.4 to normalize the box-intensities between the left- and the right-scans. Recall that we are actually applying the average activity-amplitude, so the scan-position dependence here really just indicate whether it is from a left- or a right-scan. The components on the second line of Eq. 7.37 are HT-purities P from Sec. 7.1.3. They are coming from taking into account the source purity for the activity-amplitudes. The 1000 in the front is just an arbitrary scale such that the box-intensities are not always in decimal after the normalization and so are more readable.

Since every input to Eq. 7.37 comes with an error bar, the error of the output box-intensity is obtained using the appropriate error propagation. We have to expand $R(\text{T2\_HT})$ into A's and P's in order to take account the full correlation.

Additionally, we include an extra error called the setting error, which is associated with the finite accuracy with which we can set the scan-position. The setting error is given by [140],

$$\sigma_\gamma = \left| \gamma_i X_d \sqrt{D_i(\text{rawT2}, d)^2 + R(\text{T2\_HT}, d)^2 D_i(\text{rawHT}, d)^2} \right|, \tag{7.39}$$

where X_d is the scan-position at scan-point d (Sec. 2.5.5) and,

$$\gamma = \frac{\sigma(X_d)}{\sqrt{k} A(\text{rawT2}, d)} \left(\frac{1}{w_i^2} - \frac{1}{w_0^2} \right). \tag{7.40}$$

These new parameters are $\sigma(X_d) = 0.1\,\text{mm}$ as the step size error, k as the number of run-scans involved to obtain the count in Fig. 7.36, w_i^2 is the centroid variance of the events in CM-box i across the scan-position[†], and w_0 as the scan-position centroid standard deviation for the combined counts of all CM-boxes. This error is summed in quadrature with the rest of the errors to arrive at the final error for the box-intensity.

Finally, notice that at the home-position $X_0 = 0$, we have options from both the left- and the right-scan. In this case, we form the weighted average the two box-intensities, and combine their errors accordingly.

[†]The simpler interpretation is the variance of the RCFs in Fig. 8.4 and Fig. 8.5.

7.4.2 Cross-Contamination Matrix

Before doing further corrections to box-intensity, we want to combine the information from the charge-CC ratios, 1eV2e ratios, and mass-CC ratio into what we called the cross-contamination matrices (CC-matrices). The columns of a CC-matrix correspond to the CM-boxes while the rows correspond to the dominant-bands. This means the CM-matrices are not square matrices. More specifically, the T2_HT CM-matrices are 5×8 according to Table 6.6, and the HT_T2 CM-matrices are 7×8 according to Table 6.7. As it turns out, we never really use the CC-matrices as matrices as we will see in Sec. 7.4.3; calling them matrices is to emphasize the cross-contamination correction that follows is linear in nature.

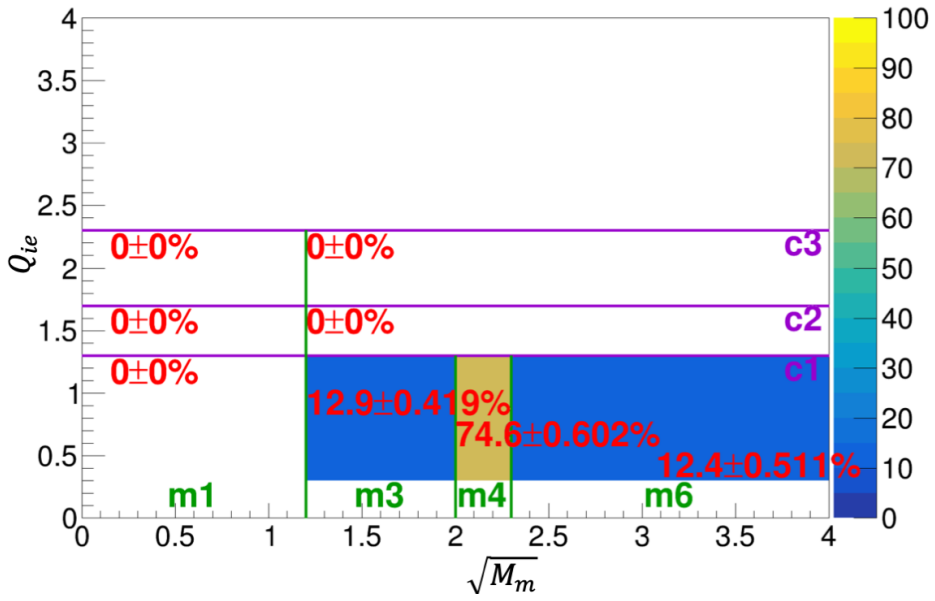

Figure 7.38: The `HT_mainM4` row of the HT_T2 CC-matrix at the home-position. The column numbers of the CC-matrix correspond to the box-ID of each CM-box defined in Table 6.7.

As an example, the `HT_mainM4` row of the HT_T2 matrix at the home-position is plotted in Fig. 7.38. The horizontal purple lines and the vertical green lines are the same charge boxing from Sec. 6.3.1. We can think of the `HT_mainM4` row as the 3$^{\text{rd}}$ row of the CC-matrix

and all the column entries are labeled by box-No from Table 6.7. If we call this CC-matrix M, since Fig. 7.38 is in percentage, it translates to $M_{32} = 0.123 \pm 0.042$, $M_{33} = 0.746 \pm 0.060$, and $M_{34} = 0.124 \pm 0.051$. The other entries of the row are 0. These ratios come from the HT_T2 mass-CC ratios for main-band `mainM4` described in Sec. 7.3.3. The ratios in Fig. 7.38 appear to be slightly different from Fig. 7.32 because as mentioned in Sec. 7.3.5, the mass-CC ratios used by the former plot combines ratios derived from both the left- and the right-scan. What Fig. 7.38 is saying is that given the `HT_mainM4` band of any band-intensity, around 75% of the band-intensity of the band ends up inside CM-box `c1m4` and around 12% in each CM-box `c1m3` and CM-box `c1m6`.

For the main-band, only the mass-CC ratios matter. As for the minor band, we apply the charge-CC ratios as well as the 1eV2e ratios, and the result for the `HT_1I2eM3` row of the HT_T2 CC-matrix at the home-position is shown in Fig. 7.39. Since the `HT_1I2eM3` band is the dominant-band of CM-box `c2m345`, the entry in this box should correspond to the charge-CC ratios in Fig. 7.19. Nevertheless, it is not quite the case. Notice, the overall percentage in Fig. 7.39 does not add up to 100%. This is because the 1eV2e ratio R_{1eV2e} is also incorporated in the CC-matrix. The normalization is such that,

$$1 + \frac{1}{2} R_{\text{1eV2e}}, \tag{7.41}$$

is set to 100% for each dominant-band that is a minor-band; each of these bands has a different R_{1eV2e}. In other words, only when $R_{\text{1eV2e}} = 0$ would Fig. 7.39 add up to 100%. If $R_{\text{1eV2e}} = 0.4$, then the percentage would add up to $\frac{1+0.4}{1+\frac{1}{2}0.4} = 116.7\%$, while if $R_{\text{1eV2e}} = 2$, then $\frac{1+2}{1+\frac{1}{2}2} = 150\%$. The reason behind this seemingly obscure normalization is related to the beta-detection efficiency (Sec. 8.2.4, Sec. 8.1.2).

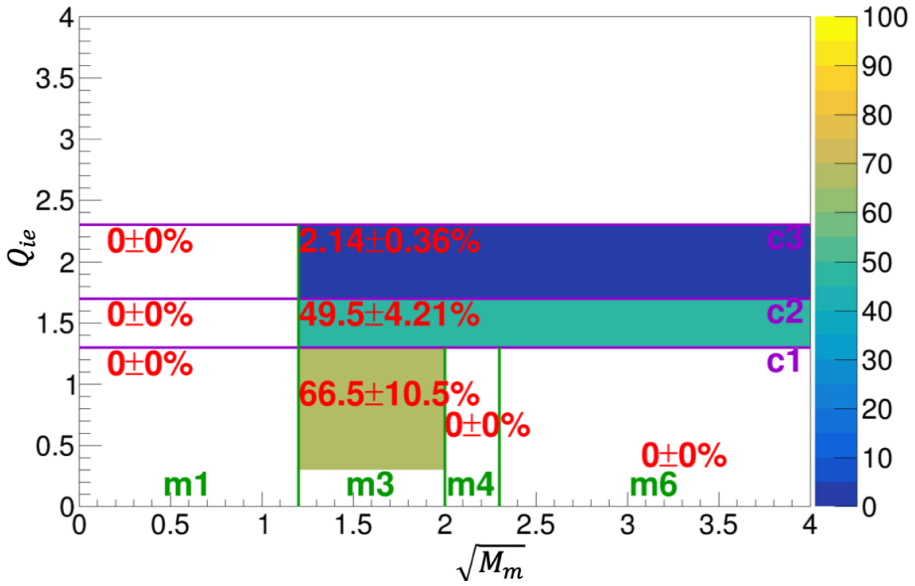

Figure 7.39: The `HT_1I2eM3` row of the HT_T2 CC-matrix at the home-position. The percentage does not add up to 100% because we have incorporated the 1eV2e ratios in the CC-matrix.

Recall from Fig. 7.27 that the 1eV2e ratio does get much greater than 1 as we scan out the ion-detector. An example of the same `HT_1I2eM3` row but from the HT_T2 CC-matrix at scan-point ($d = -10$) is provided in Fig. 7.40, where we can see from the large percentage that the 1eV2e ratio becomes the dominant factor. Without the contribution from the 1eV2e ratios, the CC-matrices would be scan-position independent.

Recall from Sec. 7.3.4 that for most of the minor-bands, their mass-CC ratios are simply taken to be 1 in the mass-box they dominate. That explained why the mass-box `m1` received 0% for the `1IM3HT` band in Fig. 7.39 and Fig. 7.40. As a bonus example, Fig. 7.41 shows the `HT_2IM32` row of the HT_T2 CC-matrix at the home-position. According to Sec. 7.3.4 again, the 2-ion $\{^3He^+, H^+\}$ events misidentified as ion-1WS events cause a leakage of the `HT_2IM32` band from mass-box `m346` to mass-box `m1`. This effect is included in the CC-matrix as promised.

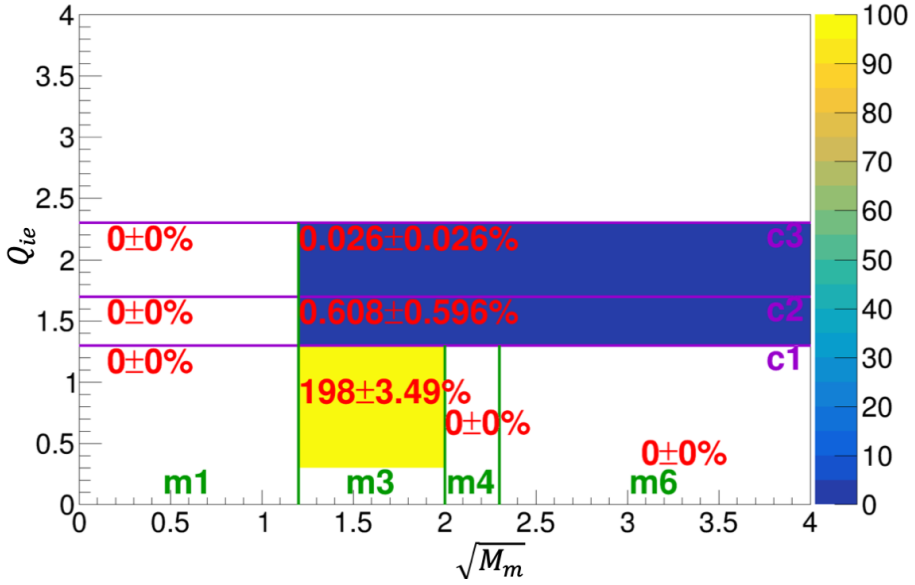

Figure 7.40: The `HT_1I2eM3` row of the HT_T2 CC-matrix at scan-point ($d = -10$). The 1eV2e ratios do contribute more significantly at the far scan-points.

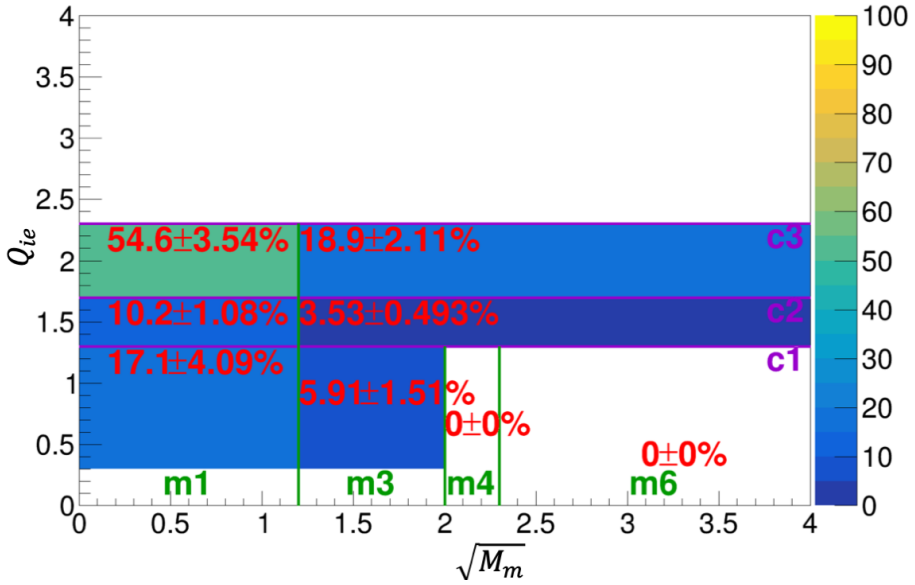

Figure 7.41: The `HT_2IM32` row of the HT_T2 CC-matrix at the home-position. The `HT_2IM32` leak to the mass-box $m1$ was discussed in Sec. 7.3.4.

7.4.3 Cross-Contamination Correction: Box-Fitting

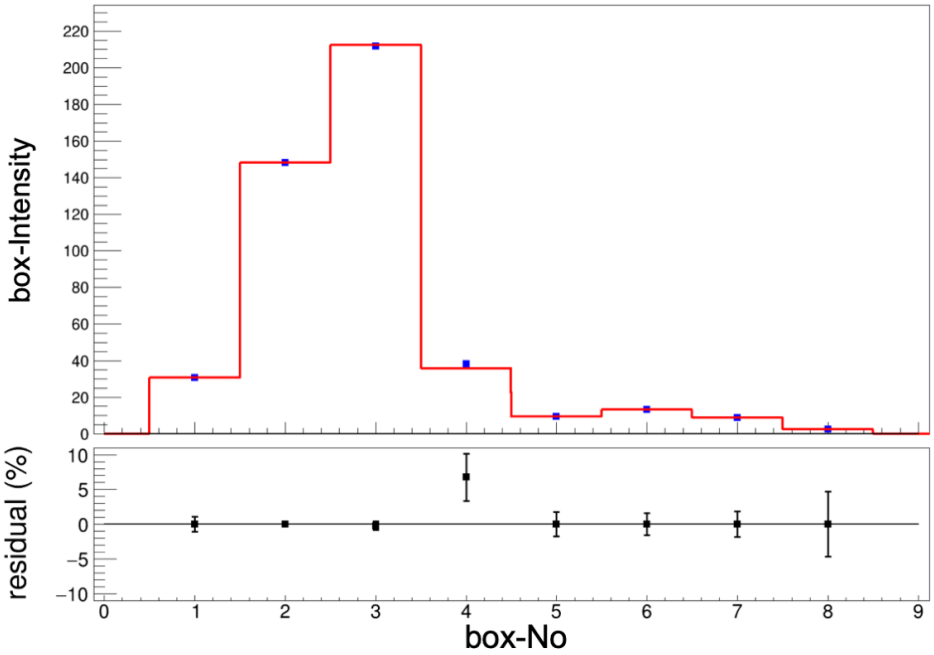

Figure 7.42: Box-fitting on the HT_T2-data (HT-box-fitting) at the home-position. Refer to Table 6.7 for the box-No. on the x-axis. The data points and their error bars come from the box-intensities (Sec. 7.4.1). The fit corrects the cross-contamination and extracts the band-intensities as the fit parameters. For the HT_T2-data, the fit has only 1 DOF. The residual in terms of percentage as normalized by the box-intensity at each box-No is given on the bottom. The box-intensity error bars are scaled accordingly for the residual as well.

What the CC-matrix does is take in the band-intensities of all the dominant-bands and "smears" them across the CM-boxes. The result of the smearing is the box-intensities from Sec. 7.4.1. Since we are looking for the band-intensities and we already have the box-intensities, it appears that all we need to do is apply the "inverted CC-matrix" on the box-intensities to get the band-intensities we want. However, to better address the uncertainty

and the conditioning* of the CC-matrices, we use the weighted least squares method from ROOT to "invert" the CC-matrices, which we refer to as the box-fitting.

As a showcase, the box-fitting on the HT_T2-data (HT-box-fitting) at the home-position is shown in Fig. 7.42. The x-axis of the plot comes from the box-No. in Table 6.7, while the y-axis is the box-intensity. The data points are obtained by applying Eq. 7.37 to the counts in Fig. 7.36. The fit function represented by the red line is made to be discrete†, and its fit parameters are exactly the band-intensities we are looking for. Take the case of Fig. 7.38 as an example. Suppose the fit function is $f(x)$ at box-No.x, and the `HT_mainM4` band-intensity is M_4, then,

$$\begin{aligned} f(x=1) &= 0 \times M_4 + ..., \\ f(x=2) &= 0.129 M_4 + ..., \\ f(x=3) &= 0.746 M_4 + ..., \\ f(x=4) &= 0.124 M_4 + ..., \\ &\vdots \end{aligned} \tag{7.42}$$

where the vertical dots indicate the function goes up to $f(x=8)$ for 8 CM-boxes; $f(x \geq 5)$ do not have contributions from M_4. The horizontal dots indicate that besides fit parameter M_4, f contains fit parameters from all the other dominant-bands in Table 6.7. The box-fitting for the HT_T2-data has 7 fit parameters and 8 data points, which amount to only 1 DOF. Hence, the χ^2`/dof` of 4.11 from Fig. 7.42 is mostly contributed by the box-intensity of the CM-box `c1m6` (box-No. 4) that does not contain a dominant-band. In this case, the fit gives $M_4 = 278.9 \pm 1.8$.

As another showcase, the box-fitting on the T2_HT-data (T2-box-fitting) at the home-position is shown in Fig. 7.43, which has 3 DOF this time.

---

*Or how close the matrix is to being singular.

†The discrete functions are implemented using the Heaviside step functions available in ROOT.

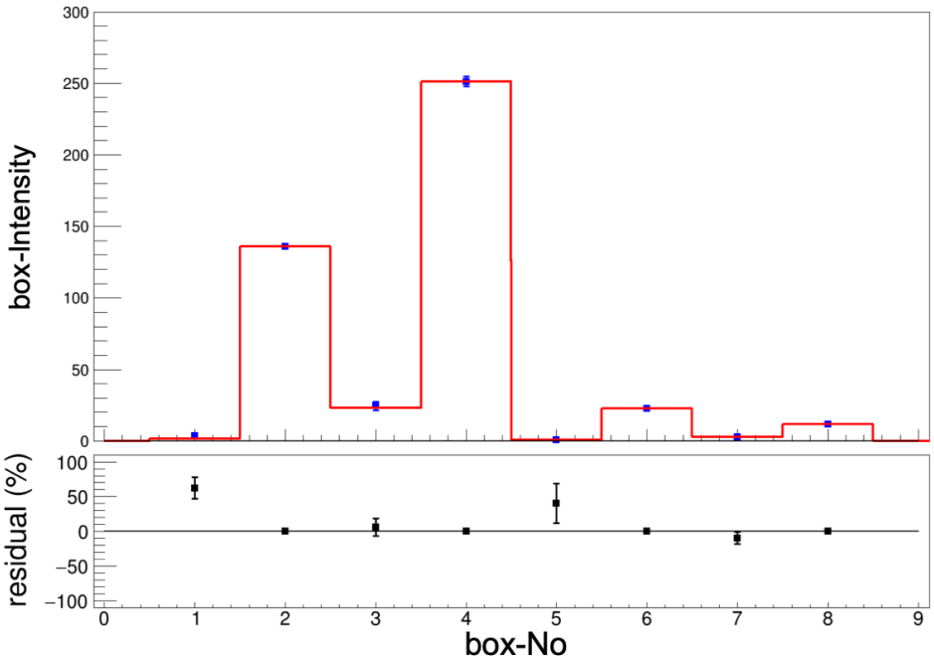

Figure 7.43: Box-fitting on the T2_HT-data (T2-box-fitting) at the home-position, which has 3 DOF. Notice the errors are contributed by the box-intensities in the CM-boxes that do not contain a dominant-band. Particularly for the T2_HT-data, these CM-boxes are box-No. 1 (`c1m1`), 3 (`c1m4`), and 5 (`c2m1`).

7.4.4 Cross-Contamination Correction: Chi-Square Normalization

The box-fitting procedure conveniently takes into account the error coming from the box-intensity Eq. 7.37. However, it does not address the systematics that we do not know how to quantify. One prime example is the disagreement between the data and the simulation on the 1eV2e ratio as we scan out the ion-detector (Fig. 7.27). This type of systematics is what causes large χ^2`/dof` in the box-fitting in such a way that the fit function derived from the CC-matrices does not exactly match the box-intensities derived from the data. For this reason, we would like to normalize the χ^2`/dof` to 1 by scaling up the error on the box-intensity. In this way, we can at least be conservative about our error estimation.

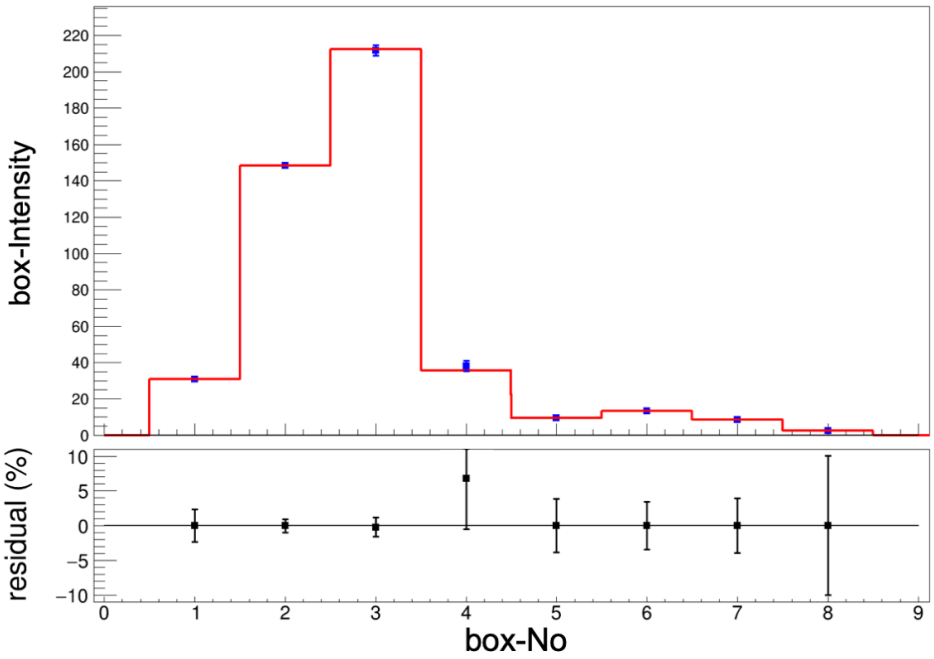

Figure 7.44: Chi-square normalized on the HT_T2-data (HT-box-fitting) at the home-position. The error bars for all the points at all the scan-points are scaled up by the same factor compared to Fig. 7.42, such that the average χ^2/dof across the scan-points becomes 1.

To do the chi-square normalization correctly however, we need to consider the average χ^2/dof across all scan-points. The reason is that due to the low DOF of the box-fitting, it is not unlikely for the data point at the CM-box with no dominant-band to statistically land right on the fit function, which would result in a χ^2/dof much smaller than 1. The average χ^2/dof from the T2-box-fitting is 1.89 and HT-box-fitting 2.15. The chi-square normalization thus scales up the error on the box-intensity of the T2_HT data by $\sqrt{1.89}$ and T2_HT data by $\sqrt{2.15}$.

As a showcase, Fig. 7.44 shows the chi-square normalized version of Fig. 7.42. Now the same fit parameter for the HT_mainM4 band-intensity gives $M_4 = 278.9 \pm 3.8$.

We are also aware that the procedures showcased by Fig. 7.44 do not take into account

the error of the CC-matrix; the entries of the CC-matrix are included as fixed values. To account for the CC-matrix errors, we apply the method similar to Sec. 7.3.5, but inducing a standard deviation on one entry of the CC-matrix at a time and summing in quadrature their contribution along with the error coming from the fit, e.g. the 3.8 error from $M_4 = 278.9 \pm 3.8$. In this way, we fully incorporate all the errors that we derived in this chapter to the band-intensities.

Chapter 8

DATA ANALYSIS: SCAN-DECONVOLUTION

This chapter covers one vital systematic associated with the detection efficiency and due to our detectors having finite detection areas. The correction for this systematics is what requires us to scan the ion-detector and apply the so-called scan-deconvolution. The motivation for and the detailed implementation of the scan-deconvolution are covered in Sec. 8.1. In addition to the scan-deconvolution, we need to apply several more systematic estimations and corrections afterward. These items are discussed in Sec. 8.2. With that, we finally arrive at the branching ratios in Sec. 8.3.

Because the following discussion heavily depends on the detector scanning, we refer to Sec. 2.5.5 for the terminologies. The center-position that describes the true ion-detector alignment position is especially important to the discussion. We set the center-position as the origin in the XY-plane (Sec. 2.1.2) and define the R-position R_b as the signed radial displacement from that origin. We refer to the binning index b as the R-point, which can be negative. We define the sign of the R-position to match that of the X-coordinate, i.e. the R-position is negative for any displacement from the center-position in the negative-X half of the XY-plane. We define the R-position this way because we are scanning the ion-detector in the X-direction, where the left-scan corresponds to the ion-detector scanning in the negative X-direction and the right-scan to positive-X-direction. However, we need to emphasize that the R-position and the scan-position are defined under different coordinates: the R-position is the displacement from the origin of the XY-plane that is independent of the ion-detector's physical position, while the scan-position is the physical ion-detector position.

8.1 Scan-Deconvolution

The scan-deconvolution follows the following formula,

$$\mathrm{RCF} = \mathrm{PSF} * \mathrm{DDF},$$

where RCF stands for the raw count function, PSF for the point spread function, and DDF for the data distribution function. The RCFs are essentially the band-intensities coming from Sec. 7.4.4 at each scan-point; each RCF is a vector whose indices are exactly the scan-points. The DDFs are the vectors that contain the information about the branching ratios of the physical branches, and the PSF is a smearing matrix that broadens the DDFs. The PSF convolving a DDF by matrix multiplication gives us an RCF. So the basic idea is to obtain the DDFs by deconvolving the known RCFs. That is the main topic of this chapter.

This section starts out by explaining the necessity of the scan-deconvolution in Sec. 8.1.1 as well as how we derive our PSF. The RCF from the data is covered in Sec. 8.1.2, and the DDF we obtain from the scan-deconvolution is covered in Sec. 8.1.3.

8.1.1 Point Spread Function and the Reason Behind Scanning

To understand the systematic associated with the detector size, i.e. the area of the silicon detectors' detection surface, we first inspect the so-called data distribution function (DDF) in the simulation. Recall that in the TRIMS Geant4 simulation, we assume the ion-detector to be large in size (Fig. 3.3). The coincidence events would form a 2-D distribution on the large ion-detector, which is shown in Fig. 8.1.a). The z-axis shows the count in each bin, while the x- and the y-axes form the detection XY-plane (Sec. 2.1.2). The binning used on the XY-plane is in polar coordinates, such that the binning is equally spaced in the radial direction and $360°/72$ in the angular direction. In other words, the area of the bins increases the further they are away from the origin. The origin of the XY-plane is set to be at the center-position (Sec. 2.5.5). We call these radial displacements from the center-position the R-positions R_b, where the b is the binning index that can be negative integers. We call the

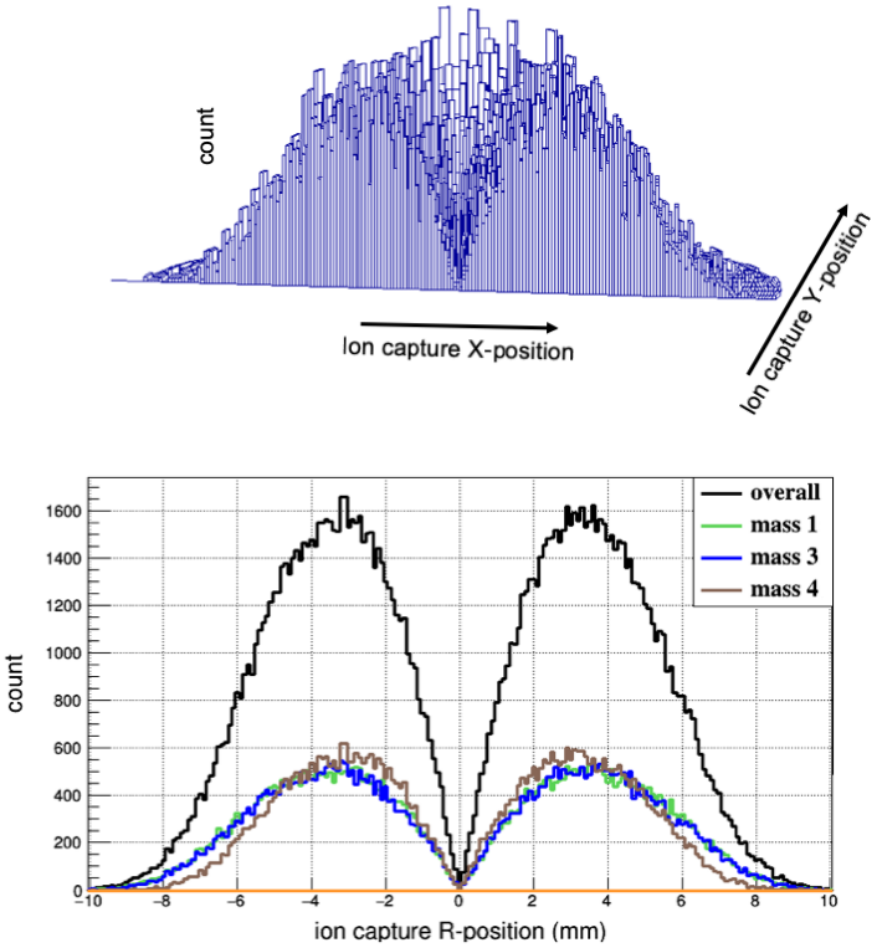

Figure 8.1: Simulated DDF. Plot a) shows what the coincidence event distribution would look like on the surface of a large ion-detector (Fig. 3.3). For visual clarity, only half of the distribution is shown. Polar coordinate are used in this case such that the binning is equally spaced in the radial direction and 360°/72 in the angular direction. Plot b) is the projection of plot a) to the radial axis. The R-position refers to the radial position, whose sign is made to follow the sign of the X-position (Sec. 2.1.2). The "All" histogram is decomposed into the colored ones according to the decay-branches. We call the histograms in plot b) the DDFs. In this HT simulation that has only the main-band, the branching ratio is set to be the same for the mass-1, mass-3 and mass-4 branches.

b an R-point, which is distinct from the scan-point d index that describes the scan-position X_d. This coordinate is more advantageous for us because the 2-D distribution is rotationally symmetric, as are the detection surfaces of the detectors.

To simplify the distribution, we separate the 2-D distributions with negative and positive X-position values, and project the distribution onto the radial axis to form the 1-D black histogram shown in Fig. 8.1.b). Because we know the decay-branch of each of the events from the simulation, we can separate the DDFs accordingly; we decompose the "All" black DDF into 3 colored distributions. They are the DDFs of each decay-branch. For simplicity, we only plot out the main-bands for this illustration. And the 3 DDFs correspond to the mass-1, mass-3 and mass-4 branches. We set these branches to have the same branching ratios using options in Table 3.4.

The main point is that our ion-detector has a radius of (4 mm) (Sec. 2.5.1), but the DDFs only drop to nearly zero roughly 10 mm away from the center-position. This spread of the DDFs is a result of the beta-detector also having finite size and the ions having gyroradii about as large as the detector radius (Sec. 2.4.2). By inspecting Fig. 8.1.b), we can see that if we simply place the ion-detector at the center-position, it will detect all the events in the R-position range of [-4, 4]mm. But if we want to derive the branching ratios, this R-position range will create bias because the DDFs have slightly different shapes. For example, compare the mass-4 band DDF shape to that of the other two in Fig. 8.1.b). And as an extreme example, if we have bands A and B that have the same branching ratio, the count C from the full DDFs should be the same, i.e. $C(\mathrm{DDF}_A)/C(\mathrm{DDF}_B) = 1$. Now if only 50% of the band-A DDF falls in the R-position range of [-4, 4]mm and 100% of the band-B DDF does, then the count c in the R-position range will give,

$$\frac{c(\mathrm{DDF}_A)}{c(\mathrm{DDF}_B)} = \frac{\frac{1}{2}C(\mathrm{DDF}_A)}{C(\mathrm{DDF}_B)} = 0.5 \neq 1. \tag{8.1}$$

Fortunately, we are able to scan the ion-detector so that we can probe the DDF count outside the range of the R-position range of [-4, 4]mm. Unfortunately, it is not simple to recover the DDF from the distribution we measure while we scan the ion-detector. The

reason is that the active area of the ion-detector has no position resolution, such that the ion-detector can only tell if a particle is captured but not where the particle is captured within the detection surface. The “scan distribution" is basically an integral of the DDF within a range of $[X-4, X+4]$mm, where X is the scan-position of the ion-detector (Sec. 2.5.5). We call this “scan distribution" the raw count function (RCF).

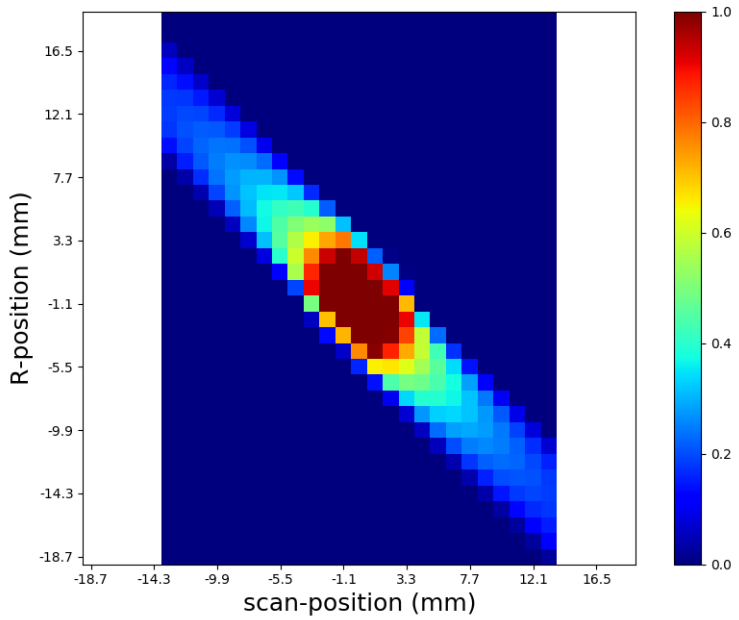

Figure 8.2: Point spread function (PSF) used in TRIMS analysis. If the RCF and the DDF are treated like vectors, then the PSF is a matrix that transforms a DDF to a RCF. The x-axis is the scan-position (Sec. 2.5.5) and y-axis the R-position. Each pixel is an entry in the PSF matrix indexed by scan-point and the R-point (d, b). Each of the entries in the PSF is a value in [0, 1].

Essentially, the ion-detector size “smears” the DDF to get the RCF. The function that is responsible for this broadening is what we call the point spread function (PSF). The PSF can be considered a geometrical detector response function, and thus explains the convolution

relation,

$$\mathrm{RCF} = \mathrm{PSF} * \mathrm{DDF}. \tag{8.2}$$

Note the DDF is a vector indexed by the R-point b from the R-position R_b and RCF indexed by the scan-point d from the scan-position X_b. Because both the RCF and the DDF are vectors, then the PSF is a matrix, and the convolution is a matrix multiplication. The PSF is a linear operator that transforms a DDF to a RCF. And the inverse process that transforms a RCF to a DDF is what we call the scan-deconvolution.

The PSF we used is given in Fig. 8.2. The x-axis is the scan-position and y-axis the R-position. Each pixel is an entry in the PSF matrix index by the scan-point and the R-point (d, b). So, if the RCF and the DDF have the same number of bins, then the PSF will be a square matrix. However, we actually would like our matrix inversion to be slightly underdetermined so that the scan-deconvolution is less sensitive to the noise. For this reason, we crop out 5 entries on both sides of PSF matrix along the x-axis.

Notice that every entry of the PSF matrix in Fig. 8.2 is within the range of [0, 1]. This is because the PSF is purely geometrical. To explain how we derive the values of the PSF entries, consider Fig. 8.3. The binning is exactly like in Fig. 8.1.b) but with half annular rings that have width of 1 mm. Only the center bin is a full circle of radius 1 mm. The black solid line indicates the X-position of the center-position. The red empty circle indicates the ion-detector and the detection area it covers. The red dot is the center of the ion-detector, which is shown to be at scan-position ($X = 3\,\mathrm{mm}$) (x-axis of Fig. 8.2). One half annular ring to the right is colored, and that ring corresponds to the DDF position of ($R = 4\,\mathrm{mm}$) (y-axis of Fig. 8.2). The portion of the half ring that is colored in orange fall inside the ion-detector. Now the (3, 4)mm PSF entry is determined by the area ratio (orange/(orange+blue)), which is the fraction of the half annular ring area that is covered by the ion-detector at that scan-position.

With this understanding of the RCF, if we take a look again at Fig. 8.2, we can see the non-zero values in each column of the PSF are the ring areas that falls inside the ion-detector detection surface. And the ion-detector "scans" from the negative scan-positions to

the positive as the PSF entries evolve from the left columns to the right.

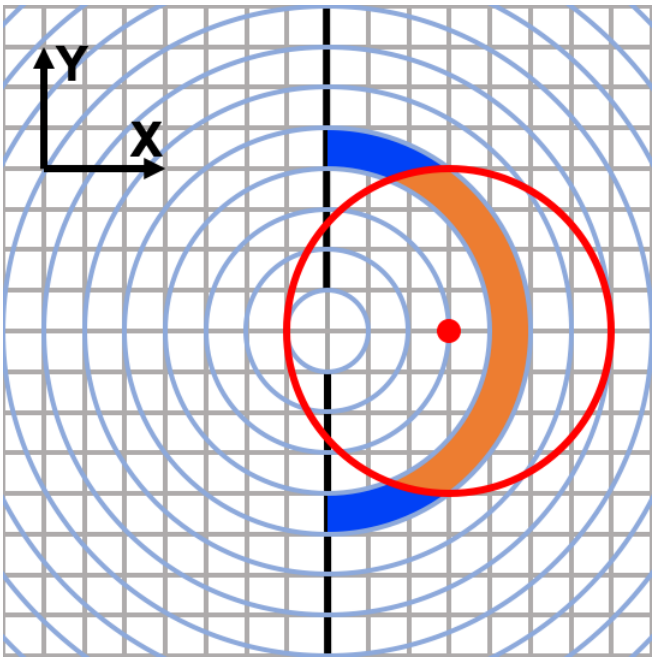

Figure 8.3: Illustration of a PSF entry. The grey lines on the background form $1\times1\,\mathrm{mm}^2$ grid and serve as a visual guide of the XY-plane (Sec. 2.1.2). The binning is shown by concentric half annular rings of width 1 mm; the binning edges are colored in light blue. The center bin is an exception; it is a circle of radius 1 mm. The black solid line indicates the X-position of the center-position. The red dot indicates the center of the ion detector and the red circle of radius 4 mm is the detection surface. The detector center is shown to be located at the scan-position ($X = 3\,\mathrm{mm}$). Notice the fifth (including the center bin) half annular ring to the right is colored; its area inside the detection area is colored orange and outside blue. The location of the half annular ring corresponds to the R-position ($R = 4\,\mathrm{mm}$) determined by the inner half-circle of the ring. Finally, the PSF entry at (3, 4)mm is evaluated by the area ratio (orange/(orange+blue)).

Under the assumption that the DDF distribution is rotationally symmetric and so is uniform within each half annular ring, the DDF entries can be understood in the following

manner. Suppose the orange area is equal to the blue area, then only 50% of the DDF events in that half annular ring will be detected by the ion-detector. So by matrix multiplication, the corresponding RCF entry at scan-position ($X = 3\,\text{mm}$) is the sum of DDF event counts found in each half annular ring multiplied by the percentage of the ring covered by the ion-detector. Many of the rings are not covered by the ion-detection, and so their DDF counts receive 0 percent multipliers and end up not contributing to the RCF at all. In other words, the RCF entry is such that given a DDF, the RCF describes how many counts would be collected within the ion-detector. Now, if we reverse the process such that we begin with the RCF entries, then we can derive the DDF counts within each annular ring. This is the goal of the scan-deconvolution.

Although Fig. 8.3 is a simplified case, once we understand its underlying concepts, further modifications are not difficult to understand. For instance, since the home-position of the ion-detector is not exactly centered, we will have to determine the X-offset and the Y-offset of the ion-detector center at each scan-position, which we already have (Sec. 7.2.2). However, we can still determine the area ratio of the half annular rings falling inside the ion-detector in exactly the same manner. Note however, because the DDF shape is determined by the half annular rings, no matter the offset of the ion-detector, the DDF is going to be centered at the center-position. Another modification required is to incorporate the actual ion-detector scan step size of 1.1 mm (Sec. 2.5.5. For that, we modify both the scan-position steps and the annular ring width to 1.1 mm, so that both the RCF and the DDF have the same bin resolution. The mentality is that if we want to determine the DDF from the RCF, the resolution of the DDF cannot be much better than that of the RCF we find. Otherwise, the scan-deconvolution would be underdetermined.

One note regarding the center bin, we found that having a single circle instead of two semicircles largely reduces the noise sensitivity near the center-position. This most likely is a result of having a large DDF count and small bin area [158]. And so we stick to the single circle binning.

Finally, we need to know that the cases are complicated when we have two electrons and

two ions. The 2-electron efficiency problem can be resolved by defining a so-called beta-coincidence event as will be discussed in Sec. 8.1.2. As for the 2-ion efficiency problem, we can resolve it by looking at one ion at a time as will be discussed in Sec. 8.2.4.

8.1.2 Raw Count Functions and Two-Electron Efficiency

Now that we have the PSF, what we need next is the RCF. In fact, we do already have the RCFs *. They are the band-intensities we determined in Sec. 7.4.3 and Sec. 7.4.4, but evaluated at every scan-position. The RCFs corresponding to the HT band-intensities are provided in Fig. 8.4, where the bands in the legends correspond to the dominant-bands in Table 6.7. The RCF entries at the home-position ($X_0 = 0\,\text{mm}$) come directly from the fit results of Fig. 7.44. Similarly for the T2 band-intensities, their RCFs are provided in Fig. 8.5, whose bands follow Table 6.6.

The first thing to note is that the center of the RCF is not quite at the home-position. The RCF centroid appears to be at around scan-position ($X = 0.9\,\text{mm}$) instead, which matches the X-offset from Sec. 7.2.2.

Another item to address is that we took our data for scan-points in an integer range of [-10, 10] (Sec. 2.5.5). So, we set the RCF values to 0 outside the range. To see why setting these RCF values to 0 is a valid choice, Fig. 8.6 provides the T2_HT mass spectrum with scan-point ($d = -10$) on the left and ($d = 10$) on the right. There are more counts at scan-point ($d = 10$) than at ($d = -10$) as expected because of the X-offset. And because the X-offset is smaller than 1 step size, we are expecting the counts at scan-point ($d = 11$) to be fewer than at ($d = 10$), which is negligibly small in count compared to Fig. 7.28. While we set the RCFs at scan-point ($d = 11$) to be 0, we set its error to be the same as that at ($d = -10$). We set all other RCF errors outside the [-10, 10] range to be 10^{-3} because we are confident that they are consistent with 0 counts. The choice does not have a major impact

*The term raw count function is used for "historical" reasons. It used to refer to the counts in Fig. 7.36 in the early iteration of the TRIMS analysis; we had not developed the CC correction at the time.

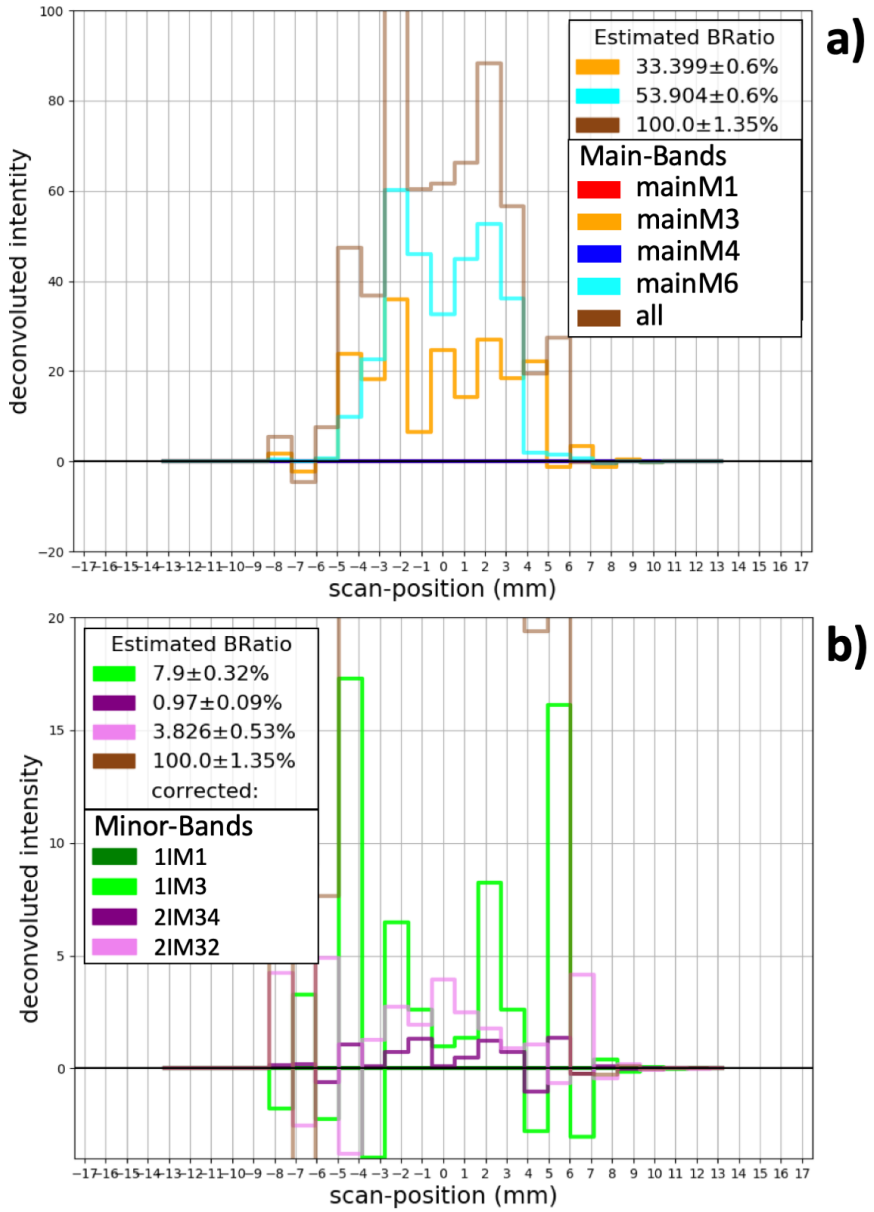

Figure 8.4: RCFs from the HT band-intensities. The band-intensities at home-position come from the fit value of the box-fitting Fig. 7.44. The RCFs in plot a) are for the main-bands, and plot b) for the minor-bands. The brown RCF comes from the sum of all the main- and minor-bands.

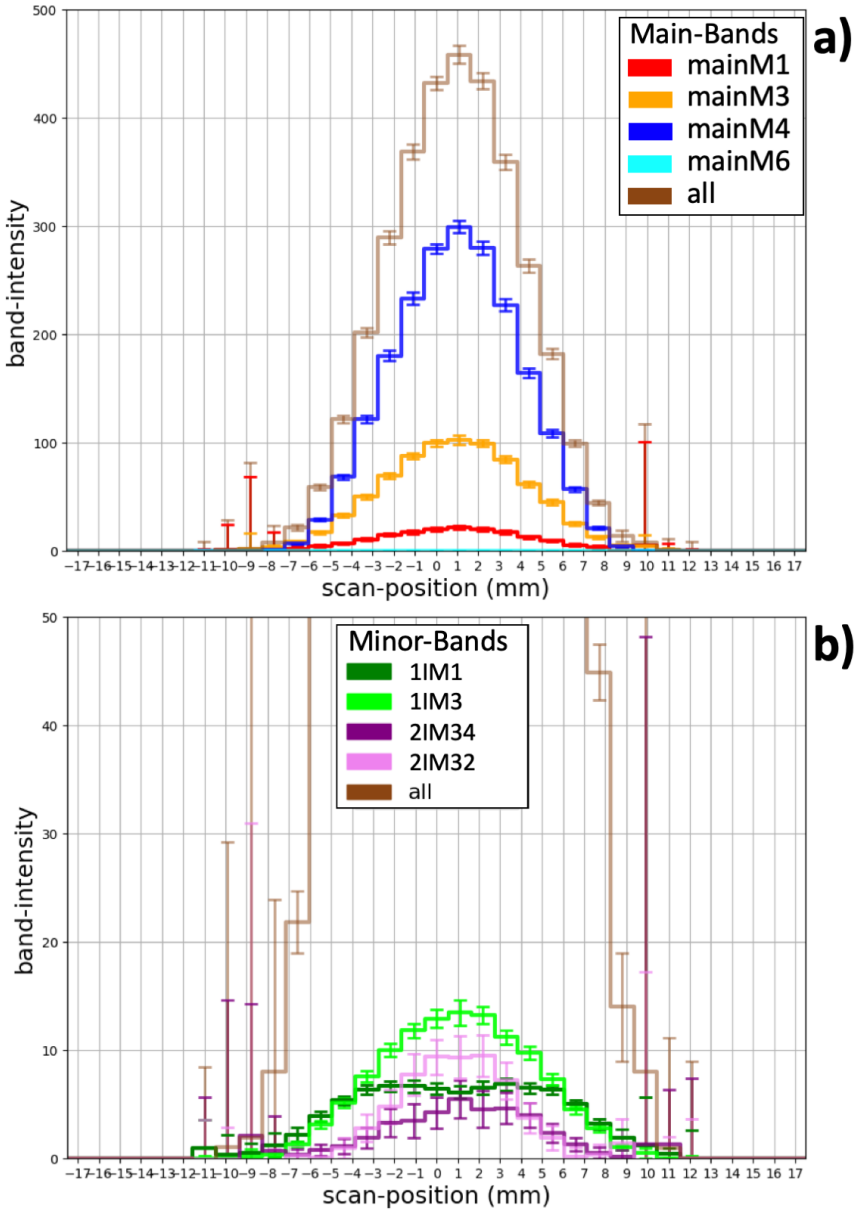

Figure 8.5: RCFs from the T2 band-intensities.

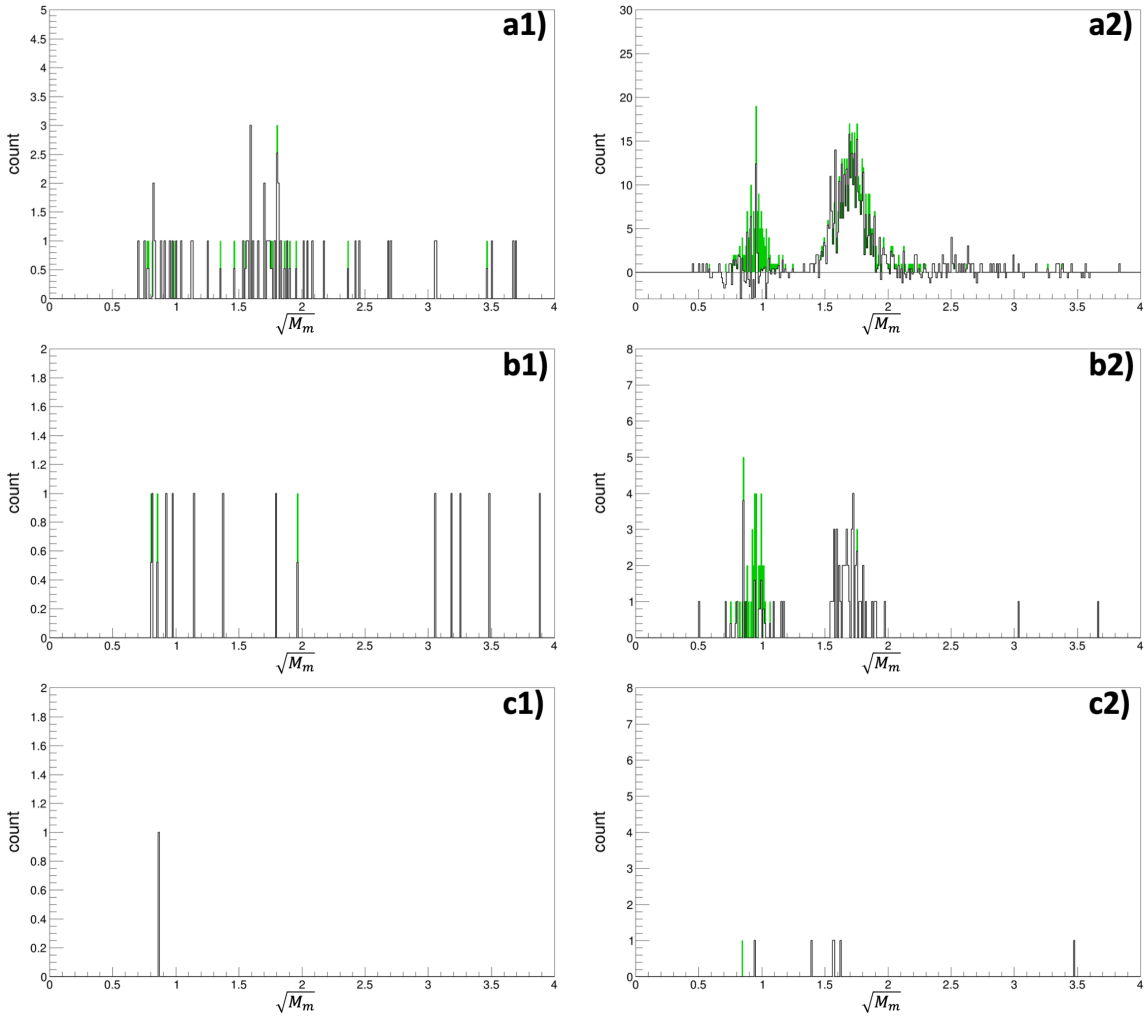

Figure 8.6: Mass spectrum for the T2_HT-data under the main-FV cut at the left-home-position. The plots are to be compared to Fig. 7.28, but with plot a1), b1), c1) at scan-point ($d = -10$) and plot a2), b2), c2) at scan-point ($d = 10$). Although the source-subtraction is carried out and removes the green portions of the histograms, no minor-band subtraction is performed in this case because that is handled by the CC-correction in Sec. 7.4 instead.

on the result as long as it is greater than 10^{-7}, otherwise the sharp drop at $(d = -11)$ and $(d = 12)$ would enhance the oscillatory noise that will be discussed later in this subsection.

One important issue that we need to address is the 2-electron efficiency, or asking how we should interpret the meaning of the RCF if the decay produces 2 electrons. Because the beta-detector only needs to detect 1 electron to be triggered, a decay producing 2 electrons is more likely to result in a coincidence event as compared to a 1-electron decay. However, in the end, we would like to compare the branching ratios of the main-bands and the minor-bands on equal footing. This is the reason why we need a way to resolve this efficiency problem.

Fortunately, the solution is simple and intuitive [140]. We define a beta-coincidence event by requiring the beta-detector to detect the beta, rather than the shake-off electron (Sec. 6.1.1) or the mesh-electron (Sec. 7.1.1). This does not make any difference to a main-band event because the beta is the only particle heading toward the beta-detector. But for minor-band events, this explains why we have an extra factor of $\frac{1}{2}$ for the 1eV2e ratio as described in Sec. 7.4.2, which translates directly to the magnitude of the RCFs in Fig. 8.4.b) and Fig. 8.5.b). The idea is that for a decay that produces a beta and a shake-off, if it results in a `2e` event, then the beta-detector must have detected the beta. If it results in a `1e` event, then the beta-detector detects either the beta or the shake-off. Assuming the efficiency of the beta-detector detecting the beta or the shake-off is the same, then a `1e` event detects a beta only 50% of the time, which explains the $\frac{1}{2}$ factor. The assumption should be a good approximation, because the gyroradius of a beta is in general small compared to the beta-detector radius in our system (Sec. 2.4.2). This beta-coincidence definition is compatible with the definition of the DDF as well.

The counterpart of the 2-electron efficiency problem is the 2-ion efficiency problem. The intuition behind the solution of the 2-ion efficiency problem is the same, and it explains why some RCFs in Fig. 8.4.b) and Fig. 8.5.b) are divided by 2 as indicated by "/2" in the legend. But the details will be provided in Sec. 8.2.4.

8.1.3 Data Distribution Functions from the Scan-Deconvolution

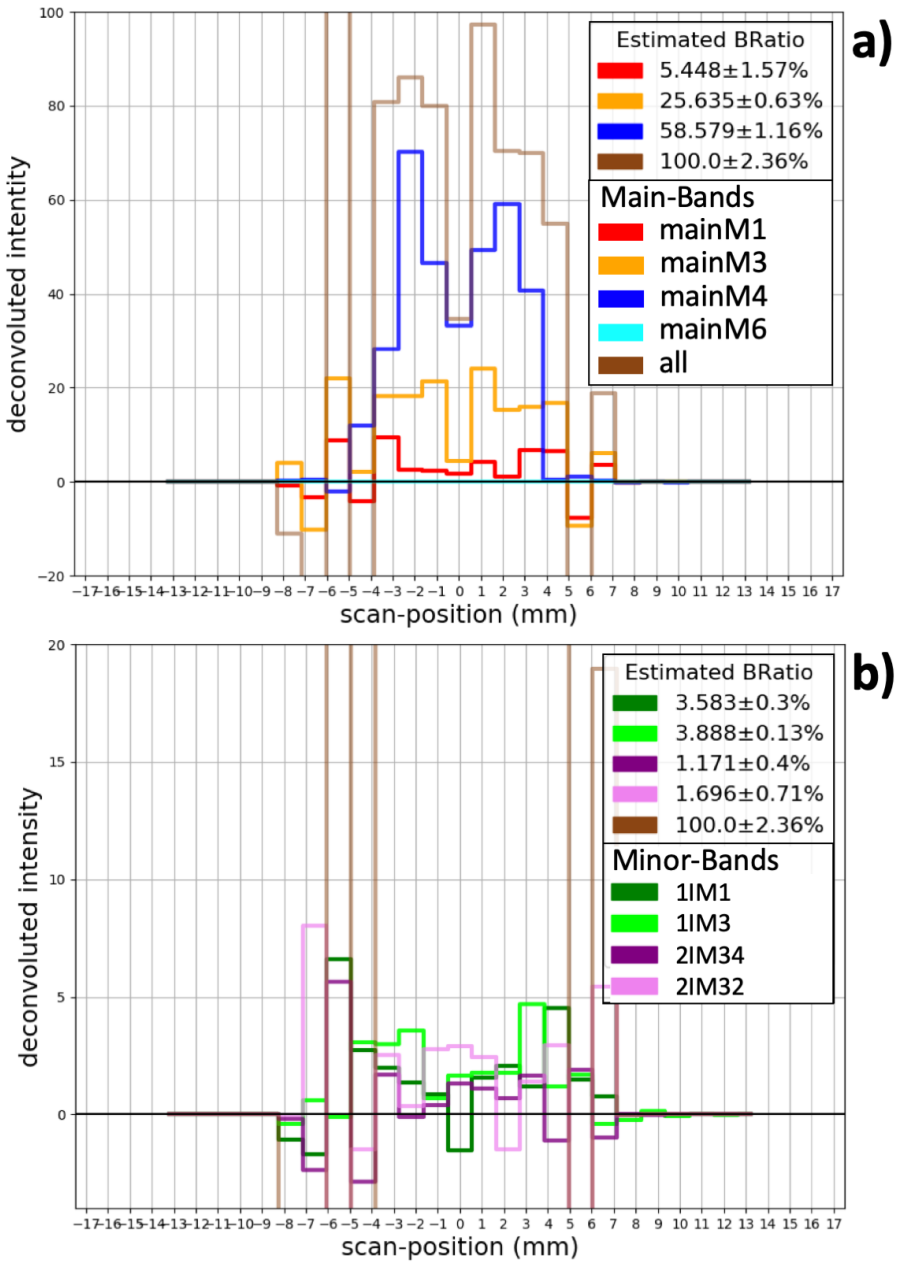

Figure 8.7: HT DDFs obtained from scan-deconvolving the RCFs in Fig. 8.4. The estimated raw branching ratios (BRatio in the legend) are coming from comparing the DDF areas or the branch of all the main- and minor-bands combined.

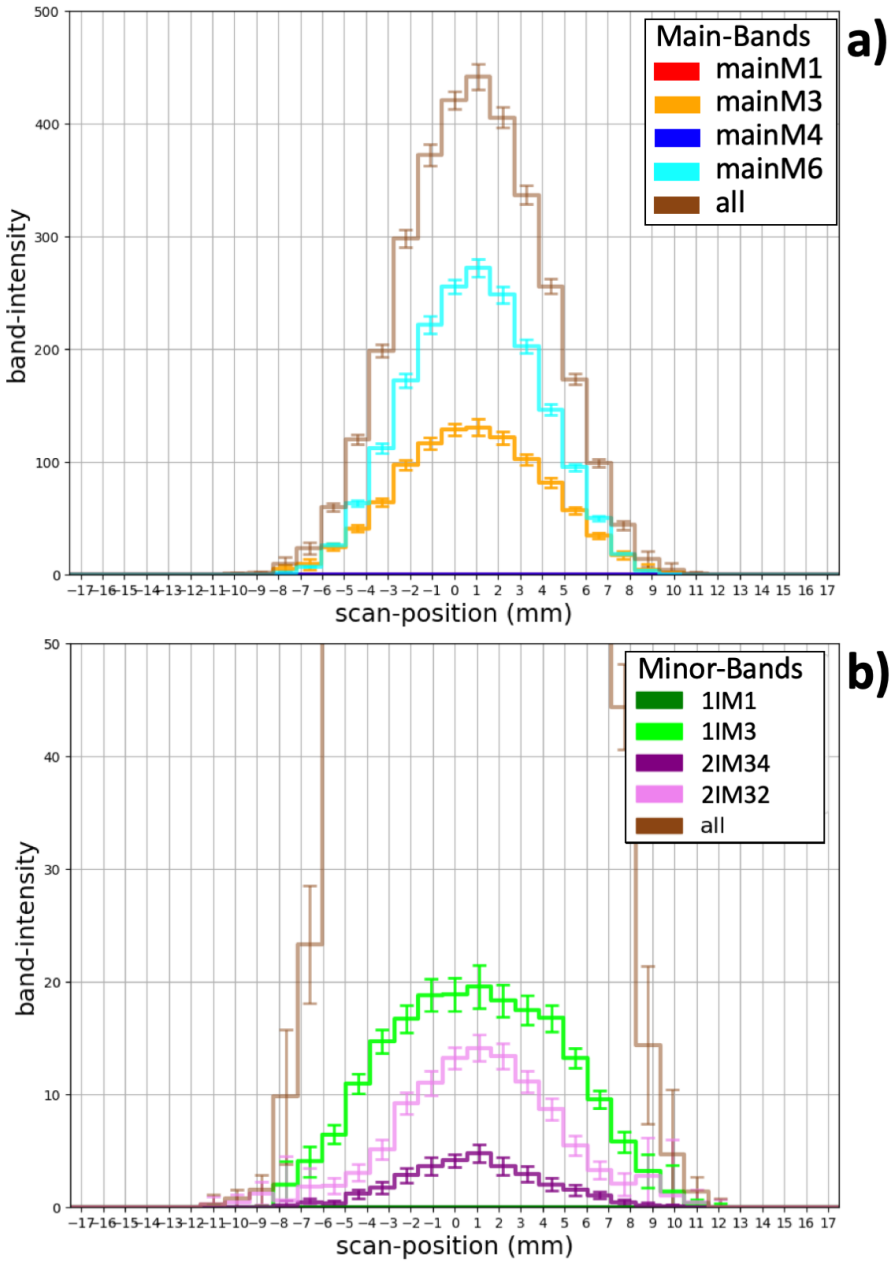

Figure 8.8: T2 DDFs obtained from scan-deconvolving the RCFs in Fig. 8.5.

Once we have the PSF and the RCFs, we applied the weighted least squares method (App. C.2) to perform the scan-deconvolution in `Python`. The resulting DDFs for HT decays (HT DDFs) are shown in Fig. 8.7 and the DDFs for T_2 decays (T2 DDFs) in Fig. 8.8. Notice the RCFs

are wider than their corresponding DDFs by roughly a detector radius of 4 mm as expected.

The raw branching ratios* are calculated by comparing the areas of the DDFs. This is because the DDF areas are basically the event counts of each ion type as shown in Fig. 8.1. If A_i is the DDF area of the band i, then its branching ratio (BR_i) is given by,

$$\mathrm{BR}_i \equiv \frac{A_i}{\sum_j A_j}, \tag{8.3}$$

where the sum in the denominator sums over all possible main- and minor-bands of each source-type. The errors on the areas are calculated by the covariance matrix that the weighted least squares fit provides. Note that the "all" DDFs from Fig. 8.7 and Fig. 8.8 are obtained from scan-deconvolving the sum of all the other RCFs; their branching ratios are always set to 100%, but their errors are properly propagated from the errors on the RCFs. However, the area of these "all" DDFs are not the denominator used in Eq. 8.3; the denominator is obtained by summing the DDF areas.

An important point about getting the correct DDF area is that we need to sum the DDF entries in the full R-point b range. This range is determined by the column numbers of the PSF. Even the negative DDF entries should be included, and they should enter the sum as negative values. This discovery was made when we were studying results from the TRIMS Geant4 simulation when we knew the exact DDFs and the branching ratios. We believe the reason is that this particular summing strategy best averages out the oscillatory noise in the DDF.

The oscillatory noise originates from the RCF noise, i.e. the error on each RCF entry. Although the weighted least squares method has been tested to be less susceptible to the RCF noise as compared to the direct matrix inversion, the oscillatory behavior persists. We have tried other methods to smooth the DDF shape, but the smoothening introduced biases on the DDF area. In the end, we care about the accuracy of the DDF area and not the DDF shape. Fortunately, the errors from summing the DDF entries are suppressed in

*We call the branching ratios raw because we still need to apply several corrections after the scan-deconvolution (Sec. 8.2).

the following way. Suppose we have random variables $V_1, V_2, ..., V_n$ with a mean of V and a standard deviation of δV, then the expected relative error of the sum of these variables follows,

$$\mathrm{E}\left(\frac{\delta(\sum_i^N V_i)}{\sum_i^N V_i}\right) = \frac{\sqrt{\sum_i^N \delta V^2}}{\sum_i^N V} = \frac{\sqrt{N}\delta V}{NV} \propto \frac{1}{\sqrt{N}}, \tag{8.4}$$

becoming smaller as N increases. With this small exercise, we are convinced that the remain oscillatory noise in our DDFs does not have a big impact on our DDF area estimation.

Beside testing the DDF area error using the Geant4 simulation, we also test the error by Monte Carlo sampling the RCF [158]. An example is shown in Fig. 8.9.a) for the T2 DDF `M3`-branch from Fig. 8.8 and Fig. 8.9.b) for the `M6`-branch. The basic idea is that for each entry in each RCF, we modify the entry by sampling a Gaussian whose mean and standard deviation are set to be the value of the original RCF and the RCF error on that value. Every entry in every RCF is sampled by a different random variable. Then once every RCF has been modified, we conduct the scan-deconvolution and calculate their area ratios normally to obtain 1 count in Fig. 8.9, which contains 10,000 sample counts. The resulting branching ratio percentages and their errors are consistent with those from Fig. 8.8.

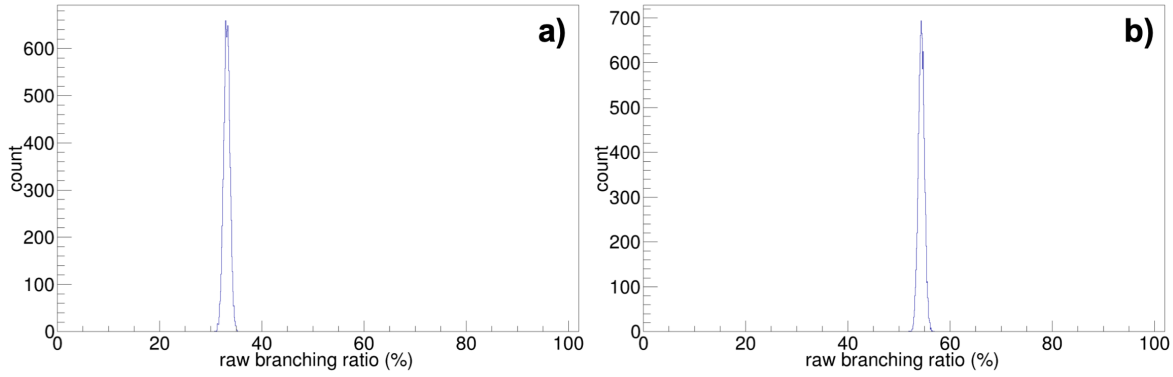

Figure 8.9: Monte-Carlo-sampled raw branching ratios from Fig. 8.8 using 10,000 different samples. Plot a) shows the branching ratio of of the `M3`-branch and plot b) `M6`-branch. Plot a) has a mean of 33.05 and a standard deviation of 0.70, while plot b) has a mean of 54.71 and a standard deviation of 0.70, which are consistent with Fig. 8.8.

And there we have the raw branching ratios we are looking for. However, in order to get accurate branching ratios for the decay-branches in Sec. 6.1.1, we need to implement several more corrections as will be discussed in Sec 8.2.

8.2 Post Scan-Deconvolution Systematics and Their Corrections

This section covers the corrections and the error estimations that are required after the scan-deconvolution. Fortunately, because the box-fitting and the scan-deconvolution are both linear operations, they can be delayed until this final stage. Each of them is independent from the other.

8.2.1 Geometrical Corrections [140]

The geometrical corrections are based on the physical variations of the ion-detector geometry at different scan-points. These variations are associated with the configuration of the ion-detector detector-arm (Sec. 2.5.4). A schematic of the detector-arm is shown in Fig. 2.20.a) with a view in the XY-plane (Sec. 2.1.2 for coordinate reference). The large light blue circle represents the decay chamber, while the small green circle the ion-detector. The structure on top of the decay chamber represents the translation stage. The view of the setup in the XZ-plane is given in Fig. 8.10.b).

Due to the rigidity of the detector-arm, the ion-detector as shown on the bottom right of Fig. 8.10.b) would tilt slightly differently at different scan-points. Although we are only scanning the ion-detector across a range as short as [-11, 11]mm, we would like to account the effect when the ion-detector is not facing perfectly toward the Z-direction. One complication comes from the holder that connects the detector-arm to the translation stage. The holder extends off-axis in the X-direction by x_m (Fig. 8.10). Care must be taken to correctly incorporate the x_m offset in the geometrical corrections [140].

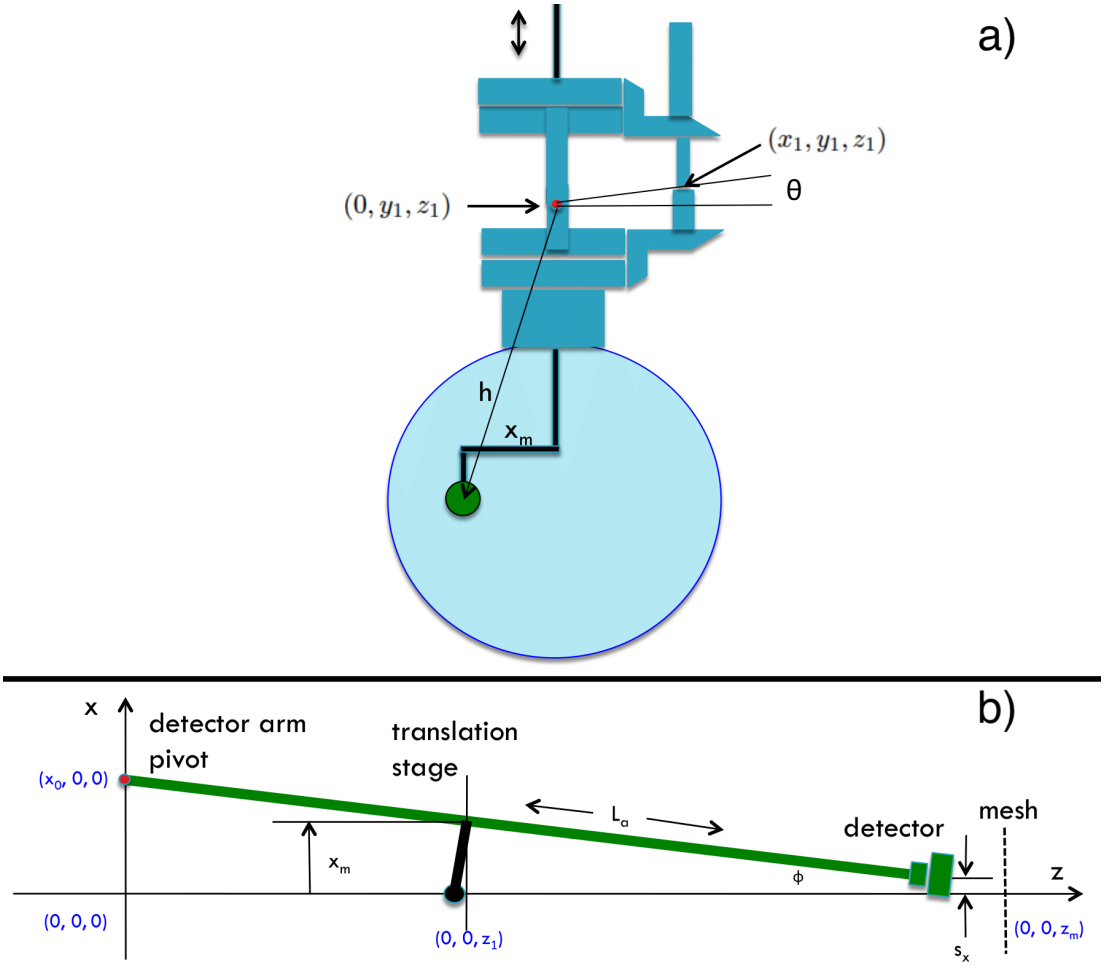

Figure 8.10: Schematic of the ion-detector arm [41]. Plot a) shows the view in the XY-plane, and plot b) in the XZ-plane (Sec. 2.1.2 for coordinate reference). This plot is the 2D schematic of Fig. 2.20, but with the ion-detector pointing to the right in plot b).

The corrections have been calculated and converted into correction factors to multiply the RCF entries, i.e. the band-intensities, such that this factor is 1 at the home-position. Since ultimately we are interested in ratios and not absolute values, the correction can always be normalized to the home-position. The same correction factors are applied to each RCF. These factors are given under the "Total" column in Table 8.1.

Scan-Points	Step Size	Projected Area	Magnetic Field	Dead Layer	Total
-10	1.0701	0.9954	0.9991	0.998	1.0621
-9	1.0506	0.9958	0.9992	0.9982	1.0435
-8	1.0353	0.9962	0.9992	0.9984	1.0289
-7	1.0235	0.9967	0.9993	0.9986	1.018
-6	1.0147	0.9971	0.9994	0.9988	1.0099
-5	1.0085	0.9976	0.9995	0.999	1.0046
-4	1.0043	0.998	0.9996	0.9992	1.0011
-3	1.0018	0.9985	0.9997	0.9994	0.9994
-2	1.0005	0.999	0.9998	0.9996	0.9989
-1	1.0001	0.9995	0.9999	0.9998	0.9993
0	1	1	1	1	1
1	0.9999	1.0005	1.0001	1.0002	1.0007
2	0.9995	1.001	1.0002	1.0004	1.0011
3	0.9982	1.0016	1.0003	1.0006	1.0007
4	0.9957	1.0021	1.0004	1.0008	0.999
5	0.9916	1.0027	1.0005	1.001	0.9958
6	0.9856	1.0032	1.0006	1.0012	0.9905
7	0.9772	1.0038	1.0008	1.0014	0.9831
8	0.9661	1.0044	1.0009	1.0016	0.9728
9	0.9522	1.005	1.001	1.0018	0.9596
10	0.935	1.0056	1.0011	1.002	0.9432

Table 8.1: Geometric correction ratios. These corrections are all in ratios compared to the value at the home-position; these ratios should directly multiply each RCF entry at that scan-point. The description of each entry is provided in the text, and the derivations can be found in [140].

The correction factors are derived from several aspects. The “Step Size” column describes how the scan step size of 1.1 mm (Sec. 2.5.4) actually changes at different scan-points. The “Projected Area" describes how the detection-area as projected in the Z-direction changes as the ion-detector tilts relate to the pivot of the detector-arm. The “Magnetic Field” describes the change in the magnetic field amplitude. This change slightly increases the gyroradii of the betas*, which effectively increases the “image size” on the ion-detector considering that the RCFs are defined under the beta-coincidence events (Sec. 8.1.2). Lastly, the “Dead Layer" describes the change in the effective dead layer width under different ion-detector tilt. A particle that is incident to the ion-detector at an angle θ needs to travel through the dead layer at an angle and effectively extends the dead layer width by $\frac{1}{\sin\theta}$. Now if we multiply all these factors together, we get the “Total" that we used as the geometrical correction factors.

The geometrical corrections are already small, and their errors are negligible. Hence, we did not incorporate their errors. The detailed derivation of each of these factors is given in [140].

8.2.2 Point Spread Function Error

The error on the PSF can be treated as the error of the scan-deconvolution itself. Table 8.2 lists the items of how we think the PSF contributes to the branching ratio systematics. We label the items by the PSF-Error-No. The way we access these errors is similar to that of Sec. 7.3.5. We modify the PSF according to the “Implementation” from Table 8.2, do the scan-deconvolution, evaluate the branching ratios from the DDF areas accordingly, and sum in quadrature the difference of the branching ratios from those obtained by using the default PSF. The sum in quadrature of the differences from all the PSF-Error-No. is how we evaluate the PSF error.

---

*It also increases the gyroradii of the ions, but that difference is captured by the scan-deconvolution.

PSF-Error-No.	Error Origin	Implementation
0	Default PSF	Default setup
1	Scan step size	Increase step size from 1.1 mm to 1.2 mm.
2	PSF row dimension	Increase row dimension from $2 \times 17 + 1$ to $2 \times 19 + 1$.
3	PSF column dimension	Increase column dimension from $2\times(17-5)+1$ to $2 \times (17 - 3) + 1$.
4	Home-position X-offset	Increase X-offset from 0.9 mm to 1.0 mm.
5	Home-position Y-offset	Increase Y-offset from 0.18 mm to 0.3 mm.

Table 8.2: List of PSF systematics, their origin, and the implementation to derive their errors.

Since each of these PSF errors affects all the branching ratios of the same source-type at the same time, their contributions will be given together in the systematic table later in Sec. 9.1.1.

8.2.3 Fiducial Volume Correction

Recall that we are using the main-FV when we are evaluating the count in each CM-box (Sec. 7.4.1) for the RCFs. Recall also that we are correcting the ion-energy from the dead layer (and the pulse-height defect) using Eq. 6.8, which is precisely corrected only for $^3He^+$. However, the dead layer affects the ions differently depending on their ion types. In other words, the [20, 40)keV main-FV energy range can be "stretched or squeezed" for a band that does not come from $^3He^+$. In this regard, the main-FV cut gives us different fiducial volumes for different ion types. This is the reason why we need the FV correction.

Fortunately, Table 3.10 provides both back and forth conversion between the detected energy and the incident energy of all the ion types of interest. By assuming each of the bands

to be uniformly distributed around the [20, 40)keV corrected ion-energy range (Fig. 6.11), we can estimate the "stretch or squeeze" of the main-FV and scale it back to $(40 - 20) = 20\,\text{keV}$ to carry out the correction.

Ion-energy	$^3He^+$	$^3H^+$	$^3T^+$	$^3HeH^+$	$^3HeT^+$
20 keV	19.83	17.99	17.30	22.04	21.57
40 keV	39.94	36.11	34.88	42.79	42.22
Difference, keV	20.11	18.12	17.58	20.74	20.64
	$^3He^+$	$\{^3He^+, H^+\}$	$\{^3He^+, T^+\}$		
20 keV	19.83	21.49	21.25		
40 keV	39.94	42.54	41.73		
Difference, keV	20.11	21.04	20.48		
75 keV	75.03	79.34	78.10		
95 keV	94.90	99.57	98.48		
Difference, keV	19.87	20.23	20.38		

Table 8.3: Fiducial volume correction under the main-FV and the high-FV for each ion detection-channel. The small deviations of the column "^{3}He" entries from the set values in the column "Ion-energy" come from the use of the fit polynomials (Table 3.10). The table comes from [140].

The resulting scales are given in Table 8.3. To explain the table by an example, take the column of "$^3H^+$", the value in the "**20 keV**" row is obtained by,

$$\text{DtoI}_\text{H}(\text{ItoD}_\text{He}(20)) = 17.99\,\text{keV}, \tag{8.5}$$

where the functions come from the polynomials in Table 3.10. The first function ItoD_He basically undoes the corrected ion-energy from Eq. 6.8 to obtain the detected ion-energy. From there, the second function converts the detected ion-energy to the incident ion-energy

using the ion type $^3H^+$ of interest. We do the same for 40 keV and obtain 36.11 keV. This means the interval [17.99, 36.11]keV is the actual FV for the $^3H^+$ events under the main-FV cut. And the "**Difference, keV**" row just gives the difference ($36.11 - 17.99 = 18.12$ keV), and the corresponding FV correction scale is given by $\frac{20}{18.12}$. *

Because this FV correction scalar multiples are not scan-position dependent†, and the scan-deconvolution is linear, these FV corrections can be done directly on the DDF areas. This is fortunate, especially considering that we can quite reliably distinguish the ion types of the main- and minor-bands at the DDF stage.

We also included the FV correction scales for the high-FV of [75, 95]keV of the corrected ion-energy. It was used in Sec. 7.3.4.

There are a few sources of systematics from the FV correction. The first is the error on the polynomials from Table 3.10. For instance, ideally, the ItoD_{He} should be the direct inverse of DtoI_{He}, but it is not. This is why the energy difference for $^3He^+$ is 20.11 keV instead of the original 20 keV. The error is expected because the polynomial fits are performed separately for ItoD and DtoI relations, even though they use the same SRIM data points; a polynomial of cubic order cannot be easily inverted. We evaluated that each of our polynomial operations generates a 0.008 error for each interval [140], and so $0.008\sqrt{2}$ with the two operations that we do. The error is small because the upper and lower bounds of an interval are correlated to have an error of the same sign, and so the difference receives less error than each value. Note that this 0.008 uncertainty should include uncertainty on the coefficients from the polynomial fit (Sec. 3.2.2).

Another systematic is associated with the ion-energy correction Eq. 3.13. Recall that we are referring to the detected energy of 50 keV from the H^+'s with 60 keV incident energy (Sec. 3.2.2 and App. B.1). Now, we are taking the uncertainty of 50 keV to be 2 keV as

---

*Note again that the overall scale does note matter because we only care about the ratios between DDF areas. So the numerator in the correction can be 20 or any other positive scalar. But the same numerator must be used for the FV correction from every column.

†Energy detection does not depend on the scan-position.

a rather conservative heuristic estimation. Then we refit the polynomials by moving the 50 keV reference by a sigma to 48 keV. However, this refitting at the [20, 40]keV FV can be roughly estimated by shifting the FV to [22, 42]keV on the original polynomial. For this reason, we generate Table 8.4 that has this 2-keV shift. Then the error can be calculated by the difference between the FV correction scales estimated by Table 8.4 as compared to Table 8.3.

Ion-energy	$^3He^+$	$^3H^+$	$^3T^+$	$^3HeH^+$	$^3HeT^+$
22 keV	21.82	19.86	19.08	24.20	23.69
42 keV	41.96	37.86	36.63	44.82	44.23
Difference, keV	20.14	18.00	17.55	20.62	20.54
	$^3He^+$	$\{^3He^+, H^+\}$	$\{^3He^+, T^+\}$		
22 keV	21.82	23.57	23.26		
42 keV	41.96	44.66	43.81		
Difference, keV	20.14	21.10	20.55		
77 keV	77.01	81.39	80.16		
97 keV	96.89	101.55	100.50		
Difference, keV	19.88	20.16	20.33		

Table 8.4: Fiducial volume correction under the main-FV and the high-FV that are shifted up by 2 keV. The table comes from [140].

One caveat is that the ion-detector energy resolution would not contribute to the FV correction error under the assumption that the bands are uniform in ion-energy; the broadening "sends" as many events out of the FV as it "sends" in. Because of how we define our FV, the assumption translates to our FV being uniform in the main-FV range. However, after we perform the scan-deconvolution, the non-uniformity that could be contributed by the gyroradius should be eliminated; there is no reason to assume non-uniformity in the

main-FV. We keep the assumption in this work, but there are future plans to investigate this issue using the TRIMS Geant4 simulation (Sec. 9.2.1).

Once again, there is a problem arising from the $^3He^+$ versus T^+ degeneracy for the T_2 decay (Sec. 6.1.1). We estimate the FV correction factor and its error of the `T2_mainM3` band in exactly the same manner as Eq. 7.26 and Eq. 7.28. This error is substantial because $^3He^+$ and T^+ ions behave rather differently in the dead layer.

8.2.4 Two-Ion Efficiency Correction and Branch-Intensity

The 2-ion efficiency problem is the counterpart of the 2-electron efficiency problem in Sec. 8.1.2. And the solution is the same, which is to "look at" 1 ion at a time for the 2-ion events.

It is noteworthy to mention that this approach has another advantage in terms of avoiding the complication from the 85% mesh transmission rate on the ion-electrode (Sec. 2.1.3). Because the width of the mesh is macroscopic compared to the ions, this transmission rate is ion type independent. Now since we are always looking at 1 ion at a time, every branch is affected by the same 85% transmission rate. And as we are looking for the ratios of the branches, the transmission rate just gets factored out.

To give more detail about the ion efficiency correction, we first look at the $\{^3He^+, H^+\}$ decay-branch from HT decay. This channel contributes to detection-channels `HT_2I2eM32`, `HT_2I1eM32`, `HT_1I2eM3`, `HT_1I1eM3`, `HT_1I2eM1`, and `HT_1I1eM1` (Table 6.2). Recall that the area A of each DDF is obtained by summing of the DDF entries at every R-point b index (Sec. 8.1.3). Then from the beta-efficiency correction, we already have from Sec. 7.4.2,

$$\begin{aligned} A(\texttt{HT\_2IM32}) &\equiv A(\texttt{HT\_2I2eM32}) + \frac{1}{2}A(\texttt{HT\_2I1eM32}) \\ &\approx \left(1 + \frac{1}{2}R_{\text{1eV2e}}(\texttt{2IM32HT})\right) A(\texttt{HT\_2I2eM32}), \end{aligned}$$

$$
\begin{aligned}
A(\texttt{HT\_1IM3}) &\equiv A(\texttt{HT\_1I2eM3}) + \frac{1}{2}A(\texttt{HT\_1I1eM3}) \\
&\approx \left(1 + \frac{1}{2}R_{\text{1eV2e}}(\texttt{1IM3HT})\right) A(\texttt{HT\_1I2eM3}), \\
A(\texttt{HT\_1IM1}) &\equiv A(\texttt{HT\_1I2eM1}) + \frac{1}{2}A(\texttt{HT\_1I1eM1}) \\
&\approx \left(1 + \frac{1}{2}R_{\text{1eV2e}}(\texttt{1IM1})\right) A(\texttt{HT\_1I2eM1}),
\end{aligned}
\tag{8.6}
$$

where the DDF areas of these three bands are provided in Fig. 8.7. The 1eV2e ratios R_{1eV2e} come from Table 7.5. Now to do the 2-ion efficiency correction, we follow the strategy of "looking at" 1 ion at time. Suppose we choose $^3\text{He}^+$, then,

$$
I(\{^3\text{He}^+, \text{H}^+\}) \equiv 2A(\texttt{HT\_2IM32}) + A(\texttt{HT\_1IM3}). \tag{8.7}
$$

The sum on the right-hand side is there because $^3\text{He}^+$ is detected by the ion-detector in both of the HT_2IM32 and the HT_1IM3 band*. The factor of 2 for the first term comes from 2-ion events in the main-FV. While the 1-ion band has ion-energy range [0, 60)keV, the 2-ion band has [0, 120)keV. The 2-ion band is thinner in event density. Hence, if we apply the main-FV cut of [20, 40)keV, we are limiting the 2-ion band to half of the FV as compared to the 1-ion band. To compensate, we give the 2-ion DDF area an extra factor of 2, so that we have the same FV for every band. The factor of $\frac{1}{2}$ of the second is missing as compared to Eq. 8.6 because unlike the beta and the shake-off electrons, we can distinguish $^3\text{He}^+$ from H^+. Moreover, we should see the following in our branching ratio result,

$$
I(\{^3\text{He}^+, \text{H}^+\}) = 2A(\texttt{HT\_2IM32}) + A(\texttt{HT\_1IM1}), \tag{8.8}
$$

when we choose H^+ for the 1 ion we "look at". This is because checking either $^3\text{He}^+$ or H^+ should give us the same physical branch $\{^3\text{He}^+, \text{H}^+\}$.

The case of the $\{^3\text{He}^+, \text{T}^+\}$ decay-branch from T2 decay is more like the 2-electron

*We are using the bands and channels interchangeably here.

efficiency correction,

$$\begin{aligned} A(\texttt{T2\_2IM32}) &\equiv A(\texttt{T2\_2I2eM32}) + \frac{1}{2}A(\texttt{T2\_2I1eM32}) \\ &\approx \left(1 + \frac{1}{2}R_{\text{1eV2e}}(\texttt{2IM32HT})\right) A(\texttt{T2\_2I2eM32}), \\ A(\texttt{T2\_1IM3}) &\equiv A(\texttt{T2\_1I2eM3}) + \frac{1}{2}A(\texttt{T2\_1I1eM3}) \\ &\approx \left(1 + \frac{1}{2}R_{\text{1eV2e}}(\texttt{1IM3HT})\right) A(\texttt{T2\_1I2eM3}), \end{aligned} \tag{8.9}$$

and,

$$I(\{^3\text{He}^+,\ \text{T}^+\}) \equiv 2A(\texttt{T2\_2IM32}) + \frac{1}{2}A(\texttt{T2\_1IM3}), \tag{8.10}$$

because once again we cannot distinguish detecting a $^3\text{He}^+$ from a T^+ from a T_2 decay.

The I's in Eq. 8.7 and Eq. 8.10 are what we call the branch-intensity, which are the final intensities we need to compare to get the branching ratios of the decay-branches. The branch-intensities for the main-bands are just the DDF areas of that band. The branch-intensities for the $^3\text{He}^{++}$ bands are just the DDF areas of the 2IM34 of Fig. 8.7 and Fig. 8.8,

$$\begin{aligned} A(\texttt{HT\_2IM34}) &\equiv 2\left(A(\texttt{HT\_2I2eM34}) + \frac{1}{2}A(\texttt{HT\_2I1eM34})\right) \\ &\approx 2\left(1 + \frac{1}{2}R_{\text{1eV2e}}(\texttt{2IM34HT})\right) A(\texttt{HT\_2I2eM34}), \\ A(\texttt{T2\_2IM34}) &\equiv 2\left(A(\texttt{T2\_2I2eM34}) + \frac{1}{2}A(\texttt{T2\_2I1eM34})\right) \\ &\approx 2\left(1 + \frac{1}{2}R_{\text{1eV2e}}(\texttt{2IM34HT})\right) A(\texttt{T2\_2I2eM34}). \end{aligned} \tag{8.11}$$

Once again, the factor of 2 is for compensating the thinner 2-ion FV, and the factor of $\frac{1}{2}$ is for singling out beta detection out of a decay that produces 2 electrons.

8.2.5 Ion-Backscattering Correction [167]

The last correction is for ion backscattering. Unlike electron backscattering (Sec. 3.1.3), ion backscattering is not implemented in the TRIMS Geant4 simulation and so it is not accounted for in the charge-CC ratios (Sec. 7.2.3). Fortunately, the effect is much smaller for

the ion backscattering, which is at percent level according to Fig. 3.7 from SRIM. Moreover, because we are taking the main-FV cut, any backscattering would knock the ion out of the main-FV. As for the case that a high energy ion ends up inside the main-FV energy range after backscattering, Fig. 3.7 tells us that the probability is negligible. Therefore, we can treat a backscattered ion as lost, i.e. missing from the box-intensity in Fig. 7.36. The correction is essentially to estimate how many of the ions are lost from the backscattering and scale it back.

Table 8.5 gives the average ion-backscattering probability of each ion type of interest within the main-FV. The errors on the rates are also provided. These corrections are directly done on the branch-intensities. Take $^3He^+$ as an example, its branch-intensity is multiplied by $\frac{100}{100-1.072} \approx 1.011$.

Ion Type	Ion-backscattering Percentage	Energy Range
$^3He^+$ or $^3He^{++}$	^{3}He: $1.072 \pm 0.015\%$	^{3}He: [20 40]keV
H^+	H: $0.251 \pm 0.007\%$	H: [20 40]keV
T^+	T: $0.0279 \pm 0.007\%$	T: [20 40]keV
$^3HeH^+$	H: $1.493 \pm 0.022\%$, ^{3}He: $1.695 \pm 0.020\%$	H: [5, 10]keV, ^{3}He: [15, 30]keV
$^3HeT^+$	T: $1.057 \pm 0.019\%$, ^{3}He: $2.864 \pm 0.031\%$	T: [10, 20]keV, ^{3}He: [10, 20]keV

Table 8.5: Average ion-backscattering probability from ion detection in main-FV for each ion type. The table comes from [167]

For the molecular ion case, each of the two particles carries much less energy when they are incident on the ion-detector, and so their ion-backscattering probabilities are much higher according to Fig. 3.7. However, whenever either of the two particles backscatter, it would send the event out of the main-FV. Hence, the correction can be done independently. Take $^3HeH^+$ as an example, its branch-intensity is multiplied by $\frac{100}{100-1.493}\frac{100}{100-1.695} \approx 1.033$.

The $^3He^{++}$ is the same as the $^3He^+$ case because the detected particles are fully ionized

once they enter the silicon detector.

Notice that after the 2-ion efficiency correction (Sec. 8.2.4), we no longer need to worry about the 2-ion cases.

Regarding the $^3He^+$ versus T^+ degeneracy problem for the T_2 decay, we estimate the ion-backscattering correction factor and its error of the `T2_mainM3` band in exactly the same manner as from Eq. 7.26 and Eq. 7.28. This case is different from the molecular and the 2-ion cases in that the `T2_mainM3` branch-intensity receives only one correction factor $\frac{1}{2}(\frac{100}{100-1.072} + \frac{100}{100-0.0279})$ instead of two consecutive ones. The error on the `T2_mainM3` correction factor is larger than all the ion-backscattering errors of the other bands however.

Finally, we do have the ion-backscattering probabilities worked out for the high-FV for applying an extra correction for Sec. 7.3.4. However, the correction is negligible.

8.3 Branching Ratios

This section covers the branching ratios from both T_2 (Table 6.1) and HT source-types (Table 6.2). The branching ratios for the main- and minor-bands are covered in Sec. 8.3.1. As for the other decay-branches with small contributions, the upper limits of their branching ratios are covered in Sec. 8.3.2 and Sec. 8.3.3.

8.3.1 Main-band and Minor-band Branching Ratios

With all the corrections and error estimations from Sec. 8.2, we finally have the branching ratios with their full errors for the HT decay branches in Table 8.6 and T_2 decay branches in Table 8.7.

To compare these branching ratios to the theory, we must include all the main-bands and minor-bands together; the theory accounts for all the dissociated final states at once [98].

As a test of consistency, we want to compare the branching ratios for the $\{^3He^+, H^+\}$ branch between estimating using $^3He^+$ and H^+. Although their branch-intensities originated from different RCFs, their results should agree because they are estimating the same physical branch (Eq. 8.7 and Eq. 8.8). And according to Table 8.6, these two results do agree within

error bars. This makes us confident about the branching ratios and their error bars as presented.

Decay-Branch	Preliminary Branching Ratio	Preliminary Absolute Error
$\{^3HeH^+, e^-\}$	56%	1%
$\{^3He^+, H, e^-\}$	24.9%	0.7%
$\{^3He, H^+, e^-\}$	6%	2%
$\{^3He^+, H^+, 2e^-\}$ from $^3He^+$	11%	1%
$\{^3He^+, H^+, 2e^-\}$ from H^+	11%	1%
$\{^3He^{++}, H, 2e^-\}$	2.3%	0.8%

Table 8.6: Branching ratios for HT decay. Refer to Table 6.2 for the decay-branches.

Decay-Branch	Preliminary Branching Ratio	Preliminary Absolute Error
$\{^3HeT^+, e^-\}$	50%	2%
$\{^3He^+, T, e^-\}$ or $\{^3He, T^+, e^-\}$	33%	2%
$\{^3He^+, T^+, 2e^-\}$	15%	1%
$\{^3He^{++}, T, 2e^-\}$	1.8%	0.2%

Table 8.7: Branching ratios for T_2 decay. Refer to Table 6.1 for the decay-branches.

8.3.2 Negative-Ion Branching Ratio Limit

For the T_2 source-type, the decay-branch $\{^3He^{++}, T^-, e^-\}$ from Table 6.1 is missing in Table 8.7. This decay-branch has a negative ion in the product, so we call it the negative-ion band. The same goes for the HT source-type. As mentioned in Sec. 6.1.1, we do not see a lot of these events in our data, but we do want to give rough upper limits. For this work, we do not quantify the confidence level of these limits.

To estimate the branching ratios of the negative-ion band, we once again inspect the mass projection in the high-FV as shown in Fig. 8.11. The T_2 mass spectrum is shown in Fig. 8.11.a) that can be compared to Fig. 7.6. Because the negative-ion band produces a $^3He^{++}$ and a beta, if both of them are detected, the event should look exactly like a $^3He^{++}$ event. The only difference is that the extra T^- would be detected by the beta-detector after the beta's detection, which would result in a beta-2WS event like in Sec. 7.1.1. The difference as compared to Sec. 7.1.1 is that the second beta-detector detection cannot be from mesh electrons. The reason is that if the $^3He^{++}$ is responsible for knocking out mesh electrons, then the ion-detector would not detect anything, and so the event would not be a coincidence event to be included in the analysis data. Hence, the $^3He^{++}$ beta2WS event should be coming from the $\{^3He^{++}, T^-, e^-\}$ decay-branch*.

To avoid unnecessary noise events, we choose only the data at the home-position. And to single out the the $^3He^{++}$ events from the 2-ion events, we apply a $(0 \leq \sqrt{M_m} < 1\,\sqrt{\text{u}})$ cut. Then the blue filled peak in Fig. 8.11.a) arises from the beta1WS events and the orange peak from the beta2WS events. The corresponding count in each peak is provided in the plot in matching color. And the branching ratio upper limit for $\{^3He^{++}, T^-, e^-\}$ can be calculated on top of the $\{^3He^{++}, T, 2e^-\}$ decay-branch from Table 8.7 by,

$$\text{BR}(\{^3He^{++}, T^-, 2e^-\}) < \frac{21}{2040} \times P(\{^3He^{++}, T, 2e^-\}) = 0.01 \times 1.8\% = 0.018\%. \quad (8.12)$$

*The 3-charge branch from Sec. 8.3.3 would also produce $^3He^{++}$ beta2WS events, but that would only make this upper limit even tighter.

Similarly for the HT source-type from Fig. 8.11.b)[†], we get,

$$\mathrm{BR}(\{^3\mathrm{He}^{++},\ \mathrm{H}^-,\ 2\mathrm{e}^-\}) < \frac{16}{1770} \times P(\{^3\mathrm{He}^{++},\ \mathrm{H},\ 2\mathrm{e}^-\}\ ) = 0.009 \times 2.3\% = 0.021\%. \quad (8.13)$$

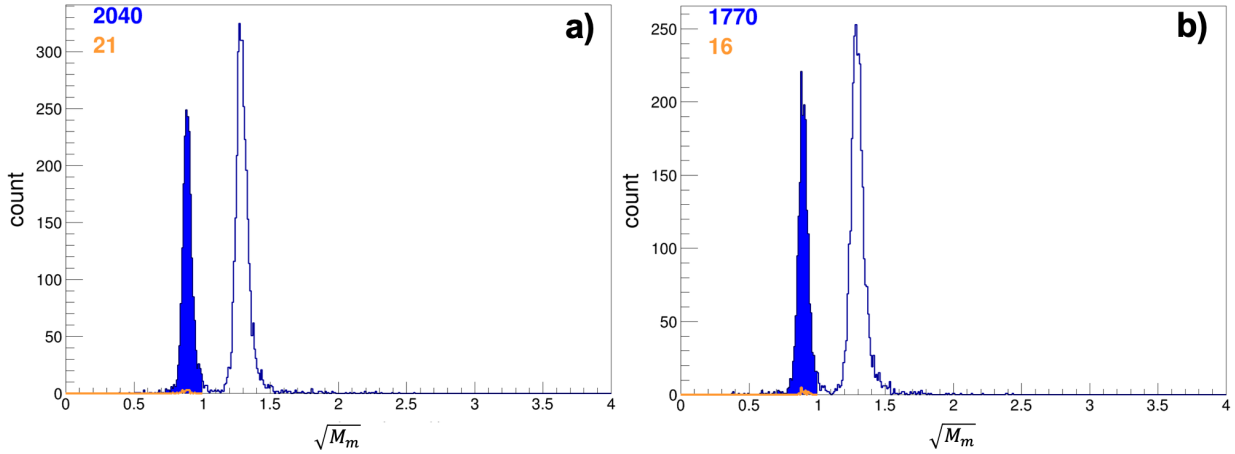

Figure 8.11: Mass spectrum for the raw-T2-data (plot a) and raw-HT-data (plot b) at the home-position in the high-FV. Similar to Fig. 7.6 and Fig. 7.7, the left peak is associated with the $^3\mathrm{He}^{++}$ events and the right peak with the 2-ion events. The focus is on the $^3\mathrm{He}^{++}$ events, and so a ($\sqrt{M_m} < 1\ \sqrt{\mathrm{u}}$) cut is applied. The beta1WS events form the blue filled peak and the beta2WS form the orange peak. The corresponding count in each peak is provided in the plot in matching color; the counts provide information about the T^- and H^- event intensity of the data.

8.3.3 Three-Charge Branching Ratio Limit

For the T_2 source-type, other than the negative-ion decay-branch, the decay-branch $\{^3\mathrm{He}^{++}, \mathrm{T}^+, 3\mathrm{e}^-\}$ from Table 6.1 is also missing in Table 8.7. We call these events the 3-charge events, because if all the particles are detected, the decay should gives ($Q_{ie} = 3$) and a third band parallel

[†]The background non-filled blue histograms are from beta1WS events, which are different from the ion1WS background in Fig. 7.7. For this reason, the 2-ion peak heights are different for these two plots.

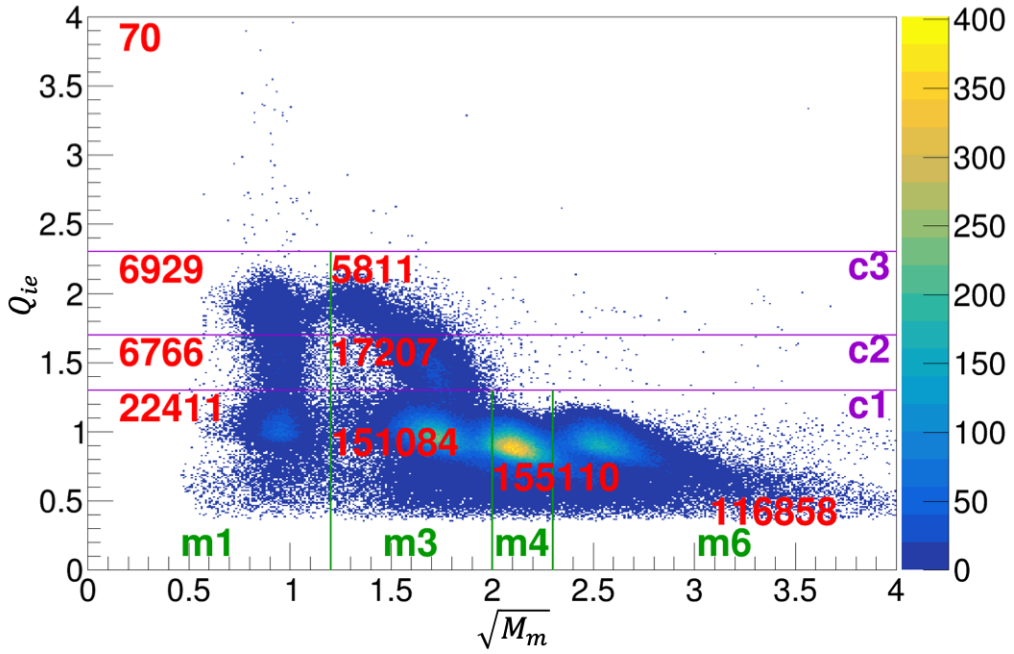

Figure 8.12: Counts in each CM-box of the combined left- and right-scan and combined raw-T2- and raw-HT-data in the main-FV at the home-position. The counts are colored in red and are displayed inside each box. The plot is to be compared to Fig. 7.36, but this time the count of 70 given on the top left are no longer outliers; it is the count of events inside the box defined by $(0 \leq \sqrt{M_m} < 4\,\sqrt{\mathrm{u}})$ and $(2.3 \leq Q_{ie} < 4\,\mathrm{e})$.

to the main-band and `2I2e`-band from Fig. 6.4 (Sec. 6.3.2). The same thing goes for the HT source-type. Since we do not see a lot of the 3-charge events (Sec. 6.1.1), we combine T_2 and HT source-types to give rough upper limits to the branching ratio to the 3-charge events. For this work, we do not quantify the confidence of these limits.

Since the 3-charge events give $(Q_{ie} = 3)$, we can find their abundance in a charge-mass plot like in Fig. 7.36. Combining the raw-T2- and raw-HT-data as well as the left- and the right-scans, we arrive at Fig. 8.12. However, Fig. 8.12 only contains the data at the home-position so that for most of the 3-charge events, both of the $\{^3\mathrm{He}^{++}, \mathrm{T}^{+}\}$ ions are detected. Unlike in Fig. 7.36, the top-left count in Fig. 8.12 does not count outliers, it is the

count inside the box defined by $(0 \leq \sqrt{M_m} < 4\sqrt{\mathrm{u}})$ and $(2.3 \leq Q_{ie} < 4\,\mathrm{e})$. This box should contain the the 3-charge events*. Therefore, the upper limit is,

$$\begin{aligned} &\mathrm{BR}(\{^3\mathrm{He}^{++},\ \mathrm{T}^{+},\ 3\mathrm{e}^{-}\} \text{ or } \{^3\mathrm{He}^{++},\ \mathrm{H}^{+},\ 3\mathrm{e}^{-}\}) \\ &\quad < \frac{70 \times 100\%}{22411 + 151084 + 155110 + 116858 + 6766 + 17207 + 6929 + 5811} \\ &\quad = 0.015\%. \end{aligned} \tag{8.14}$$

*Band-No. a10) from Fig. 6.2 would also produce events in this box because the multiple mesh-electrons detected can increase the charge value over ($Q_{ie} = 2$). But that would only make this upper limit even tighter. Also, these Band-No. a10) events that show up in Fig. 6.2 look minuscule in Fig. 8.12 because the former include the whole data, while the latter includes only the data at the home-position. As a reference for the whole data, see Fig. 6.16.

Chapter 9
CONCLUSIONS AND PROSPECTS

The chapter provides the systematic tables of the TIRMS experiment in Sec. 9.1. The section also covers other sources of systematics that were not considered in the previous chapters, although their contributions are arguably negligible. Following the systematic tables, the outlook of the TRIMS experiment is provided in Sec. 9.2. Then, we conclude the result of this work in Sec 9.3.

9.1 Branching Ratio Systematics

The systematics tables for the branching ratios are provided in Sec. 9.1.1. As for two other subsections, Sec. 9.1.2 covers the systematics from deuterium (DT molecule), while Sec. 9.1.3 from field misalignment between the magnetic and electric field.

9.1.1 Branching Ratio Systematics Table

To summarize the results covered in Sec. 8.3, the systematics table for the HT decay-branches from Table 6.2 is provided in Table 9.1, while the table for the T_2 decay-branches from Table 6.1 is in Table 9.2. The decay-branch labels are shortened to list the only product ions, since there is no ambiguity in this identification. The errors are categorized into errors from before the scan-deconvolution in the "Pre-decon" column and errors from the post-deconvolution corrections (Sec. 8.2) in the rest of the columns. These errors are summed in quadrature to arrive at the "Total" error we provided previously in Sec. 8.3.1.

The "Pre-decon" errors contain all the CC contributions introduced in Sec. 7 before the scan-deconvolution; these errors are combined into error bars on the RCFs (Sec. 8.1.2). Because of the evaluations need to go through the box-fitting (Sec. 7.4.3), the chi-square

normalization (Sec. 7.4.4), and the scan-deconvolution, there is no simple way to disentangle individual error contributions from statistics, the source-SC ratios (Sec. 7.1.5), charge-CC ratios (Sec. 7.2.3), 1eV2e ratios (Sec. 7.2.4), and the mass-CC ratios (Sec. 7.3). For this work, we will not break up the "Pre-decon" errors further; however, we are developing a method to do so in the near future (Sec. 9.2.1).

Decay-Branch	BR	Pre-decon	PSF	FV	Ion-BkS	Total
$^3HeH^+$	56.3%	1.22%	0.30%	0.35%	0.01%	1.3%
$^3He^+$	24.87%	0.65%	0.06%	0.27%	0.01%	0.71%
H^+	5.8%	1.67%	0.40%	0.09%	<0.01%	1.7%
$\{^3He^+, H^+\}$ from $^3He^+$	10.8%	1.42%	0.30%	0.14%	<0.01%	1.4%
$\{^3He^+, H^+\}$ from H^+	10.7%	1.30%	0.16%	0.14%	<0.01%	1.3%
$^3He^{++}$	2.27%	0.39%	0.70%	0.05%	<0.01%	0.80%
$\{^3He^{++}, H^-\}$	<0.021%					
$\{^3He^{++}, H^+\}$	<0.015%					

Table 9.1: Branching ratio systematics for the HT decay. All the presented errors are absolute errors. The "BR" stands for branching ratio. The "Pre-decon" covers the errors from before the scan-deconvolution, which are the RCF errors derived from error propagating all the CC-contributions (Ch. 7). The "PSF" from the point spread function error of the scan-deconvolution (Sec. 8.2.2), the "FV" column contribution comes from the fiducial volume correction (Sec. 8.2.3), and the "Ion-BkS" from the ion-backscattering correction (Sec. 8.2.5). These errors are summed in quadrature to arrive at the error in the "Total" column.

An important remark is that the denominator in the branching ratio calculation involves all the DDF areas (Eq. 8.3), and so the error of each branching ratio is affected by the

errors from all the DDFs at once, which results in some reduction of the branching ratio error due to correlation. For the HT source-type, the largest source of error comes from decay-branch $\{^3\text{He}, \text{H}^+, \text{e}^-\}$ in "Pre-decon", which is as expected considering the error bars on the `mainM1` band RCF in Fig. 8.4. As for the T2 source-type, the largest source of error comes from the FV correction on the decay-branches ($\{^3\text{He}^+, \text{T}, \text{e}^-\}$ or $\{^3\text{He}, \text{T}^+, \text{e}^-\}$). This is also not a surprise considering that the decay-branches are degenerate and can only be observed under the same detection-channel in TRIMS. Moreover, the dead layer corrections to these two decay-branches are rather different, and so it leads to a large FV correction error (Sec. 8.2.3).

Decay-Branch	BR	Pre-decon	PSF	FV	Ion-BkS	Total
$^3\text{HeT}^+$	50.3%	0.70%	0.41%	1.26%	0.07%	1.5%
$^3\text{He}^+$ or T^+	33.2%	0.65%	0.46%	1.61%	0.09%	1.8%
$\{^3\text{He}^+, \text{T}^+\}$	14.8%	0.91%	0.29%	0.62%	0.05%	1.1%
$^3\text{He}^{++}$	1.80%	0.16%	0.09%	0.06%	<0.01%	0.19%
$\{^3\text{He}^{++}, \text{T}^-\}$	<0.018%					
$\{^3\text{He}^{++}, \text{T}^+\}$	<0.015%					

Table 9.2: Branching ratio systematics for T2 decay. This table follows the same description as Table 9.1.

9.1.2 Deuterium

One possible source of systematics that we have not yet considered is the deuterium. If there are DT molecules in our system, they would give additional mass-2 (D^+) and mass-5 ($^3\text{HeD}^+$) background signals. So we would like to estimate the amount of DT in our system.

To estimate the amount of DT, we need to realize first that the catalytic effect of the ion-gauge would convert much of the DT to HT and HD. The HD molecule would not give us any signal, and so we need to look into the raw-T2-data. Also, the mass-2 and mass-5

peaks would be covered by the main-band peaks (Fig. 6.20.a), so we need to search in the `1I2e`-band in charge-box `c2` instead, which is what is shown in Fig. 9.1.

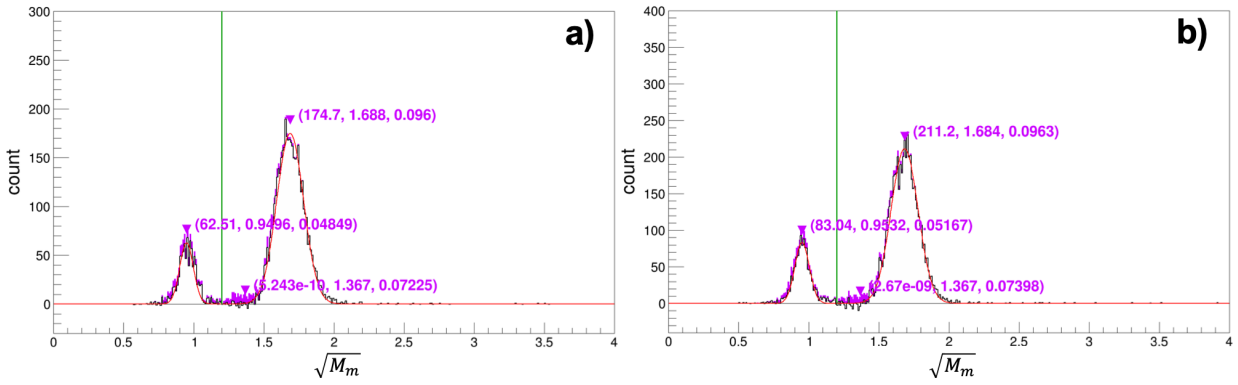

Figure 9.1: Mass spectrum for the left-scan (plot a) and the right-scan (plot b) raw-T2-data at the home-position in the main-FV. The plot is to be compared to Fig. 7.28 b), but without the source-subtraction. The magenta portion of the peak is still subtracted out using the charge subtraction. The green lines are associated with the mass-boxes defined in Sec. 6.3.1 for the charge-box `c2`. Each spectrum is fitted using 3 independent Gaussians, where the middle one is for the DT contribution. The fit values are provided near the top of each peak pointed out by a magenta triangle. The fit values are also provided in magenta color and in a format of (amplitude, mean, sigma).

The mass projection in Fig. 9.1.a) is for the left-scan and Fig. 9.1.b) for the right-scan. The left peak in the spectrum is mass-1 from the H^+ ions produced by the HT contaminant in the raw-T2-data, and the right peak from the He^+ or the T^+ ions. And so the task is to find a mass-2 D^+ in between the two conspicuous peaks. To do that, we first subtract out the $2I2e$ contribution in the spectrum because they can mimic the mass-2 spectrum. Then we fit the spectrum with 2 independent Gaussians, fix the mean and the sigma of the Gaussians, and then do a second fit with 3 independent Gaussians. The mean of the 3$^{\text{rd}}$ Gaussian is fixed at $\sqrt{2}\sqrt{\text{u}}$, while the sigma is fixed to be the average of the other two peaks. Recall that the mass peaks are not exactly at the integer atomic mass unit (Sec. 6.2.2). In fact, both the

mass-1 and mass-3 peaks are shifted to a slightly lower mass. And so on the mass-2 peak, we apply the average shift between the mass-1 and mass-3 on the mass-2 mean. So for the 3 independent Gaussian fit, only the amplitudes of the 3 peaks are allowed to change.

The fit results are also provided in Fig. 9.1 near the top of each peak in a format of (amplitude, mean, sigma). We can see the amplitudes for the mass-2 peaks are at the $10^{-9} \pm 10^{-3}$ count level*. If we associated this DT peaks with the $^3He^{++}$ peaks, i.e. the ($\sqrt{M_m}$<1.2) peaks in Fig. 9.1, that are roughly 70 in amplitude. Take the 2% as the approximated $^3He^{++}$ branching ratio from Table. 9.1 and Table. 9.2, a rough upper limit of the DT contribution to the overall branching ratios is $\frac{10^{-3}}{70} \times 2\% \approx 3 \times 10^{-5}\%$. For this reason, we consider the systematics due to DT are negligible in our system.

9.1.3 Field Alignment

Another source of systematics we have not covered yet is the misalignment between the magnetic field and electric field. With help from the CENPA engineers [155] when we were aligning the decay chamber with the magnet coils during the construction, the misalignment should be small. But we do want an estimation of it.

We used the TRIMS Geant4 simulation to estimate the field misalignment. We happened to find in the simulation that the field misalignment is positively correlated to the relative shifts between the centroids of the RCFs(Fig. 8.4). Particularly, we found the shift is most apparent between mass-1 and mass-4 RCFs from the HT decay. This can be explained by that the misalignment provides ions with an additional $E \times B$ drift, whose magnitude depends on the mass-to-charge ratio of the ions. Since we can tilt the magnetic field in the simulation using the `SetBTilt` functions from Table 3.3, we can figure out the mass-1 and mass-4 relative centroid positions as a function of the magnetic field tilt. The example of the tilt toward the Y-direction by using the `SetBTiltY` function in Fig. 9.2, where the red points are the results from the simulation. We then fit the simulation result with a line, shown as

*The error on the fit parameters are not shown in the figure.

the blue line in Fig. 9.2. Then we place the relative centroid position obtained from the data to the fitted blue line as shown by the green point in Fig. 9.2. The green point's error bar on the y-axis comes from errors on estimating the centroids. On the other hand, the error bar of the x-axis are actually the evaluated error from combining the y-axis error bar and coefficient errors from the fit. The resulting tilt is 0.27±0.04° toward the Y-direction [156].

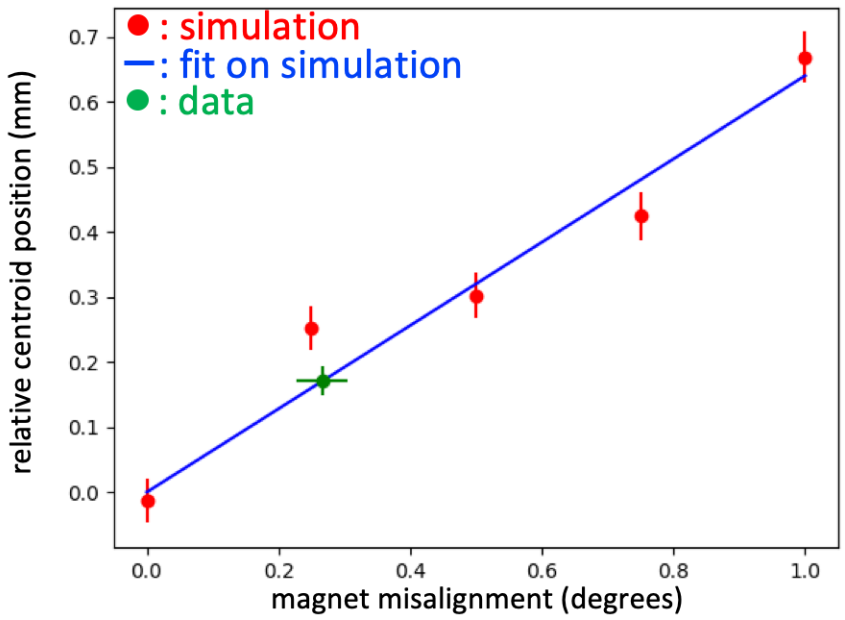

Figure 9.2: Magnetic field misalignment relative to the electric field, or to the axis of the decay chamber [156]. The x-axis represents the magnetic field tilt toward the Y-direction from the chamber axis (tilting in the YZ-plane). The y-axis represents the centroid position difference between the `HT_mainM1` and the `HT_mainM4` RCFs from Fig. 8.4 a). The red points come from the Geant4 simulation, and the blue line is fitted to these simulated points. The y-value of the green point comes from the data, while the x-value is obtained by placing the green point on the blue line. The error bar on the green point comes from the error of the fit. The result shows that our magnetic field misalignment is only 0.27±0.04°.

It is difficult to translate degrees in field misalignment to the systematics on the branching

ratios; what the misalignment affects is the uniformity assumption of the PSF (Sec. 8.1.1). However, this initial result shows that the misalignment is small. When we compared a simulation with a 0.3° tilt to one with no tilt, we could not obtain a measurable difference in their scan-deconvoluted branching ratios. Although we are working on a combined estimation that involves tilt toward both the Y- and the X-directions (Sec. 9.2.1), we believe that the field misalignment provide a negligible contribution to our systematics.

9.2 TRIMS Outlook

9.2.1 Upcoming Tasks

The following is a selected list of the analysis tasks that we plan to complete in the near future. The tasks are geared toward improving and understanding our systematics.

Data quality and deficit run handling:

Because we have the fuzzy runs, deficit runs, and excess runs in our data (Sec. 6.1.4), we would like a more systematic way to verify that our data are of good quality.

We already have a plan to trim out the unusable portions of the deficit runs (Fig. 6.7). This will help us improve the error from source activity-amplitude (Sec. 7.1.4) for left- and right-scan normalization (Sec. 7.4.1).

Polynomial fit to the 1eV2e ratios

Because the 1eV2e ratios are ill-defined at the far scan-positions (Fig. 7.23) and likely cause the to large `HT_massM1` RCF error in Fig. 8.1.2, we would like to fit the 1eV2e ratio versus the scan-position using a symmetric polynomial. The error of the far scan-position 1eV2e ratios should be significantly reduced using the fitted polynomial. Moreover, we can alway limit the fit range in a scan-position interval where the 1eV2e ratios have non-zero denominators.

Fiducial volume uniformity check in the simulation:

As mentioned in Sec. 8.2.3, in order to perform the FV correction, we assume the main-FV to be uniform. We would like to confirm this using the TRIMS Geant4 simulation.

Pre-scan-deconvolution systematics:

We are planning on implementing a new strategy to separate out the systematic contributions before we perform the scan-deconvolution (Sec. 9.1.1). The basic ideas are similar to that described in Sec. 7.3.5, where we increase a parameter by one sigma, see how the output changes, take the change as that parameter's error contributions, and add all the errors in quadrature to derive the overall systematics. The difference however, is that the output we are looking for are the final branching ratios. In other words, for each one sigma shift in the parameter, we perform the box-fitting and the scan-deconvolution, and calculate how the output branching ratios change.

This method would also help us handle the correlation errors of the scan-position independent parameter, e.g. charge-CC ratios, between scan-positions. This is because if a parameter p is scan-position independent, we apply the same p value at every scan-point, i.e on every RCF entry. Moreover, in the current scheme, we propagate the error of p at each scan-point separately, without accounting for p's correlation error between the scan-points. In the new method, we only change p by one sigma once to be applied at every scan-point, and so should account for the correlation.

Extra noise events:

There are two other types of events that we need to account for in order to correctly estimate our systematics, even though their contributions are small.

The first comes from band-No. a10) of Fig. 6.2. Recall that the DDFs are defined such that the event requires a coincidence when the beta is detected by the beta-detector (Sec. 8.1.2). In a band-No. a10) event however, the beta misses the beta-detector, which instead detects the

secondary electrons from the mesh. Therefore, we do not want to include the band-No. a10) events in our analysis. However, the band-No. a10) events also form a 3-finger band just like in Fig. 7.2, but with ion-TOF as the timing on the x-axis. Therefore, band-No. a10) has the right-finger band like band-No. c3) of Fig. 7.2. The band-No. a10) right-finger band overlaps with band-No. a1) and so needs to be removed. However, there is no simple way to isolate these right-finger events.

Another source of systematics comes from the ion-2WS events shown in the (ion-energy $< 40\,\mathrm{keV}$) region of Fig. 7.33. These events are the 1-ion events that have small-amplitude waveforms such that they are mis-identified as ion-2WS events. The ion-TOF for each of these events is therefore shifted to a large value because the second pulse timing is used to evaluate the ion-TOF instead. The ion-TOF shift corresponds to the shift in $\sqrt{M_m}$, causing unwanted leakage in mass-boxes. We will need a way to account for this type of events in our systematics as well.

T_2 purity over days:

Because we have a method to estimate the HT-purity of our data (Sec. 7.1.3), we can evaluate the T_2 purity of our T_2 source over the span of our one-year-long data-taking as well. The T_2 purity is not just affected by the tritium's decay half life, it is also affected by the interaction with the wall of the container cell that converts T_2 into HT.

Magnetic field tilt:

We would like to reevaluate the misalignment between the magnetic field and electric field in our system. As mentioned in Sec. 9.1.3, we will include the tilt in toward both the Y- and the X-directions.

9.2.2 Potential Analysis and Investigations

This final subsection covers a few analysis projections that we can potentially do with the TRIMS data, as well as investigations of some features that we see in the data.

Gaseous krypton secondary nuclear transition lifetime

We have only been using krypton-data for the time-zero correction (Sec. 6.1.2). However, based on the exponential tails in Fig. 6.1, we can potentially extract the lifetime of the 2^{nd} internal conversion transition for gaseous krypton.

Joule-Thomson cooler update

As mentioned in Sec. 2.5.3, we did not reach our original goal of $-40\,^{\circ}\text{C}$. There are quite a few things we can try out to prevent whistling and water frost, so there is potential for improvement.

Investigating feature in data

Some of the features that we see in the tritium-data are not completely resolved and worth deeper investigation:

- The cause of the gain instability of our detector setup (Sec. 5.2.3).

- The natures of the fuzzy-, deficit-, and excess-runs (Sec. 6.1.4). Handling them correctly may rescue some run-scans that we dropped and improve our statistics.

- The long trailing tail of the reconstructed ion mass peaks toward higher mass (see Fig. 7.28 and Fig. 7.29). The tail is more pronounced in M_m instead of $\sqrt{M_m}$. The timing resolution (Fig. 5.12) alone may not be able to explain the asymmetry.

- The mass-3 shoulder from Sec. 7.3.2, although Fig. 7.30 is convincing.

Hardware upgrade

Considering the potential hardware upgrade to the TRIMS experiment that can improve the accuracy of the branching ratio measurement, we would to give the following remarks. The detector energy resolution is as about as good as one can get from silicon diode detectors (they are limited by the intrinsic FET voltage noise Sec. 5.2.4), but these events can certainly still be improved via cooling. A stronger electric field can help improve the timing resolution by allowing a higher FV cut (Sec. 5.3.3, Sec. 6.2.3). Having better energy and timing resolution would make the data more localized in the CM-boxes than shown in Fig. 7.36. However, the current HV potential is also about as high as one can realistically get without breakdown with the NEC decay chamber under vacuum. Perhaps a longer decay chamber would help in this situation.

With proper hardware upgrades, we can skip the scan-deconvolution step in the data analysis. An obvious upgrade would be to increase the strength of the magnetic field to reduce the DDF width by reducing the gyroradii of the ions. It does requires more than superconducting coils to achieve a stronger magnetic field. A more effective upgrade would be to make the detection area of the ion-detector larger than that of the beta-detector. According to the definition of the DDF (Sec. 8.1.1), the DDF width would increase with the beta-detector detection area. Therefore, the idea is to fix the beta-detector size, and have the ion-detector size larger than the DDF width of all ion types. In this case, when the detectors are aligned, the ion-detector does not need to be scanned to capture all the possible coincidence events to the beta-detector.

With this outlook of the TRIMS experiment, we conclude this work.

9.3 Conclusion

The goal of the TRIMS experiment is to reexamine the branching ratio of the final state being a bound state after a tritium molecule beta decays, i.e. to determine the P_{bound} defined

in Sec. 1.5.3. From Table 9.2, we have,

$$P_{\text{bound}}(\text{T}_2) = P(^3\text{HeT}^+) = 50.3 \pm 1.5\%, \tag{9.1}$$

and from Table 9.1,

$$P_{\text{bound}}(\text{HT}) = P(^3\text{HeH}^+) = 56.3 \pm 1.3\%. \tag{9.2}$$

These results are consistent with the theoretical results shown in Table 1.1.

With these preliminary results, the TRIMS experiment resolves the 60-year mystery (Sec. 1.5.3). The results disagree with the past experiments from Snell and Wexler, even though the TRIMS experiment also covers the whole beta range. This indicates that there should be some systematics that the past experiments were not able to account for. Furthermore, the TRIMS P_{bound} results fall inside the range of the theoretical prediction. This validation using our data plays a fundamental role in determining neutrino mass from molecular tritium beta decay. Other observables measured by the TRIMS experiment can also help future advancement of the theory.

The preliminary results shown in this work should be close to the final TRIMS results, which will be established in the near future.

Appendix A

MISCELLANEOUS RUN INFORMATION

A.1 Tritium Runs

Run numbers for the runs that went into the final tritium analysis described in Sec. 6.1.4. These numbers are provided in code-friendly format. Recall from Sec. 4.2, that this list was generated as a part of the tritium data spreadsheet. The underscore means that the runs in between were not included, e.g. 2098_2100 mean run 2098 and 2100 are included in the analysis, while run 2099 was not. The dash means the runs in between were included, e.g. 2670-2680 means all runs 2670, 2671, 2672, 2673, 2674, 2675, 2676, 2677, 2678, 2679, and 2680 are included. The T2-runs and the HT-runs were identified separately and are provided as follows:

T2:

2084-2098_2100_2118-2129_2155_2157_2159_2161_2163_2165_2167_2169_2171_2173-2174_2176_2178_2180_2182-2183_2359-2384_2696-2717_2719-2729_2765-2786_2788-2809_2811-2832_2834-2855_2886-2896_3000-3010_3048-3069_3082-3103_3116-3137_3139-3149_3151-3161_3163-3173_3185-3195_3197-3229_3231-3252_3438-3444_3446-3460_

HT:

2258-2271_2275-2287_2292-2304_2308-2324_2329-2341_2345-2357_2397-2407_2411-2421_2467-2477_2481-2491_2553-2560_2562_2564-2565_2569-2579_2584-2594_2598-2608_2613-2623_2627-2637_2670-2680_2860-2870_2874-2884_2942-2952_2956-2966_2971-2981_3258-3268_3276-3286_3305-3315_3334-3344_3350-3360_3364-3374_3379-3389_3411-3421_3425-3435_3465-3475_3479-3489_3494-3504_3508-3518_

A.2 Fuzzy Runs

The specific run numbers for the fuzzy runs are:

2543, 2546, 2664, 2736, 2901, 2918, 2922, 2932, 2993, 3016, 3020, 3027, 3042, 3073, 3075, 3107, 3111, 3180, 3293, 3330, 3393, 3345.

Run 3559 was identified as an odd run; the run had an order of magnitude more coincidence events than other runs at the same ion-detector position of (0.225 in, 80 mm). In fact, 3537-3547 and 3551-3561 were dropped because they had intense `m6` signatures for HT-runs.

A.3 Deficit Runs

The first type of the deficit runs are associated with the run time being shorter than the standard SI300s = 5 min. Run 2573 has 230 s and run 2977 has 120 s.

The main type of the deficit runs described in Sec. 6.1.4 is heuristically separated into two categories. The deficit runs with severe degradations are:

2256, 2257, 2259, 2261, 2263, 2266, 2696, 2697, 2698, 2700, 2721, 2723, 2724, 2725, 2850, 2853, 2854, 2963, 2965, 3064, 3066, 3348, 3349, 3353, 3354, 3355.

And the deficit runs that would likely induce negligible impact are:

2381, 2835, 2838, 2858, 2870, 2887, 2888, 2979, 3001, 3010, 3050, 3051, 3055, 3057, 3267, 3268.

This runs are manually identified by inspecting Fig. 6.7 for all the runs.

A.4 Excess Runs

The suspected excess runs are:

3066, 3209, 3210, 3284, 3516

This runs are manually identified by inspecting Fig. 6.8 for all the runs.

Appendix B

DATA REFERENCE

B.1 Reference for Energy Correction

It turns out in order to identify the "clean" H^+ band in our data for the dead layer correction (Sec. 3.2.2), it requires information across several sections. Figure. B.1 is a version of Fig. 6.2 in Sec. 6.1.3 without the corrections from Sec. 6.1.2; the x-axis is the ion TOF given by Eq. 6.1 and y-axis is the ion detected energy `ion_edep` from Table 5.4.

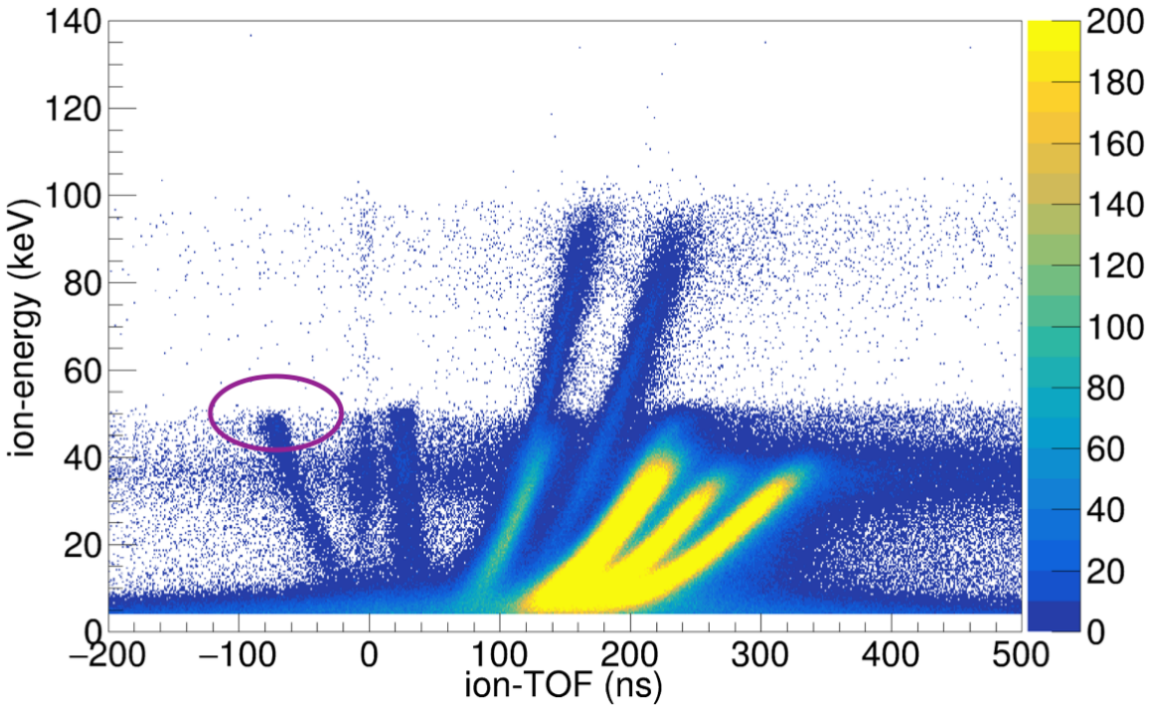

Figure B.1: Uncorrected ion-energy versus ion-TOF histogram for the raw-T2-data.

The maximum of the clean H^+ band is circled in purple at 50 keV, where the uncertainty

of 2 keV is a conservative estimation based on visual inspection. The question is then, how can we tell this band belongs to H^+? The band is labeled by band-No. a10) according to Table 6.3 with another band. They are in fact corresponding to the beta2WS band-No. c1) and c2) in Fig. 7.1, but in cases when the betas actually miss the beta-detector. And according to Table 7.1, the band circled in purple is indeed the H^+ band we are looking for.

Appendix C

DERIVATIONS

C.1 Three-Gaussian Error

Consider that we want to fit a distribution using sums of gaussians and determine the area ratio of the distribution inside certain interval. Let R be the ratio of this multiple gaussian shape in range ($-\infty$, X) over the entire range ($-\infty$, ∞). For a single gaussian, the amplitude of the gaussian gets canceled out,

$$R(X) = \frac{1}{\sigma\sqrt{2\pi}} \int_{-\infty}^{X} \exp\left[-\frac{1}{2}\left(\frac{x-\mu}{\sigma}\right)^2\right] dx. \tag{C.1}$$

But for K gaussians we have,

$$R(X) = \frac{1}{\sum_k^K A_k} \sum_k^K \frac{A_k}{\sigma_k\sqrt{2\pi}} \int_{-\infty}^{X} \exp -\frac{1}{2}\left(\frac{x-\mu_k}{\sigma_k}\right)^2 dx. \tag{C.2}$$

Define,

$$z_k = \frac{x-\mu_k}{\sigma_k\sqrt{2}}, \tag{C.3}$$

$$dx = dz_k\sigma_k\sqrt{2}, \tag{C.4}$$

$$Z_k = \frac{X-\mu_k}{\sigma_k\sqrt{2}}, \tag{C.5}$$

then we can define the area function I,

$$R(X) = \frac{1}{\sqrt{\pi}\sum A_k} \sum A_k \int_{-\infty}^{Z_k} \exp\left(-z_k^2\right) dz_k \tag{C.6}$$

$$\equiv \frac{1}{\sum A_k} \sum A_k I(Z_k). \tag{C.7}$$

The function I can be thought of as the cumulative distribution function/complementary error function of a standard gaussian. With this formula, if we want the ratio within any

range [X, Y], it can be calculated by,

$$R(Y) - R(X) = \frac{1}{\sum A_k} \sum A_k [I(Z_k(Y)) - I(Z_k(X))]. \tag{C.8}$$

If we wish to fit a distribution with the multiple gaussians, we need the partial derivatives with respect to each of the fit parameters to properly propagate errors on $R(X)$:

$$\begin{aligned}
\frac{\partial c}{\partial A_k} &= \frac{(\sum A) - A_k}{(\sum A)^2} I(Z_k) && \text{(C.9)} \\
\frac{\partial c}{\partial \mu_k} &= \frac{A_k}{\sum A} \frac{\partial Z_k}{\partial \mu_k} \frac{\partial I(Z_k)}{\partial Z_k} && \text{(C.10)} \\
&= -\frac{A_k}{\sum A} \frac{\exp(-Z_k^2)}{\sigma_k \sqrt{2\pi}} && \text{(C.11)} \\
\frac{\partial c}{\partial \sigma_k} &= \frac{A_k}{\sum A} \frac{\partial Z_k}{\partial \sigma_k} \frac{\partial I(Z_k)}{\partial Z_k} && \text{(C.12)} \\
&= -\frac{A_k}{\sum A} \frac{X - \mu_k}{\sigma_k^2 \sqrt{2\pi}} \exp(-Z_k^2) && \text{(C.13)}
\end{aligned}$$

With products of these partial derivatives the variances and covariances from the fits may be used to determine the error of the $R(X)$.

In practice, we used three gaussians (A, μ, σ), (A_2, μ_2, σ_2), (A_3, μ_3, σ_3) to fit each mass peak, such that they are related in the following way,

$$\begin{aligned}
A_2 &= a_2 A && \text{(C.14)} \\
\mu_2 &= \mu + b_2 \sigma && \text{(C.15)} \\
\sigma_2 &= c_2 \sigma && \text{(C.16)} \\
A_3 &= a_3 A_2 = a_3 a_2 A && \text{(C.17)} \\
\mu_3 &= \mu_2 + b_3 \sigma_2 = \mu + b_2 \sigma + b_3 c_2 \sigma && \text{(C.18)} \\
\sigma_3 &= c_3 \sigma_2 = c_3 c_2 \sigma, && \text{(C.19)}
\end{aligned}$$

where a_2, b_2, c_2, a_3, b_3, and c_3 are fit parameters shared by all the mass peaks in the fit.

Therefore, we can define the R in Eq. C.13 in the following way,

$$R(x) = \frac{AI\left(\frac{x-\mu}{\sigma\sqrt{2}}\right) + a_2 AI\left(\frac{x-(\mu+b_2\sigma)}{c_2\sigma\sqrt{2}}\right) + a_3a_2AI\left(\frac{x-(\mu+b_2\sigma+b_3c_2\sigma)}{c_3c_2\sigma\sqrt{2}}\right)}{A + a_2A + a_3a_2A} \tag{C.20}$$

$$= \frac{I\left(\frac{x-\mu}{\sigma\sqrt{2}}\right) + a_2 I\left(\frac{x-\mu-b_2\sigma}{c_2\sigma\sqrt{2}}\right) + a_2a_3I\left(\frac{x-\mu-(b_2+b_3c_2)\sigma}{c_2c_3\sigma\sqrt{2}}\right)}{1 + a_2(1+a_3)} \tag{C.21}$$

$$\equiv \frac{I(Z_1) + a_2 I(Z_2) + a_3a_2I(Z_3)}{1 + a_2(1+a_3)}. \tag{C.22}$$

The partial derivatives of the fit parameters for each peak are then given by,

$$\frac{\partial R(x)}{\partial A} = 0 \tag{C.23}$$

$$\frac{\partial R(x)}{\partial \mu} = \frac{\frac{\partial Z_1}{\partial \mu}\frac{\partial I(Z_1)}{\partial Z_1} + a_2\frac{\partial Z_2}{\partial \mu}\frac{\partial I(Z_2)}{\partial Z_2} + a_2a_3\frac{\partial Z_3}{\partial \mu}\frac{\partial I(Z_3)}{\partial Z_3}}{1 + a_2(1+a_3)} \tag{C.24}$$

$$= \frac{\frac{-1}{\sigma\sqrt{2}}\frac{\exp\left(-Z_1^2\right)}{\sqrt{\pi}} + a_2\frac{-1}{c_2\sigma\sqrt{2}}\frac{\exp\left(-Z_2^2\right)}{\sqrt{\pi}} + a_2a_3\frac{-1}{c_2c_3\sigma\sqrt{2}}\frac{\exp\left(-Z_3^2\right)}{\sqrt{\pi}}}{1 + a_2(1+a_3)} \tag{C.25}$$

$$= -\frac{\exp\left(-Z_1^2\right) + \frac{a_2}{c2}\exp\left(-Z_2^2\right) + \frac{a_2a_3}{c_2c_3}\exp\left(-Z_3^2\right)}{\sigma\sqrt{2\pi}(1 + a_2(1+a_3))} \tag{C.26}$$

$$\frac{\partial R(x)}{\partial \sigma} = \frac{\frac{\partial Z_1}{\partial \sigma}\frac{\partial I(Z_1)}{\partial Z_1} + a_2\frac{\partial Z_2}{\partial \sigma}\frac{\partial I(Z_2)}{\partial Z_2} + a_2a_3\frac{\partial Z_3}{\partial \sigma}\frac{\partial I(Z_3)}{\partial Z_3}}{1 + a_2(1+a_3)} \tag{C.27}$$

$$= \frac{\frac{-Z_1}{\sigma}\exp\left(-Z_1^2\right) + a_2\frac{-Z_1}{c_2\sigma}\exp\left(-Z_2^2\right) + a_2a_3\frac{-Z_1}{c_2c_3\sigma}\exp\left(-Z_3^2\right)}{\sqrt{\pi}(1 + a_2(1+a_3))} \tag{C.28}$$

$$= -\frac{Z_1\left(\exp\left(-Z_1^2\right) + \frac{a_2}{c_2}\exp\left(-Z_2^2\right) + \frac{a_2a_3}{c_2c_3}\exp\left(-Z_3^2\right)\right)}{\sigma\sqrt{\pi}(1 + a_2(1+a_3))} \tag{C.29}$$

$$\frac{\partial R(x)}{\partial a_2} = -\frac{(1+a_3)(I(Z_1)+a_2I(Z_2)+a_3a_2I(Z_3))}{(1+a_2(1+a_3))^2} + \frac{I(Z_2)+a_3I(Z_3)}{1+a_2(1+a_3)} \quad \text{(C.30)}$$

$$= \frac{-(1+a_3)I(Z_1)+I(Z_2)+a_3I(Z_3)}{(1+a_2(1+a_3))^2} \quad \text{(C.31)}$$

$$\frac{\partial R(x)}{\partial b_2} = \frac{\cancel{\frac{\partial Z_1}{\partial b_2}}\frac{\partial I(Z_1)}{\partial Z_1} + a_2\frac{\partial Z_2}{\partial b_2}\frac{\partial I(Z_2)}{\partial Z_2} + a_2a_3\frac{\partial Z_3}{\partial b_2}\frac{\partial I(Z_3)}{\partial Z_3}}{1+a_2(1+a_3)} \quad \text{(C.32)}$$

$$= \frac{a_2\frac{-1}{c_2\sqrt{2}}\exp(-Z_2^2) + a_2a_3\frac{-1}{c_2c_3\sqrt{2}}\exp(-Z_3^2)}{\sqrt{\pi}(1+a_2(1+a_3))} \quad \text{(C.33)}$$

$$= -\frac{\frac{a_2}{c_2}\exp(-Z_2^2) + \frac{a_2a_3}{c_2c_3}\exp(-Z_3^2)}{\sqrt{2\pi}(1+a_2(1+a_3))} \quad \text{(C.34)}$$

$$\frac{\partial R(x)}{\partial c_2} = \frac{\cancel{\frac{\partial Z_1}{\partial c_2}}\frac{\partial I(Z_1)}{\partial Z_1} + a_2\frac{\partial Z_2}{\partial c_2}\frac{\partial I(Z_2)}{\partial Z_2} + a_2a_3\frac{\partial Z_3}{\partial c_2}\frac{\partial I(Z_3)}{\partial Z_3}}{1+a_2(1+a_3)} \quad \text{(C.35)}$$

$$= \frac{a_2\frac{\partial Z_2}{\partial c_2}\exp(-Z_2^2) + a_2a_3\frac{\partial}{\partial c_2}\left(\frac{x-\mu-b_2\sigma}{c_2c_3\sigma\sqrt{2}} + \frac{\cancel{-b_3c_2\sigma}}{c_3\sqrt{2}\cancel{c_2\sigma}}\right)\exp(-Z_3^2)}{\sqrt{\pi}(1+a_2(1+a_3))} \quad \text{(C.36)}$$

$$= \frac{a_2\frac{-Z_2}{c_2}\exp(-Z_2^2) + \frac{a_2a_3}{c_3}\frac{\partial}{\partial c_2}\left(Z_2 + \frac{-b_3}{\sqrt{2}}\right)\exp(-Z_3^2)}{\sqrt{\pi}(1+a_2(1+a_3))} \quad \text{(C.37)}$$

$$= -\frac{Z_2\left(\frac{a_2}{c_2}\exp(-Z_2^2) + \frac{a_2a_3}{c_2c_3}\exp(-Z_3^2)\right)}{\sqrt{\pi}(1+a_2(1+a_3))} \quad \text{(C.38)}$$

$$\frac{\partial R(x)}{\partial a_3} = -\frac{a_2\Big(I(Z_1)+a_2I(Z_2)+a_3a_2I(Z_3)\Big)}{(1+a_2(1+a_3))^2}+\frac{a_2I(Z_3)}{1+a_2(1+a_3)} \tag{C.39}$$

$$= -\frac{a_2\Big(I(Z_1)+a_2I(Z_2)-(1+a_2)I(Z_3)\Big)}{(1+a_2(1+a_3))^2} \tag{C.40}$$

$$\frac{\partial R(x)}{\partial b_3} = \frac{\cancel{\frac{\partial Z_1}{\partial b_3}}\frac{\partial I(Z_1)}{\partial Z_1}+a_2\cancel{\frac{\partial Z_2}{\partial b_3}}\frac{\partial I(Z_2)}{\partial Z_2}+a_2a_3\frac{\partial Z_3}{\partial b_3}\frac{\partial I(Z_3)}{\partial Z_3}}{1+a_2(1+a_3)} \tag{C.41}$$

$$= \frac{a_2a_3\frac{-\cancel{c_2}\sigma}{c_3\sqrt{2}\cancel{c_2}\sigma}\exp\left(-Z_3^2\right)}{\sqrt{\pi}(1+a_2(1+a_3))} \tag{C.42}$$

$$= -\frac{a_2a_3\exp\left(-Z_3^2\right)}{c_3\sqrt{2\pi}(1+a_2(1+a_3))} \tag{C.43}$$

$$\frac{\partial R(x)}{\partial c_3} = \frac{\cancel{\frac{\partial Z_1}{\partial c_3}}\frac{\partial I(Z_1)}{\partial Z_1}+a_2\cancel{\frac{\partial Z_2}{\partial c_3}}\frac{\partial I(Z_2)}{\partial Z_2}+a_2a_3\frac{\partial Z_3}{\partial c_3}\frac{\partial I(Z_3)}{\partial Z_3}}{1+a_2(1+a_3)} \tag{C.44}$$

$$= -\frac{a_2a_3Z_3\exp\left(-Z_3^2\right)}{c_3\sqrt{\pi}(1+a_2(1+a_3))}. \tag{C.45}$$

A caveat is that the derivation shown so far uses the normalized gaussians that have a prefactor $\frac{1}{\sigma\sqrt{2\pi}}$. The default gaussian function in ROOT is not normalized and that is used in the analysis code. All the partial derivatives in the actual implementations are different than shown in this section, although they follow the same derivation.

C.2 Derivation of Generalized Least Squares Estimator

Consider we with to solve x in the equation using the generalized (weighted) least squares method,

$$Ax+\epsilon=b, \tag{C.46}$$

where b is the data m-vector, x is the signal/target n-vector, and A is the response/convolution $m\times n$ matrix. The ϵ is the error m-vector that accounts for the finite resolution in term of data taking.

In order to incorporate the weight, consider W as the $m\times m$ weight matrix. For our

purpose, W is a diagonal matrix, and,

$$\sqrt{W} \equiv \text{diag}(\sqrt{w_1}, \sqrt{w_2}, ..., \sqrt{w_m}) = \text{diag}\left(\frac{1}{\sigma_1}, \frac{1}{\sigma_2}, ..., \frac{1}{\sigma_m}\right), \tag{C.47}$$

where σ_i is the standard deviation assigned to data b_i. Suppose now we wish to estimate x using estimator $\hat{x}$, which gives the estimated error function,

$$\hat{\epsilon} \equiv b - \hat{b}, \text{ where } \hat{b} \equiv A\hat{x}. \tag{C.48}$$

Then to use the least squares method, consider the residual sums of squares (RSS) with weight is given by,

$$\begin{aligned} RSS(\hat{x}) &\equiv \sum_{i=0}^{m-1} [\sqrt{w_i}\hat{\epsilon_i}]^2 \\ &= \sum_{i=0}^{m-1} \left[\sqrt{w_i}\left(b_i - \hat{b}_i\right)\right]^2 \\ &= \sum_{i=0}^{m-1} [\sqrt{w_i}\,(b_i - (A\hat{x})_i)]^2 \\ &= (b - A\hat{x})^T W (b - A\hat{x}) \\ &= b^T W b - b^T W A\hat{x} - \hat{x}^T A^T W b + \hat{x}^T A^T W A\hat{x}, \end{aligned} \tag{C.49}$$

and so setting $\partial RSS(\hat{x})/\partial\hat{x} = 0$ gives,

$$\begin{aligned} \frac{\partial RSS(\hat{x})}{\partial\hat{x}} = 0 \quad &= -b^T W A - \left(\frac{\partial A\hat{x}}{\partial\hat{x}}\right)^T W b + \left(\frac{\partial A\hat{x}}{\partial\hat{x}}\right)^T W A\hat{x} + \hat{x}^T A^T W A \\ &= -b^T W A - A^T W b + A^T W A\hat{x} + \hat{x}^T A^T W A \\ &= -2A^T W b + 2A^T W A\hat{x}, \end{aligned} \tag{C.50}$$

where the first equation is true because gradient and transpose commute, while the last equation follows because the transpose of a scalar is still a scalar. And so, the estimate of x is,

$$\boxed{\begin{aligned} \hat{x} &= \left(A^T W A\right)^{-1} A^T W b \\ &= \left(B^T B\right)^{-1} B^T \sqrt{W} b, \quad B \equiv \sqrt{W} A. \end{aligned}} \tag{C.51}$$

The expectation value (vector) of the estimator is,

$$\begin{aligned} E[\hat{x}] &= \left(A^T W A\right)^{-1} A^T W E[b] \\ &= \left(A^T W A\right)^{-1} A^T W E[Ax] + \left(A^T W A\right)^{-1} A^T W E[\epsilon]. \\ &= \left(A^T W A\right)^{-1} A^T W A x \\ &= x, \end{aligned} \tag{C.52}$$

if we assume the error function is unbiased, i.e. $E[\epsilon] = 0$. Note that the third equation follows from that Ax is a constant. The result of $E[\hat{x}] = x$ means that $\hat{x}$ is also unbiased, which is a property we'd like to have.

The variance (covariance matrix) of the estimator is *,

$$\begin{aligned} V(\hat{x}) &= E\left[(\hat{x} - E[\hat{x}])(\hat{x} - E[\hat{x}])^T\right] \\ &= E\left[(\hat{x} - x)(\hat{x} - x)^T\right] \\ &= E\left[\hat{x}\hat{x}^T - x\hat{x}^T - \hat{x}x^T + xx^T\right] \\ &= E\left[\hat{x}\hat{x}^T - x\hat{x}^T\right] - \cancel{E[\hat{x}]x^T - xx^T} \\ &= E\left[\left(A^T W A\right)^{-1} A^T W A x\hat{x}^T + \left(A^T W A\right)^{-1} A^T W \epsilon\hat{x}^T - x\hat{x}^T\right] \\ &= E\left[\cancel{x\hat{x}^T - x\hat{x}^T} + \left(A^T W A\right)^{-1} A^T W \epsilon(Ax + \epsilon)^T \left(\left(A^T W A\right)^{-1} A^T W\right)^T\right] \\ &= \left(A^T W A\right)^{-1} A^T W \cancel{E[\epsilon]}^{0} (Ax)^T \left(\left(A^T W A\right)^{-1} A^T W\right)^T \\ &+ E\left[\left(A^T W A\right)^{-1} A^T W \epsilon\epsilon^T \left(\left(A^T W A\right)^{-1} A^T W\right)^T\right] \\ &= E\left[A^{-1}\cancel{\left(A^T W\right)^{-1} A^T W} \epsilon\epsilon^T \left(A^{-1}\cancel{\left(A^T W\right)^{-1} A^T W}\right)^T\right] \\ &= E\left[A^{-1}\epsilon\epsilon^T (A^T)^{-1}\right]. \\ &= E\left[\left(A^T(\epsilon\epsilon^T)^{-1}A\right)^{-1}\right]. \end{aligned} \tag{C.53}$$

Now if we assume the error function to be $\epsilon = (\sigma_1, \sigma_2, ..., \sigma_m)$ and assume the sigmas are

*The transpose on the right-hand side is necessary for the term in the expectation value to be a matrix.

uncorrelated, i.e. $E(\sigma_i \sigma_j) = 0$ if $i \neq j$, then $W = E\left[(\epsilon\epsilon^T)^{-1}\right]$, and so

$$\boxed{\begin{aligned} V(\hat{x}) &= \left(A^T W A\right)^{-1} \\ &= \left(B^T B\right)^{-1}, \end{aligned}} \tag{C.54}$$

which will give the standard error of the estimator $\hat{x}$.

BIBLIOGRAPHY

[1] J. Chadwick. "Intensitätsverteilung im magnetischen Spectrum der β-Strahlen von radium B + C". *Verhandl. Dtsch. Phys.* 16 (1914), p. 383.

[2] W. Pauli. "Rapports du Septième Conseil de Physique Solvay, Brussels" (1933).

[3] W. Pauli. "A letter to a local meeting on radioactivity at Tübingen" (1930).

[4] F. Reines and C. Cowan. "The Reines-Cowan Experiments: Detecting the Poltergeist". *Los Alamos science* 25 (1997), p. 4.

[5] E. Fermi. "Versuch einer Theorie der β-Strahlen. I". *Zeitschrift für Physik* 88.3-4 (1934), p. 161.

[6] C. L. Cowan et al. "Detection of the Free Neutrino - a Confirmation". *Science* 124.3212 (1956), p. 103.

[7] C. S. Wu et al. "Experimental Test of Parity Conservation in Beta Decay". *Physical Review* 105.4 (1957), p. 1413.

[8] T. D. Lee and C. N. Yang. "Question of Parity Conservation in Weak Interactions". *Physical Review* 104.1 (1956), p. 229.

[9] M. Goldhaber, L. Grodzins, and A. W. Sunyar. "Helicity of Neutrinos". *Physical Review* 109.3 (1958), p. 1015.

[10] G Danby et al. "Observation of High-Energy Neutrino Reactions and the Existence of Two Kinds of Neutrinos". *Physical Review Letters* 9.1 (1962), p. 36.

[11] M. L. Perl et al. "Evidence for Anomalous Lepton Production in $e^+ - e^-$ Annihilation". *Physical Review Letters* 35.22 (1975), p. 1489.

[12] DONUT Collaboration. "Observation of tau neutrino interactions". *Physics Letters B* 504.3 (2001), p. 218.

[13] A. S. Eddington. "The Internal Constitution of the Stars". *The Scientific Monthly* 11.4 (1920), p. 297.

[14] H. A. Bethe. "Energy Production in Stars". *Physical Review* 55 (1939), p. 434.

[15] J. N. Bahcall, A. M. Serenelli, and S. Basu. "New Solar Opacities, Abundances, Helioseismology, and Neutrino Fluxes". *The Astrophysical Journal Letters* 621 (2005), p. L85.

[16] J. N. Bahcall et al. "Solar Neutrino Flux". *Astrophysical Journal* 137 (1963), p. 344.

[17] J. N. Bahcall and N. A. Bahcall. "Present Status of the Theoretical Predictions for the ^{36}Cl Solar-Neutrino Experiment". *Physical Review Letters* 20 (1968), p. 1209.

[18] V. Gribov and B. Pontecorvo. "Neutrino astronomy and lepton charge". *Physics Letters B* 28.7 (1969), p. 493.

[19] K. A. Olive et al. "Review of Particle Physics". *Chin. Phys. C* 38 (2014), p. 090001. DOI: 10.1088/1674-1137/38/9/090001.

[20] Particle Data Group. *11. THE CKM QUARK-MIXING MATRIX*. 2012. URL: http://pdg.lbl.gov/2013/reviews/rpp2012-rev-ckm-matrix.pdf.

[21] D. Griffith. *Introduction to Elementary Particles*. 2nd ed. WILEY-VCH, 2008, p. 390.

[22] B. Kayser. "Neutrino Oscillation Physics". *arXiv:1206.4325* (2012).

[23] Super-Kamiokande Collaboration. "Constraints on Neutrino Oscillations Using 1258 Days of Super-Kamiokande Solar Neutrino Data". *Physical Review Letters* 86.25 (2001), p. 5656.

[24] SNO Collaboration. "Measurement of the Rate of $\nu_e + d \rightarrow p + p + e^-$ Interactions Produced by ^8B Solar Neutrinos at the Sudbury Neutrino Observatory". *Physical Review Letters* 87.7 (2001), p. 071301.

[25] Jr. R. Davis, D. S. Harmer, and Kenneth C. Hoffman. "Search for Neutrinos from the Sun". *Physical Review Letters* 20.21 (1968), p. 1205.

[26] A.B. Balantekin and W.C. Haxton. "Neutrino oscillations". *Progress in Particle and Nuclear Physics* 71 (2013), p. 150.

[27] Super-Kamiokande Collaboration. "Evidence for Oscillation of Atmospheric Neutrinos". *Physical Review Letters* 81.8 (1998), p. 1562.

[28] MACRO collaboration. "Measurement of the atmospheric neutrino-induced upgoing muon flux using MACRO". *Physics Letters B* 434.3-4 (1998), p. 451.

[29] W. W. M. Allison et al. "The atmospheric neutrino flavor ratio from a 3.9 fiducial kiloton-year exposure of Soudan 2". *Physics Letters B* 449.1-2 (1999), p. 137.

[30] Double Chooz Collaboration. "Indication of Reactor $\bar{\nu}_e$ Disappearance in the Double Chooz Experiment". *Physical Review Letters* 108 (2012), p. 131801.

[31] RENO Collaboration. "Observation of Reactor Electron Antineutrinos Disappearance in the RENO Experiment". *Physical Review Letters* 108 (2012), p. 191802.

[32] Daya Bay Collaboration. "Spectral Measurement of Electron Antineutrino Oscillation Amplitude and Frequency at Daya Bay". *Physical Review Letters* 112 (2014), p. 061801.

[33] KamLAND Collaboration. "Constraints on θ_{13} from a three-flavor oscillation analysis of reactor antineutrinos at KamLAND". *Physical Review D* 83 (2011), p. 052002.

[34] K2K Collaboration. "Measurement of neutrino oscillation by the K2K experiment". *Physical Review D* 74 (2006), p. 072003.

[35] MINOS Collaboration. "Search for Muon-Neutrino to Electron-Neutrino Transitions in MINOS". *Physical Review Letters* 103 (2009), p. 261802.

[36] R.Acciarri et al. "Long-Baseline Neutrino Facility (LBNF) and Deep Underground Neutrino Experiment (DUNE) Conceptual Design Report, Volume 4 The DUNE Detectors at LBNF". *arXiv:1601.02984* (2016).

[37] I. Esteban et al. "Updated fit to three neutrino mixing: exploring the accelerator-reactor complementarity". *Springer JHEP* 1 (2017), p. 087.

[38] R. D. Klauber. *Student Friendly Quantum Field Theory*. 2nd ed. Sandtrove Press, 2013.

[39] S. Riemer-Sørensen and D. Parkinson and T. M. Davis. "Combining Planck data with large scale structure information gives a strong neutrino mass constraint". *Physical Review D* 89 (2014), p. 103505.

[40] K. Langanke, G. Martinez-Pinedo, and A. Sieverding. "Neutrino nucleosynthesis: An overview". *arXiv:1901.03741* (2019).

[41] R. G. H. Robertson. *Plot Origin*. rghr@u.washington.edu.

[42] Hyper-Kamiokande Proto-Collaboration. "Physics potential of a long-baseline neutrino oscillation experiment using a J-PARC neutrino beam and Hyper-Kamiokande". *Progress of Theoretical and Experimental Physics* 2015 (2015), p. 053C02. DOI: 10.1093/ptep/ptv061.

[43] Hirata et al. "Observation in the Kamiokande-II detector of the neutrino burst from supernova SN1987A". *Physical Review D* 38.2 (1988), p. 448.

[44] R. M. Bionta et al. "Observation of a neutrino burst in coincidence with supernova 1987A in the Large Magellanic Cloud". *World Scientific* (1991).

[45] E. N. Alexeyev et al. "Detection of the neutrino signal from SN 1987A in the LMC using the INR Baksan underground scintillation telescope". *Nuclear Physics B* 205 (1988), p. 209.

[46] W. D. Arnett and J. L. Rosner. "Neutrino Mass Limits from SN1987A". *Physical Review Letters* 58.18 (1987), p. 1906.

[47] Planck Collaboration. "Planck 2013 results. I. Overview of products and scientific results". *arXiv:1303.5062v2* (2013).

[48] D. J. Eisenstein. "Detection of the Baryon Acoustic Peak in the Large-Scale Correlation Function of SDSS Luminous Red Galaxies". *The Astrophysical Journal* 633.2 (2005), p. 560.

[49] S. R. Elliott, A. A. Hahn, and M. K. Moe. "Direct evidence for two-neutrino double-beta decay in ^{82}Se". *Physical Review Letter* 59.18 (1987), p. 2020.

[50] J. Schechter and J. W. F. Valle. "Neutrinoless double-β decay in SU(2)×U(1) theories". *Physical Review D* 25.11 (1982), p. 2951.

[51] C. Giunti and C. Kim. *Fundamentals of Neutrino Physics and Astrophysics*. Oxford University Press, 2007.

[52] S. M. Bilenky et al. "Constraints from neutrino oscillation experiments on the effective Majorana mass in neutrinoless double β-decay". *Physical Letters B* 465 (1999), p. 193.

[53] MAJORANA Collaboration. "The MAJORANA DEMONSTRATOR Neutrinoless Double-Beta Decay Experiment". *Advances in High Energy Physics* 2014.365432 (2014). DOI: 10.1155/2014/365432.

[54] GERDA Collaboration. "Probing Majorana neutrinos with double-β decay". *Science* 365.6460 (2019), p. 1445. DOI: 10.1126/science.aav8613.

[55] EXO-200 Collaboration. "Search for Majorana neutrinos with the first two years of EXO-200 data". *Nature* 510 (2014), p. 229.

[56] KamLAND-Zen Collaboration. "Search for Majorana Neutrinos Near the Inverted Mass Hierarchy Region with KamLAND-Zen". *Physical Review Letters* 117 (2016), p. 082503.

[57] CUORE Collaboration. "The projected background for the CUORE experiment". *Eur. Phys. J. C* 77 (2017), p. 543. DOI: 10.1140/epjc/s10052-017-5080-6.

[58] SuperNEMO Collaboration. "Probing new physics models of neutrinoless double beta decay with SuperNEMO". *The European Physical Journal C* 40.4 (2010), p. 927.

[59] MAJORANA Collaboration. "A Search for Neutrinoless Double-Beta Decay in ^{76}Ge with 26 kg-yr of Exposure from the MAJORANA DEMONSTRATOR". *arXiv:1902.02299* (2019).

[60] EXO-200 Collaboration. "Search for Neutrinoless Double-Beta Decay with the Complete EXO-200 Dataset". *arXiv:1906.02723* (2019).

[61] CUORE Collaboration. "First Results from CUORE: A Search for Lepton Number Violation via $0\nu\beta\beta$ Decay of ^{130}Te". *Physical Review Letters* 120.132501 (2018).

[62] J. E. Purcell and C. G. Sheu. "Nuclear Data Sheets for A = 3". *Nuclear Data Sheets* 130 (2015), p. 3.

[63] S. C. Curran, J. Angus, and A. L. Cockcroft. "Beta Spectrum of Tritium". *Nature* 162 (1948), p. 302.

[64] D. R. Hamilton and L. Gross. "An Electrostatic Beta-Spectrograph". *Review of Scientific Instruments* 21 (1950), p. 912.

[65] D. R. Hamilton, W. P. Alford, and L. Gross. "Upper Limits on the Neutrino Mass from the Tritium Beta Spectrum". *Physical Review* 92.6 (1953), p. 1521.

[66] K-E Bergkvist. "A high-luminosity, high-resolution study of the end-point behaviour of the tritium β-spectrum (I). basic experimental procedure and analysis with regard to neutrino mass and neutrino degeneracy". *Nuclear Physics B* 39 (1972), p. 317.

[67] K-E Bergkvist. "A high-luminosity, high-resolution study of the end-point behaviour of the tritium β-spectrum (II). The end-point energy of the spectrum. comparison of the experimental axial-vector matrix element with predictions based on PCAC". *Nuclear Physics B* 39 (1972), p. 371.

[68] V.A.Lubimov et al. "An estimate of the ν_e mass from the β-spectrum of tritium in the valine molecule". *Nuclear Physics B* 28 (1980), p. 266.

[69] T. A. Claxton, S. Schafroth, and P. F. Meier. "Molecular final states after β decay of tritium-substituted molecules". *Physical Review A* 45.9 (1991), p. 6209.

[70] E. Holzschuh, M. Fritschi, and W.Kündig. "Measurement of the electron neutrino mass from tritium β-decay". *Physics Letters B* 287 (1992), p. 381.

[71] R. G. H. Robertson et al. "Limit on ν_e^- mass from observation of the β decay of molecular tritium". *Physical Review Letters* 67.8 (1991), p. 957.

[72] W. Stoeffl and D. J. Decman. "Anomalous Structure in the Beta Decay of Gaseous Molecular Tritium". *Physical Review Letter* 75.18 (1995), p. 3237.

[73] R. S Van Dyck, D. L. Farnham Jr., and P. B. Schwinberg. "Tritium-helium-3 mass difference using the Penning trap mass spectroscopy". *Physical Review Letters* 70.19 (1993), p. 2888.

[74] Sz. Nagy et al. "On the Q-value of the tritium β-decay". *Europhysics Letters* 74 (2006), p. 404.

[75] H. Kawakami et al. "New upper bound on the electron anti-neutrino mass". *Physics Letters B* 256.1 (1991), p. 105.

[76] H. C. Sun, D. Q. Liang, and S. P. Chen. "An upper limit for the electron anti-neutrino mass". *Chinese Journal of Nuclear Physics* 15.3 (1993), p. 261.

[77] Ch. Kraus et al. "Final results from phase II of the Mainz neutrino mass searching tritium β decay". *The European Physical Journal C* 40 (2005), p. 447.

[78] V. N. Aseev et al. "Upper limit on the electron antineutrino mass from the Troitsk experiment". *Physical Review D* 84 (2011), p. 112003.

[79] Particle Data Group. "The Review of Particle Physics (2006)". *Journal of Physics G: Nuclear and Particle Physics* 33.1 (2006).

[80] E. W. Otten and C. Weinheimer. "Neutrino mass limit from tritium β decay". *IOP Science, Reports on Progress in Physics* 71.086201 (2008).

[81] G. Drexlin et al. "Current Direct Neutrino Mass Experiments". *Advances in High Energy Physics* 2013.293986 (2013).

[82] KATRIN Collaboration. "KATRIN Design Report 2004". *FZKA Scientific Report* 7090 (2005).

[83] L. Kuckert et al. "Modelling of gas dynamical properties of the Katrin tritium source and implications for the neutrino mass measurement". *Vacuum* 158 (2018), p. 195.

[84] KATRIN Collaboration. "An improved upper limit on the neutrino mass from a direct kinematic method by KATRIN". *arXiv:1909.06048* (2019).

[85] Project 8 Collaboration. "Determining the neutrino mass with cyclotron radiation emission spectroscopy-Project 8". *Journal of Physics G: Nuclear and Particle Physics* 44.5 (2017).

[86] W. C. Pettus. "Overview of Project 8 and Progress Towards Tritium Operation". *arXiv:1710.01826* (2017).

[87] Project 8 Collaboration. "Project 8: Determining neutrino mass from tritium beta decay using a frequency-based method". *arXiv:1309.7093* (2013).

[88] HOLMES Collaboration. "Measuring the electron neutrino mass with improved sensitivity: the HOLMES experiment". *arXiv:1612.03947* (2017).

[89] NuMECS Collaboration. "Development of Holmium-163 Electron-Capture Spectroscopy with Transition-Edge Sensors". *J Low Temp Phys* 184 (2016), p. 958. DOI: 10.1007/s10909-015-1451-2.

[90] ECHo Collaboration. "Recent Results for the ECHo Experiment". *J Low Temp Phys* 184 (2016), p. 910. DOI: 10.1007/s10909-016-1541-9.

[91] ECHo Collaboration. "Direct Measurement of the Mass Difference of ^{163}Ho and ^{163}Dy Solves the Q-Value Puzzle for the Neutrino Mass Determination". *Physical Review Letters* 115 (2015), p. 062501.

[92] L. I. Bodine, D. S. Parno, and R. G. H. Robertson. "Assessment of molecular effects on neutrino mass measurements from tritium β decay". *Physical Review C* 91 (2015), p. 035505.

[93] R. G. H. Robertson and D. A. Knapp. "Direct Measurements of Neutrino Mass". *Annual Review of Nuclear and Particle Science* 38 (1988), p. 185.

[94] D. H. Wilkinson. "Small terms in the beta-decay spectrum of tritium". *Nucl. Phys. A* 526 (1991), pp. 131–140. DOI: 10.1016/0375-9474(91)90301-L.

[95] S. Gardner, V. Bernard, and U. G. Meissner. "Radiative tritium beta-decay and the neutrino mass". *Phys. Lett. B* 598 (2004), pp. 188–196. DOI: 10.1016/j.physletb.2004.08.006. arXiv: hep-ph/0407077 [hep-ph].

[96] F. Simkovic, R. Dvornicky, and A. Faessler. "Exact relativistic tritium beta-decay endpoint spectrum in a hadron model". *Phys. Rev. C* 77 (2008), p. 055502. DOI: 10.1103/PhysRevC.77.055502. arXiv: 0712.3926 [hep-ph].

[97] D. Parno. *Plot Origin*. dparno@cmu.edu.

[98] A. Saenz, S. Jonsell, and P. Froelich. "Improved Molecular Final-State Distribution of HeT^+ for the β-Decay Process of T_2". *Phys. Rev. Lett.* 84 (2000), pp. 242–245. DOI: 10.1103/PhysRevLett.84.242.

[99] N. Doss et al. "Molecular effects in investigations of tritium molecule β decay endpoint experiments". *Physical Review C* 73 (2006), p. 025502.

[100] B. H. Bransden and C. J. Joachain. *Physics of Atoms and Molecules*. 2nd ed. Pearson, 2003.

[101] W. Kołos and L. Wolniewicz. "Accurate Computation of Vibronic Energies and of Some Expectation Values for H_2, D_2, and T_2". *J. Chem. Phys.* 41.12 (1964), pp. 3674–3678. DOI: http://dx.doi.org/10.1063/1.1725797. URL: http://scitation.aip.org/content/aip/journal/jcp/41/12/10.1063/1.1725797.

[102] N. Doss et al. "Molecular effects in investigations of tritium molecule β decay endpoint experiments". *Phys. Rev. C* 73 (2006), p. 025502. DOI: 10.1103/PhysRevC.73.025502.

[103] David M. Bishop and Lap M. Cheung. "Rigorous theoretical investigation of the ground state of H_2". *Phys. Rev. A* 18 (5 Nov. 1978), pp. 1846–1852. DOI: 10.1103/PhysRevA.18.1846. URL: http://link.aps.org/doi/10.1103/PhysRevA.18.1846.

[104] B. G. Anex. "Ground State of the HeH^+ Molecule Ion". *J. Chem. Phys.* 38 (1963), p. 1651. DOI: 10.1063/1.1776937.

[105] J. D. Stuart and F. A. Matsen. "One-Center Wavefunction for the Ground State of the HeH^+ Molecular Ion". *J. Chem. Phys.* 41 (1964), p. 1646. DOI: 10.1063/1.1726137.

[106] H. H. Michels. "Molecular Orbital Studies of the Ground and Low-Lying Excited States of the HeH^+ Molecular Ion". *J. Chem. Phys.* 44 (1966), p. 3834. DOI: 10.1063/1.1726541.

[107] O. Fackler et al. "Accurate theoretical β-decay energy spectrum of the tritium molecule and its neutrino mass dependence". *Phys. Rev. Lett.* 55 (1985), p. 1388. DOI: 10.1103/PhysRevLett.55.1388.

[108] R. L. Martin and J. S. Cohen. "Excitation and ionization accompanying the beta decay of T_2". *Phys. Lett. A* 110 (1985), p. 95. DOI: 10.1016/0375-9601(85)90327-5.

[109] Y. V. Vanne and A. Saenz. "Numerical treatment of diatomic two-electron molecules using a B-spline based CI method". *J. Phys. B.: At. Mol. Opt. Phys.* 37 (2004), p. 4101. DOI: 10.1088/0953-4075/37/20/005.

[110] N. Doss. "Calculated final state probability distributions for T_2 β-decay measurements". PhD thesis. University of London, 2007.

[111] S. Jonsell, A. Saenz, and P. Froelich. "Neutrino-mass determination from tritium β decay: Corrections to and prospects of experimental verification of the final-state spectrum". *Physical Review C* 60.034601 (1999).

[112] D. K. Veirs and G. M. Rosenblatt. "Raman Line Positions in Molecular Hydrogen: H_2, HD, HT, D_2, DT, and T_2". *J. Molec. Spectrosc.* 121 (1987), p. 401. DOI: 10.1016/0022-2852(87)90058-0.

[113] M.-C. Chuang and R. N. Zare. "Rotation-Vibration Spectrum of HT: Line Position Measurements of the 1-0, 4-0, and 5-0 Bands". *J. Molec. Spectrosc.* 121 (1987), p. 380. DOI: 10.1016/0022-2852(87)90057-9.

[114] A. Carrington et al. "Infrared bound to quasibound vibration-rotation spectrum of HeH^+ and its isotopes". *Chem. Phys.* 81 (1983), p. 251. DOI: 10.1016/0301-0104(83)85319-1.

[115] M. W. Crofton et al. "Infrared spectra of $^4HeH^+$, $^4HeD^+$, $^3HeH^+$, and $^3HeD^+$". *J. Chem. Phys.* 91 (1989), p. 5882. DOI: 10.1063/1.457456.

[116] F. Matsushima, T. Oka, and K. Takagi. "Observation of the Rotational Spectra of $^4HeH^+$, $^4HeD^+$, $^3HeH^+$, and $^3HeD^+$". *Phys. Rev. Lett.* 78 (1997), p. 1664. DOI: 10.1103/PhysRevLett.78.1664.

[117] H. G. M. Edwards, D. A. Long, and H. R. Mansour. "Pure Rotational and Vibration-Rotational Raman Spectra of Tritium, $^3H_2$". *J. Chem. Soc., Faraday Trans. 2* 74 (1978), p. 1203. DOI: 10.1039/F29787401203.

[118] H. G. M. Edwards et al. "The pure rotational and vibration-rotational Raman spectra of $^1H^3H$ and $^2H^3H$". *J. Raman Spectrosc.* 8 (1979), p. 251. DOI: 10.1002/jrs.1250080507.

[119] D. E. Tolliver, G. A. Kyrala, and W. H. Wing. "Observation of the infrared spectrum of the helium-hydride molecular ion $^4HeH^+$". *Phys. Rev. Lett.* 43 (1979), p. 1719. DOI: 10.1103/PhysRevLett.43.1719.

[120] A. Carrington et al. "Observation of bound to quasibound vibration-rotation transitions in the HeH^+ ion". *Molecular Physics* 44.5 (1981), pp. 1233–1237. DOI: 10.1080/00268978100103151. eprint: http://dx.doi.org/10.1080/00268978100103151. URL: http://dx.doi.org/10.1080/00268978100103151.

[121] P. Bernath and T. Amano. "Detection of the infrared fundamental band of HeH^+". *Phys. Rev. Lett.* 48 (1982), p. 20. DOI: 10.1103/PhysRevLett.48.20.

[122] D.-J. Liu, W.-C. Ho, and T. Oka. "Rotational spectroscopy of molecular ions using diode lasers". *J. Chem. Phys.* 87 (1987), p. 2442. DOI: 10.1063/1.453084.

[123] Z. Liu and P. B. Davies. "Infrared laser absorption spectroscopy of rotational and vibration rotational transitions of HeH^+ up to the dissociation threshold". *J. Chem. Phys.* 107 (1997), p. 337. DOI: 10.1063/1.474394.

[124] Z. Liu and P. B. Davies. "Measurement of the pure rotational quasibound spectrum of HeH^+ in a laboratory plasma by direct laser absorption". *Phys. Rev. Lett.* 79 (1997), p. 2779. DOI: 10.1103/PhysRevLett.79.2779.

[125] J. Purder et al. "Diode laser spectra and potential energy curve for the molecular ion HeH^+". *J. Molec. Spectrosc.* 153 (1992), p. 701. DOI: 10.1016/0022-2852(92)90504-H.

[126] W. Y. Fan et al. "Infrared laser spectrum of high J pure rotational transitions of $^4HeD^+$". *Chem. Phys. Lett.* 298 (1998), p. 222. DOI: 10.1016/S0009-2614(98)01185-3.

[127] C.E. Blom, K. Möller, and R.R. Filgueira. "Gas discharge modulation using fast electronic switches: application to HeH^+". *Chemical Physics Letters* 140.5 (1987), pp. 489–492. ISSN: 0009-2614. DOI: http://dx.doi.org/10.1016/0009-2614(87)80474-8. URL: http://www.sciencedirect.com/science/article/pii/0009261487804748.

[128] I. Dumitriu and A. Saenz. "Photodissociation of the HeH^+ molecular ion". *J. Phys. B.: At. Mol. Opt. Phys.* 42 (2009), p. 165101. DOI: 10.1088/0953-4075/42/16/165101.

[129] H. B. Pedersen et al. "Crossed Beam Photodissociation Imaging of HeH^+ with Vacuum Ultraviolet Free-Electron Laser Pulses". *Phys. Rev. Lett.* 98 (2007), p. 223202. DOI: 10.1103/PhysRevLett.98.223202.

[130] A. H. Snell, F. Pleasonton, and H. E. Leming. "Molecular dissociation following radioactive decay: Tritium hydride". *Journal of Inorganic and Nuclear Chemistry* 5.2 (1957), p. 112.

[131] S. Wexler. "Dissociation of TH and T_2 by β-decay". *Journal of Inorganic and Nuclear Chemistry* 10.1-2 (1959), p. 8.

[132] TRIMS Collaboration. *TRIMS ELOG and Unidoc Entries*. dparno@cmu.edu, rghr@u.washington.edu.

[133] L. Bodine. *Plot Origin*. lbodine@u.washington.edu.

[134] R. V. Latham. *High Voltage Vacuum Insulation: Basic Concepts and Technological Practice*. 1st ed. Academic Press, 1995, p. 229.

[135] A. A. Neuber et al. "The Role of Outgassing in Surface Flashover under Vacuum". *IEEE Trans. Plasma Sci.* 28 (2000), p. 1593.

[136] M. Kallander. *Plot Origin*. mkallander94@gmail.com.

[137] T. Burritt. *Plot Origin*. thb@u.washington.edu.

[138] Autodesk. *Autodesk Inventor*. Version 22.0. 2018. URL: `https://www.autodesk.com/products/inventor/overview`.

[139] H. F. Dylla. "Glow discharge techniques for conditioning high-vacuum systems". *Journal of Vacuum Science & Technology A* 6.1276 (1988).

[140] R. G. H. Robertson. *Internal Contribution*. rghr@u.washington.edu.

[141] G. F Knoll. *Radiation Detection and Measurement*. 4th ed. WILEY-VCH, 2010.

[142] P. M. Stier and C. F. Barnett. "Charge exchange cross sections of hydrogen ions in gases". *Physical Review* 103 (1956), p. 896.

[143] *Manual: Leybold-Heraeus, Ionivac Gauge Tubes and Nude Gauge Heads*. Atlas Copco.

[144] P. R. Norton and P. J. Richards. "Hydrogen isotope chemisorption and equilibration on platinum". *Surface Science* 41 (1974), p. 293.

[145] E. A. McCutchan. "Nuclear Data Sheets for A = 83". *Nuclear Data Sheets* 125 (2015), p. 263.

[146] D. Vénos et al. "Properties of ^{83m}Kr conversion electrons and their use in the KATRIN experiment". *Journal of Instrumentation* 13 (2018).

[147] C. D. Nesaraja. "Nuclear Data Sheets for A = 241". *Nuclear Data Sheets* 130 (2015), p. 183.

[148] *Manual: Passivated Implanted Planar Silicon (PIPS) Detectors*. CANBERRA Industries, Inc. 2012.

[149] D. Peterson. *Custom built at CENPA*. dp33@uw.edu.

[150] T. V. Wechel. *Custom built at CENPA*. timvanw@uw.edu.

[151] L. I. Bodine. "Molecular Effects in Tritium Beta-Decay Neutrino-Mass Measurements". PhD thesis. University of Washington, 2015.

[152] *Manual: Technical Information Manual, MOD. DT5720, 4 CHANNEL 12 BIT, 250 MS/S DIGITIZER*. Version Revision n. 5. CAEN - Tools for Discovery. Feb. 6, 2012.

[153] J. M. Pfotenhauer BZ Maytal. *Miniature Joule-Thomson Cryocooling: Principles and Practice*. Springer, 2013.

[154] ChemicaLogic Corporation. *CO_2 Mollier Diagram (Pressure-Enthalpy Diagram)*. 1999. URL: http://www.chemicalogic.com/Documents.

[155] T. Burritt. *Custom built at CENPA*. thb@u.washington.edu.

[156] M. Kallander. *Internal Contribution*. mkallander94@gmail.com.

[157] G. Spieler. *Semiconductor Detector Systems*. Oxford Science Publications, 2005.

[158] E. Machado. *Internal Contribution*. emachado@uw.edu.

[159] R. Ostertag. *Internal Contribution*. raphael.ostertag@student.kit.edu.

[160] S. Agostinelli et al. "Geant4: A Simulation toolkit". *Nucl. Instr. Meth. A* 506 (2003), p. 250. DOI: 10.1016/S0168-9002(03)01368-8.

[161] E. W. Weisstein. *Disk Point Picking. From MathWorld—A Wolfram Web Resource*. URL: http://mathworld.wolfram.com/DiskPointPicking.html.

[162] E. W. Weisstein. *Sphere Point Picking. From MathWorld—A Wolfram Web Resource.* URL: http://mathworld.wolfram.com/SpherePointPicking.html.

[163] P. Renschler. "KESS - A new Monte Carlo simulation code for low-energy electron interactions in silicon detectors". PhD thesis. Karlsruhe Institute of Technology, 2011. URL: http://digbib.ubka.uni-karlsruhe.de/volltexte/documents/1919154.

[164] P. Dondero et al. "Electron backscattering simulation in Geant4". *Nuclear Instruments and Methods in Physics Research Section B: Beam Interactions with Materials and Atoms* 425 (2018), p. 18. DOI: 10.1016/j.nimb.2018.03.037.

[165] J. P. Biersackc J. F. Zieglera M. D. Zieglerb. "SRIM - The stopping and range of ions in matter (2010)". *Nucl. Instr. Meth. B* 268 (2010), p. 1818. DOI: 10.1016/j.nimb.2010.02.091.

[166] J. F. Zieglera et al. *SRIM - The Stopping and Range of Ions in Matter.* 2008.

[167] A. P. Vizcaya Hernández. *Internal Contribution.* avizcaya@andrew.cmu.edu.

[168] B. L. Wall et al. "Dead layer on silicon p–i–n diode charged-particle detectors". *Nucl. Instr. Meth. A* 744 (2014), p. 73. DOI: 10.1016/j.nima.2013.12.048.

[169] A. P. Vizcaya Hernández. *Plot Origin.* avizcaya@andrew.cmu.edu.

[170] *Manual: Introduction to COMSOL Multiphysics, Version: COMSOL 5.2.* COMSOLAB. 2015. URL: www.comsol.com.

[171] High Temp Metals. *Kovar Technical Data.* URL: https://www.hightempmetals.com/techdata/hitempKovardata.php.

[172] C. Heise et al. "Radiometric characterization of a Penning discharge in the vacuum ultraviolet". *Applied Optics* 33.22 (1994), p. 5111.

[173] M. A. Howe et al. "Sudbury neutrino observatory neutral current detector acquisition software overview". *IEEE* 51.3 (2004), p. 878.

[174] G. Holman. *IT at CENPA.* holman@uw.edu.

[175] Stefan Ritt. *ELOG*. Version 3.1.3. 2017. URL: https://elog.psi.ch.

[176] R. Brun and F. Rademakers. "ROOT - An Object Oriented Data Analysis Framework". *Nucl. Instr. & Meth. in Phys. Res. A* 389 (1997), p. 81. DOI: 10.1016/S0168-9002(97)00048-X.

[177] The Engineering Toolbox. *Thermocouples - types, principles and temperature ranges*. URL: https://www.engineeringtoolbox.com/thermocouples-d_496.html.

[178] D. Parno. *Internal Contribution*. dparno@cmu.edu.

[179] C. Claessens. *Plot Origin*. claessen@uni-mainz.de.

[180] R. F. Pierret. *Semiconductor Device Fundamentals*. Addison-Wesley Publishing Company, Inc., 1996.

[181] V. T. Jordanov and G. F. Knoll. "Digital synthesis of pulse shapes in real time for high resolution radiation spectroscopy". *Nuclear Instruments and Methods in Physics Research Section A* 345.2 (1994), p. 337.

[182] *Manual: Agilent 33220A 20 MHz Waveform Generator, User's Guide*. Agilent Technologies. May 4, 2007.

[183] Wikipedia. *Dynamic Equilibrium*. 2019. URL: https://en.wikipedia.org/wiki/Dynamic_equilibrium.

[184] P. R. Bevington and D. K. Robinson. *Data Reduction and Error Analysis*. 3rd ed. McGraw-Hill Education, 2003.